Optical Rectification in Semiconductor Waveguides.

By:

Valentín Loyo-Maldonado

A DISERTATION SUBMITTED FOR THE DEGREE OF

DOCTOR OF PHILOSOPHY

OF THE DEPARTMENT OF ELECTRONICS AND ELECTRICAL ENGINEERING

OF THE FACULTY OF ENGINEERING,

UNIVERSITY OF GLASGOW.

September 2002

Para Carmen y Sebastián

Abstract.

In this thesis, we study optical to microwave conversion and generation of ultrashort electrical pulses by the use of optical rectification at telecommunication wavelengths, $\lambda = 1550$ nm. By using optical rectification, an electromagnetic pulse is generated in a completely passive semiconductor waveguide. This pulse is coupled in a microwave transmission line with periodically loaded ground electrodes to create a velocity-matched structure. The optical waveguide and the microwave transmission line form the optical rectification device. Although in theory, the width of the electrical pulse in a travelling wave structure is limited only by the duration of the optical excitation pulse, imperfections in the velocity matching will attenuate and disperse most of the electrical pulse. The calculated effective optical refractive index of the rectification devices, $n_{opt} = 3.30$, matches the measured effective microwave index in one of our structures namely Dev068 ($n_{mw} = 3.30$). If the structure is slightly velocity-mismatched, losses as high as 14 dB/mm at frequencies of 1 THz will affect the propagation of the electrical pulse. The optical rectification device was fabricated using conventional photolithography techniques and e-beam lithography techniques. The advantages of e-beam lithography are: better pattern definition, perfect alignment and easier lift-off process. The only disadvantage is the cost associated with running the e-beam writer and maybe the time it takes to complete a pattern. The semiconductor material system of choice for the rectification devices is GaAs / AlGaAs due to its well-known large nonlinear coefficient. The use of GaAs/AlGaAs with light at $\lambda = 1550$ nm, presents serious absorption effects. The absorption effects mask the pure optical rectification signal and therefore must be minimised. The most significant absorption effect at $\lambda = 1550$ nm is two-photon absorption (TPA), which in more than one experiment gave us pulses of a few nanosecons duration. Our rectification device is engineered to minimise TPA, and this is the perhaps the hardest challenge in the design of the device. This also maybe the reason why there is not rectification devices such as ours reported in the literature working at $\lambda = 1550$ nm. The reason why we wanted to work with GaAs/AlGaAs is the potential integration of the rectification device in optoelectronic systems. In the

final rectification device, we could observe a clear polarization dependence of the generated signal indicating optical rectification. The signal detected was small in magnitude, ~75 dBm and on top of an offset signal which is believed to be TPA. Nevertheless, we proved that an optical rectification signal could be generated and detected by experimental means. Finally, Q-switched diode lasers in Al-quaternary material were fabricated and evaluated as possible sources for the rectification devices. The lasers produced a pulse train ranging from 1 GHz to 2 GHz depending on the bias current. We reckon that our measurement set-up is not ideal to characterize the rectification signal but is the simplest set-up capable of giving us an indicative result. The time domain observation of the optical rectification signal has still to be done and the integration of a photoconductive switch to the optical rectification device seems to be the most obvious solution to achieve this.

Acknowledgements.

First, I would like to thank the Consejo Nacional de Ciencia y Tecnología (CONACyT); México, for providing the financial support to carry on this research.

I would like to thank four people in particular who are, in a sense, the technical pillars of my formation as a scientist. Oscar Bárcenas, who constantly told me I had potential for carrying on further studies after my first degree. René de Jesús Romero Troncoso, who gave me his invaluable friendship during my MSc. and encourage me to do a PhD. Javier Sánchez Mondragón, who encouraged me and facilitate me the opportunity to pursue a PhD abroad. J. Stewart Aitchison, who accepted me in his research group and supervise my thesis in his very own way, letting you develop your own ideas fully but bringing you into perspective every now and then. Thank you all.

I would also like to thank my family, but I will do it so in Spanish.

Quiero aprovechar este espacio para agradecer a mis padres Valentín y María Magdalena por darme la mejor herencia que se le puede dar a un hijo: Educación. A mi hermana Ana Elena por apoyarme a través de los años. Espero

que la realización de esta tesis les devuelva algo de su apoyo en forma de satisfacción personal. Gracias.

Finalmente, quiero agradecer a dos personas muy especiales, mi esposa Carmen y mi hijo Sebastián, por compartir conmigo tantos momentos, buenos y no tan buenos, en el curso de la realización de esta investigación y la escritura de esta tesis. Quiero agradecer a Carmen en especial por su apoyo y comprensión durante mis largos años de estudiante los cuales culminan con este trabajo. Este apoyo incondicional es una de las razones por lo cual la quiero y admiro tanto. Muchas gracias y sigamos compartiendo nuestros sueños y ambiciones como familia.

List of figures.

List of tables.

List of publications.

Periodicals.

1. **V. Loyo-Maldonado**, H. K. Lee, C. R. Stanley, S. Venugopal-Rao, K. Moutzouris, M. Ebrahimzadeh, J. S. Aitchison, " Generation of Ultrashort Electrical Pulses in Semiconductor Waveguides," *IEEE Photonics Technology Letters*, vol. 15, pp. 428-430, 2003.
2. **V. Loyo-Maldonado**, S. D. McDougall, C. C. Button, J. H. Marsh and J. S. Aichison, "Demonstration of Passive Q-switching in multiquantum well InGaAs/AlGaInAs diode laser," *Electronics Letters*, Vol. 36, No. 11, pp. 952-953, 2000.

International Conferences.

1. **V. Loyo-Maldonado**, S. Venugopal-Rao, K. Moutzouris, M. Ebrahimzadeh, J. S. Aitchison, " Generation of Ultrashort Electrical Pulses in Semiconductor Waveguides," *Proceedings CLEO 2002*, pp. 256-257, Long Beach, Ca. May 2002.
2. **V. Loyo-Maldonado**, H. K. Lee, T. Lohdi, I. G. Thayne and J.S. Aitchison, "Design and fabrication of an Optical Rectification device," *Quantum Electronics and Photonics 15 Technical Digest*, p. 169, Glasgow, Scotland, September 2001
3. **V. Loyo-Maldonado** and J. S. Aichison, "Optical to Microwave conversion in Semiconductor Waveguides," *The Rank Prize Funds Mini-Symposium on Microwave Photonic Devices and Systems*, Grasmere, England, April 2000.
4. **V. Loyo-Maldonado**, S. D. McDougall, C. C. Button, J. S. Aichison and J. H. Marsh, "Demonstration of Passively Q-switched Multiple Quantum Wells Two-section InGaAs/AlGaInAs Diode Laser," *Proceedings LEOS annual meeting 1999*, vol. 2, p. 719, San Francisco Ca.

Contents

1. Introduction.

During the last decade, ultrafast phenomena have received a great deal of attention by research groups all over the world. Ultrafast devices and systems are an integral part of most research laboratories in photonics and electronics around the world. The continuous search for generation of shorter optical pulses have, in a way, pushed electronics to move to devices with faster response times. We can now see state of the art optoelectronic devices such as electro-absorption modulators and photo-receivers, available to be commercially deployed in 40 GHz telecommunication systems. Future generation of devices may not be too far away now that the time between the first demonstration in the laboratory of a device and its availability on the market has been greatly reduced in the past five years.

Microwave Photonics is the term that has been forged to refer to the study of optoelectronic devices and systems working at microwave frequencies and to the use of optoelectronic devices and systems for signal handling in microwave systems [1]. Photons in free space will always be faster than electrons in any media. While the generation of optical pulses of a few femtoseconds duration is commonly found in the literature, photodetectors (PD) with cut-off frequencies of only a few hundreds of GHz have been demonstrated in the laboratory. Hence, ultrashort optical pulses have always been measured using indirect methods such

as autocorrelation with a second-harmonic crystal. Optical to microwave conversion plays an important role in telecommunication systems where higher electrical bandwidths are constantly required. Higher bandwidth means shorter pulse generation and detection. Not only bandwidth is important, optical to microwave conversion using the minimum energy consumption (bias) will always be desirable. To find new and non-conventional ways of doing optical to microwave conversion is therefore imperative. Only by exploring this field, devices capable of covering up to THz frequencies can be created.

Optical to microwave conversion has predominantly been achieved with the use of photodetectors. A wide range of structures has bee reported in the literature and a comprehensive review can be seen in [2] and references therein. Here we will briefly describe the most common ones.

Waveguide photodetectors (WGPD) have been investigated extensively for the last two decades. The advantage of WGPD over a conventional broad-area PD is the close proximity of the absorptive layer and the contacts, which translate in much faster response times (higher bandwidth). Also, less voltage is require to drain the photo-excited carriers from the junction. WGPD are edge coupled p-i-n structures in a ridge configuration. The ridge width is commonly around 2 μm wide. Frequency response is limited by transit time effects and the depletion capacitance of the diode. To increase the electrical bandwidth of a WGPD, small device dimensions are require together with specific geometries to preserve the RC constant as small as possible. The material of choice for telecommunication applications is InGaAs/InP grown in semi-insulated InP (SI-InP) substrates. The absorptive region can be bulk semiconductor or can be form by multiple-quantum-wells (MQW). Bandwidths of 110 GHz at 1550 nm wavelength have been achieved using a mushroom-mesa waveguide p-i-n photodiode [3]. A very similar structure (mushroom-mesa) was used in a vertically illuminated PD (incident light perpendicular to the junction) resulting in bandwidth of 120 GHz at long wavelength [4].

Waveguide-fed Photodetectors consist in an input waveguide, which is optimised for coupling (not necessarily optimum for absorption), and a separate absorption

layer at certain distance of the input waveguide. The input waveguide can be designed to match the modal shape of the incoming light. The light is coupled into the semiconductor and then directed to the absorption layer by means of butt coupling or evanescent coupling. Evanescent coupling seems to be most efficient method of the two in optical and electrical terms. Waveguide-fed photodetectors using evanescent coupling have been reported in the literature with an electrical bandwidth of 70 GHz [2].

Travelling-wave photodetectors (TWPD) are perhaps the most popular PD configuration to date. As for WGPD, TWPD are edged coupled using a ridge structure. TWPD distribute the absorption along the length of the ridge avoiding heating and saturation at the facets. TWPD work under the principle of velocity matching between the optical and the electrical wave. The velocities to match are the electrical phase velocity and the optical group velocity. Although TWPD are p-i-n structures, if velocity-matched is achieved, the limitation of the RC constant intrinsic in lumped devices can be overcome. To obtain velocity matching, the metal electrodes of the TWPD are normally capacitive loaded to slow down the electrical wave. If perfect velocity-match could be achieved, then the bandwidth will be limited by the dispersion of the metal electrodes, which are commonly coplanar waveguide lines (CPW). As for the WGPD, the material of choice for telecommunication wavelengths is InGaAs/InP grown in SI-InP substrates. Bandwidths of above 100 GHz are commonly achieved in these structures. TWPD with bandwidth of 172 GHz have been reported in the literature before [5]. Optical Heterodyne millimetre wave generation using TWPD has also been used with success. An integrated photonics transmitter module using this technique can be seen in [6].

More recently, uni-travelling-carrier photodiodes (UTC-PD) with bandwidth of 310 GHz have been reported [7]. The structural feature of the UTC-PD is that the diode is configured with a p-type photoabsorption layer and a wide-gap electron collector layer [2]. The holes generated in the photoabsorption layer are majority carriers, which respond very quickly with dielectric relaxation time and therefore do not contribute to the photocurrent. The electrons in the other hand diffuse and travel through the depletion layer contributing to the photocurrent. If the

depletion layer is very thin, the electrons can drift at the overshoot velocity, which is five times higher than the saturation velocity. All the PD discussed above are summarised in table 1.1.

Table 1.1. Comparison between different PD structures.

Structure	Bandwidth (GHz)	Reference
WGPD	110	[3]
WG-fedPD	70	[2]
TWPD	172	[5]
UTC-PD	310	[7]

An alternative way to the PD to achieve optical to microwave conversion is the use of photoconductive switches. These devices are explained on detail in chapter 7. Photoconductive switches are surface illuminated metal-semiconductor-metal (MSM) structures. The semiconductor gap is typically biased at 5V. An optical beam in the form of an ultrashort pulse is used to hit the gap. The gap is effectively closed by the photo-exited carriers by an amount of time determined by the response of the semiconductor material. Pioneering work in these structures was done by Auston [8] in early 1970's. Photoconductive switches have always been a very popular research topic. Hence, is very easy to find reports in the literature where almost any kind of material is used in the gap. The most popular materials used in photoconductive switches are radiation-damaged Si (RD-Si), RD-GaAs, and low temperature grown GaAs (LT-GaAs). By exploiting the ultrafast recombination time of LT-GaAs, electrical pulses as short as 200 fs have been produced [9]. The main application for these switches is to generate ultrashort electrical pulses in transmission lines for terahertz time-domain spectroscopy [10].

All the photoconductors described above have an inherent maximum speed associated with the response of photo-excited carriers. This limitation is not severe if pulses of picoseconds or sub-picosecond duration are of interest. However, if the interest is to match ultrashort optical pulses (femtoseconds) then this limitation becomes critical. The use of non-linear effects to achieve optical to microwave conversion has been studied since early 1960's when nonlinear

optics was born (See for instance [11]). The use of nonlinear effects provides an instantaneous electrical response to an optical excitation and therefore ultrashort electrical pulses (femtoseconds) can be generated. Once the electrical pulse is generated, it can propagate on the sample's surface using transmission lines or it can propagate free-space as terahertz radiation. Nonlinear effects such as difference frequency mixing have been used to generate microwave signals [12], of up to 40 GHz [13]. However, when the aim is the generation of ultrashort electrical pulses, optical rectification is the preferred nonlinear effect. (*see for instance* [14] *and references therein for a review*).

The set-up for the generation of terahertz optical rectification can be described as follows. A sub-picosecond optical pulse excites the device, which is fabricated in a nonlinear material. This optical source is typically a Ti:Saphire lasers with pulse duration of less than 200 fs. The peak power can vary between tens of kilowatts to tens of megawatts depending on the substrate material and device configuration. Immediately after the optical pulse hits the device, an electromagnetic field is radiated with a far field proportional to the second time derivative of the dielectric polarization. The radiated electrical transient typically consist of one or one-and-a half oscillations of the electromagnetic and therefore has a broadband THz frequency bandwidth. To detect the electromagnetic radiation, a photo-conducting antenna is used in conjunction with a pump probe experimental set-up. At this point, a bipolar electrical pulse will appear at the terminals of the antenna. This pulse can propagate in a transmission line coupled to the antenna. Bandwidths as large as 30 THz have been obtained using terahertz optical rectification [15],[16]. The niche applications for this technique are terahertz spectroscopy and imaging.

Another possible way to exploit optical rectification is the generation of electrical transient directly in transmission lines. A detail review of this method is given in chapter 2. Optical rectification has been proposed as a potential solution for applications such as characterization of high-speed electronic devices, spectroscopy and characterization of transmission lines. The ultrashort electrical pulses required for these applications have commonly been produced so far by photoconductive switches, which, as mentioned above, exhibit a

fundamental limitation in response time related to the transient dynamics of the photo-exited carriers or propagation characteristics of the device. Apart of the use of optical rectification as an "alternative" to photoconductive switches, a metal-oxide-semiconductor (MOS) transistor gate controlled by the generated optical rectification signal has been proposed before [17]. Practical demonstration of guided light (waveguide) generating ultrashort electrical pulses via optical rectification has never been reported before. To the best of our knowledge, this thesis is the first demonstration of that [18]. Novel potential applications for these devices are discussed before the end of this chapter.

Optical rectification has historically been achieved in electro-optic (EO) crystals [11], [19], and only until mid 1990's, semiconductor crystals have been used as optical rectification media [20]. The interest in semiconductors is that they present higher nonlinear coefficients than EO crystals (See table 1.2). A higher nonlinear coefficient translates into a better optical to microwave conversion efficiency and, consequently, less input optical power is required to produce the electrical signal. Semiconductors also offer great potential for the integration of a nonlinear effect device (i.e. an optical rectification device) and state of the art InP or GaAs optoelectronic components. EO crystals, however, present an advantage over semiconductors: they do not suffer from absorption mechanisms. Absorption effects can easily mask an optical rectification signal. When using semiconductors as nonlinear media, the operating wavelength is > 8 μm where the main absorption mechanisms are greatly reduced. All the materials shown in table 1.2 have been used in optical rectification experiments. In addition, organic crystals [21] and polymers [22] have also been use successfully.

Optical rectification experiments are reported in a variety of nonlinear materials and in a variety of structures. A popular structure with rectification devices is the periodically poled $LiNbO_3$ [23], [24]. Here, the sign of the nonlinear coefficient of the material is periodically inverted along the optical propagation axis to improve the conversion efficiency. Bandwidths of around 1.7 THz have been achieved with these structures. Optical rectification can also been seen in new structures such as photonic crystals [25].

Table 1.2. Absolute magnitudes of second-order nonlinear coefficients measured by the SHG method at 1064 nm wavelength [26].

	Crystal	d_{ij}	Second-order nonlinear coefficient (pm/V)
Electro-optic	$LiNbO_3$	d_{33}	25.2
		d_{31}	4.6
	$LiTaO_3$	d_{33}	13.8
		d_{31}	0.85
	KTP	d_{33}	14.6
		d_{31}	3.7
		d_{32}	2.2
		d_{15}	3.7
		d_{24}	1.9
	KDP	d_{36}	0.39
	Quartz	d_{11}	0.30
Semiconductor	GaAs	d_{36}	**170**
	GaP	d_{36}	70.6
	ZnSe	d_{36}	53.8*
	CdTe	d_{36}	109

* at 852 nm

Despite of all the devices and materials currently available to perform optical to microwave conversion, the generation of terahertz signals via optical rectification in semiconductor waveguides at telecommunication wavelengths has never been achieved. In this thesis, the study a novel alternative to achieve high frequency optical to microwave conversion in semiconductor waveguides is presented. Being a nonlinear effect, optical rectification does not depend on the physics of carrier transport phenomena; it relies on the manipulation of the internal electrical dipoles of the material to generate an electrical polarization. The problems with absorption in semiconductors such as GaAs are minimised purely by device design and not by shifting the wavelength (longer) at which we perform the experiments. The aim of this research can be summarise as: ***The creation of a waveguide device capable of producing ultrashort electrical pulses at telecommunication wavelengths using optical rectification. The electrical pulses will be coupled in coplanar transmission lines obviating the need of microwave interfaces. The substrate material will be GaAs due to the high nonlinear coefficient and the great potential for integration.*** As an added benefit, this device is 100 % passive.

In principle, an optical rectification signal produced by continuous wave (CW) laser radiation can be detected and quantified, but to the best of our knowledge,

no one has yet managed to observe it experimentally. Both, CW and pulsed optical rectification experiments are detailed in this thesis. Semiconductor waveguides using the optical rectification effect (ORE) are of interest for the following reasons:

1. In principle, the ORE can be used to produce single electrical pulses of 10^{-12}-10^{-15} seconds duration, and to produce a series of ultrashort electrical pulses at repetition frequencies limited only by the modulation frequency of the light beam.
2. By using non-linear crystals (with a wide transmission band) in microwave systems, it is possible to obtain millimetre and sub-millimetre oscillators with operating frequencies governed by the parameters of the optical pulses which produce the ORE.
3. A non-linear crystal is a wide-band element with a temporal resolution exceeding the capacity of all existing photodetectors.
4. By using GaAs based semiconductor devices as the nonlinear crystal, compatibility with state of the art integrated optical and electronic circuits is assured.

As discussed above, current solid-state laser technology allows us to obtain femtosecond optical pulses with high peak powers. Semiconductor lasers have never been used for an ORE experiment due to their intrinsic power limitations. In the devices presented in this work, a semiconductor laser could be a real alternative as light sources. This is possible due to the relative low power required to operate our rectification devices. They use at least 3 orders of magnitude less power than the latest similar experiment reported in rectification. The combination of the semiconductor lasers with optical amplifiers and pulse compressors could be an alternative, which was not explored on this thesis.

The electrical signal obtained from our optical rectification device is expected to have the same shape and the same temporal resolution as the optical pulse. If we generate the ORE using picosecond, or femtosecond pulses, we expect to detect picosecond or femtosecond electrical pulses respectivelly. Obviously, dispersion effects have to be considered and pulse broadening is cannot be avoided.

Potentially, the ORE can produce electrical signals that exceed the resolution of the fastest sampling oscilloscopes. Due to this, and to the fact that sampling oscilloscopes suffer from relatively high noise levels, trigger jitter and reflections, the best way to characterise the electrical signal in the time domain is using photoconductive sampling. Photoconductive sampling utilises picosecond optical pulses to trigger photoconductive switches made normally from ion-bombarded semiconductor materials. Due to the time and effort spent in minimise all the parasitic effects that accompany optical rectification in our device, the integration of a photoconductive switch was not possible but it is strongly supported as future work. The rectification signals were detected in the frequency domain using a high frequency microwave probe and a microwave spectrum analyser with bandwidth resolution of 40 GHz.

As we have seen in the above paragraphs, the novelty of our rectification devices relies in the use of light at 1550 nm wavelength in a GaAs substrate. The use of a waveguide is also new. The applications for these rectification devices are:

1. Characterization of transmission lines. By studying the pulse propagation characteristics on transmission lines, attenuation and dispersion can be calculated and compared to numerical models.
2. As an alternative to conventional edge-coupled discrete photodetectors. The rectification devices are completely passive and do not require bias circuits for long arrays of photodetectors.
3. As in-line photodetectors. An electrical signal can be generated without absorbing or attenuating the optical signal more than the inherent propagation loss.
4. As receiver in telecommunication systems. Serving as interface between the optical backbone and wireless communications.
5. Underground applications. Reducing the power consumption and, therefore, the number of copper wires that need to be laid for underground optoelectronic systems that operate with active components such as photodetectors.
6. Intracavity optical to microwave conversion. If the nonlinear conversion is carried out intracavity in a mode-locked laser, with the RF output

replacing the optical output, then high optical peak intensities are available.

The fabrication facilities at the University of Glasgow allowed us to implement a system where generation (semiconductor lasers), conversion (optical rectification device) and detection (photoconductive switch) of the optical rectification signal can be achieved. This thesis describes the approach we have taken to achieve optical to microwave conversion in semiconductor optical waveguides using optical rectification.

This thesis is organised in seven chapters, this introduction being the first one. Chapter 2 describes the basis of optical rectification. It provides an historical background of experiments in optical rectification as well as a description of the material system used to fabricate the optical rectification devices. The design philosophy of the optical waveguide is also presented here. Chapter 3 explains all the loss mechanisms affecting the propagation of an optical pulse in a transmission line. It also explain the design of the slow-wave electrodes used to create a velocity-matched device and modelling results are compared with experimental characterisation of the transmission lines. Chapter 3 underlines the importance of a velocity-matched optical rectification device. Chapter 4 deals with all the issues related to the fabrication of a rectification device. Different fabrication methods are explored showing their advantages and disadvantages with respect to each other. Chapter 5 describes in detail all the experimentation done on the different generations of optical rectification devices, from initial trials with first generation devices, to optimised devices in a fourth generation where finally signs of rectification where recorded. Chapter 6 shows our approach in finding a semiconductor source that could be employed in conjunction with the rectification devices. The lasers described in chapter six are fabricated in Al-quaternary material system providing higher thermal stability to their counterpart P-quaternary systems. Chapter 7 gives a recommendation for future experiments and underlines the importance of the integration of a photoconductive switch with the rectification devices to provide temporal resolution of the electrical pulses. Finally, the thesis is summarised in a general conclusion.

1.1 References.

1. A. J. Seeds, "Microwave Photonics," *IEEE Trans on Microwave Theory and Techniques*, vol. 50, pp. 877-887, 2002.

2. K. Kato, "Ultrawide-Band/High-Frequency Photodetectors," *IEEE Trans on Microwave Theory and Techniques*, vol. 47, pp. 1265-1281, 1999.

3. K. Kato, A. Kozen, Y. Muramoto, Y. Itaya, T. Nagatsuma and M. Yaita, "110-GHz, 50%-Efficiency Mushroom-Mesa Waveguide p-i-n Photodiode for a 1.55-μm Wavelength," *IEEE Photonics Technology Letters*, vol. 6, pp. 719-721, 1994.

4. I-H Tan, C-K Sun, K. S. Giboney, J. E. Bowers, E. L. Hu, B. I. Miller and R. J. Capik, "120-GHz Long-Wavelength Low-Capacitance Photodetector with an Air-Bridged Coplanar Metal Waveguide," *IEEE Photonics Technology Letters*, vol. 7, pp. 1477-1479, 1995.

5. K. S. Giboney, R. L. Nagarajan, T. E. Reynolds, S. T. Allen, R. P. Mirin, M. J. W. Rodwell and J. E. Bowers, "Travelling-Wave Photodetectors with 172-GHz Bandwidth and 76-GHz Bandwidth-Efficiency Product," *IEEE Photonics Technology Letters*, vol. 7, pp. 412-414, 1995.

6. A. Stohr, R. Heinzelmann, K. Hagedorn, R. Gusten, F. Schafer, H. Stuer, F. Siebe, P. van der Wal, V. Krozer, M. Feiginov and D. Jager, "Integrated 460 GHz Photonics Transmitter Module," *Electronics Letters*, vol. 37, pp. 1347-1348, 2001.

7. H. Ito, T. Furuta, S. Kodama and T. Ishibashi, "InP/InGaAs Uni-Travelling-Carrier Photodiode with 310 GHz Bandwidth," *Electronics Letters*, vol. 36, pp. 1809-1810, 2000.

8. D. H. Auston, "Picosecond Optoelectronic Switching and Gating in Silicon," *Appl. Phys. Lett.* vol. 26, pp. 101-103, 1975.

9. U. D. Keil, D. R. Dykaar, "Electro-Optic Sampling and Carrier Dynamics at Zero Propagation Distance," *Appl. Phys. Lett.* vol. 61, pp. 1504-1506, 1992.

10. D. R. Grischkowsky, "Optoelectronic Characterization of Transmission Lines and Waveguides by Terahertz Time-Domain Spectroscopy," *IEEE Journal on Selected Topics in Quantum Electronics*, vol. 6, pp. 1122-1135, 2000.

11. M. Bass, P. A. Franken, J. F. Ward, and G. Weinreich, "Optical Rectification," *Phys. Rev. Letters*, vol. 9, pp. 446-448, 1962.

12. T. J. Hanlon, A. F. Fray, J. R. James, M. F. Lewis and P. Sample, "Improvement in Microwave Generation using Optical Difference Frequency Mixing," *Electronics Letters*, vol. 33, pp. 1808-1809, 1997.

13. T. Hori, K-H. Park, T. Kawanishi and M. Izutsu, "Generation of CW Millimeter Wave Signals in a Lithium Niobate Nonlinear Optical Waveguide Using Modulated Optical Input," *Jpn. J. Appl. Phys.* vol. 39, pp. L667-L669, 2000.

14. Y. H. Jin and X. C. Zhang, "Terahertz Optical Rectification," *Journal of Nonlinear Optical Physics and Materials*, vol. 4, pp. 459-495, 1995.

15. M. Joffre, A. Bonvalet, A. Migus, J.-L. Martin," Femtosecond Diffracting Fourier-Transform Infrared Interferometer," *Optics Letters*, vol. 21, pp. 964- 966, 1996.

16. Q. Wu and X.-C. Zhang, "Free-Space Electro-Optics Sampling of Mid-Infrared Pulses," *Appl. Phys. Lett.* vol. 71, pp. 1285-1286, 1997.

17. G. Moagar-Poladian, "An MOS transistor with an optical rectification controlled gate," *Semicond. Sci. Technol.*, vol. 12, pp. 210-216, 1997.

18 V. Loyo-Maldonado, H. K. Lee, C. R. Stanley, S. Venugopal-Rao, K. Moutzouris, M. Ebrahimzadeh and J. S. Aitchison, " Generation of Ultrashort Electrical Pulses in Semiconductor Waveguides," *IEEE Photonics Technology Letters*, vol. 15, pp. 428-430, 2003.

19. A. Nahata and T. F. Heinz, "Generation of subpicosecond electrical pulses by optical rectification," *Optics Letters*, vol. 23, pp. 867-869, 1998.

20. A. Rice, Y. Jin, X. F. Ma, X.-C. Zhang, D. Bliss, J. Larkin and M. Alexander, "Terahertz Optical Rectification from <110> Zinc-Blende Crystals," *Appl. Phys. Lett.* vol. 64, pp. 1324-1326, 1994.

21. T. J. Carrig, G. Rodriguez, T. S. Clement, A. J. Taylor and K. R. Stewart, "Scaling of Terahertz Radiation via Optical Rectification in Electro-Optic Crystals," *Appl. Phys. Lett.* vol. 66, pp. 121-123, 1995.

22. A. Nahata, "Nonlinear Optical Generation and Detection of Ultrashort Electrical Pulses in Transmission Lines," *Optics Letters*, vol. 26, pp. 385-387, 2001.

23. Y.-S. Lee, T. Meade, V. Perlin, H. Winful, T. B. Norris and A. Galvanauskas, "Generation of Narrow-Band Terahertz Radiation via Optical Rectification of Femtosecond Pulses in Periodically Poled Lithium Niobate," *Appl. Phys. Lett.* vol. 76, pp. 2505-2507, 2000.

24. C.Weiss, G. Torosyan, J.-P Meyn, R. Wallenstein, R. Belgang and Y. Avetisyan, "Tuning Characteristics of Narrowband THz Radiation Generated via Optical Rectification in Periodically Poled Lithium Niobate," *Optics Express*, vol. 8, pp. 497-502, 2001.

25. L. Yan-Qing, X. Min and G. J. Salamo, "Coherent Microwave Generation in a Nonlinear Photonic Crystal," *IEEE Journal of Quantum Electronics*, vol. 38, pp. 481-485, 2002.

26. I. Shoji, T. Kondo, A. Kitamoto, M. Shirane and R. Ito, "Absolute scale of second-order nonlinear-optical coefficients," *J. Opt. Soc. Am. B*, vol. 14, pp. 2268-2294, 1997.

2. Optical Rectification.

2.1 Introduction.

Optical rectification is a second order nonlinear effect, which can be used to generate an electrical signal in a totally passive device such as an optical waveguide. The gallium arsenide (GaAs) based system is one of the best nonlinear materials due to the large nonlinear coefficient at the communication wavelengths ($\chi_{14}^{(2)}$= 238 pm/V at λ = 1.548 μm [1]). Optical rectification in GaAs waveguides can be exploited to achieve optical to microwave conversion, which is of interest at the interface of wireless and optical communication systems. In addition, the mature fabrication technology of GaAs based semiconductor devices offers the potential for monolithic integration of the optical rectification waveguides with other key components, such as semiconductor lasers, optical switches, multiplexers and demultiplexers and photoconductive switches. Semiconductor lasers and photoconductive switches are particularly relevant in this work.

In this chapter, the optical rectification effect (ORE) is explained with the help of some basic equations and a discussion of its physical origin given. The original work in optical rectification, as well as some of the most relevant recent works are presented and reviewed. While there has been a considerable amount of

research done in optical rectification in particular as the main mechanism for terahertz generation (see for instance [2]), we concentrate here on the use of optical rectification to generate ultrashort electrical pulses on transmission lines contained within the same device. Being the material of choice, the relevant properties of the GaAs/AlGaAs material system are also covered in this chapter. Finally, the basic requirements to create an optimum device to detect the ORE signal in GaAs waveguides are presented in the final section of the chapter.

It is important to mention at this point that, to the best of our knowledge, experimental observation of the ORE in GaAs at λ=1.55 μm has not been reported in a clearly identifiable way before.

2.2 The optical rectification effect (ORE).

Optical rectification is a second order nonlinear effect, and usually refers to the generation of a dc electric polarization by an intense optical beam propagating in a nonlinear medium [3]. As explained in previous works on optical rectification [4], the simplest nonlinear dependence of the optical polarization P on an applied optical electric field E is:

$$P \alpha E^2 . \tag{2.1}$$

Suppose that a lightwave is incident on the medium and E has a $\cos(\omega t)$ time dependence, then this nonlinear relation predicts,

$$P \alpha \cos^2 \omega t = \tfrac{1}{2}(1+\cos 2\omega t). \tag{2.2}$$

That part of the polarization in Eq. (2.2) with a $\cos(2\omega t)$ dependence is responsible for the generation of second harmonic signals from certain crystals. The unit term describes the steady polarization referred to as optical rectification.

In a more detailed way, the nonlinear coefficient tensor d, forms a 3x6 matrix interacting with the $\mathbf{E}^2$ tensor inducing a polarization $\mathbf{P}$ according to:

$$\begin{pmatrix} P_x \\ P_y \\ P_z \end{pmatrix} = \begin{pmatrix} d_{11} & d_{12} & d_{13} & d_{14} & d_{15} & d_{16} \\ d_{21} & d_{22} & d_{23} & d_{24} & d_{25} & d_{26} \\ d_{31} & d_{32} & d_{33} & d_{34} & d_{35} & d_{36} \end{pmatrix} \begin{pmatrix} E_x^2 \\ E_y^2 \\ E_z^2 \\ 2E_yE_z \\ 2E_zE_x \\ 2E_xE_y \end{pmatrix} . \qquad (2.3)$$

GaAs is a class $\bar{4}3m$ crystal and has only one independent nonvanishing second-order nonlinear coefficient, namely, $d_{14} = d_{25} = d_{36}$, all other terms are equal to zero. Therefore, Eq. (2.3) for GaAs becomes,

$$P_x = 2d_{14}E_yE_z \qquad (2.4a)$$

$$P_y = 2d_{14}E_zE_x \qquad (2.4b)$$

$$P_z = 2d_{14}E_xE_y \qquad (2.4c)$$

If the two electric fields involved in a particular direction of the polarization have frequency dependence ω, then Eq. (2.4c), for instance, will be:

$$P_z^{(0:\omega-\omega)} = 2d_{14}^0 E_x^\omega E_y^\omega \qquad (2.5a)$$

and $$P_z^{(2\omega:\omega+\omega)} = 2d_{14}^{2\omega} E_x^\omega E_y^\omega \qquad (2.5b)$$

where d_{14}^0 and $d_{14}^{2\omega}$ are the representations for the optical rectification coefficient and the second harmonic generation coefficient respectively. Equation (2.5a) corresponds to optical rectification whilst Eq. (2.5b) corresponds to second harmonic generation. In the case, that one of the electric fields has dc dependence, Eq. (2.4a) will be:

$$P_x^{(\omega:\omega\pm0)} = 2d_{14}^\omega E_y^\omega E_z^0 \qquad (2.6)$$

Equation (2.6) describes the electro-optic effect. The fact that $d_{14}^{0} = d_{14}^{\omega}$, independent of crystal symmetry considerations, shows the close relationship between the ORE and the electro-optic effect.

2.2.1 The physical origin of optical rectification.

The physical origin of the nonlinearities in zincbende material is directly related to the bonding of the two different atoms, which form the lattice. In the case of GaAs, the partly covalent and partly ionic nature of the bonding between the Ga and As atoms in the crystal generates an uneven charge distribution in the bonding. This uneven charge distribution creates a built-in dipole, which can be affected by an applied electric field, changing the optical properties of the material. If one, or more, of the optical properties of the material are changed proportionally to the square of the applied electric filed, then we can say that the material presents a second order nonlinearity. To be specific, the material property that is changed by the applied electric field is the refractive index. However, the change of refractive index is so small that generally they can only be detected when the amplitude of the electric field is of the same order of magnitude as the interatomic fields.

The instant response of the non-resonant nonlinearities, such as optical rectification, arises from the motion of the dipoles in the bonds, which act collectively to the optical excitation. In contrast, resonant nonlinearities arise from free carriers close to the bottom of the first conduction band (electrons) and close to the top of the valence band (holes). Resonant nonlinearities have a time constant associated with these carriers.

When an optical signal passes through a nonlinear material, it will generate an optical rectification polarization. If the optical signal is modulated, the optical rectification polarization will be a wave with a frequency equal to that of the modulation frequency. This can be understood by considering Fig. 2.1. The electric field of an optical carrier travelling at a frequency ω_{opt} can be described at any given time in terms of $E_{opt} = E_0 \cos \omega_{opt} t$. Equation 2.2 shows that the

electric field of the optical carrier will produce a constant (dc) polarization in the material (Fig 2.1a). This polarization is in principle possible to be measure. However, if we modulated the optical carrier at a frequency ω_{mod}, the steady polarization, will now be changing in time at a frequency proportional to ω_{mod} (Fig. 2.1b). In the same way, for a pulse of light, the optical rectification polarization will be an exact replica of the optical pulse (Fig. 2.1c). Ultrashort optical pulses are of interest on this thesis.

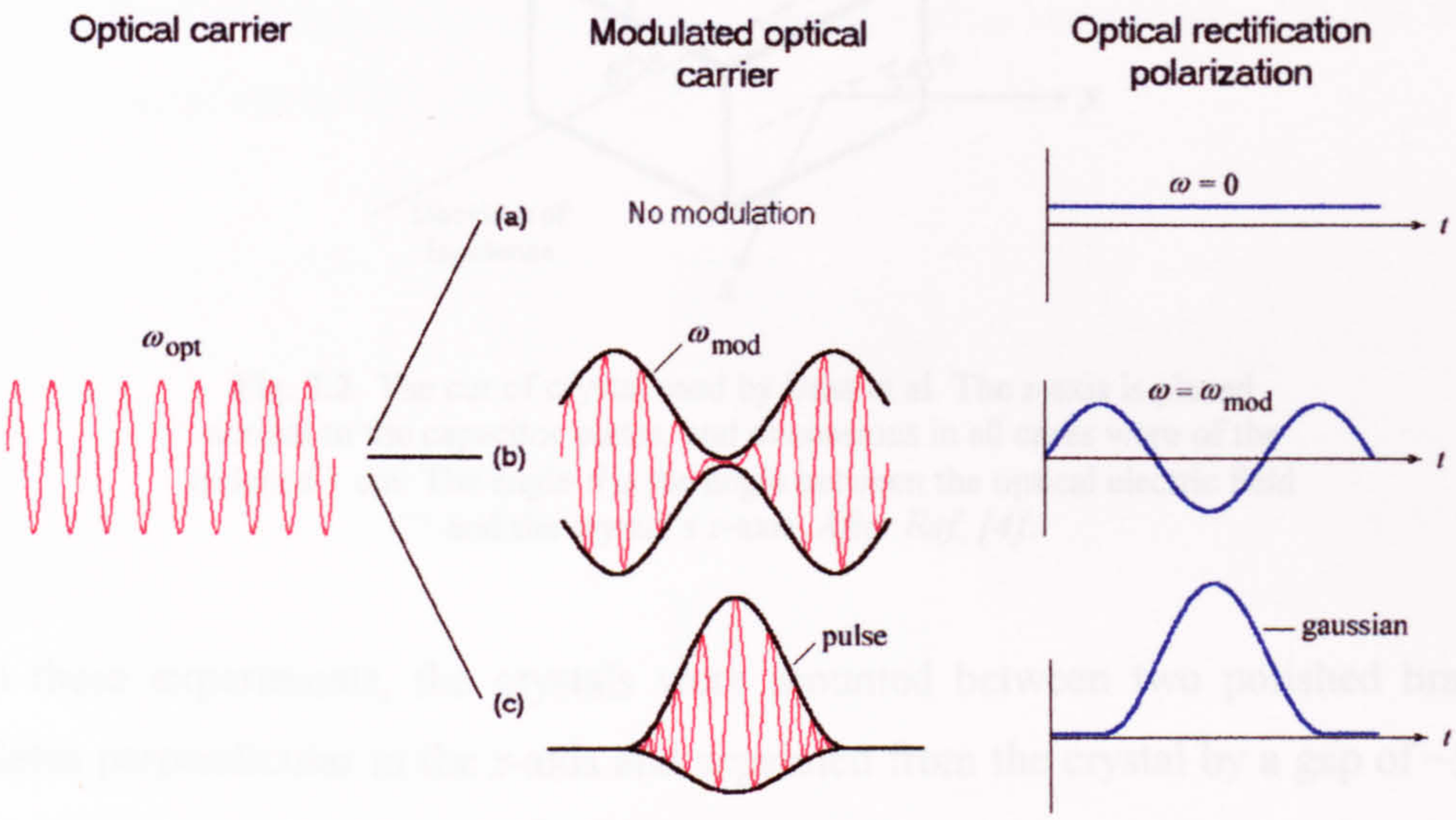

Fig. 2.1. Optical rectification polarization (ORP) for different modulation of the optical carrier. (a) For no modulation signal, the ORP is a steady dc polarization. (b) When the optical carrier is modulated with a sinusoidal signal, the ORP will be as well sinusoidal following the envelope of the modulated carrier. (c) In the same way, for a light pulse of gaussian shape, the ORP will be gaussian following the pulse shape.

2.3 History of optical rectification.

2.3.1 First observation of the ORE.

In the original work [5], the observation of a dc polarization accompanying the passage of an intense ruby laser beam through certain crystals was reported. The crystals used were potassium dihydrogen phosphate (KDP) and potassium dideuterium phosphate (KD_dP), which exhibit a large linear electro-optic effect. A high power ruby laser provided a linearly polarised (6943 Å) beam of light

with an intensity of ~ 1 MW and duration of 100 ns. The crystals of KDP and KD_dP were prepared in rectangular blocks of approximately 1 cm dimensions with highly polished surfaces. The *z*-axis was normal to the two faces and the *x* and *y*-axes intersected the other faces at 45° (Fig. 2.2).

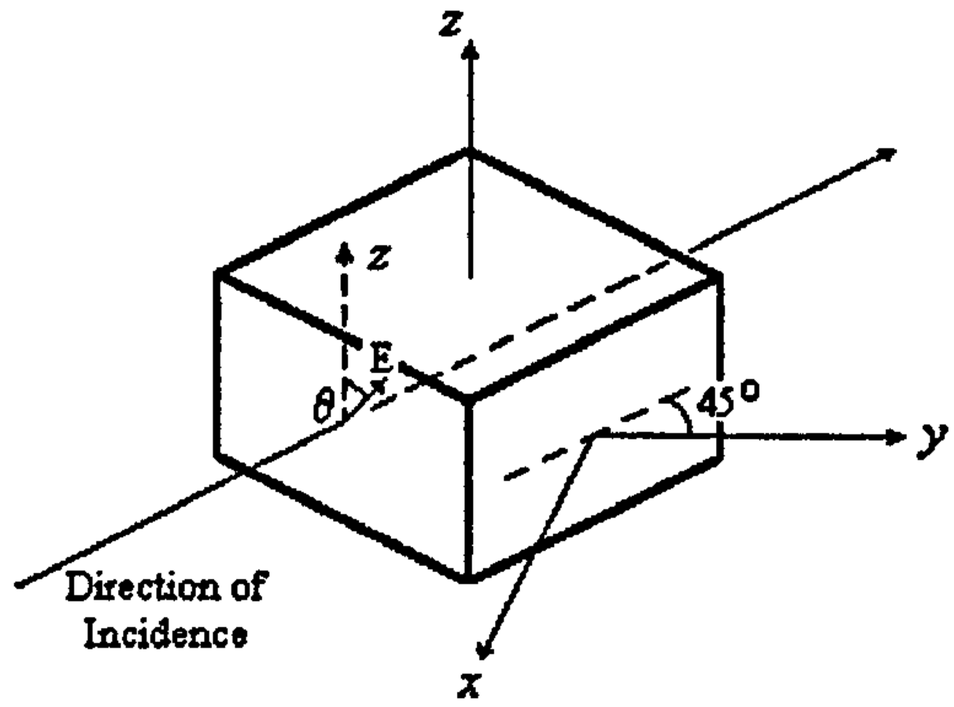

Fig. 2.2. The cut of crystal used by Bass et al. The *z*-axis is placed normal to the capacitor plates, and dimensions in all cases were of the order of 1 cm. The angle θ is the angle between the optical electric field and the crystal's *z*-axis. *After Ref. [4].*

In these experiments, the crystals were mounted between two polished brass plates perpendicular to the *z*-axis and separated from the crystal by a gap of ~50 μm (Fig. 2.3). This gap and the high polish of the plates and crystal minimised spurious effects due to scattered light and consequent pyroelectric phenomena. The laser beam was transmitted through the crystal normal to one of the faces, which contains the optical axis. The crystal and plate assembly formed a capacitor across which potentials appeared due to the laser-induced dc polarization in the crystal. This capacitor was coupled to a cathode follower, whose output was amplified by a wide band system and subsequently displayed on an oscilloscope. The laser beam intensity was monitored by a fast photocell after its passage through the crystal.

The ratio of the observed dc voltage, V_{dc} to the laser beam intensity I in the geometry shown in Fig. 2.2 was predicted by:

$$V_{dc}/I = K\beta \sin^2\theta \qquad (2.7)$$

Where θ is the angle between the optical electric field and the crystal z-axis, β is the dc effect coefficient [5] and K is a constant which depends on geometrical factors and circuit parameters. The experimental results matched very well with the $\sin^2$ behaviour predicted by Eq. (2.7).

Since the first observations of the ORE, many experiments related to this topic have been performed. For example: measurements of the optical rectification coefficients [4], [6], analysis of electromagnetic shock waves from transmission lines [7], electromagnetic radiated field due to optical rectification [8], [9] and generation of electrical pulses [10,11].

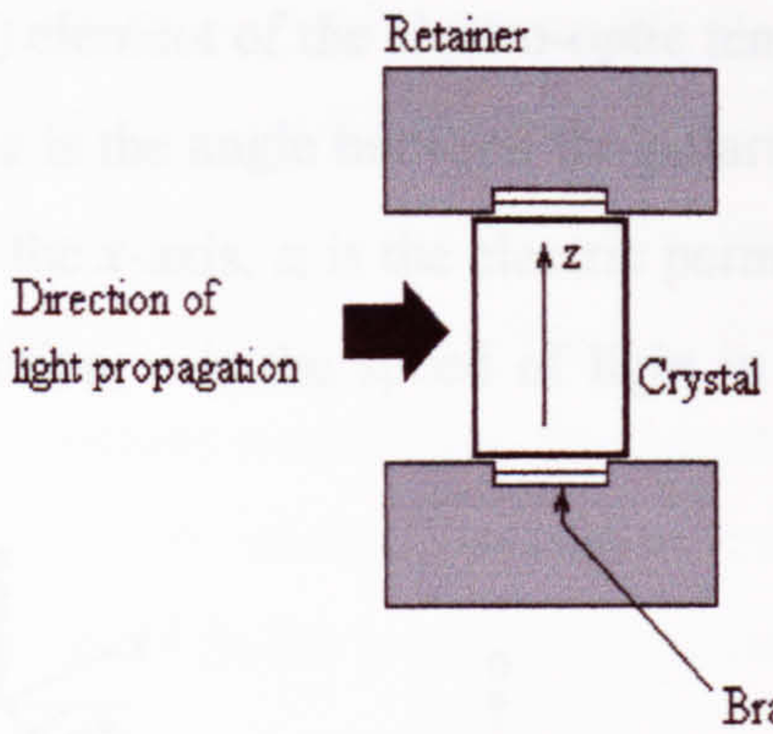

Fig. 2.3. A sectional view of the crystal-capacitor mounting. *After Ref.[4].*

There are some papers of particular interest to the work presented in this thesis, as they describe similar approaches to achieving electrical pulses from semiconductor and microwave waveguides. These papers are described in the next section.

2.3.2 Generation of electrical pulses using the ORE (a review).

In 1997, Moagar-Poladian [10] proposed a new kind of photodetector, based on a MOS transistor with an optical rectification controlled gate. The photodetector structure is shown schematically in Fig. 2.4. The device consists of a typical

MOS transistor structure to which a non-linear medium, *NM*, and an electrode area, *E1*, were added (see Fig. 2.4). The typical MOS transistor is formed by the *E2-DE-Sub* and *D-S* structure. The polarization direction of the light beam is perpendicular to the paper. The light beam propagates through the non-linear medium between the electrodes and a voltage due to the ORE is generated. With a structure like this, the total voltage required to drive the gate, V_T, is a superposition of the voltage applied from an external circuit, V_G, and the voltage due to optical rectification, V_{DC}, which is given by:

$$V_{DC} = \frac{\pi \chi_{zxy} d \sin 2\alpha}{2\varepsilon_i c} \Phi \tag{2.8}$$

where χ_{zxy} is the (zxy) element of the electro-optic tensor, d is the thickness of the non-linear medium, α is the angle between the polarization direction of the light beam with respect to the x-axis, ε_i is the electric permitivity of the medium along the propagation direction, c is the speed of light in vacuum and Φ is the light intensity.

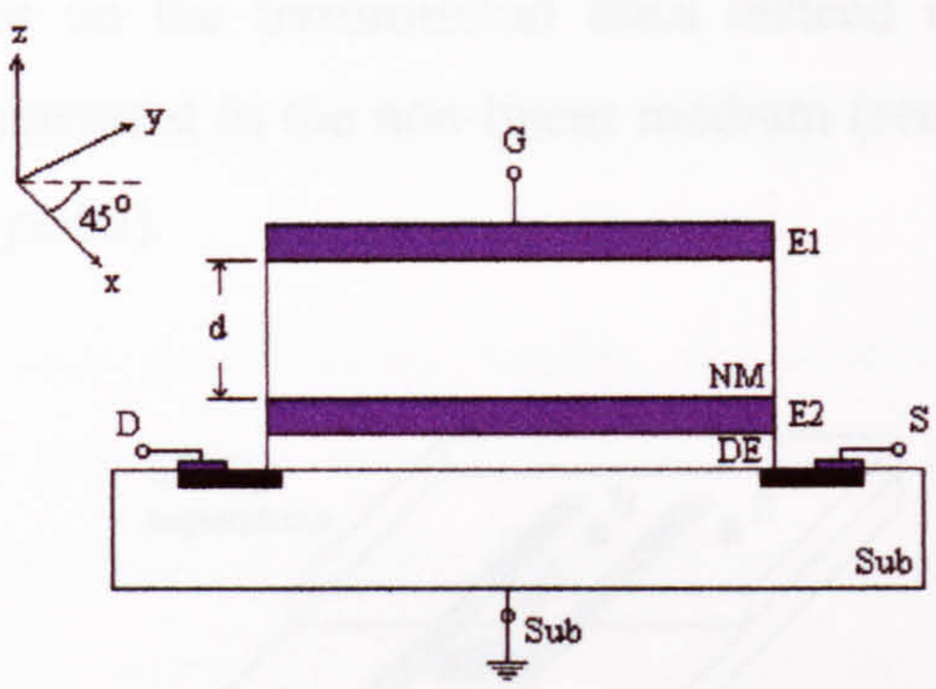

Fig. 2.4. Schematic diagram of the structure of the optical rectification MOS: *G*, gate; *E1*, upper electrode; *NM*, optical non-linear medium; *E2*, lower electrode; *DE*, dielectric; *D*, drain; *S*, source; *Sub*, substrate. *After Ref. [10].*

In this way, the transistor can be switched on and off only by controlling the light beam which is propagating in the *NM* region. The *NM* region can in principle be KDP or GaAs. This work does not present experimental results or even suggestions for the fabrication of the device but does present numerical results showing the electrical behaviour of the MOS transistor with this new kind of gate.

A more recent work was presented by Nahata and Heinz [11] in 1998. They describe the generation of sub-picosecond electrical pulses by using optical rectification of ultrashort optical pulses. The device used in the experiment is shown in Fig. 2.5, and is basically a coplanar strip-line geometry with a $LiTaO_3$ crystal superstrate acting as the non-linear medium. A photoconductive switch was defined by coplanar strips separated by an electrode gap.

A mode-locked Ti:Sapphire laser producing 160 fs pulses at 800 nm with a 76 MHz repetition rate was used as the optical source. The pump beam, with optical pulse energy of 0.65 nJ was positioned at point A and the temporal waveform of the sub-picosecond electrical pulse generated by optical rectification was observed. The effects on propagation by translating the pump beam to point B were also observed. No signal was observed in the absence of the $LiTaO_3$ crystal. When the pump beam was positioned at point C, the temporal waveform signal became a flat signal demonstrating that the measured electrical pulses were indeed guided waves on the transmission lines instead of freely propagating terahertz radiation generated in the non-linear medium (*see ref. [11] for the plot of the signal in each point*).

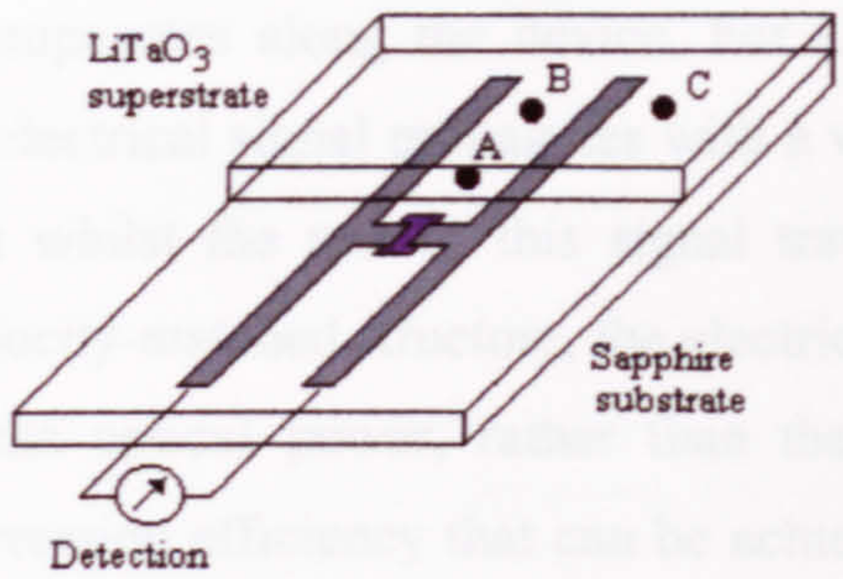

Fig. 2.5. Schematic drawing of the device with a coplanar strip-line transmission line and an integrated photoconductive switch. The $LiTaO_3$ crystal superstrate is bonded onto the device. Points A-C, represent the positions of the pump beam used in the experiment. *After Ref. [11].*

A complete work on optical rectification in waveguide like structures was presented by U. Peschel et al [12]. In this paper, they suggest an optical waveguide structure with a metal strip on the top and a doped substrate on the

bottom providing the electrodes to collect the electrical signal. (Fig. 2.6). A GaAs core is sandwiched between two AlAs layers to allow for optical guiding. Lateral confinement is provided by a rib etched into the cladding layer. The microwave field is created between both electrodes. This structure is designed to avoid losses due to free carrier absorption, and there is a small separation between the electrodes to provide a maximum overlap between optical and microwave fields.

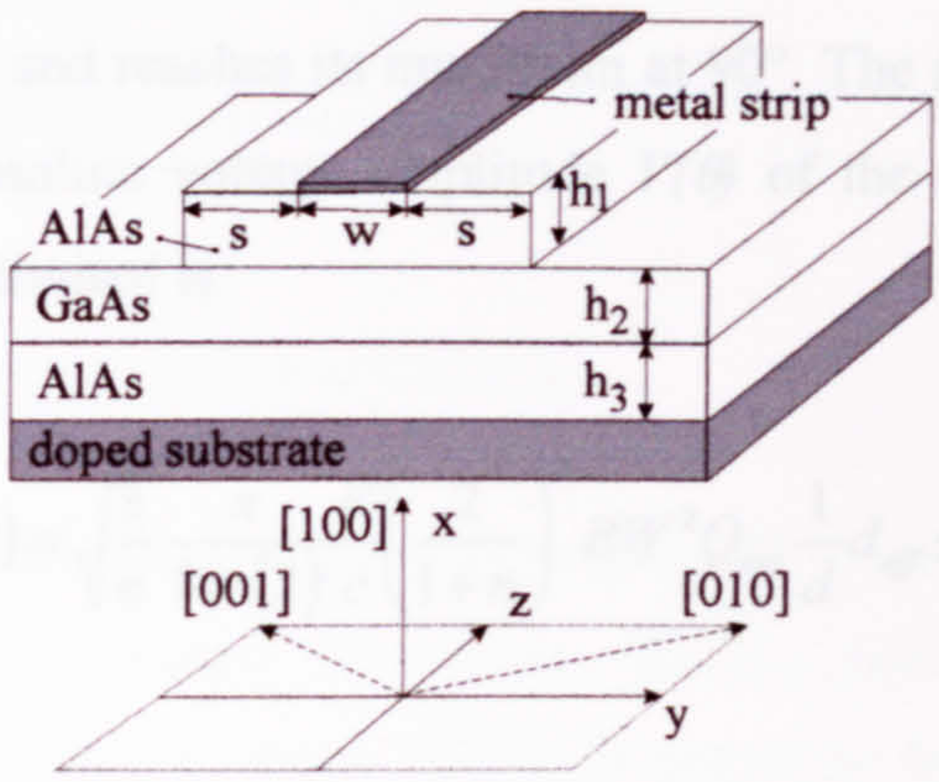

Fig. 2.6. Structure under investigation (top: geometry, bottom: coordinate system). *After Ref. [12].*

Their simulations show encouraging results; the optical pulse generates an electrical pulse that propagates along the device. For a non-velocity matched structure, most of the electrical signal propagates with a velocity dictated by the microwave waveguide whilst the rest of this signal travels together with the optical pulse. For a velocity-matched structure, the electrical field is proportional to the derivative of the optical power, rather than the optical power itself. Unfortunately, the conversion efficiency that can be achieved in waveguide like structures is very small.

Finally, the work reported by S. Graf et al. [13], is a very close experimental approach to the work described in this thesis. They used a SI-GaAs substrate as the nonlinear material. The light coupling into the SI-GaAs is from the [110]-cleaved edge. A gold layer evaporated on the topside of the slab with the ground metallization on the backside forms a microstrip structure. See Fig. 2.7. The

dimensions are d = 380 μm thick and l = 4.6 mm long. An optical rectification signal is obtained by exciting the device with light pulses of energy Q = 4μJ at a wavelength of 8 μm. The pulse width was on the range of 1ps to 6 ps. The signal shape closely follows the time derivative gaussian pulse with a width corresponding to the bandwidth of the sampling scope (36 GHz in this case). The plots in this paper show that the electrical signal obtained is in the order of 60 mV peak. Changing the angle of polarization of the incident beam proved that the signal was really been produced by optical rectification. The amplitude of the signal vanishes at 0° and reaches its maximum at 90°. The analytical expression they give for the absolute voltage amplitude $V(\theta)$ of the expected ORE peak signal, which is BW limited is:

$$V(\theta)=\sqrt{\frac{3}{e}}\frac{\pi}{8\ln(2)}\frac{R}{c}\left(\frac{2}{1+n}\right)^2 BW^2 Q_{ext}\frac{1}{d}d_{eff}\sin(\theta)^2 \qquad (2.9)$$

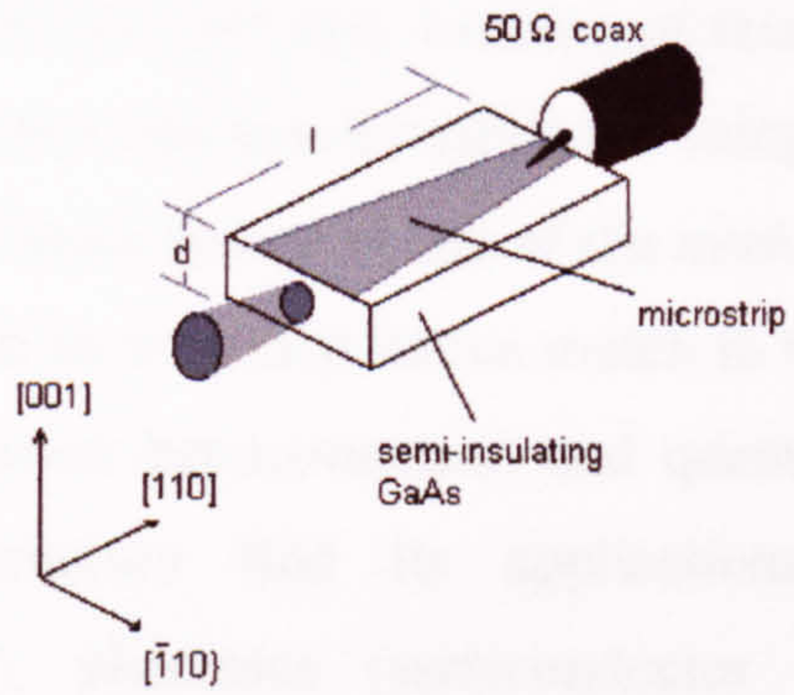

Fig. 2.7. Schematic structure of the ORE device with coaxial connector. The plane axes are also shown. *After Ref. [13].*

As we can see, there have been different approaches, theoretical and experimental, to obtain very short electrical pulses by means of the ORE. Our particular approach has its bases in create a device compatible with integrated optics and in the best of our knowledge this has not been demonstrated before. The summary of the four approaches presented above and the details of the device explained in chapter 5 of this thesis is shown in table 2.1.

Table 2.1. Comparative table of previous ORE experiments.

Reference No.	Structure	Nonlinear Media	Wavelength (nm)	Peak Power (KW)	Approach	Guided light
[10]	Bulk	GaAs/KDP	--	--	Theory	Yes
[11]	Bulk	$LiTaO_3$	800	4.062*	Experimental	No
[12]	Double Heterostructure	GaAs/AlAs	1500	1.0	Theory	Yes
[13]	Bulk	SI-GaAs	8000	$0.6x10^3$ to $4.0x10^3$*	Experimental	Yes
This work ORE4** [14]	Double Heterostructure	GaAs/AlGaAs	1500	1.38	Experimental	Yes

* Calculated using a square pulse approximation.
** Sample ID used in chapter five.

2.4 $GaAs/Al_xGa_{1-x}As$ system.

Gallium Arsenide (GaAs) has been a very popular III-V semiconductor material on the fields of high-speed electronics (FETs), optoelectronics (LEDs, photodetectors) and nonlinear optics (SHG). Its properties have been extensively studied in different works [15,16] and, because of this, most of its optical and electrical design parameters can now be estimated using simple analytic models. In the same way, the AlGaAs system is one of the most important alloy systems. This popularity is due to its excellent lattice match to GaAs substrates allowing us to create many different heterostuctures and quantum well structures. The GaAs/AlGaAs heterostructure find its applications again in high-speed electronics (MODFET), photonics (semiconductor laser, modulators) and nonlinear optics (semiconductor waveguides, solitons).

2.4.1 The Gallium Arsenide lattice.

GaAs is a direct band material and therefore attractive to optoelectronic applications. GaAs has a zincblende lattice, one As atom bonded to four Ga atoms forms the primitive cell. The GaAs cell can be defined using a three-dimensional coordinate system with unit basis vectors **a**, **b**, **c** that in this case are orthogonal. Any distance within the lattice can be defined by the vector $\mathbf{r} = h\mathbf{a} + k\mathbf{b} + l\mathbf{c}$, where h, k, and l are integers. According to this, any direction in the crystal can be defined by the set of integers [hkl]. Therefore, directions [100],

[010] and [001] are directions pointing along the vectors **a**, **b**, and **c** within the cell. These directions are also perpendicular to the planes (100), (010) and (001) respectively which are defined by the Miller indexes. Fig 2.8 shows a conventional unit cell for GaAs.

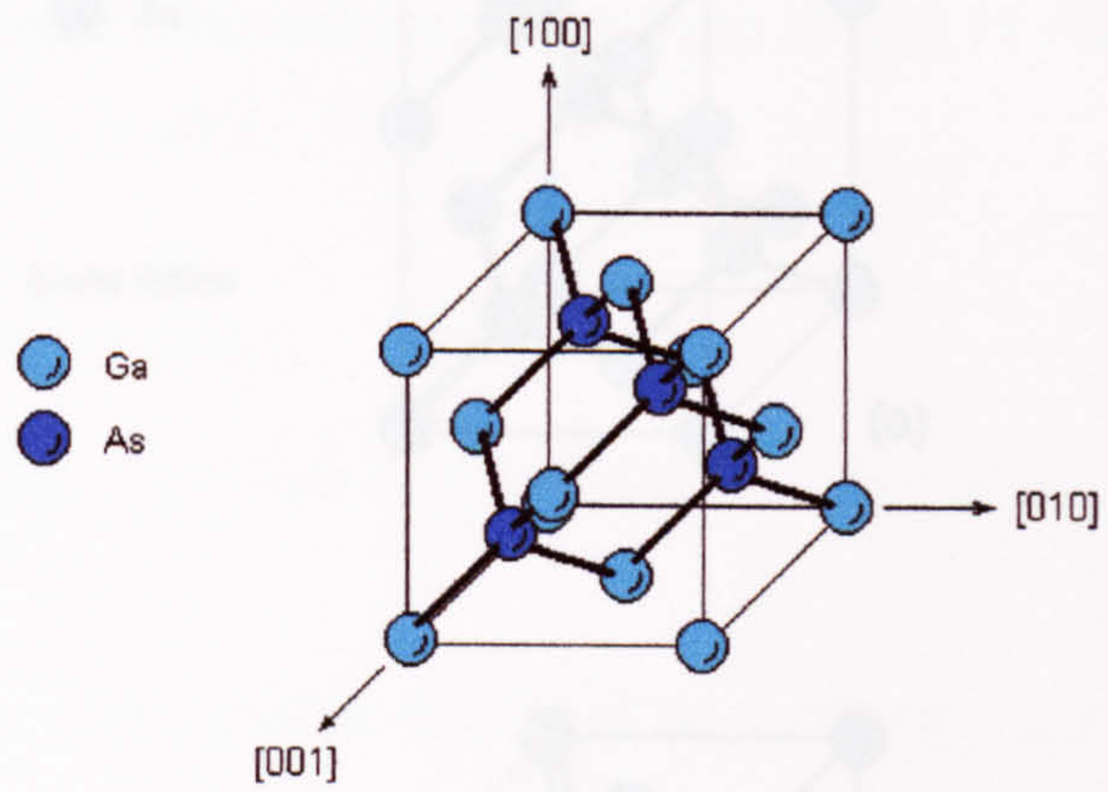

Fig. 2.8. GaAs (zincblend) structure containing four primitive cells.

GaAs is a noncentrosymmetric crystal, which means that the coordinate **r** cannot be replaced by $-\mathbf{r}$. This property makes GaAs attractive to NLO experiments as well as electro-optic devices. GaAs cleaves most readily on the {110} family of planes.

2.4.2 The AlGaAs alloy.

The precise control available in the growth of AlGaAs, allows tuning of the refractive index of the layers while still being lattice matched to a GaAs substrate. Fig. 2.9 shows three comparative lattices of GaAs, AlGaAs and a GaAs/AlAs superlattice. The AlGaAs alloy is grown perfectly random. The Al atoms occupy the place of the Ga atoms and the control parameter is the concentration of Al in the alloy usually referred as a percentage.

The alloy presents a switching in the band gap form direct to indirect for an Al fraction above ~35%. This is a reason why most device structures use a composition below this value [17].

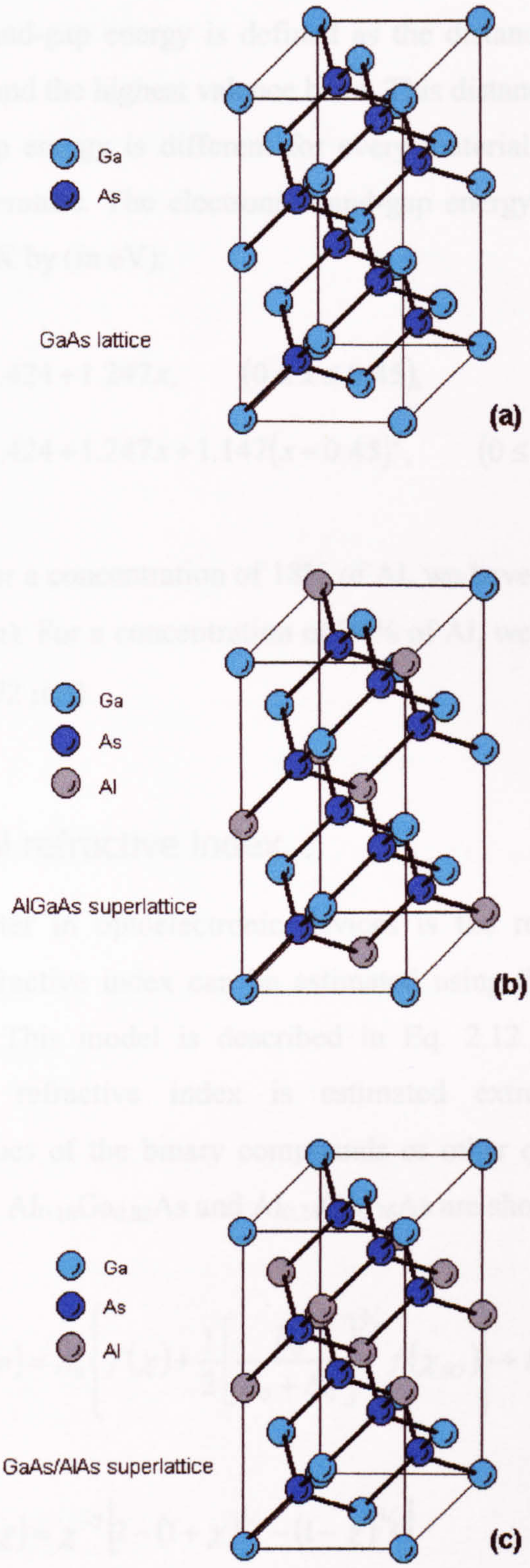

Fig.2.9. Comparison between (a) GaAs lattice, (b)AlGaAs lattice and (c) GaAs/AlAs superlattice.

2.4.2.1 Electronic band-gap energy.

The electronic band-gap energy is defined as the distance between the lowest conduction band and the highest valence band. This distance is normally given in eV. The band-gap energy is different for every material, or compound and is affected by temperature. The electronic band-gap energy in $Al_xGa_{1-x}As$ can be calculated at 300 K by (in eV):

$$E_g^{\Gamma}(x) = 1.424 + 1.247x, \qquad (0 \le x \le 0.45), \tag{2.10}$$

$$E_g^{\Gamma}(x) = 1.424 + 1.247x + 1.147(x - 0.45)^2, \qquad (0 \le x \le 0.45). \tag{2.11}$$

Using eq. (2.6), for a concentration of 18% of Al, we have $Al_{0.18}Ga_{0.82}As$ = 1.648 eV (λ = 0.750 μm). For a concentration of 24% of Al, we have $Al_{0.24}Ga_{0.76}As$ = 1.723 eV (λ = 0.72 μm).

2.4.2.2 Optical refractive index.

One key parameter in optoelectronic devices is the refractive index of the material. The refractive index can be estimated using the model proposed by Adachi in [16]. This model is described in Eq. 2.12. As with many other parameters, the refractive index is estimated extrapolating the known experimental values of the binary compounds or other quaternary compounds. Results for GaAs, $Al_{0.18}Ga_{0.82}As$ and $Al_{0.24}Ga_{0.76}As$ are shown in Fig. 2.10.

$$\varepsilon(\omega) = A_0\left\{f(\chi) + \frac{1}{2}\left[\frac{E_0}{E_0 + \Delta_0}\right]^{3/2} f(\chi_{SO})\right\} + B_0 \tag{2.12a}$$

with

$$f(\chi) = \chi^{-2}\left[2 - (1+\chi)^{1/2} - (1-\chi)^{1/2}\right] \tag{2.12b}$$

$$\chi = \hbar\omega / E_0 \tag{2.12c}$$

$$\chi_{S0} = \hbar\omega / (E_0 + \Delta_0) \tag{2.12d}$$

$$A_0(x) = 6.3 + 19.0x \tag{2.12e}$$

$$B_0(x) = 9.4 - 10.2x \tag{2.12f}$$

$$n(\omega) \approx \sqrt{\varepsilon(\omega)} \tag{2.12g}$$

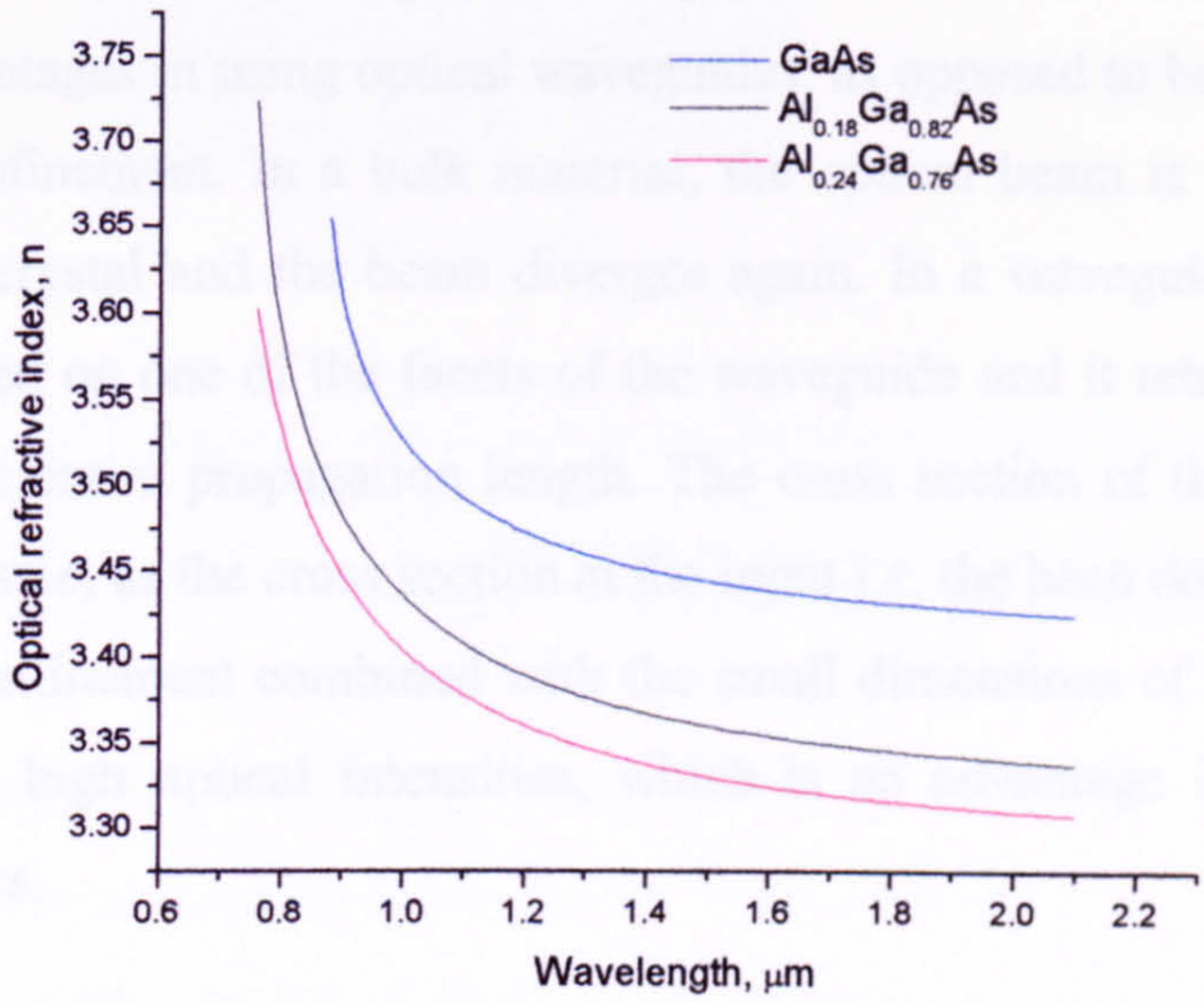

Fig. 2.10. Calculated refractive index of $Al_xGa_{1-x}As$ as a function of the wavelength.

It can be seen that the refractive index decreases when the concentration of aluminium increases.

Table 2.2 shows some parameters of the GaAs/AlGaAs system used in this thesis.

Table 2.2. Properties of GaAs and AlGaAs.

	GaAs	**$Al_{0.18}Ga_{0.82}As$**	**$Al_{0.24}Ga_{0.76}As$**
Eg (eV)	1.424	1.648	1.723
n @ 1550 nm	3.4415	3.3566	3.3274
χ (pV/m)	238[a] 340[b]	327[c]	319[c]
ε	12.9	11.26[d]	11.07[d]

[a] Optical susceptibility calculated as $\chi = 2d_{36}$ at 1.533 μm. d_{36} = 119 pV/m taken from Ref. [18].
[b] Optical susceptibility calculated as $\chi = 2d_{36}$ at 1.064 μm. d_{36} = 170 pV/m taken from Ref. [18].
[c] Values estimated with the results shown in Ref. [19]. d_{GaAs} = 170 pV/m @ 1.064 μm.
[d] calculated from the relationship $n \approx \sqrt{\varepsilon}$.

2.5 Semiconductor optical waveguides.

Semiconductor optical waveguides are a very important part of modern integrated optoelectronic systems. Applications range from optical filters, switches, modulators and perhaps the most popular semiconductor lasers. One of the main advantages in using optical waveguides, as opposed to bulk material, is the power confinement. In a bulk material, the optical beam is focused at the centre of the crystal and the beam diverges again. In a waveguide, the optical beam is focused on one of the facets of the waveguide and it retains a constant width over the entire propagation length. The cross section of the beam at the output is the same, as the cross section at the input i.e. the bean does not diverge. This power confinement combined with the small dimensions of the waveguide produces very high optical intensities, which is an advantage in the field of nonlinear optics.

2.5.1 Design of the optical waveguide.

There are different ways in which you can create an optical waveguide. The rib waveguide, or strip-loaded waveguide, is the option chosen here. The waveguides used in this work, were fabricated in the GaAs/AlGaAs system. The vertical confinement is achieved by the difference in refractive index produce by the different composition of aluminium in the cladding and core layers. The lateral confinement is produce by etching part of the material layers away. The whole structure is grown on a SI-GaAs substrate. A schematic of a typical rib waveguide is shown in Fig. 2.11.

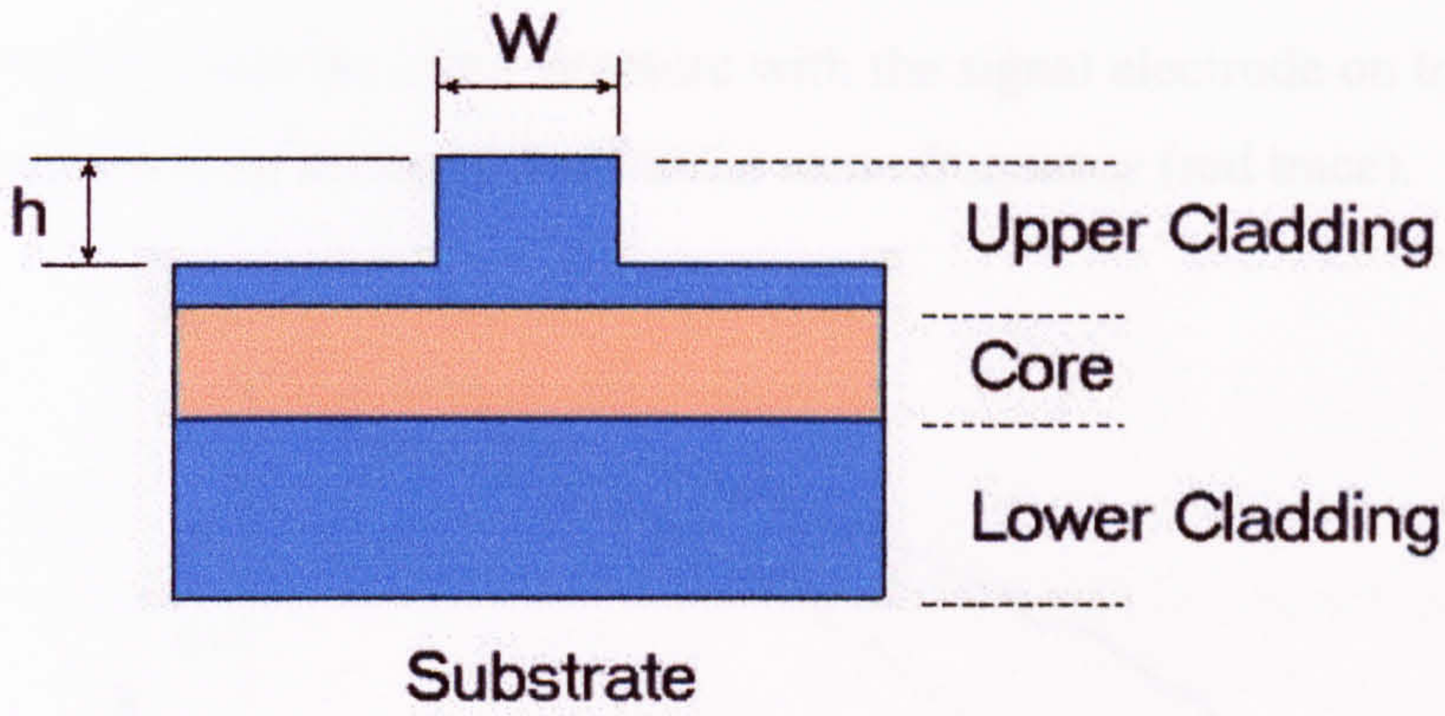

Fig. 2.11. Schematic of a rib waveguide showing three epitaxial layers forming the upper cladding, core and lower cladding which provide the vertical confinement. The lateral confinement is gain by etching part of the material away to a depth *h*. *W* defines the width of the waveguide.

In order to design a low-loss single mode optical waveguide, we need to have a look first at the requirements of the device. Optical rectification in AlGaAs uses the ultrafast nonlinear refraction in the mid-band-gap well demonstrated in [20]. The choice of the Aluminium composition in the layers has to be made according to the application of the device. If we are intending to work at the communication wavelength of around 1.5 μm, the corresponding energy (0.826 eV) must coincide with an energy below half band-gap of our optimum material. In other words, we are looking for a material with a band-gap of 1.652 eV, which compares with the value calculated in section 2.4.2.1 for an aluminium concentration of 18 %. For the lower and upper cladding, a concentration of Al of 24 % was taken from previous optimised designs [21]. As the optical refractive index of the SI-GaAs substrate is higher that the guiding layer, a thick lower cladding is required to reduce leakage losses. A value of 4μm is commonly used in AlGaAs waveguides. Finally, the upper cladding is 1 μm thick because we do not want to disturb too much the planarity of the electrical structure on top of the device. What this means is that having a signal conductor on a different plane that the ground electrode, combined with the small gap between the electrodes, will affect the frequency response of the line. The geometry of our device will be explained further in section 2.6, but as a rule, the higher the central conductor compared to the ground plane, the lossier the electrical structure will be. This concept is illustrated in Fig. 2.12. A transmission line fabricated on a

planar sample has a transmission loss (S21 parameter) of around 0.2 dB at 40 GHz (blue trace) while the same structure with the signal electrode on top of the ridge presents a loss of around 0.5 dB at the same frequency (red trace).

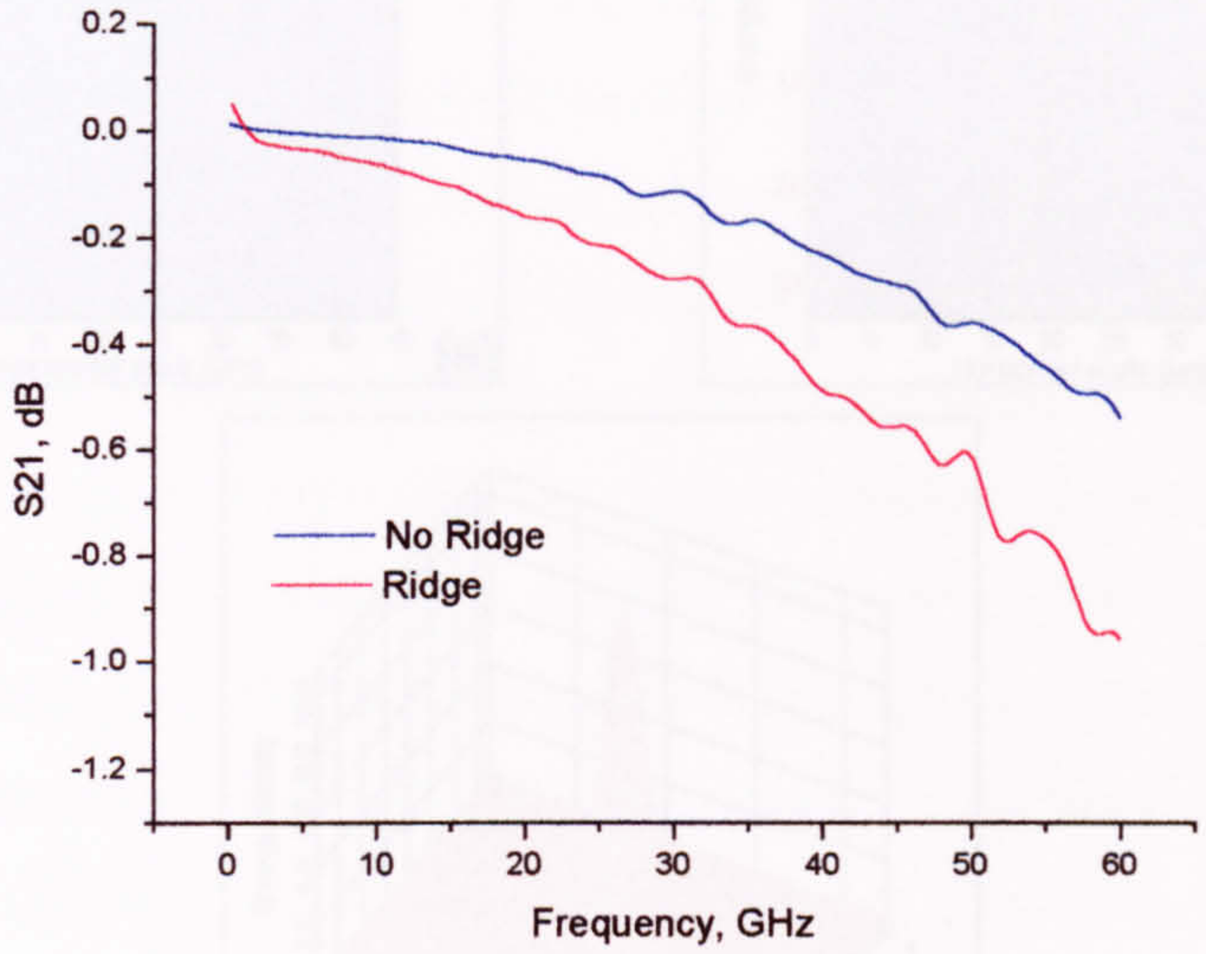

Fig. 2.12. Measured S21 parameter for a CPW line with no ridge (blue trace) and a CPW line with the central conductor on top of the ridge (red trace).

The different wafers utilized in this work are detailed in on the corresponding sections in Chapter 5. To illustrate the design of the waveguide, we are going to use the wafer A1500. The layer structure of this wafer is given in section 5.4.4. To find the optimum geometry for which we have maximum light confinement in a single mode device, we use the help of software called FimmWave. A width of 5 μm was chosen for the waveguide. The etch depth, *h* was scanned from 0.1 μm to 0.9 μm. For the layer composition of wafer A1500, the optimum etch depth in function of power confinement and a single mode structure, was found to be 0.85μm. The results of the simulation are shown in Fig. 2.13.

The confinement factor on the core layer is 0.8253 and the effective refractive index is 3.33.

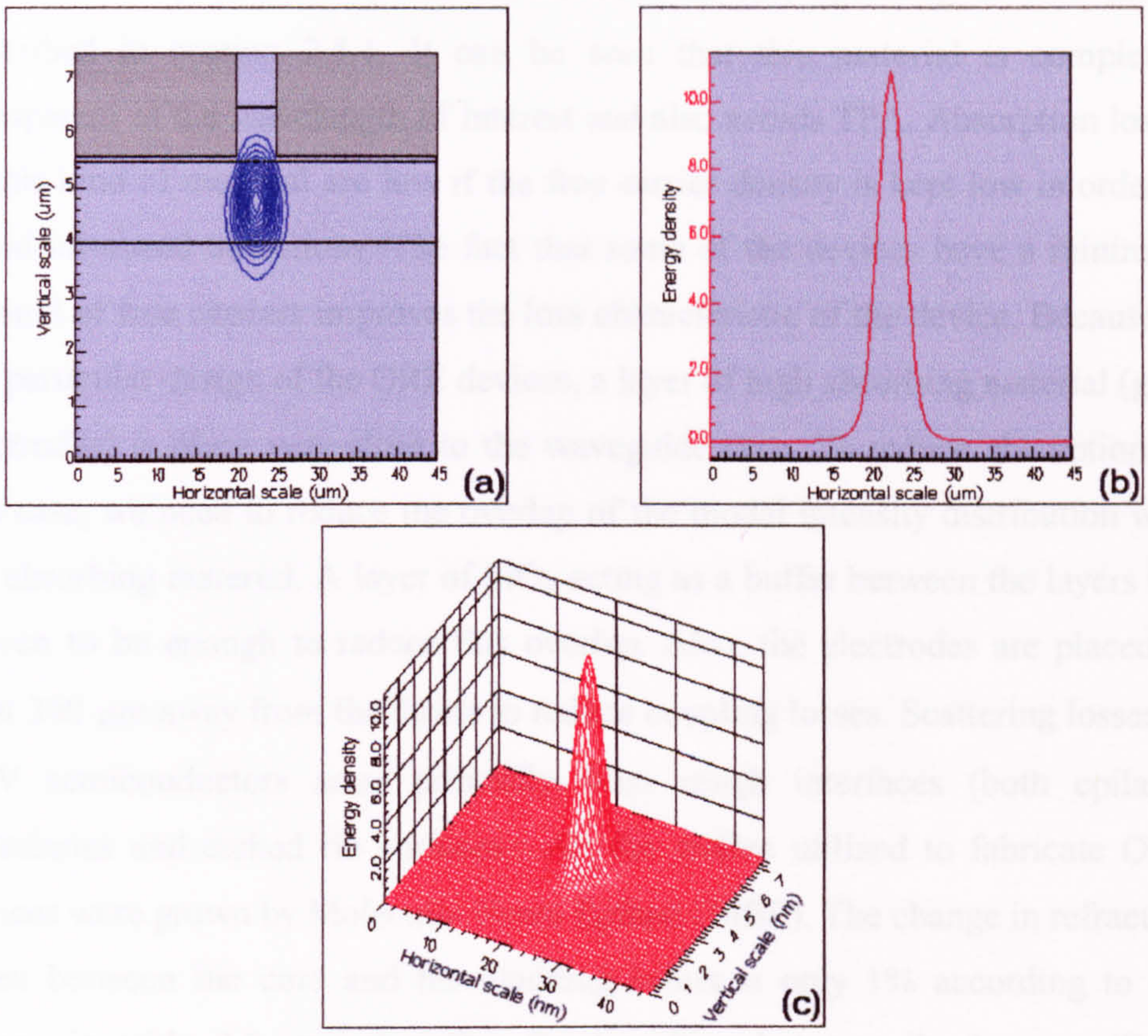

Fig. 2.13. Simulation in FimmWave for the wafer A1500 with $W = 5$ μm and $h = 0.85$ μm. (a) modal intensity distribution, (b) energy density and (c) 3D energy density.

2.5.2 Loss measurements.

Attenuation of the signal in most of the components of an optical/electrical system is for the most part undesirable but unavoidable; optical waveguides are no exception. According to [22], there are three different loss mechanisms in a semiconductor waveguide: absorption, scattering and leakage. The way to deal with these different loss mechanisms depends on the performance of the device (what the device is suppose to do). In general, for a low loss waveguide we can minimize the loss by using a low refractive index contrast (loss is $\propto \Delta n^2$), which creates a smooth interface between the cladding and the core layers. We can also use a lower cladding which is sufficiently thick to minimise leakage. The way losses mechanisms in an ORE device were dealt are described in the next paragraphs.

The material structure required for an ORE device, operating at 1.55 μm is described in section 2.5.1. It can be seen that this material is completely transparent at the wavelength of interest and also avoids TPA. Absorption losses in this kind of material are low if the free carrier density is kept low in order to avoid intraband transitions. The fact that some of the devices have a minimum amount of free carriers improves the loss characteristic of the device. Because of the particular design of the ORE devices, a layer of high absorbing material (gold electrodes) is place very close to the waveguide core. To reduce absorption on this case, we need to reduce the overlap of the modal intensity distribution with the absorbing material. A layer of SiO_2 acting as a buffer between the layers has proven to be enough to reduce this overlap. Also, the electrodes are placed at least 300 μm away from the facets to reduce coupling losses. Scattering losses in III-V semiconductors arise primarily from rough interfaces (both epilayer boundaries and etched rib surfaces). All the wafers utilized to fabricate ORE devices were grown by Molecular Beam Epitaxi (MBE). The change in refractive index between the core and the cladding layers is only 1% according to the figures in table 2.2, and therefore the transition between the layers will be smooth. The ridges were shallow etched by reactive ion etching. For shallow etched structures, the quality of the wall is not a critical parameter. Nevertheless, the quality of the etching used here is acceptable as shown in chapter 4. As for leakage losses, the design described in section 2.5.1 minimise the slab radiation loss and the guided light into the substrate due to its greater refractive index. The design of low loss optical waveguides is reviewed in [22] and references therein.

Propagation losses of the ORE devices were measured using the Fabry-Perot contrast method [23][24]. This technique relies on the oscillating behaviour of the transmitted intensity of the waveguide resonator, formed by the waveguide itself and the cleaved end facets. The transmitted intensity varies periodically with the optical phase difference, which can be tuned by temperature, applied electrical field, or wavelength. Tuning of the wavelength is the method used here. Propagation losses, α (dB/cm) are evaluated utilizing the following equation [25]:

$$\alpha = -\frac{1}{L} 4.34 \ln\left(\frac{1}{R}\frac{\sqrt{K}-1}{\sqrt{K}+1}\right) \quad , \qquad K = \frac{T_{\max}}{T_{\min}} \tag{2.13}$$

where L is the waveguide length, and R is the reflectivity of a cleaved facet. T_{max} and T_{min} are the maximum and minimum value of the transmission.

The set-up used for loss measurements is shown in Fig. 2.14. A tunable laser tunes the wavelength on a stepped sweep whilst the corresponding value of transmission is recorded by a photodetector and a Lock-in amplifier, which is synchronised to an optical chopper. The light is end-fire coupled into the ORE device. The polarizing beamsplitter is controlling the input polarization of the light. Finally, a 50/50 beamsplitter at the input allows the use of a CCD camera to aid with the alignment.

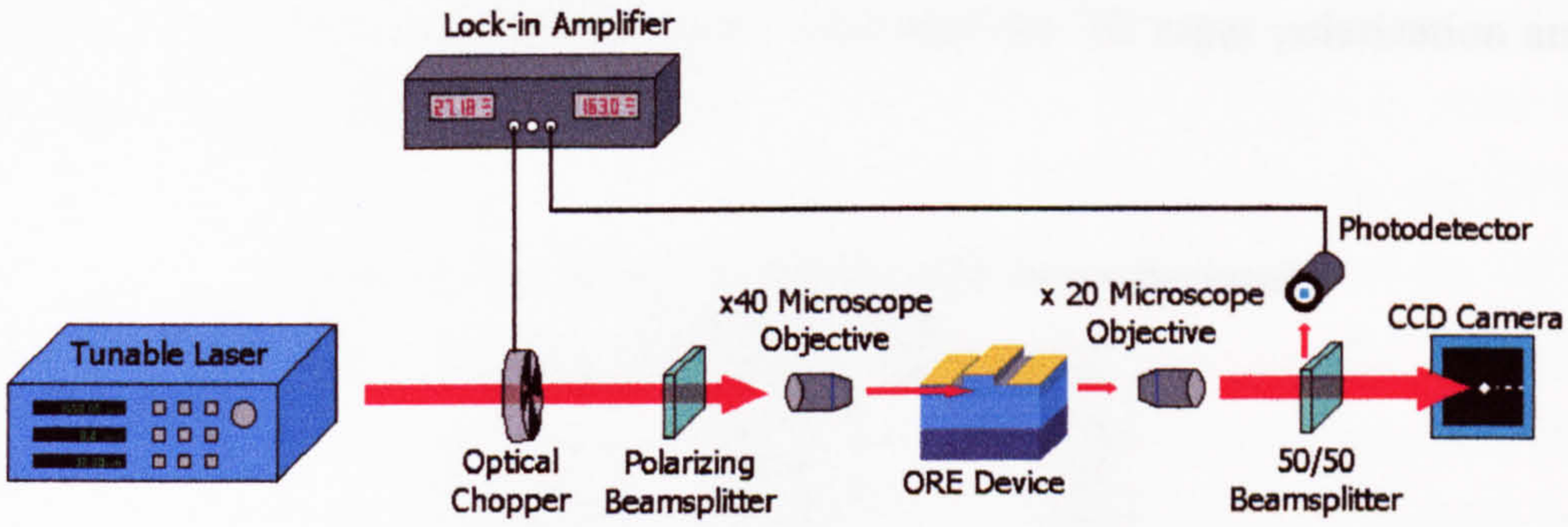

Fig. 2.14. Loss measurement set-up. The oscillations in transmission are obtained by tuning the wavelength.

A typical transmission characteristic for and ORE device using the set-up described above can be seen in Fig. 2.15. Here, by using equation 2.13, we find a value of α = 1.8 dB/cm. This value was obtained for an ORE4 (see chapter 5) using TE input polarization. The wafer used to fabricate these devices was A1500. The Polarization dependence loss (PDL) between TE and TM input polarization was found to be < 1.5 dB/cm. TE and TM are the conventional waveguide notations for transversal electric and transversal magnetic respectively. TE polarization has its electric field perpendicular to the plane of incidence of the beam TM polarization has its electric field parallel to it.

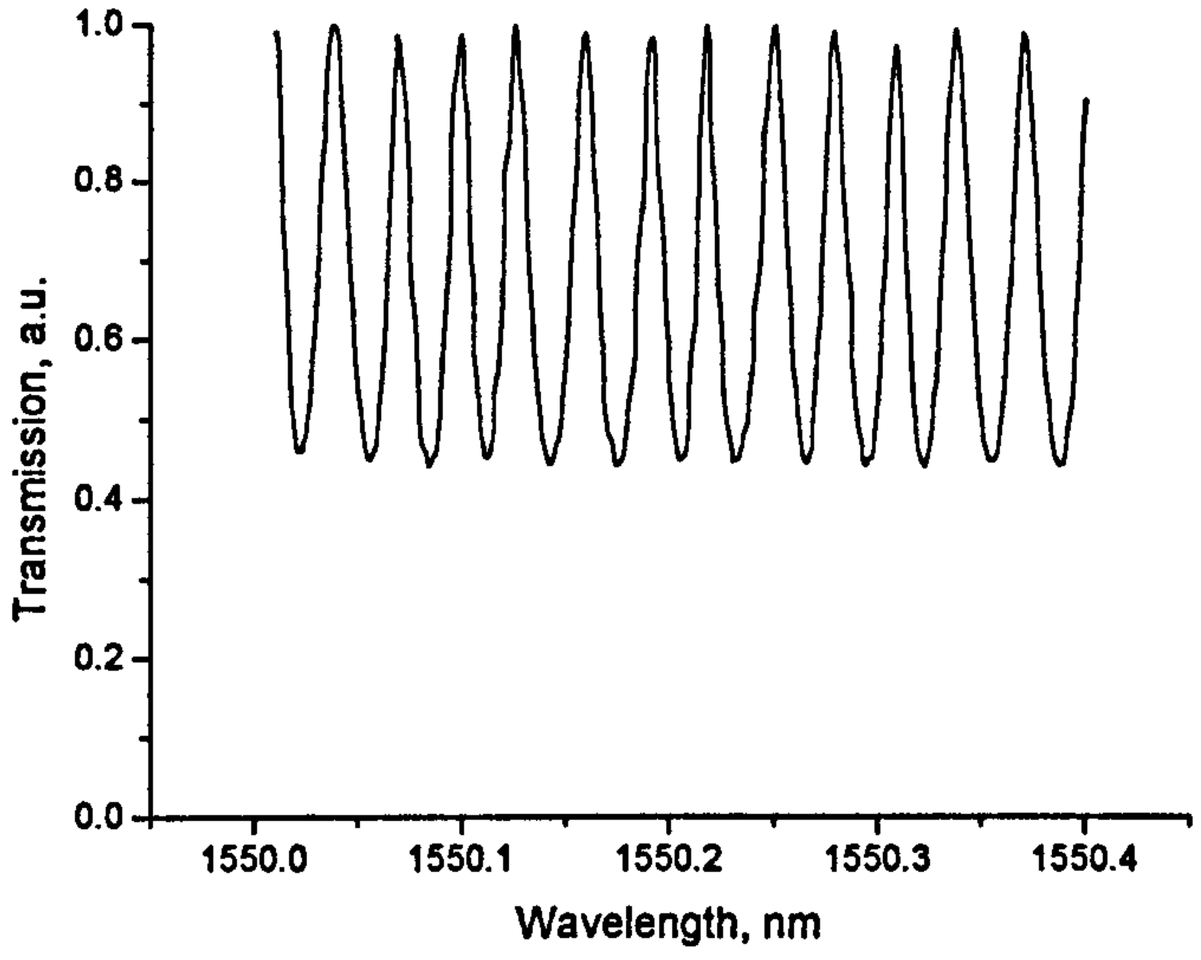

Fig. 2.15. Measured resonator transmission versus wavelength. Losses can be evaluated by measuring the ratio between maximum and minima.

Losses for different ORE devices were evaluated for TE input polarization and the best results are shown in table 2.3.

Table 2.3. Optical losses for different ORE devices fabricated on different wafers.

Sample I.D.	Wafer	Loss (dB/cm)
ORE1	B792	NA
ORE2	B828	1.00
ORE3-05	A1445	4.90
ORE3-08	A1445	3.54
ORE4-28	A1500	1.45
ORE4-32	A1500	1.77
ORE4-36	A1500	2.2
ORE4-80	A1500	2.00
ORE4-116	A1500	2.72

Most of the ORE3 devices had problems on the etching step. The formation of "grass" produced poor quality devices and this is reflected on the loss value. This though, is believed to be associated with the performance of the RIE tool at the time of the fabrication and not with the wafer growth. Relatively low loss values can be seen for the rest of the devices. The variation of loss among devices fabricated in the same wafer is because they were made on different batches and therefore exposed to a variation in the fabrication process.

2.6 Optical rectification in semiconductor waveguides.

In this chapter, we made clear that an optical rectification polarization is expected to appear across the ORE device. The way we are going to quantify this polarization (in volts), is by using electrodes on top of the waveguide. This is a critical point because we have to design the two devices independently, one optical (waveguide) and one electrical (CPW line), then put them together to create the ORE device. The design of the optical waveguide is described in section 2.5.1 whilst the details of the design of the CPW line are discussed in chapter three. In this section, we are going to show the design requirements of an ORE device as a whole and the equations that describe its behaviour.

An ORE device can be envisaged in Fig. 2.16. The fabrication process of the device is covered in chapter four. It is very important to notice that the device has a CPW line with the central conductor right on top of the ridge. In order to maximise the overlap of the optical mode and the microwave mode, the CPW line must be in close proximity with the waveguide. The design of the ORE device presents two options: the non-velocity matched case and the velocity-matched case using slow-wave electrodes. For the velocity-matched case, the conversion efficiency has been modelled in similar structures to be 1% whilst for the non-velocity matched case; an efficiency of 8.8×10^{-7} % was obtained [12]. The velocities to match are the group velocity of the optical signal with the phase velocity of the microwave signal. If this condition is obtained, then we have a travelling wave optical rectification device where the bandwidth is given by the intrinsic resistivity of the electrodes and the quality of the material instead of the *RC* constant of the device. The reason why we need a small separation between electrodes can be seen in Fig. 2.17. Here, the microwave field (red lines) is overlapping the optical field (blue lines). It is easy to imagine that if the electrodes are far from each other, the microwave field is going to move closer to the surface and the overlap with the optical field will be reduced.

The optical rectification polarization will induce a current on the CPW line with given impedance Z_0. The ORP will follow the optical pulse (Fig 2.1c) and the induced current on the CPW line will be proportional to the first derivative of the ORP. Therefore the voltage we are expecting to measure will be a bipolar pulse.

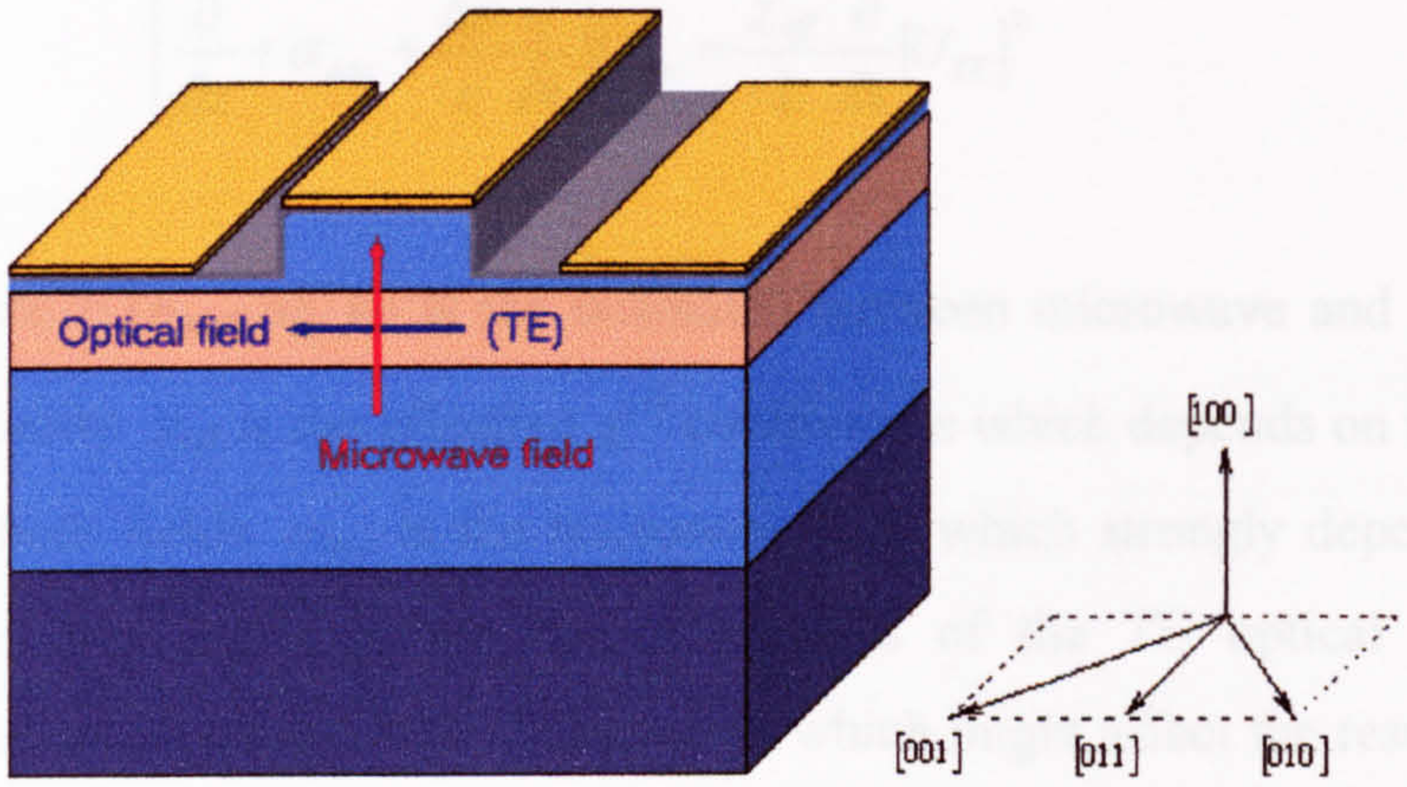

Fig. 2.16. Schematic of an ORE device with [100] growth direction and [011] cleaving direction. The blue arrow shows the direction of the TE applied optical field while the the red arrow indicates the direction of the microwave field. The central conductor of the CPW line is placed on top of the ridge to maximize the overlap between the modes.

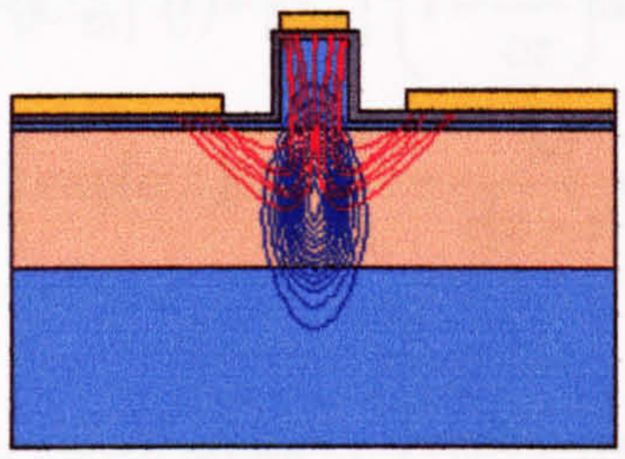

Fig. 2.17. Cross-section of the ORE device shown in Fig. 2.16 showing the overlap between the optical mode (blue lines) and the microwave mode (red lines). The electric field lines for the microwave mode travelling into the air have been omitted for simplicity.

The design's philosophy of the ORE device has been presented before in [26] and [27].

2.6.1 Formulas for optical rectification in waveguides.

The basic equations describing optical rectification in GaAs, for the device shown in Fig. 2.16 with growth direction in [100], have been derived by Bubke [28]:

$$\left[\frac{\partial}{\partial z}+\alpha_{mic}+\frac{\Delta n}{c}\frac{\partial}{\partial t}\right]U_{mic}=\frac{\chi_{eff}}{2}\frac{\partial}{\partial t}\left|U_{TE}\right|^2 \tag{2.14}$$

where $\Delta n/c = (n_{mic}-n_{TE}^{gr})/c$ is the mismatch between microwave and TE optical group velocity. χ_{eff} is the effective $\chi^{(2)}$ coefficients which depends on the overlap between both fields. α_{mic} is the microwave loss which strongly depends on the frequency. U_{TE} and U_{mic} are the magnitudes of the TE optical mode and microwave mode respectively. Dispersion, which might affect the result for very short pulses, is neglected.

A non-velocity matched structure can be represented by $\Delta n \neq 0$ in Eq. 2.14. In this case, the generated microwave consists of two signals,

$$\begin{aligned}U_{mic}=\frac{c\chi_{eff}}{2\Delta n}[&\left|U_{TE}\right|^2(t)-\left|U_{TE}\right|^2\left(t-\frac{\Delta n}{cz}\right)\exp(-\alpha z)\\&-\alpha\int_0^z\exp(\alpha z)\left|U_{TE}\right|^2\left(t-\frac{\Delta n}{c(z-z')}\right)dz']\end{aligned} \tag{2.15}$$

The maximum amplitude is hence given by $U_{mic}^{\max}=P_{TE}^{\max}\chi_{eff}\,{}^{c}\!/_{2\Delta n}$.

A velocity matched structure can be represented by $\Delta n = 0$. The generated microwave is the growing single signal,

$$U_{mic}=\frac{\chi_{eff}}{2}\frac{1-\exp(-\alpha z)}{\alpha}\frac{\partial\left|U_{TE}\right|^2}{\partial t} \tag{2.16}$$

The final amplitude depends on the loss in the structure. Further, $\lim_{\alpha \to 0} \frac{1-\exp(-\alpha z)}{\alpha} = z$ which corresponds to linear growth when there are no losses.

The work described in [12] bases its calculations on these equations.

2.7 Conclusions.

In this chapter, we presented a concise explanation of the optical rectification effect and explained how to engineer an ORE device. The understanding of the ORE is vital to make the right material choice for the ORE device. To the best of our knowledge, a physical ORE device using the semiconductor material of choice has never been reported in the literature before. The review of the previous work in rectification showed how other research groups have been approaching the concept (and/or fabrication) of a device capable of generating ultrashort electrical pulses using optical rectification. The literature review also shows the novelty of the idea and the difficulties of making a semiconductor ORE device at communication wavelengths. The main problem when working with semiconductors is the fact that is virtually impossible to eliminate free carriers effects which can act in decrement of the device performance. These effects, however, can be minimized. This chapter underlines the uniqueness of the research presented on this thesis.

2.8 References.

1. J. B. Khurgin, "Second-Order Nonlinearities and Optical Rectification," *Semicond. Semimet.* Vol. 59, pp. 1-82, 1999.

2. Y. H. Jin and X. C. Zhang, "Terahertz Optical Rectification," *Journal of Nonlinear Optical Physics and Materials*, vol. 4, pp. 459-495, 1995.

3. Y. R. Shen, *The Principles of Nonlinear Optics*, John Wiley & Sons, p. 57, 1984.

4. M. Bass, P. A. Franken and J. F. Ward, "Optical Rectification," *Phys. Rev.*, vol. 138, pp. A534-A542, 1965.

5. M. Bass, P. A. Franken, J. F. Ward, and G. Weinreich, "Optical Rectification," *Phys. Rev. Letters*, vol. 9, pp. 446-448, 1962.

6. J. F. Ward, "Absolute Measurement of an Optical-Rectification Coefficient in Antimonium Dihydrogen Phosphate," *Phys. Rev.*, vol. 143, pp. 569-574, 1966.

7. D. Grischkowsky, I. N. Duling III, J. C. Chen, and C. C. Chi. "Electromagnetic Shock Waves from Transmission Lines," *Phys. Rev. Letters*, vol. 59, pp. 1663-1666, 1987.

8. A. Rice et al., "Terahertz optical rectification from <110> zinc-blende crystals," *Appl. Phys. Lett.*, vol. 64, pp. 1324-1326, 1994.

9. A. Bonvalet, M. Joffre, J. L. Martin and A. Migus, "Generation of ultrabroadband femtosecond pulses in the mid-infrared by optical rectification of 15 fs light pulses at 100 MHz repetition rate," *Appl. Phys. Lett.*, vol. 67, pp. 2907-2909, 1995.

10. G. Moagar-Poladian, "An MOS transistor with an optical rectification controlled gate," *Semicond. Sci. Technol.*, vol. 12, pp. 210-216, 1997.

11. A. Nahata and T. F. Heinz, "Generation of subpicosecond electrical pulses by optical rectification," *Optics Letters*, vol. 23, pp. 867-869, 1998.

12. U. Peschel, K. Bubke, D. C. Hutchings, J. S. Aitchison, and J. M. Arnold, "Optical rectification in a travelling-wave geometry," *Phys Rev A*, vol. 60, pp. 4918-4926, 1999.

13. S. Graf, H Sigg and W. Bächtold, "High-frequency electrical pulse generation using optical rectification in bulk GaAs," *Appl. Phys. Lett.* vol. 76, pp. 2647-2649, 2000.

14 V. Loyo-Maldonado, H. K. Lee, C. R. Stanley, S. Venugopal-Rao, K. Moutzouris, M. Ebrahimzadeh, J. S. Aitchison, " Generation of Ultrashort Electrical Pulses in Semiconductor Waveguides," *IEEE Photonics Technology Letters*, vol. 15, pp. 428-430, 2003.

15. J. S. Blakemore, "Semiconducting and other major properties of gallium arsenide," *J. Appl. Phys.* vol.53, pp. R123-R181, 1982.

16. S. Adachi, "GaAs,AlAs,and $Al_xGa_{1-x}As$: Material parameters for use in research and device applications," *J. Appl. Phys.* vol 58, pp. R1-R29, 1985.

17. J. Singh, *Physics of semiconductors and their heterostructures*, McGraw-Hill, p. 187, 1993.

18. I. Shoji, T. Kondo, A. Kitamoto, M. Shirane and R. Ito, "Absolute scale of second-order nonlinear-optical coefficients," *J. Opt. Soc. Am. B*, vol. 14, pp. 2268-2294, 1997.

19. M. Ohashi, T. Kondo, R. Ito, S. Fukatsu, Y. Shiraki, K. Kumata and S. S. Kano, "Determination of quadratic nonlinear optical coefficient of $Al_xGa_{1-x}As$ system by the method of reflected second harmonics," *J. Appl. Phys.* vol. 74, pp. 596-601, 1993.

20. D. C. Hutchings and B. S. Wherrett, "Theory of the dispersion of ultrafast nonlinear refraction in zinc-blende semiconductors below the band edge," *Phys. Rev. B*, vol. 50, pp. 4622-4630, 1994.

21. J. S. Aitchison, A. H. Kean, C. N. Ironside, A.Villenueve and G. I. Stegeman, "Ultrafast all-optical switching in $Al_{0.18}Ga_{0.82}As$ directional coupler in 1.55 μm spectral region," *Electron. Lett.* vol. 27, pp. 1709-1710, 1991.

22. R. J. Deri and E. Kapon, "Low-Loss III-V Semiconductor Optical Waveguides," *IEEE J. Quantum Electron.* vol. 27, pp.626-640, 1991.

23. R. G. Walker, "Simple an Accurate Loss Measurement Technique for Semiconductor Optical Waveguides," *Electron. Lett.* vol. 21, pp. 581-583, 1985.

24. R. Regener and W.Sohler, "Loss in Low-Finesse Ti:$LiNbO_3$ Optical Waveguide Resonators," *Appl. Phys. B*, vol. 36, pp. 143-147, 1985.

25. H. Takeuchi and K. Oe, "Low-Loss Single-Mode GaAs/AlGaAs Miniature Optical Waveguides with Straight and Bending Structures," *J. Lightwave Technol.* vol. 7, pp. 1044-1054. 1989.

26. V. Loyo-Maldonado and J. S. Aichison, "Optical to Microwave conversion in Semiconductor Waveguides," *The Rank Prize Funds Mini-Symposium on Microwave Photonic Devices and Systems*, Grasmere, England, April 2000.

27. V. Loyo-Maldonado, H. K. Lee, T. Lohdi, I. G. Thayne and J.S. Aitchison, "Design and fabrication of an Optical Rectification device," *Quantum Electronics and Photonics 15 Technical Digest*, p. 169, Glasgow, Scotland, September 2001.

28. K.Bubke, personal communication.

3. Planar transmission lines: Coplanar waveguides.

3.1 Introduction.

Transmission lines have been, throughout the years, the most popular way to propagate electromagnetic energy at microwave frequencies. Modern technology integrates transmission lines on microwave integrated circuits to interconnect different elements within the circuit and, when this is the case, transmission lines can then be called planar transmission lines. A planar transmission line implies that the characteristics of the line can be determined by the dimensions in a single plane. The cross-section of four of the most commonly used types of planar transmission lines can be seen in Fig. 3.1. With the exception of the microstrip, all the structures have the signal and ground electrodes on the same side of the substrate. This condition makes the electrical characteristics of the line almost independent of the substrate thickness. Moreover, lines such as coplanar waveguides are ideal for on-wafer testing and avoid the need of extra processing, on the waveguide such as via etching. On the other hand, microstrip lines are widely used because their relatively easy design and simple transitions to coaxial cables. In a strict sense, the coplanar waveguide (CPW) and the coplanar strips (CPS), are a variant of the slotline but with their own fundamental

differences such as the width and the number of the electrodes. The CPW has the peculiarity of having the signal electrode situated between two ground electrodes and separated from them by a finite gap. The CPW line has proven to be, as we will discuss in this chapter, an ideal structure to propagate electrical signals with a broad frequency spectra. A complete analysis of the transmission lines shown in Fig. 3.1 is available in [1]

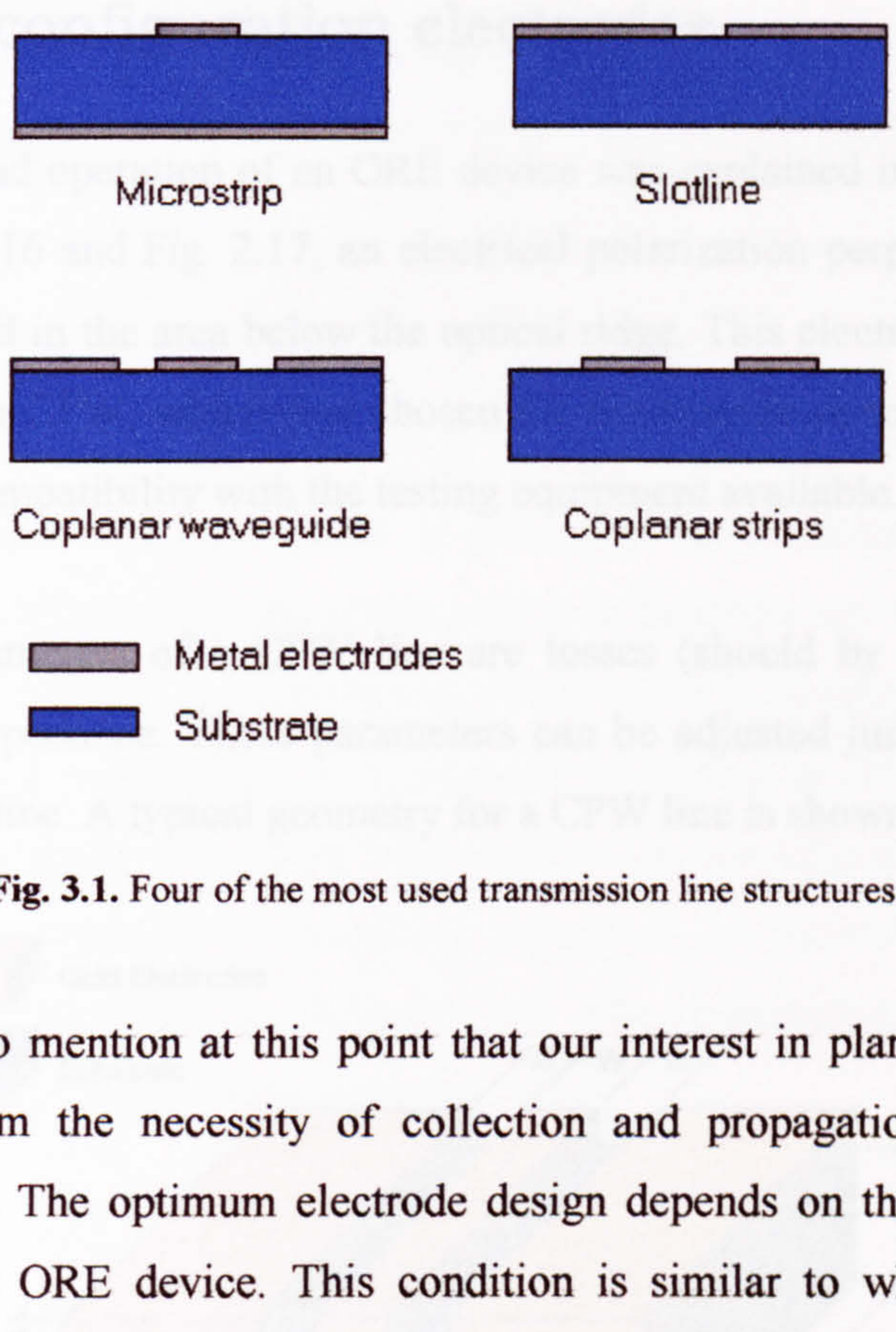

Fig. 3.1. Four of the most used transmission line structures.

It is important to mention at this point that our interest in planar transmission lines comes from the necessity of collection and propagation of ultrashort electrical pulses. The optimum electrode design depends on the operation and geometry of the ORE device. This condition is similar to what we have in electro-optic modulators where all kinds of transmission lines are used. See for instance [2] for microstrip, [3] for slotline, [4] for CPS and [5] for CPW. As there is an intimate relationship between the ORE and the linear electro-optic effect (*see section 2.2*), the mature design techniques for electro-optic modulators can, in principle, be used to design the ORE device.

In this chapter, the propagation characteristic of an electrical pulse is reviewed, giving the reader all the tools needed to understand propagation. An understanding of losses is fundamental to understand what could happen when an

electrical pulse does not travel attached to an optical wave (which is regenerating the pulse). The design parameters of CPW lines are discussed to some detail. By the end of the chapter, we proposed two structures, which will create two types of ORE devices. The two types of ORE devices were modelled and then compared with the experimental results. Emphasis is made in the need of using slow-wave electrodes to achieve a velocity-matched ORE device.

3.2 CPW configuration electrodes.

The geometry and operation of an ORE device was explained in section 2.6. As shown in Fig. 2.16 and Fig. 2.17, an electrical polarization perpendicular to the surface is created in the area below the optical ridge. This electrical polarization is coupled into a CPW, which was chosen for the reasons described above and because of its compatibility with the testing equipment available.

The design parameters of a CPW line are losses (should by minimised) and characteristic impedance. These parameters can be adjusted just by altering the geometry of the line. A typical geometry for a CPW line is shown in Fig. 3.2.

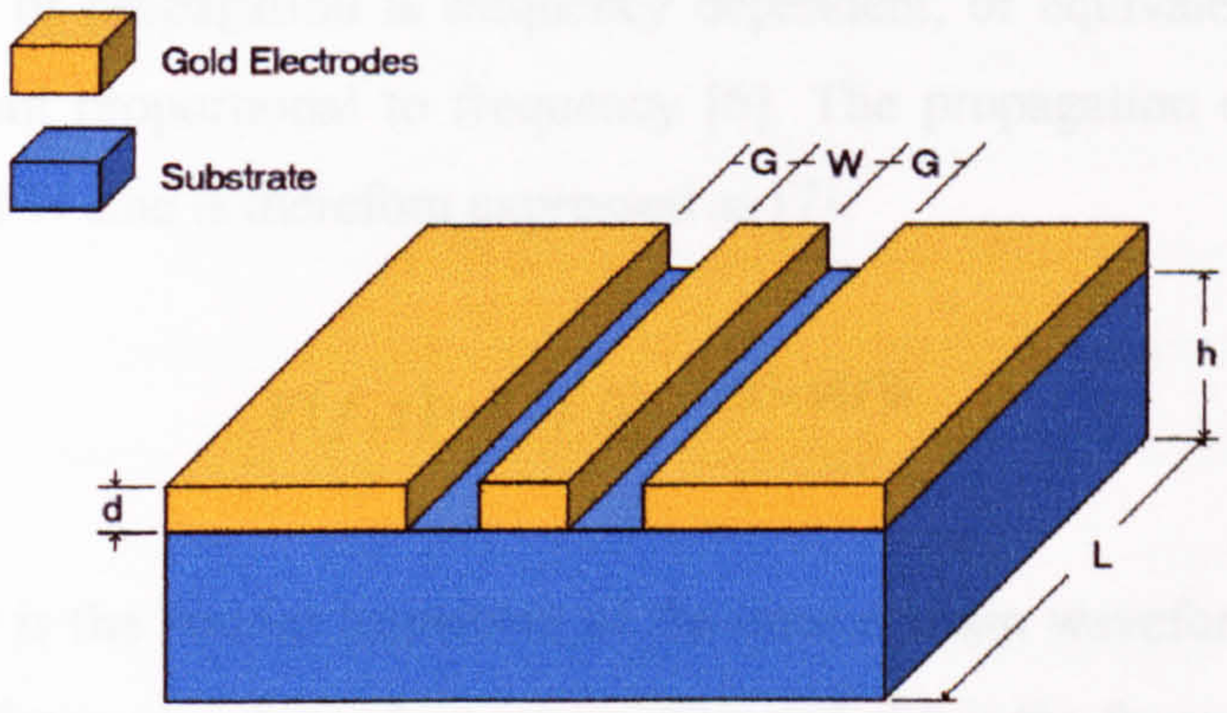

Fig. 3.2. CPW geometry.

In a CPW line, the phase velocity in m/s is given by:

$$v_{ph} = \frac{c}{\sqrt{\varepsilon_q}} \tag{3.1}$$

where c is the speed of light in m/s and ε_q is the quasi-static effective dielectric constant of the line and is defined by,

$$\varepsilon_q = \frac{\varepsilon_r + 1}{2} \tag{3.2}$$

ε_r is the substrate dielectric constant.

Equation 3.2 is the representation of the fact that, in a CPW line, half of the electromagnetic fields exist in the air above the substrate and half within the substrate itself.

3.2.1 Losses in CPW transmission lines.

Once an ultrashort electrical pulse is generated on a transmission line, its propagation is determined by the characteristic attenuation and dispersion of the line. Attenuation refers to the exponential decay of the field amplitude of a mode in the direction of propagation. It is normally expressed in dB per unit length. Dispersion is a property of a planar transmission line whereby the phase velocity of the mode of propagation is frequency dependent, or equivalently, the phase constant is not proportional to frequency [6]. The propagation of an electrical signal in a CPW line is therefore expressed as [7]:

$$V(f,z) = V(f,0)e^{-(\alpha(f)+j\beta(f))z} \tag{3.3}$$

where $V(f, z)$ is the Fourier transform of the time domain waveform at a distance z, $\alpha(f)$ is the frequency dependent attenuation and $\beta(f)$ is the frequency dependent phase constant which determine the distortion of the electrical signal due to dispersion. In a CPW line, $\beta(f)$ is given by [8],

$$\beta(f) = 2\pi \frac{f}{c}\sqrt{\varepsilon_{eff}(f)} \tag{3.4}$$

ε_{eff} is the frequency dependant effective dielectric constant and will be defined in equation 3.6.

The loss mechanisms involved in the propagation of short electrical pulses in CPW lines have been studied throughout the years (see [7], [9], [10] and [11]) and as a result, analytical expressions for every loss mechanism have been derived from the numerical solution of the electromagnetic problem. Attenuation of the electrical signal propagating in a CPW line can occur because of: radiation losses, conductor (or ohmic) losses, dielectric losses and magnetic losses (only in magnetic substrates i. e. none in GaAs). As mentioned before, the CPW mode propagates at the interface between the air space and the substrate. The CPW mode will then propagate with a phase velocity that exceeds that of a TEM wave in the higher dielectric constant material. This condition gives rise to radiation from the guided CPW wave into the substrate at certain angle θ defined as [12]:

$$\cos\theta = \frac{\sqrt{\varepsilon_{eff}}}{\sqrt{\varepsilon_r}} \tag{3.5}$$

where ε_{eff} is the effective dielectric constant seen by the CPW mode and ε_r is the dielectric constant seen by the radiated mode. Analytic formulas for the attenuation of electrical transients due to radiation losses have been deduced by Frankel [7]. Above 200 GHz, radiation losses are the main mechanism for losses in a CPW line. Radiation losses increase with frequency in an almost strict f^3 dependence, where f is the frequency. The fact that the effective dielectric constant varies slightly with frequency modifies the f^3 dependence of the radiation losses. The variation of the effective dielectric constant with frequency can be approximated by:

$$\sqrt{\varepsilon_{eff}(f)} = \sqrt{\varepsilon_q} + \frac{\left(\sqrt{\varepsilon_r} - \sqrt{\varepsilon_q}\right)}{\left(1 + a\left(\frac{f}{f_{te}}\right)^{-b}\right)} \tag{3.6}$$

Here,

$$f_{te} = \frac{c}{4h\sqrt{\varepsilon_r - 1}} \tag{3.7a}$$

is the cut-off frequency of the lowest order TE mode, b (~1.8) is taken to be independent of geometry while a is computed from

$$\log(a) \sim u\log(W/G) + v \tag{3.7b}$$

where u and v depend on the substrate thickness h as follows:

$$u \sim 0.54 - 0.64q + 0.015q^2 \tag{3.7c}$$

$$v \sim 0.43 - 0.86q + 0.54q^2 \tag{3.7d}$$

$$q = \log(W/h) \tag{3.7e}$$

The geometric parameters W, G, and h are defined in Fig. 3.2. In summary, radiation losses depend on the dielectric constant, the substrate thickness and the geometric parameters.

The attenuation coefficient for radiation losses can be calculated by:

$$\alpha_{rad} = 4.34\left(\frac{\pi}{2}\right)^5 2\left(\frac{\left(1-\frac{\varepsilon_{eff}(f)}{\varepsilon_r}\right)^2}{\sqrt{\frac{\varepsilon_{eff}(f)}{\varepsilon_r}}}\right)\frac{(W+2G)^2\varepsilon_r^{3/2}}{c^3K'(k)K(k)}f^3 \text{ dB/unit length} \tag{3.8}$$

where $k = W/(W+2G)$, $K(k)$ is the complete elliptic integral of the first kind, and $K'(k) = K\left(\sqrt{1-k^2}\right)$. This equation is valid for geometries approximately constrained by $0.1 < W/G < 10$ and $h > 3G$. α_{rad} for different geometries of lines as a function of frequency is shown in Fig. 3.3a. The geometric parameters of CPW1 are $W = 4$ μm, $G = 3$ μm, for CPW2, $W = 10$ μm, $G = 7.5$ μm and for CPW3, $W = 20$ μm, $G = 15$ μm. In all the cases $h = 400$ μm. The characteristic impedance Z_0 of the three lines fabricated in GaAs is 50 Ω ± 1.5Ω. CPW1 is

what we could call a non-standard CPW line because of the very small dimensions of the line but is included here because of its similarity with an ORE device (section 3.2.4). CPW3 is a more standard line and this sort of geometry is utilised in MW circuits, electro-optic modulators and antennas. CPW2 is not very common either but is include as a middle point of the comparison between CPW1 and CPW3. It can be clearly seen in Fig 3.3a that above 200 GHz, losses increase considerably being more critical for CPW3. A common practice to overcome the problem of radiation losses is reducing the dimensions of the central conductor as is the case of CPW1 which is the less affected by radiation loss. However, reduction in the central conductor width increases the conductor losses. To reduce radiation losses, the thickness of the substrate (in μm) can be adjust to be $h < 0.12\lambda_r$ where λ_r is the wavelength of the wave propagating into the substrate [12]. The ORE devices have a $\lambda_r = 4100$ μm at 20 GHz and $h = 420$ μm, therefore the latter condition is fulfilled, $h < 492$ μm.

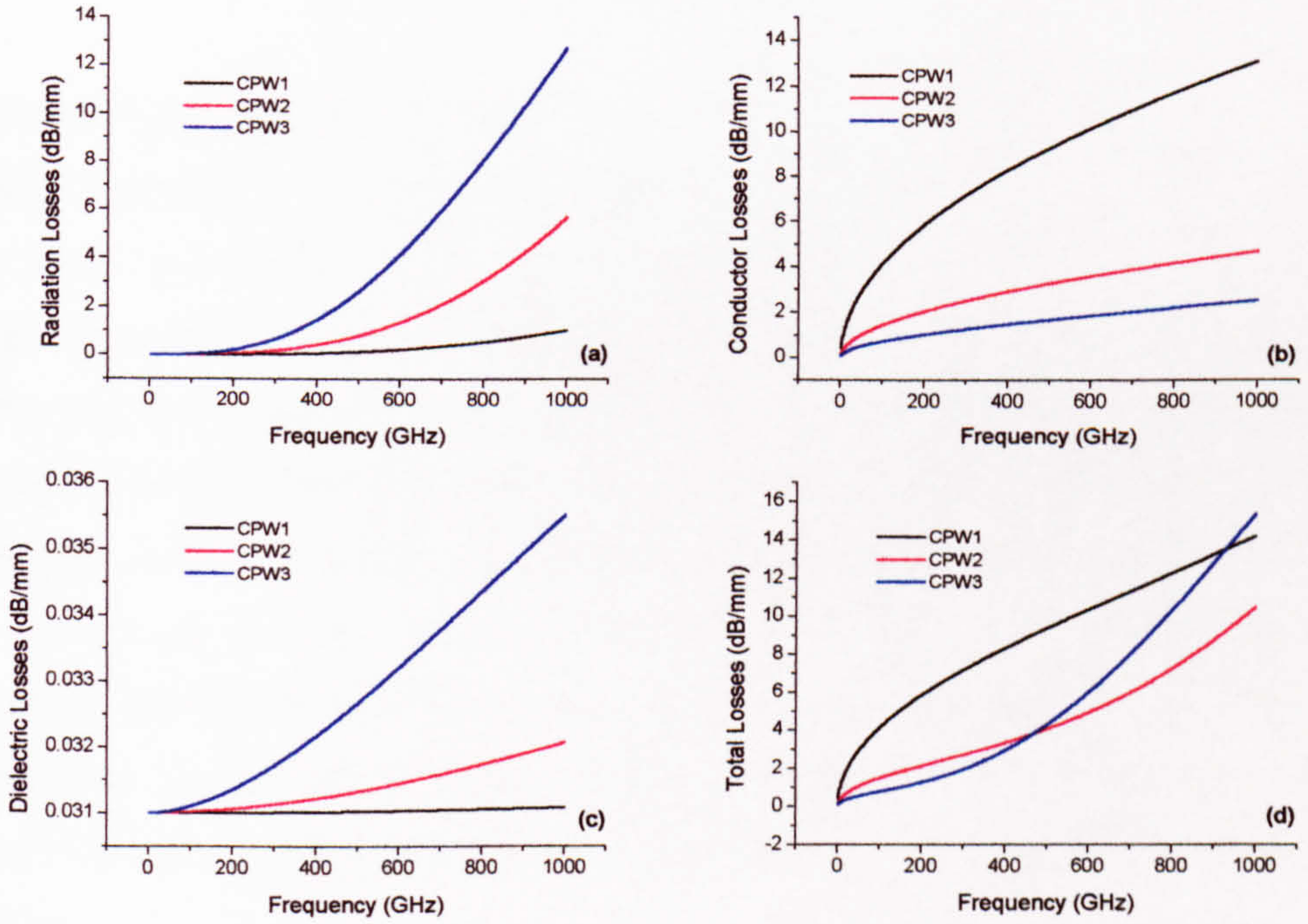

Fig. 3.3. Attenuation coefficient for (a) radiation, (b) conductor, (c) dielectric and (d) total losses, as a function of frequency. CPW1, W=4 μm, G=3 μm. CPW2, W=10 μm, G=7.5 μm. CPW3, W=20 μm, G=15 μm. For all the lines h=400 μm.

In conventional CPW design, conductor losses between the signal and the ground electrode dominate over radiation losses. Conductor losses are determined by conductivity, skin effect and substrate roughness, all of which are related to the composition of the metal electrodes. Conductivity σ depends on the material used for metalization, in the case of gold, which is the material use on the devices described on this thesis, $\sigma_{Au} = 4.098x10^7$ S/m. For a finite conductivity (practical case), the current density will decrease exponentially from the surface. This condition can be represented as a uniform current flowing to a certain depth from the surface on the metal. This depth is commonly known as skin depth, δ. The skin depth of a conductor is defined as the distance to the conductor where the current density drops to $1/e$ from a maximum current density I_{max}, or 36.8 percent of its value at the surface of the conductor [13]. The skin depth can be calculated from:

$$\delta = \sqrt{\frac{1}{f \pi \mu_0 \sigma}} \tag{3.9}$$

Where f is the frequency in Hz and $\mu_0 = 4\pi x10^{-7}$ H/m is the permeability in free-space. Therefore, the skin depth of gold ($\sigma_{Au} = 4.098x10^7$ S/m) at 40 GHz will be 393 nm. To minimize conductor loss, the conductor thickness should be greater than approximately three to five times the skin depth. Conductor losses increase when decreasing the electrodes size due to the greater resistance of narrow strips. Another factor affecting conductor losses is the surface roughness. If the substrate surface is uneven, the deposited metal electrode will be uneven also, as it follows the former. Uneven metal electrodes mean that the current flows through an uneven path that is larger than the path on a smooth surface and therefore, it encounters greater resistance. Closed form equations for the conductor loss can be obtain from [1]. There, the conductor loss can be computed using:

$$\alpha_{ohm} = 4.88x10^{-4} R_s \varepsilon_{eff} Z_0 \frac{P'}{\pi W} \bullet \left(1+\frac{W}{G}\right) \bullet \left\{ \frac{\frac{1.25}{\pi}\ln\frac{4\pi W}{d} + 1 + \frac{1.25d}{\pi W}}{\left[2+\frac{W}{G} - \frac{1.25d}{\pi G}\left(1+\ln\frac{4\pi W}{d}\right)\right]^2} \right\} \text{ dB/unit length} \qquad (3.10)$$

Where $R_s = \sqrt{\pi f \mu_0 / \sigma}$ is the surface resistivity of the conductors, ε_{eff} is the effective dielectric constant defined in Eq. 3.6, Z_0 is the characteristic impedance of the line and P' is defined by:

$$P' = \left(\frac{K(k)}{K'(k)}\right)^2 P \qquad (3.11a)$$

and,

$$P = \begin{cases} \dfrac{k}{\left(1-\sqrt{1-k^2}\right)\left(1-k^2\right)^{3/4}} & for \quad 0.0 \le k \le 0.707 \\ \dfrac{1}{(1-k)\sqrt{k}}\left(\dfrac{K'(k)}{K(k)}\right)^2 & for \quad 0.707 \le k \le 1.0 \end{cases} \qquad (3.11b)$$

where k is the same geometric factor used in Eq. 3.8. α_{ohm} as a function of frequency is shown in Fig. 3.3b for CPW1, CPW2 and CPW3. As expected, conductor losses for CPW1 are the highest while losses for CPW2 and CPW3 are reasonable low.

Finally, dielectric losses depend directly on the material used as substrate. Alumina, quartz and sapphire are commonly used as low-loss substrates. When this is the case, dielectric loss α_d is negligible compared to the total loss α. However, when semiconductor substrates such as GaAs are used, the dielectric loss factor can be dominant. Dielectric loss can be computed using:

$$\alpha_d = 4.34 \frac{1}{\sqrt{\varepsilon_{eff}}} \frac{\varepsilon_{eff} - 1}{\varepsilon_r - 1} \sqrt{\frac{\mu_0}{\varepsilon_0}} \sigma_d \text{ dB/unit length} \qquad (3.12)$$

Fig 3.3c shows the value of α_d for the three lines under investigation as a function of frequency. Even when the losses are higher in CPW3, the magnitude of the losses on the three lines is very similar and much smaller that in the other two loss mechanisms. The total loss α is the linear combination of all the three factors described above, i. e.

$$\alpha = \alpha_{rad} + \alpha_{ohm} + \alpha_d \tag{3.13}$$

The total loss can be seen in Fig. 3.3d. For CPW1, the high losses start at low frequency while for CPW2 and CPW3, they have relatively low loss up to 400 GHz. At around 900 GHz, the losses in CPW1 and CPW3 are comparable. CPW2 seems to be the optimum structure of this three to minimize losses. To appreciate which loss mechanism is dominant in our different lines we have plotted in Fig 3.4 the different mechanisms on a semi-logarithmic scale.

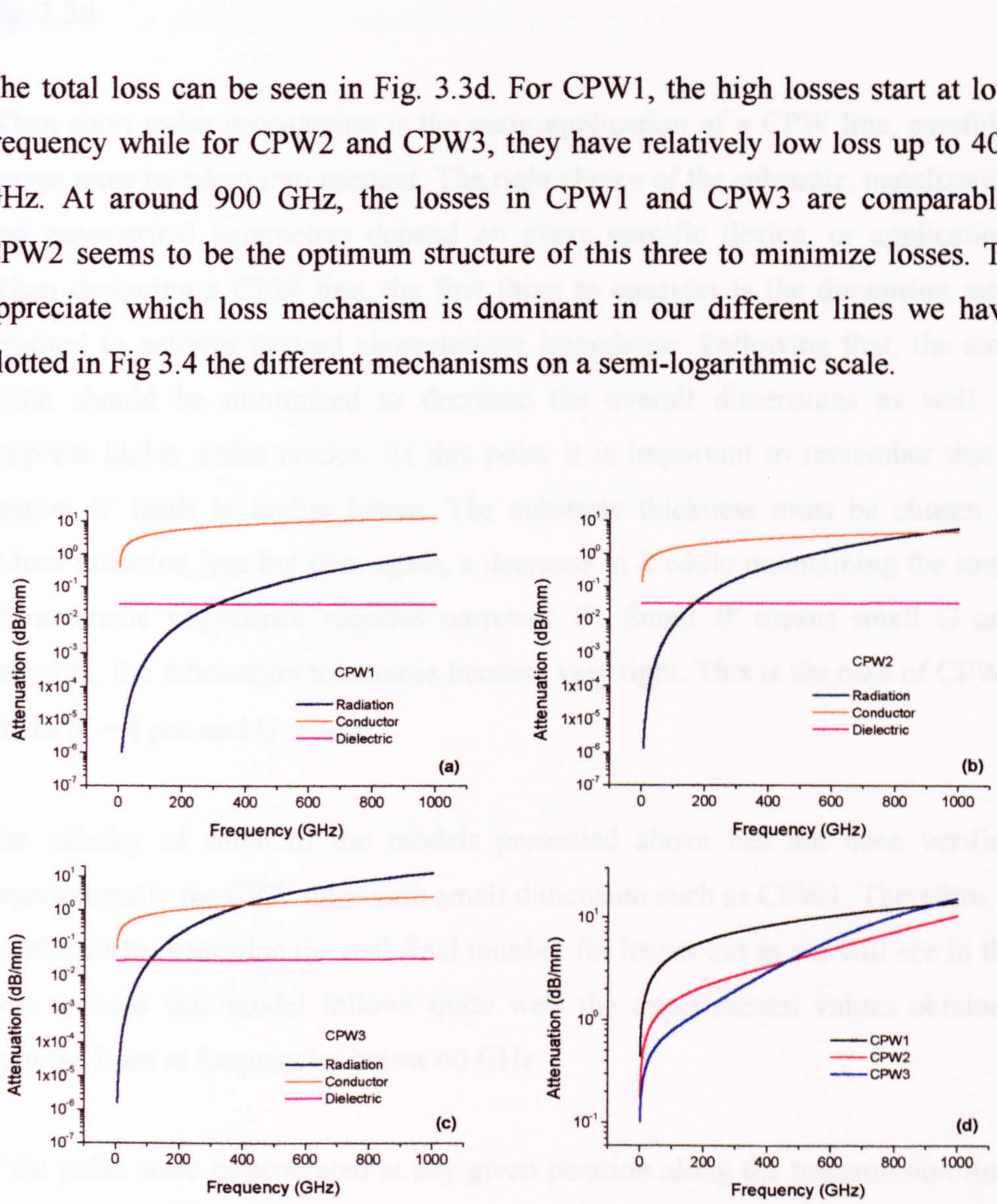

Fig. 3.4. Loss mechanisms for the same CPW lines defined in Fig. 3.3.

At low frequencies, when radiation losses are small, conductor loss is always going to be the dominant mechanism of loss in a CPW line. Radiation losses are not a factor here for any geometry. For CPW1 (Fig. 3.4a), conductor loss is by far dominant over the other two mechanisms at any frequency. The reason for this has already been explained above. In CPW2 (Fig.3.4b), again conductor loss is the dominant mechanism up to 700 GHz when radiation loss starts to be comparable in value. For CPW3 (Fig 3.4c), radiation loss is the dominant mechanism above 400 GHz. Finally, in Fig. 3.4d we re-plotted the total loss as in Fig. 3.3d.

When short pulse propagation is the main application of a CPW line, carefully design must be taken into account. The right choice of the substrate, metalization and geometrical parameters depend on every specific device, or application. When designing a CPW line, the first thing to consider is the dimension ratio required to achieve desired characteristic impedance. Following that, the strip width should be minimized to decrease the overall dimensions as well as suppress higher order modes. At this point it is important to remember that a smaller W leads to higher losses. The substrate thickness must be chosen to reduce radiation loss but then again, a decrease in h while maintaining the same characteristic impedance requires narrower W. Small W means small G and therefore, the fabrication tolerances become very tight. This is the case of CPW1 where $W = 4\ \mu m$ and $G = 3\mu m$.

The validity of some of the models presented above has not been verified experimentally for CPW lines with small dimension such as CPW1. Therefore, it is difficult to determine the real final number for losses but as we will see in the next sections this model follows quite well the experimental values obtained from the lines at frequencies below 60 GHz.

If the pulse were re-generated at any given position along the transmission line, then we would have a way to overcome the very high loses produced by narrow lines and high operation frequencies. The concept of a travelling wave ORE device provides an electrical pulse travelling attached to an optical pulse and

therefore, even when the former will be subjected to losses, it will maintain a minimum distortion and attenuation during its propagation.

3.2.2 Characteristic impedance.

The impedance (ratio of voltage to current) experienced by a wave travelling in a transmission line is known as the characteristic impedance, Z_0, of the line. Z_0 in a CPW line is determined by the geometric factors and the material used as substrate. The characteristic impedance is given by [1]

$$Z_0 = \frac{30\pi}{\sqrt{\varepsilon_{eff}}} \frac{K(k)}{K'(k)} \tag{3.14}$$

k, $K(k)$ and $K'(k)$ are defined as in Eq. 3.8. The elliptical integral can be solved by numerical methods, or using the following approximations:

$$\frac{K(k)}{K'(k)} = \frac{1}{\pi} \ln\left[2\frac{1+\sqrt{k}}{1-\sqrt{k}}\right] \qquad for\ 0.707 \le k \le 1 \tag{3.15a}$$

$$\frac{K(k)}{K'(k)} = \frac{\pi}{\ln\left[2\frac{1+\sqrt{k'}}{1-\sqrt{k'}}\right]} \qquad for\ 0 \le k \le 0.707 \tag{3.15b}$$

as a reminder, $k = W/(W+2G)$ and $k' = \sqrt{1-k^2}$.

The characteristic impedance of a CPW line in function of the ratio between the electrode gap G and the central conductor width W is shown in Fig. 3.5.

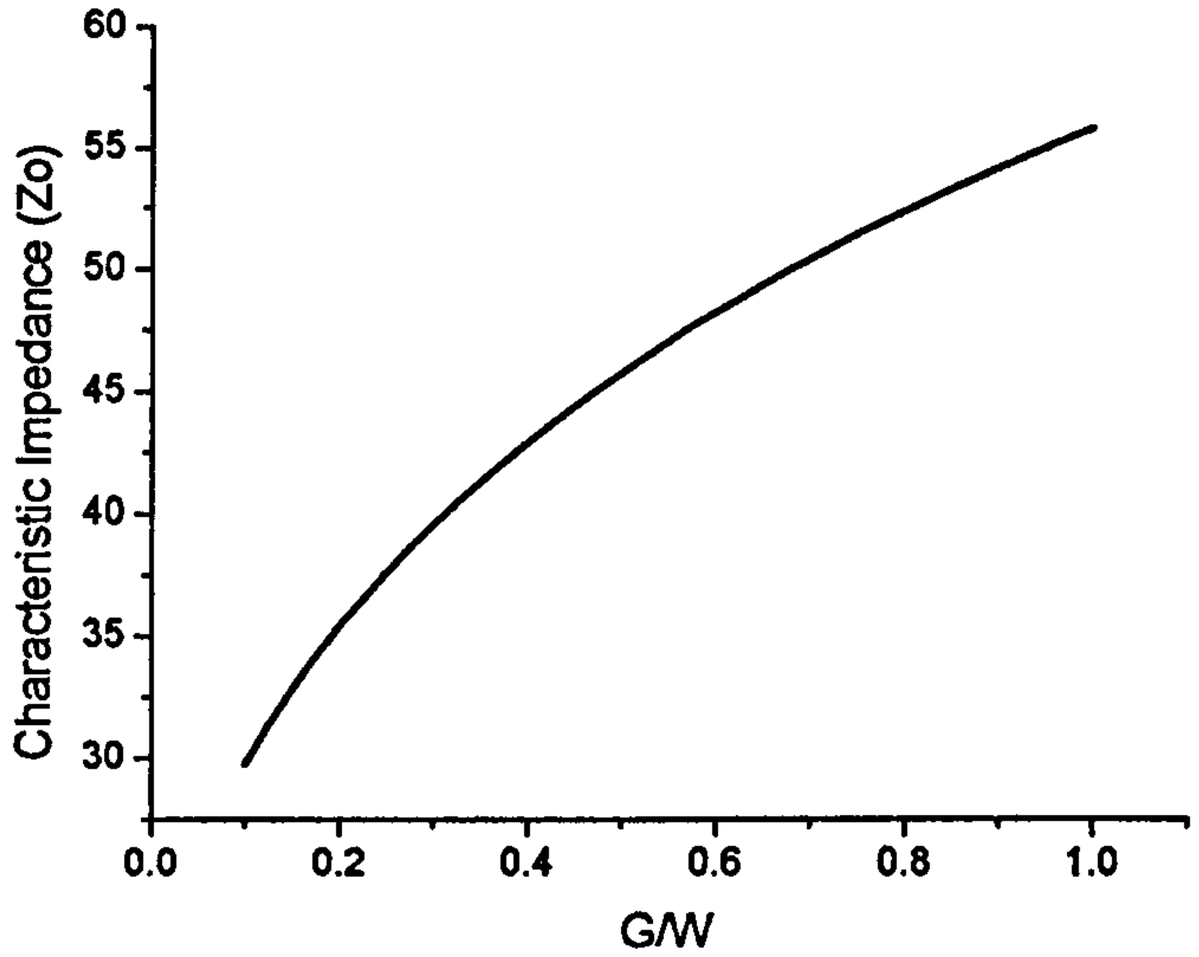

Fig. 3.5. Characteristic impedance as a function of the gap between electrodes *G* over the central conductor width *W*.

3.2.3 Relation between the scattering and the ABCD matrix.

Different CPW lines were fabricated based on computer simulations and then electrically characterised to obtain the scattering parameters. The scattering parameters or s-parameters of an *N*-port network relate incident and reflected voltage waves at the ports of the network, and provide all the relevant information concerning with passive microwave components including transmission lines. These parameters are normally arranged into a matrix known as scattering matrix defined, for a two-port network, as:

$$S = \begin{bmatrix} S_{11} & S_{12} \\ S_{21} & S_{22} \end{bmatrix} \tag{3.16}$$

Elements on the diagonal are reflection coefficients and elements off the diagonal are transmission coefficients. In this way, S_{11} is the reflection seen by the port 1 produce by a signal injected into the port 1, S_{21} is the transmission measured at port 2 relative to port 1 and so on. A completely explanation of the s-parameters can be found in [14]. Another way to describe an *N*-port network is

using the ABCD parameters or ABCD matrix. A two-port network representation is shown in Fig. 3.6 using the ABCD parameters to relate voltages and currents on the network.

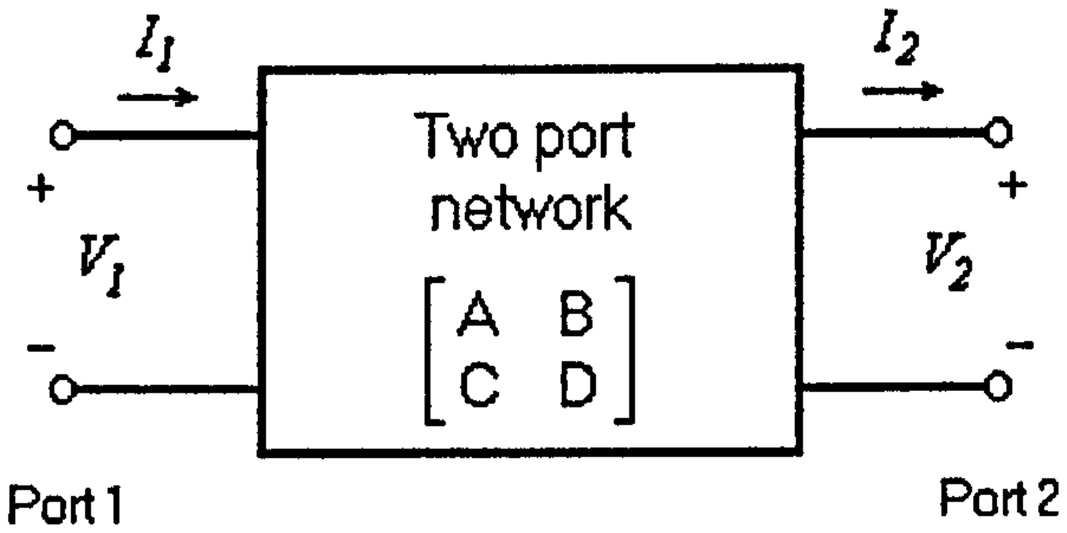

Fig. 3.6. Two-port network representation.

The relation between voltages and current is expressed as:

$$\begin{bmatrix} V_1 \\ I_1 \end{bmatrix} = \begin{bmatrix} A & B \\ C & D \end{bmatrix} \begin{bmatrix} V_2 \\ I_2 \end{bmatrix} \tag{3.17}$$

Even when all the parameters of the line can be obtained from the scattering matrix, the ABCD matrix presents certain advantages when using cascading devices. Furthermore, there are blocks already available for design in function of the ABCD matrix. In this work, ABCD parameters were use to calculate the characteristic impedance, Z_0, and the microwave refractive index, n_{mw}. The total loss of the line was obtained from the S_{21} parameter. To convert the s-parameters to ABCD parameters the following relations can be used [15]:

$$\begin{bmatrix} A & B \\ C & D \end{bmatrix} = \begin{bmatrix} \dfrac{(1+S_{11})(1-S_{22})+S_{12}S_{21}}{2S_{21}} & Z\dfrac{(1+S_{11})(1+S_{22})-S_{12}S_{21}}{2S_{21}} \\ \dfrac{1}{Z}\dfrac{(1-S_{11})(1-S_{22})-S_{12}S_{21}}{2S_{21}} & \dfrac{(1-S_{11})(1+S_{22})+S_{12}S_{21}}{2S_{21}} \end{bmatrix} \tag{3.18}$$

where Z is the reference impedance of the network and in our specific case $Z = 50\Omega$. From the ABCD parameters, the complex characteristic impedance Z_0 and the complex propagation constant γ of the line can be found respectively [5]:

$$Z_0 = \frac{2B}{D - A \pm \sqrt{(A+D)^2 - 4}} \tag{3.19}$$

$$\gamma = \frac{1}{L}\left[\ln\left(\left(\frac{A+D}{2}\right) \pm \sqrt{\left(\frac{A+D}{2}\right)^2 - 1}\right)\right] \tag{3.20}$$

where L is the length of the transmission line. The propagation constant is:

$$\gamma = \alpha + j\beta \tag{3.21}$$

where α is the attenuation coefficient defined in Eq. 3.13 in Np/unit length and β is the phase constant defined in Eq. 3.4 in rad/unit length. There are two solutions for Eq. 3.19 and Eq. 3.20. The value with a physical sense for Z_0 must be positive. The physically meaningful value of γ has a positive α. The phase velocity v_{ph} can the be calculated from

$$v_{ph} = \frac{2\pi f}{\beta} \tag{3.22}$$

and the correspondent microwave refractive index n_{mw} from

$$n_{mw} = \frac{c}{v_{ph}} \tag{3.23}$$

3.2.4 Electrodes for a non velocity-matched ORE device.

The simplest design of a CPW line as electrodes for an ORE device is based only on the characteristic impedance. A characteristic impedance of 50 Ω is desirable on the line because of the compatibility with the characterisation equipment. As

described in section 2.5.1, the width of the ridge, W_{opt}, is 5 μm and therefore the central conductor of the CPW cannot be wider than this. The dimension chosen is $W = 4$ μm. Using Eq. 3.14, $G = 2.7$ μm provides 50 Ω characteristic impedance. For easy design of the fabrication mask, a gap $G = 3$ μm was chosen for the CPW line. With this new dimensions, the characteristic impedance $Zo = 51.4$ Ω, which is completely acceptable for a transmission line. For this structure, the microwave refractive index and the losses were calculated. The actual dimensions of the line are considered as "small" on the field of planar transmission lines. Small values of W and G are not commonly used in standard microwave circuits mainly because the high conductor losses but in this case we are limited by the dimensions of the optical ridge.

3.2.4.1 Simulation.

Microwave Office™ (MWoffice) was used to simulate all the different CPW lines employed in this thesis. MWoffice provides an electromagnetic simulator using Maxwell's equations to compute the response of a structure from its physical geometry. This kind of simulator can simulate highly arbitrary structures providing accurate results. The simulation parameters are as follow: frequency sweep from 1 GHz to 61 GHz with 5 GHz steps. Layer 1 (Air) is 100 μm thick and $\varepsilon_r = 1$. Layer 2 (GaAs) is 400 μm thick and $\varepsilon_r = 12.9$. Loss tangent and bulk conductance were set to zero for both layers. The boundary conditions for the top and bottom of the enclosure are set to approximate open (337 Ω). Gold was selected as the conductor with low frequency sheet resistance of 0.025 Ω/□, high frequency loss coefficient of $3.14159x10^{-7}$ Ω/(□* $\sqrt{f}$) and null excess surface reactance. The conductor thickness was set to 1 μm and the material conductivity was $4.098x10^{7}$ S/m.

The CPW lines for the rectification device were compared with well-known transmission lines to confirm the validity of the simulation of transmission lines with small W. The reference line has $W = 20$ μm and $G = 15$ μm. This reference line is going to be labelled as "*B3*" while the line with the small geometry ($W = 4$ μm and $G = 3$ μm) will be labelled as "*plain*". The current density of the lines is

shown in Fig. 3.7. The current in the plain line tends to flow in a small area close to the gap. This, and the fact that the central conductor in only 4μm width, increases conductor losses in comparison with the B3 line where the current is more evenly distributed in the signal and ground electrodes.

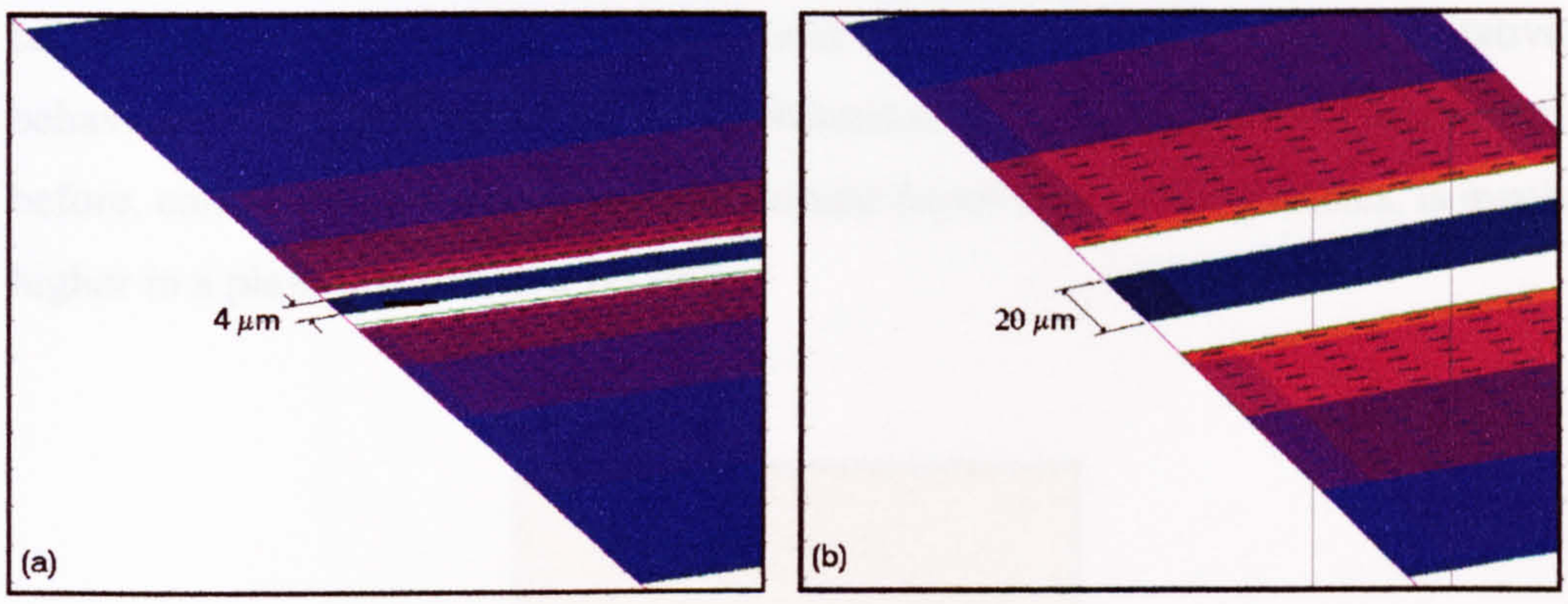

Fig. 3.7. Current density on the plain line (a) and the B3 line (b). The current density is indicated by colours where the red means high density and the blue low density.

The losses and microwave refractive index obtained from the simulations are plotted in section 3.2.4.2 together with the measured experimental data.

3.2.4.2 Electrical characterisation.

Following the simulations, the ORE3 devices (see chapter 5) were fabricated using the techniques described in chapter 4. The electrical characterisation of the CPW lines was experimentally studied using a probe station and a HP8510 network analyser. The s-parameters of the lines were measured from 10 GHz to 60 GHz. These parameters were then used to calculate the ABCD matrix from where the characteristic impedance, and microwave refractive index were calculated. The calibration used for the characterisation of the lines was made using an impedance standard substrate (ISS) with a Line-Reflect-Reflect-Match (LRRM) calibration. On a LRRM only the thru line delay and d.c. resistance of one load standard must be specified. The use of an ISS fixed the calibration reference plane at the probe tips. A full explanation and more information on LRRM can be found in [16]. To connect the lines with the external world, they were tapered out to a 50 Ω set of pads compatible with the pitch of the

microwave probe as specified in Fig. 3.8. The small triangular marks are use as a reference to always skate the probes the same distance whether from the edge to one of the marks or between two marks. Fig. 3.9 shows the comparative plot for losses between the simulations using Eq. 3.13 and the measured values. As we can see, there are some discrepancies on the absolute attenuation between the calculations with analytic formulas and measured values. The qualitative behaviour of the attenuation is well represented by the model. As we mentioned before, conductor loss, which is the dominant factor at these frequencies, is much higher in a plain line that in a B3 line.

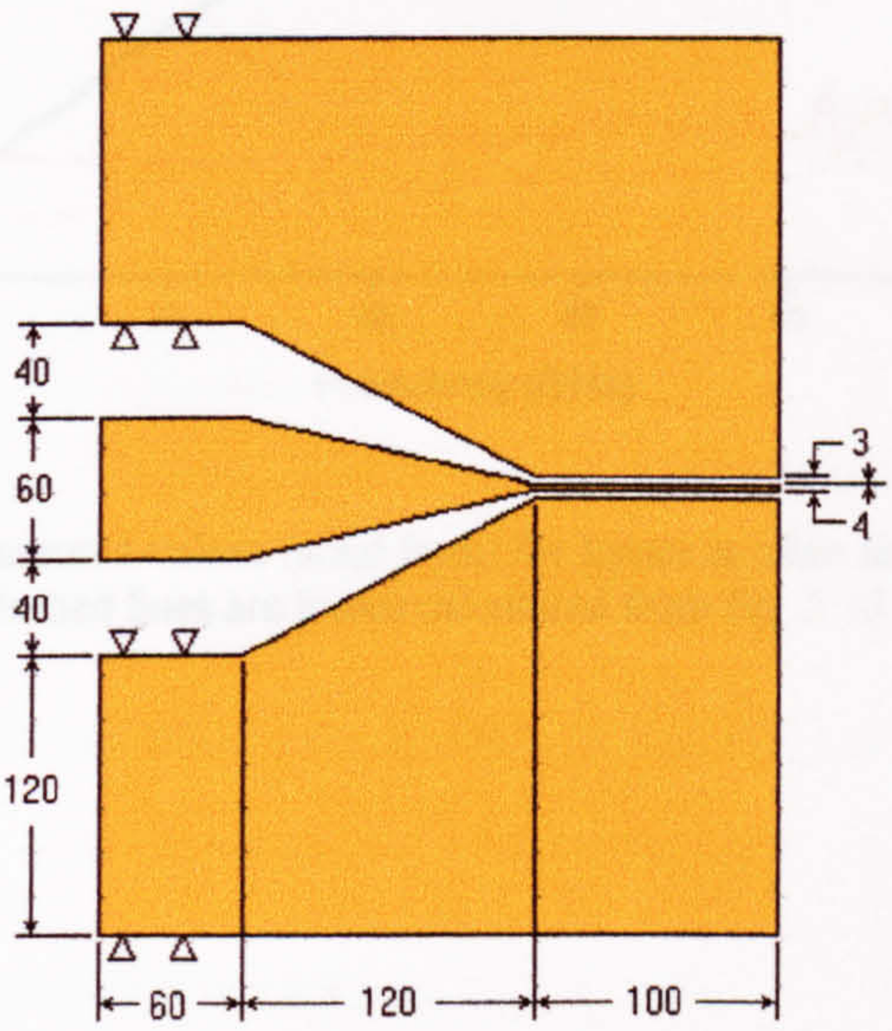

Fig. 3.8. Calibration pads used to measure the CPW lines, all distances are in micrometers.

Fig. 3.10 shows the value of the microwave refractive index for a plain line and a B3 line. The experimental measurement is compare with the simulation with MWoffice presenting a good fit over the whole frequency range. This indicates that the model shows consistency, independent of the size of the CPW line. As we can see in Fig 3.10, the microwave refractive index changes with frequency as ε changes (see equation 3.6), and if we have to set a reference frequency for our design that frequency will be 40 GHz which is the market standard at the present time. For a plain line, at 40 GHz, the measured $n_{mw} = 2.92$, which is still far from $n_{opt} = 3.33$. If these electrodes are used in an ORE device, it is clear that the structure will be non velocity-matched. In order to obtain a velocity-matched

ORE device, we need to make n_{mw} equal with n_{opt}. This can be done with slow-wave electrodes, which are explained in the next section.

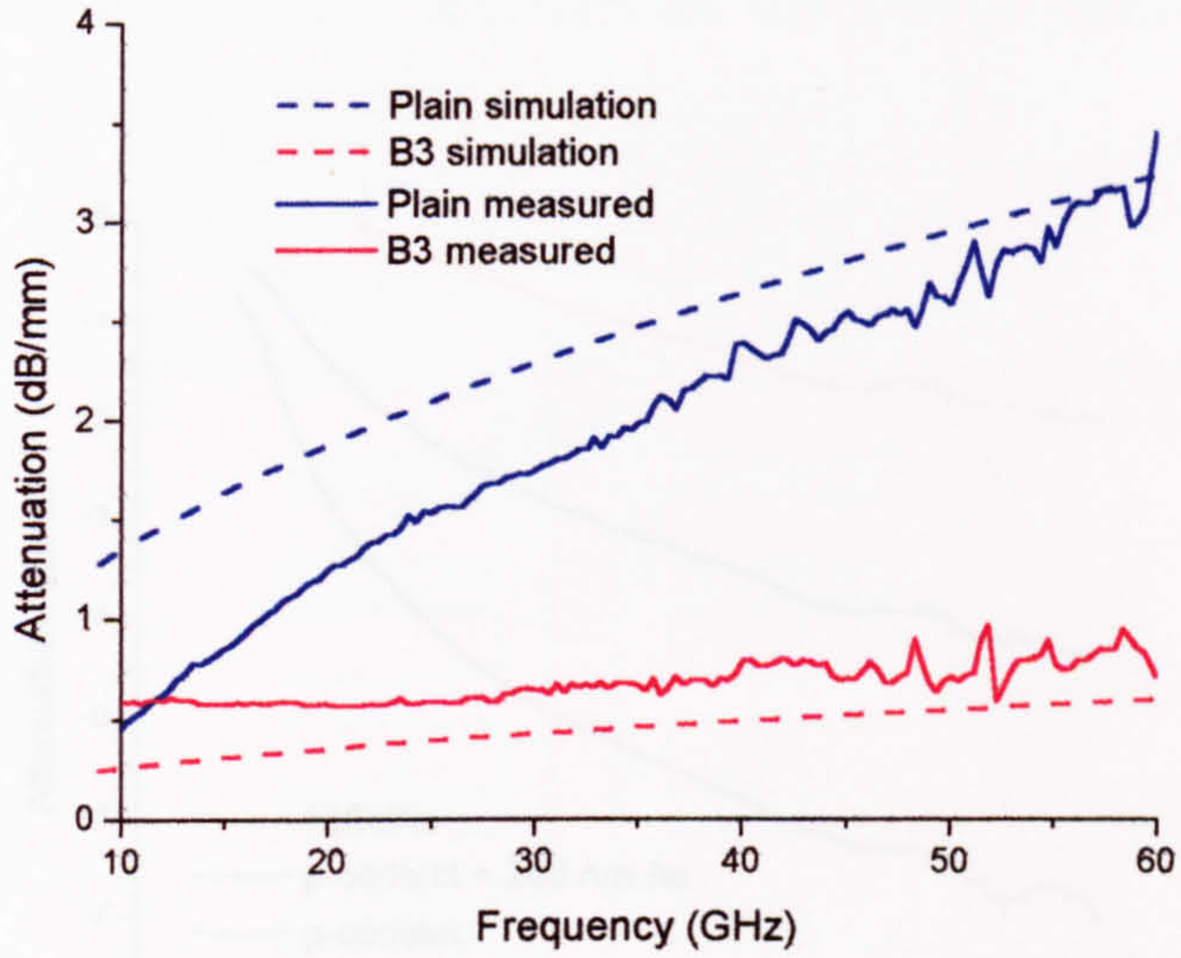

Fig. 3.9. Measured values (solid lines) for losses in plain and B3 lines. Dashed lines are losses calculated from Eq. 3.13.

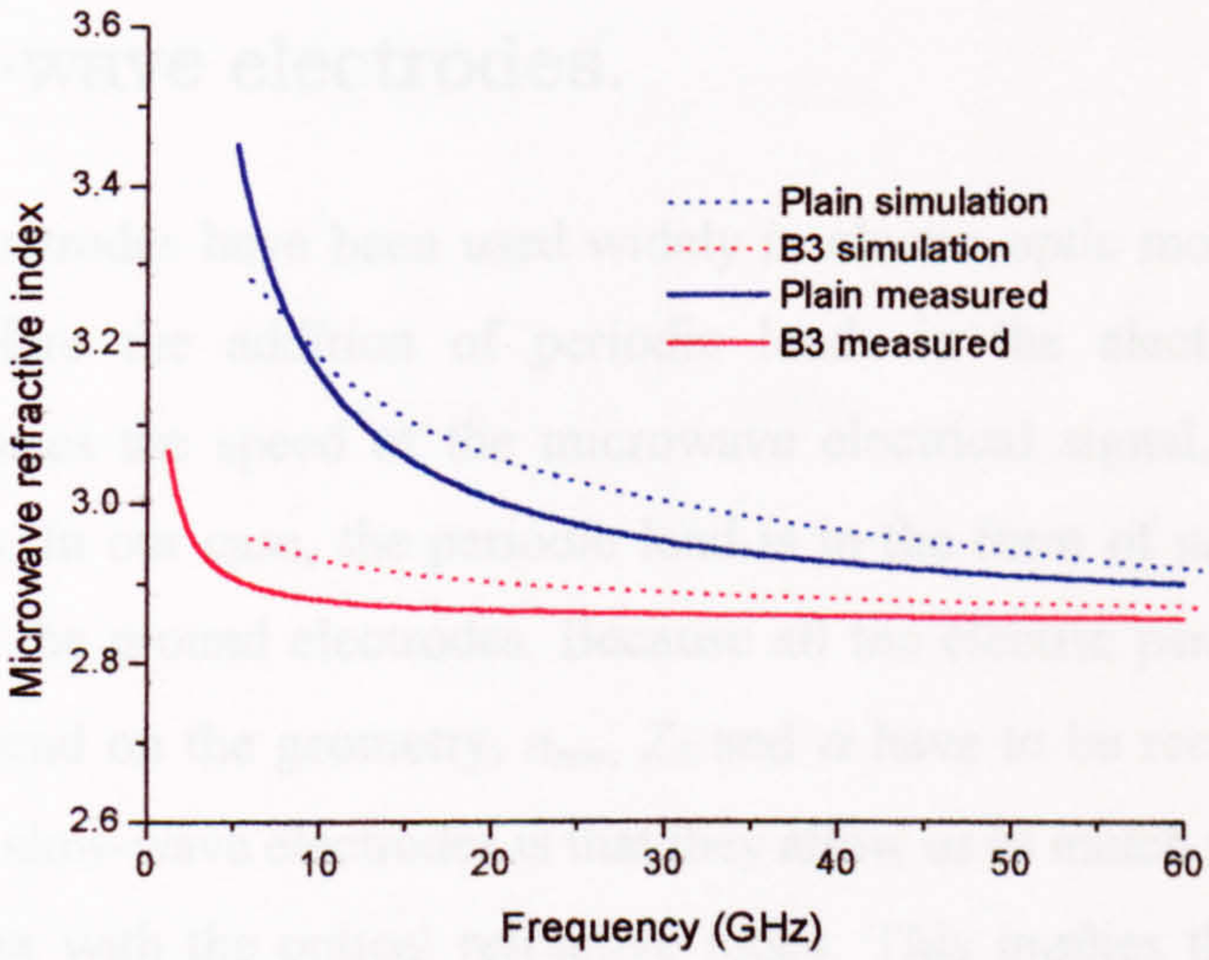

Fig 3.10. Calculated (dotted line) and experimental data (solid line) of a plain and a B3 line.

At this point, the influence of the thickness of the electrodes was explored and the results are shown in Fig. 3.11. The results were as expected according to the literature (*see for instance [17], for one of the first reports*), the thicker the electrode the less lossy it is. See chapter 4 to see the details on the different metalization used in this experiment.

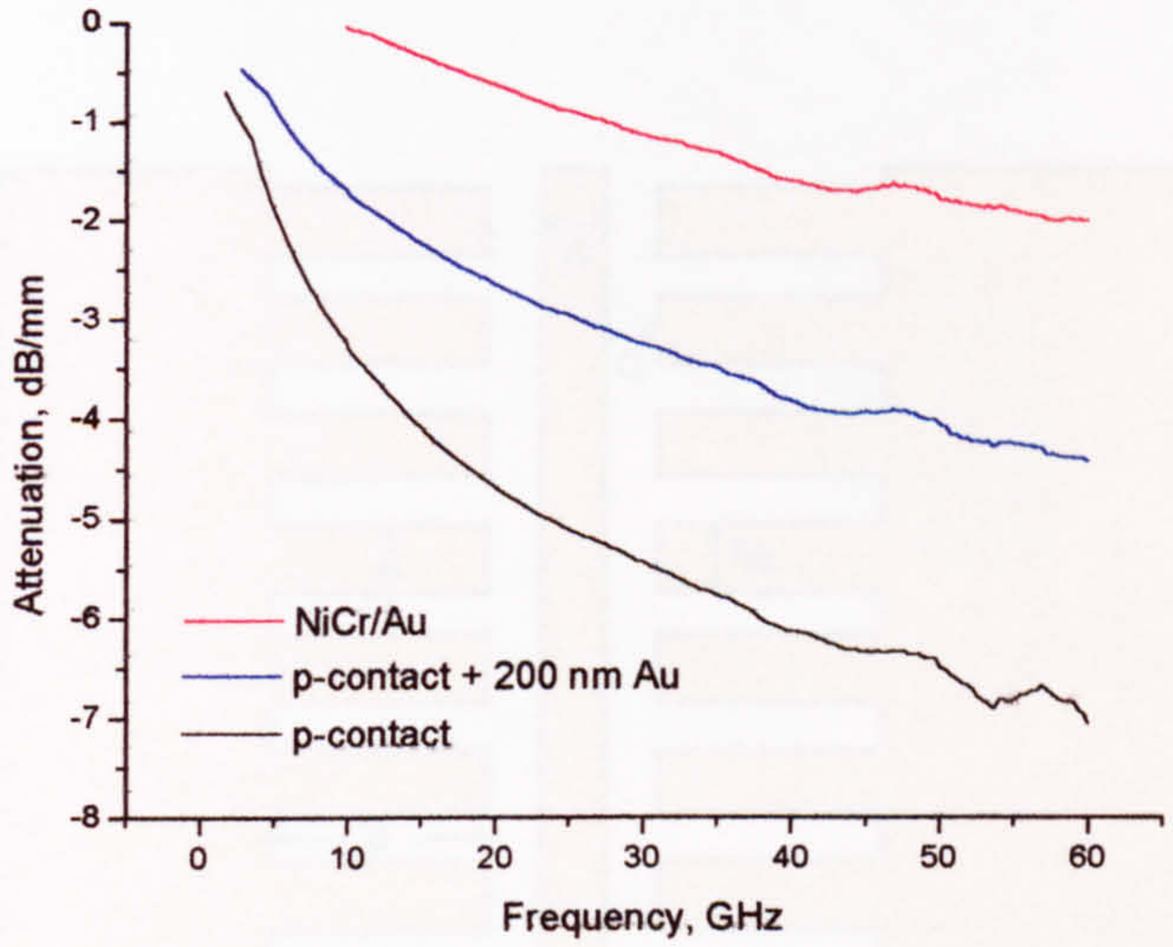

Fig. 3.11. Influence of the electrode thickness on *plain* lines.

3.3 Slow-wave electrodes.

Slow-wave electrodes have been used widely in electro-optic modulator design [4],[5],[18]. Here the addition of periodic loads in the electrodes (ground normally) reduces the speed of the microwave electrical signal, v_{ph}, therefore increasing n_{mw}. In our case, the periodic load is in the form of narrow fins and pads added to the ground electrodes. Because all the electric parameters of the CPW line depend on the geometry, n_{mw}, Z_0 and α have to be recalculated. The importance of slow-wave electrodes is that they allow us to match the microwave refractive index with the optical refractive index. This implies that the optical and the generated optical pulse will travel at the same velocity through the structure. If this is the case, the ORE device will become a travelling-wave ORE device.

3.3.1 Electrodes for a velocity-matched ORE device.

The geometries of slow-wave electrodes studied in this thesis are shown in Fig. 3.12. Fig. 3.12(a) shows the line labelled as "*fin*", Fig. 3.12(b) shows the "*finpad*" geometry. G and W, are fixed from the design described in section 3.2.4. The tuning parameters of both lines are the period p and the length of the fingers d.

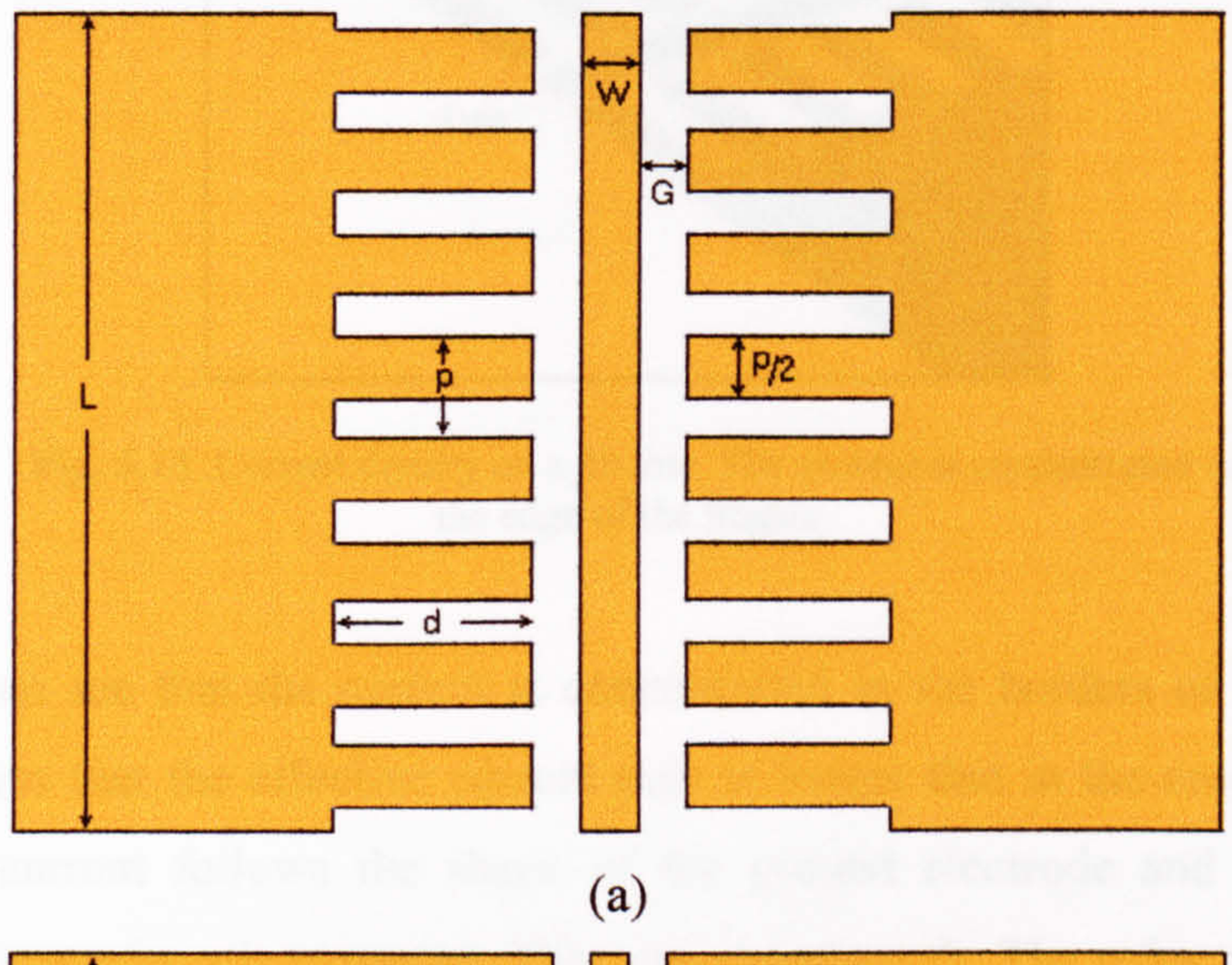

Fig. 3.12. Slow-wave electrodes geometry. (a) *fin* and (b) *finpad* configuration. All dimensions in micrometers.

3.3.1.1 Simulation.

A number of slow-wave electrodes were simulated using MWoffice with the same parameters used in section 3.2.4.1. p and d were varied to obtain a broad tunability range. The current distribution for a *fin* line is shown in Fig. 3.13.

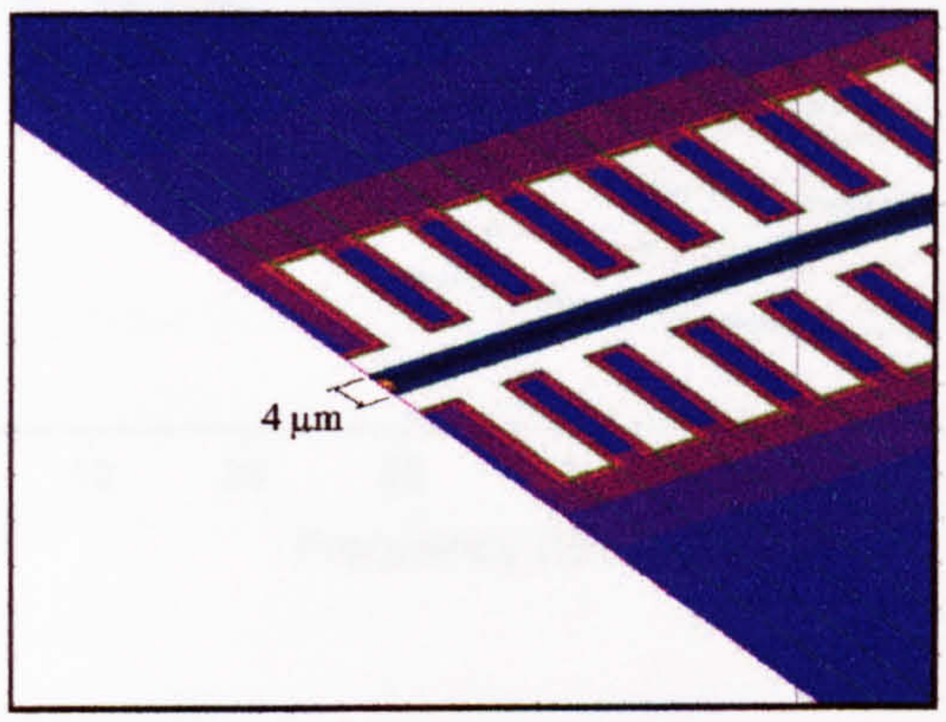

Fig. 3.13. Current density on a *fin* line. The current is concentrated in the edge of the fingers.

Here we can see that the current is concentrated in the borders of the fingers, which means that the effective current path is longer that in the case of a *plain* line. The current follows the shape of the ground electrode and therefore a slightly increase in α is expected. This also increases Z_0. The refractive index is calculated from the simulations and the results are shown in Fig. 3.14 and table 3.1.

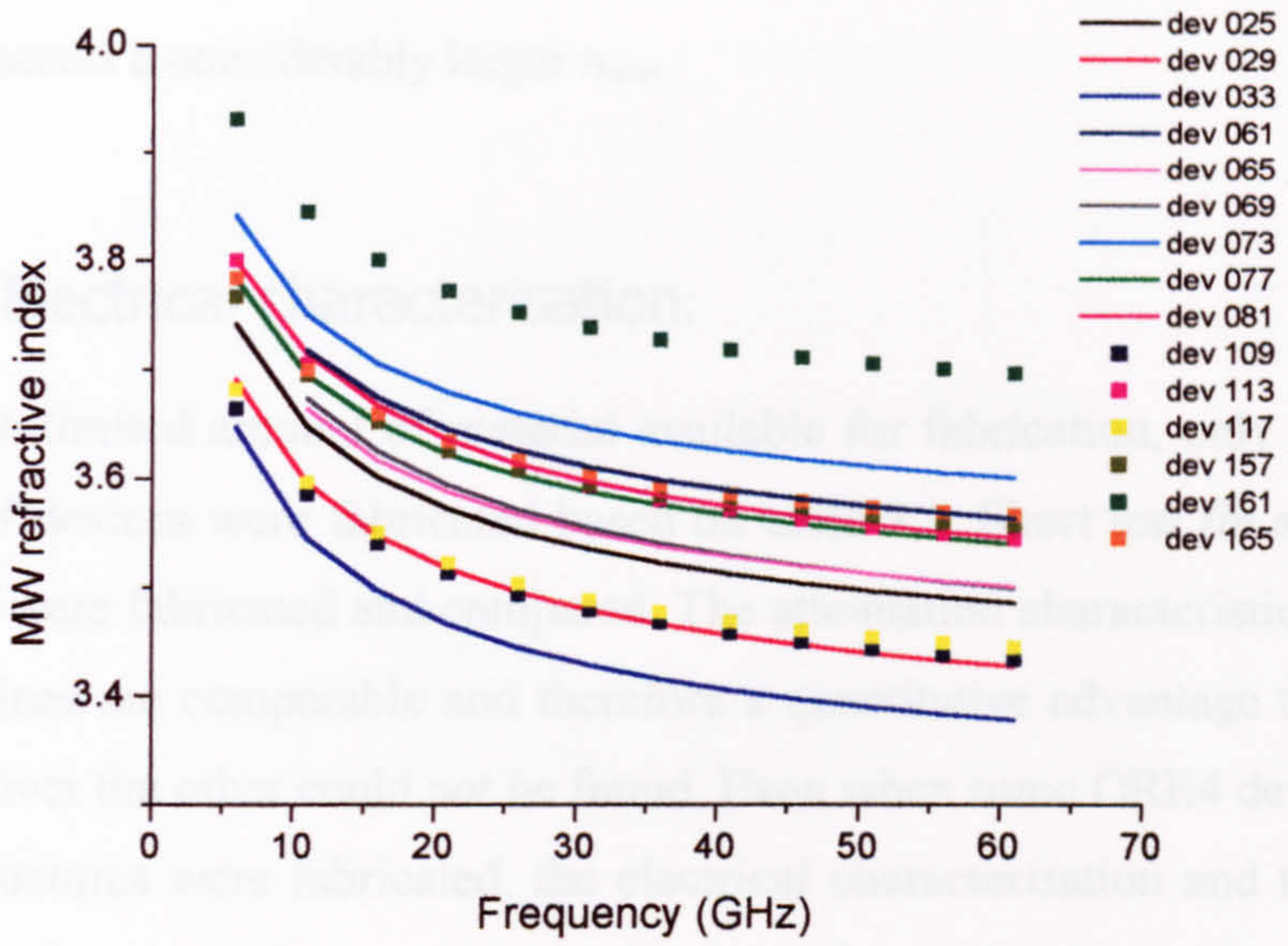

Fig. 3.14. Microwave refractive index as a function of frequency for different *fin* and *finpad* lines. The device code is explained in table 3.1.

Table 3.1. Dimensions and n_{mw} for the slow-wave electrodes used in simulation.

Device No.	Line type	p (μm)	d (μm)	n_{mw} @ 40 GHz
028	fin	4	16	3.51
032		8		3.45
036		16		3.40
064		4	25	3.59
068		8		3.53
072		16		3.53
076		4	30	3.62
080		8		3.56
084		16		3.57
112	finpad	10	18	3.45
116		15		3.56
120		20		3.46
160		10	30	3.57
164		15		3.72
168		20		3.58

$W = 4$ μm, $G = 3$ μm and $L = 100$ μm.

For a *fin* line, when d is 16 μm, the refractive index is inversely proportional to the period length p. For longer d, and for periods larger than 8 μm, there is almost no variation in the refractive index. For the *finpad* lines, for a given d,

periods of 10 μm and 20 μm present the same refractive index whilst a period of 15 μm presents a considerably larger n_{mw}.

3.3.1.2 Electrical characterisation.

Due to the limited amount of material available for fabrication, only a selected number of devices were fabricated based on table 3.1. Short test *fin* and *finpad* structures were fabricated and compared. The attenuation characteristics for both types of lines are comparable and therefore a quantitative advantage to use one structure over the other could not be found. Even when some ORE4 devices with *finpad* structures were fabricated, the electrical characterisation and the results shown in chapter 5 devices were only done for *fin* devices. The electrical characterisation for the slow-wave electrodes was done using Short-Open-Load-Thru (SOLT) calibration to the probe tips using an ISS. The total length of the lines in ORE4 devices is 1 cm, and although so far the calculation of n_{mw} has been done using the ABDC parameters, a more experimental approach was taken for the ORE4 devices. The reason for this is because, a long slow-wave electrode presents a number of resonance peaks in the return loss produced by the capacitive load and the impedance mismatch between the measurement system and the CPW line. The effective microwave index is calculated using [19]:

$$n_{mw} = \frac{c}{2L}\frac{1}{\Delta f} \tag{3.24}$$

Where Δf is the average peak-to-peak frequency. The method is illustrated in Fig. 3.15. Here we are using a device with the following characteristics: *fin* type, p = 8 μm, d = 19 μm and L = 3.3 mm. To calculate the average peak-to-peak distance, Δf, the reading of the first and last peaks is taken. The difference is divided by the number of peaks minus one. This will provide an average n_{mw} for the whole range of frequencies. Following equation 3.24, a value of $n_{mw} = 3.15$ is obtained.

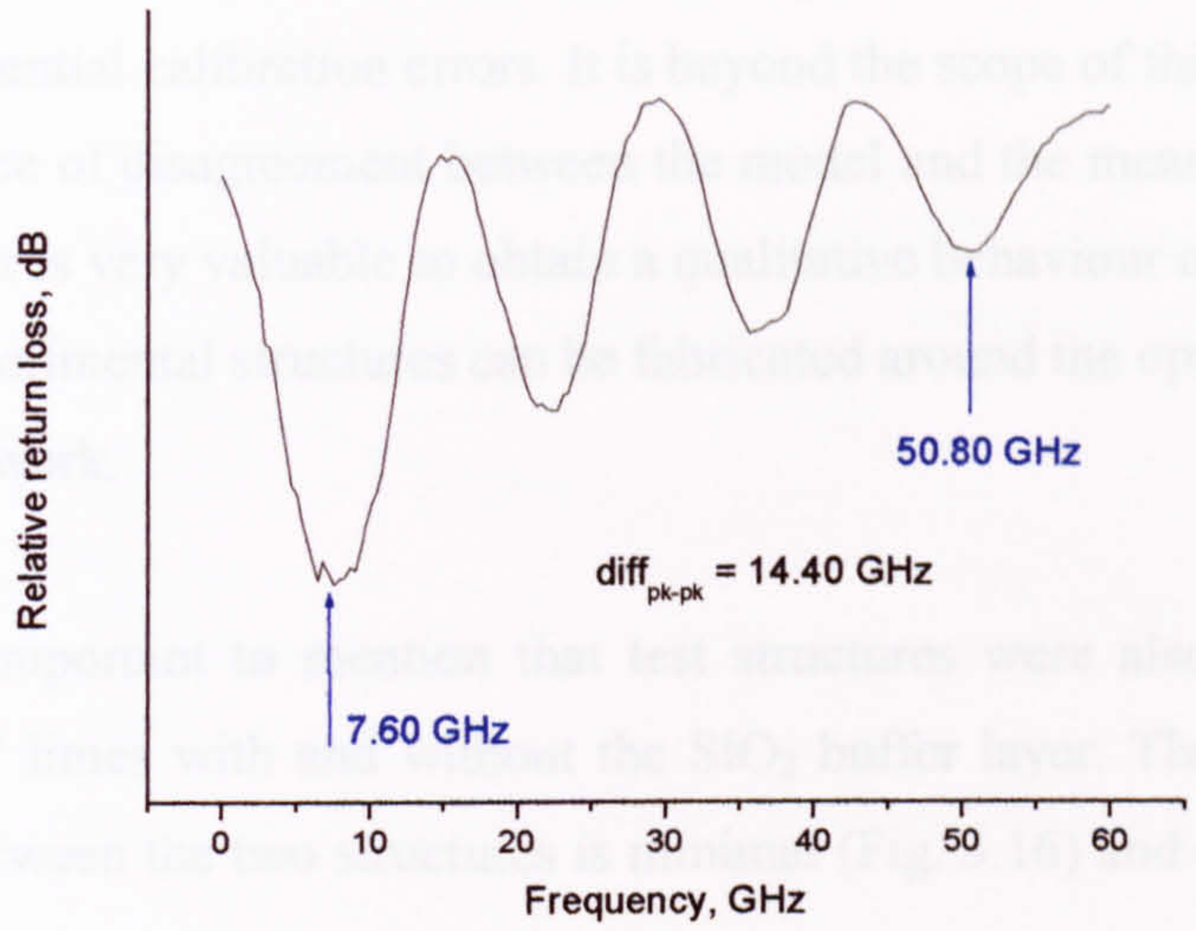

Fig. 3.15. Measured relative return loss as a function of frequency for a slow wave electrode. The markers indicate the frequency at two different resonance peaks.

In the same way, all the different slow-wave electrodes were characterized and the results can be summarised in table 3.2.

Table 3.2. Measured values of n_{mw} for different slow-wave electrodes.

Device No.	Line type	p (μm)	d (μm)	Average n_{mw}	Predicted n_{mw}
000	plain	--	--	2.63	2.92
020	fin	8	13	2.97	
028		4	16	3.20	3.51
036		16	16	3.50	3.40
044		8	19	3.10	
056		8	22	3.29	
068		8	25	3.30	3.53
080		8	30	3.40	3.56

$W = 4$ μm, $G = 3$ μm and $L = 1$ cm.

The measured values of refractive index are lower that the ones modelled with MWoffice except for device 036. This is desirable since $n_{mw} = 3.3$. The difference between the model and the experiment is less than 10 %. It is not certain if this difference come from the model, from the experimental set-up or from both. A number of things can account for the difference: 1) we are measuring average effective indexes; 2) simulations were made with a metal thickness of 1 μm compare with 450 nm in the ORE4 devices; 3) even when MWoffice presents good agreement with measured values for plain lines, this

does not guarantee that the solution for a loaded ground will be correct (it is only 2D) and 4) potential calibration errors. It is beyond the scope of this thesis to find the exact source of disagreement between the model and the measurements. The model however is very valuable to obtain a qualitative behaviour of the lines so a number of experimental structures can be fabricated around the optimum point as we did in this work.

Finally, it is important to mention that test structures were also fabricated to compare CPW limes with and without the SiO_2 buffer layer. The difference in attenuation between the two structures is minimal (Fig. 3.16) and can be ignored for practical reasons.

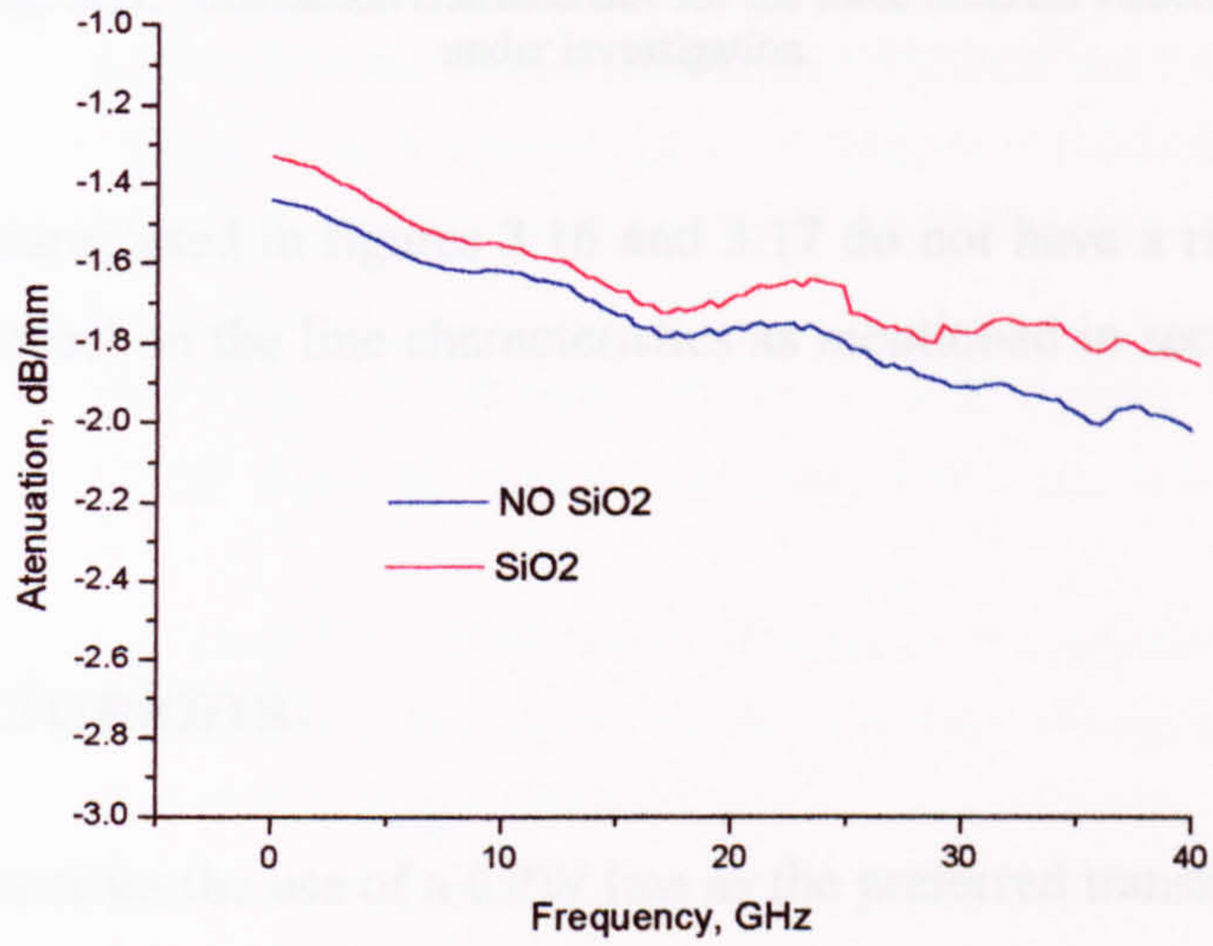

Fig. 3.16. Influence of the SiO_2 buffer layer in the ORE devices.

In the same way, the attenuation for a *plain* line was compared with its equivalent *fin* and *finpad* slow-wave electrodes. The results are shown in Fig. 3.17. At low frequencies, the plain line presents low attenuation but it is considerably increased as the frequency is increased until eventually matches the other two structures. This came as a surprise and the reason for this behaviour is not fully understood. The *fin* and *finpad* lines are more constant over the whole frequency range.

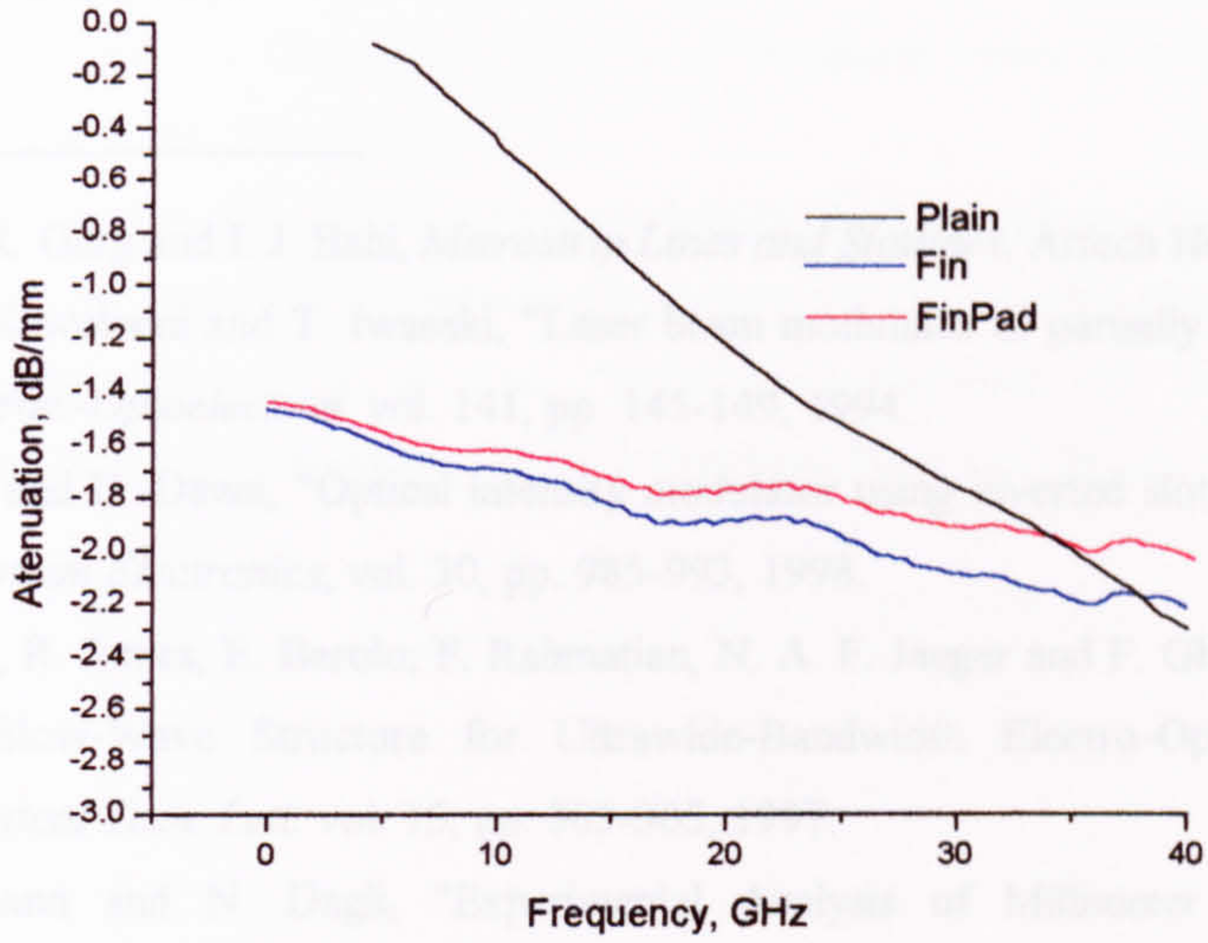

Fig. 3.17. Attenuation characteristic for the three different structures under investigation.

The test structures used in figures 3.16 and 3.17 do not have a ridge. The ridge will have an effect on the line characteristics as mentioned in section 2.5.1 (Fig. 2.12)

3.4 Conclusions.

This chapter justifies the use of a CPW line as the preferred transmission line for the ORE devices. The explanation of the loss mechanisms helps to understand the importance of a velocity-matched device. This chapter took us through all the work behind the design of the electrical electrodes. Simple structures were modelled first and then slow-wave electrodes were tried. The important point that needs to be raised here is that a starting point for fabrication was necessary even when we knew about the potential differences between the model led and the experimental results. Modelling was used as starting point so we could fabricate devices with different dimensions around a potential optimum structure. The final test will be to see if there is any difference when collecting the electrical signal from an ORE device.

3.5 References.

1. K. C. Gupta, R. Garg and I. J. Bahl, *Microstrip Lines and Slotlines*, Artech House, 1979.

2. M. Endo, T. Kawakami and T. Iwasaki, "Laser beam modulator of partially loaded microstrip line structure," *Proc.-Optoelectron.* vol. 141, pp. 145-149, 1994.

3. T. Yoneyama and D. Dawn, "Optical intensity modulator using inverted slot line at 60 GHz," *Optical and Quantum Electronics*, vol. 30, pp. 985-993, 1998.

4. H. R. Khazaei, R. James, E. Berolo, F. Rahmatian, N. A. F. Jaeger and F. Ghannouchi, "Novel Coplanar-Strip Slow-Wave Structure for Ultrawide-Bandwidth Electro-Optic Modulators," *Microwave & Optical Tech. Lett.* vol. 15, pp. 303-305, 1997.

5. R. Spickermann and N. Dagli, "Experimental Analysis of Millimeter Wave Coplanar Waveguide Slow Wave Structures on GaAs," *IEEE Trans. Microwave Theory and Tech.* vol. 42, pp. 1918-1924, 1994.

6. IEEE Standard Definitions of Planar Transmission Lines. ANSI/IEEE Std 1004-1987.

7. M. Y. Frankel, S. Gupta, J. A. Valdmanis and G. A. Mourou, "Terahertz Attenuation and Dispersion Characteristics of Coplanar Transmission Lines," *IEEE Trans. Microwave Theory and Tech.* vol. 39, pp. 910-916, 1991.

8. G. Hasnain, A. Dienes and J. R. Whinnery, "Dispersion of Picosecond Pulses in Coplanar Transmission Lines," *IEEE Trans. Microwave Theory and Tech.* vol. MTT-34, pp. 738-741, 1986.

9. C. Shu, X. Wu, E. S. Yang, X. C. Zhang and D. H. Auston, "Propagation Characteristics of Picosecond Electrical Pulses on a Periodically Loaded Coplanar Waveguide," *IEEE Trans. Microwave Theory and Tech.* vol. 39, pp. 930-936, 1991.

10. U. D. Keil, D. R. Dykaar, A. F. J. Levi, R. F. Kopf, L. N. Pfeiffer, S. B. Darack and K. W. West, "High-Speed Coplanar Transmission Lines," *IEEE J. Quantum Elect.* vol. 28, pp. 2333-2342, 1992.

11. D. R. Grischkowsky, "Optoelectronic Characterization of Transmission Lines and Waveguides by Terahertz Time-Domain Spectroscopy," *IEEE J. Select. Topics in Quantum Elect.* vol. 6, pp. 1122-1135, 2000.

12. M. Riaziat, R. Majidi-Ahy and I. J. Feng, "Propagation Modes and Dispersion Characteristics of Coplanar Waveguides," *IEEE Trans. Microwave Theory and Tech.* vol. 38, pp. 245-251, 1990.

13. L. G Maloratsky, "Reviewing The Basics of Microstrip Lines," *Microwaves & RF*, vol. 39, No. 3, pp. 79-88, 2000.

14. J. Helszajn, *Microwave Engineering: Passive, Active and Non-reciprocal Circuits*, McGraw-Hill, 1992.

15. D. M. Pozar, *Microwave Engineering, 2nd edition*, John Wiley & Sons, 1998.

16. On-Wafer Vector Analyser Calibration and Measurements, Application Note, Cascade Microtech.

17. R. Horton, B. Easter, A. Gopinath, "Variation of microstrip losses with thickness of strip," *Electron. Letters*, vol. 7, pp. 490-491, 1971.

18. H-Y. Lee, "GaAs travelling-wave optical modulator using a coplanar slow-wave electrode with periodic overlays," *Optical and Quantum Electronics*, vol. 27, pp. 487-494, 1995.

19. N. A. F. Jaeger and Z. K. F. Lee, "Slow-Wave Electrode for Use in Compound Semiconductor Electrooptic Modulators," *IEEE J. Quantum Elect.* vol. 28, pp. 1778-1784, 1992.

4. ORE devices: Fabrication

4.1 Introduction.

Fabrication of III-V devices, passives and actives, was a fundamental part of the research presented on this thesis. Different fabrication methods were used to create the rectification devices described in this work. The fabrication of passive optical waveguides is very simple and only involves one lithography step. The rectification device as a whole can be created with two lithography steps but, as we will demonstrate, the accuracy of the equipment available forced us to develop a three-lithography steps process. The general description of the fabrication can be presented as follows. The ORE devices were fabricated using photolithography and e-beam lithography techniques. The 5 μm width optical ridge was etched down using a $SiCl_4$ process on an RIE-80 machine. The electrodes were evaporated and latter defined using either lift-off, or metal etching.

A process flow will be used to describe the fabrication process of the ORE devices. It is understood that the fabrication steps and the fabrication flow itself is related to our specific GaAs/AlGaAs system. The chemicals using for cleaning, etching, etc. can be different to those used on different material

systems. General literature discussing fabrication processes for III-V semiconductors can be seen in [1],[2] and [3].

The ORE devices studied in this thesis will have either of the three electrode configurations shown in Fig. 4.1. The pads used to probe the device are shown in Fig. 3.8 in chapter 3. A real 1 mm long ORE3 device (see caption in Fig. 4.1) is shown in Fig. 4.2.

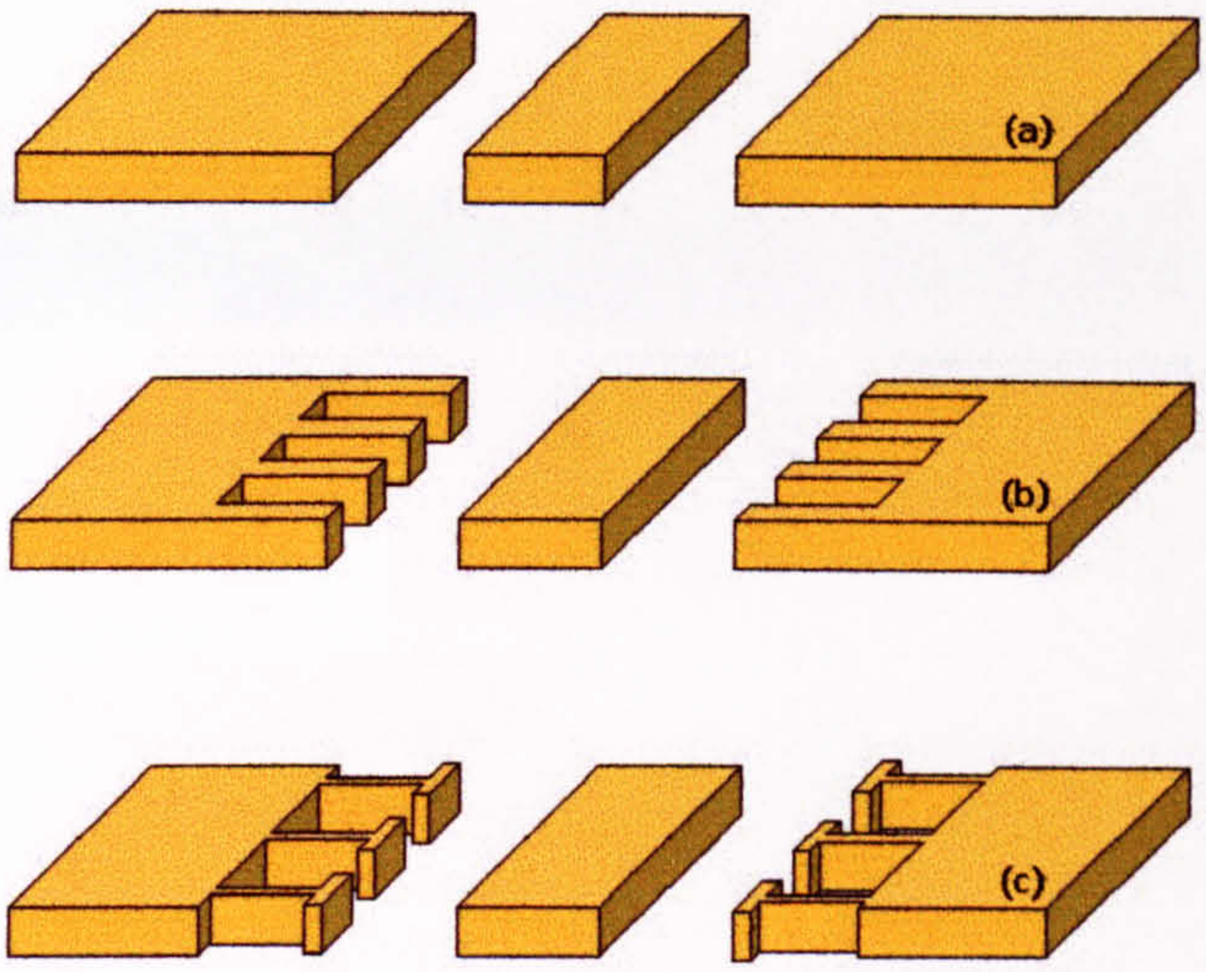

Fig 4.1. Electrodes for ORE devices. (a) ORE2 and ORE3, (b) and (c) ORE4

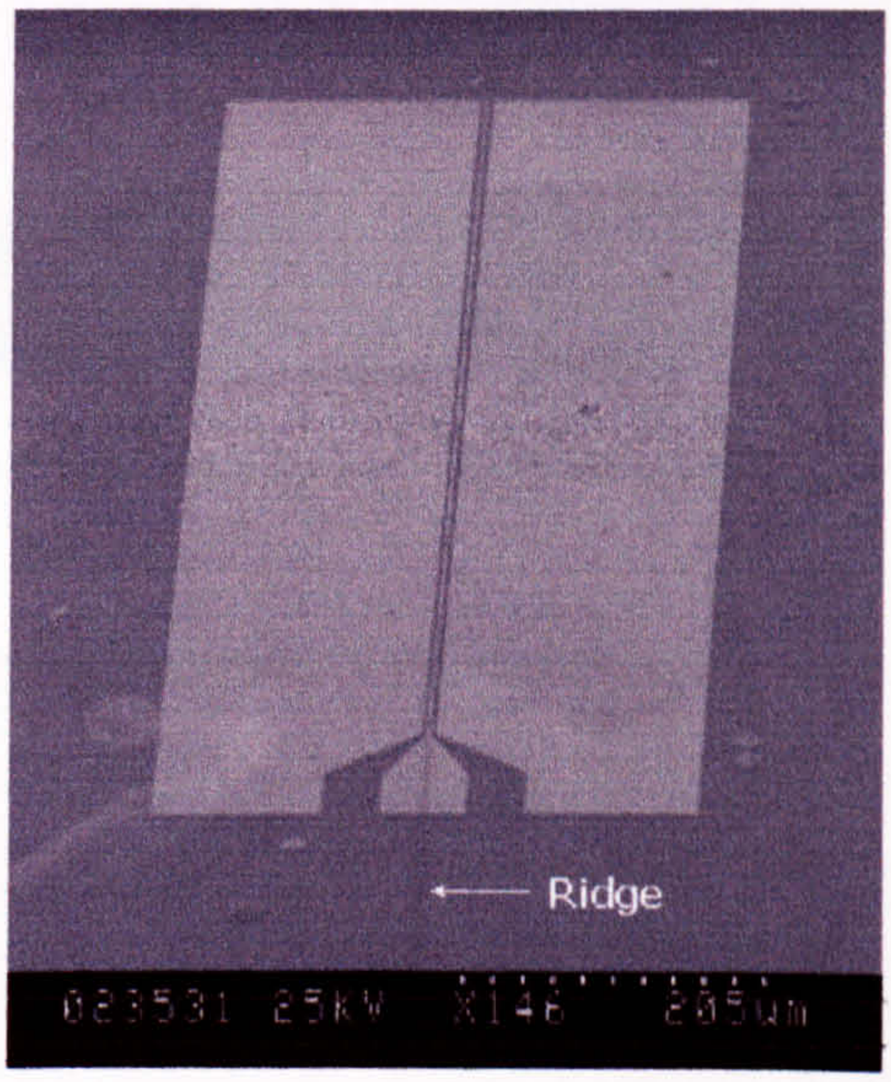

Fig 4.2. SEM photo of a 1 mm long ORE device with the set of electrodes shown in Fig 4.1a. The central electrode is on top of the ridge.

4.2 Mask Design.

The mask used on the fabrication of ORE devices was made using Wavemaker™ (WAM). WAM is software that generates GDSII files (binary file type for pattern data), which can be processed to be compatible with the beam writer. WAM uses the concept of cells, which are the basic unit of all designs. Hierarchical design allows you have cells within the cells, which leads to designs of high complexity that are easy to modify. A screenshot of the software can be seen in Fig. 4.3.

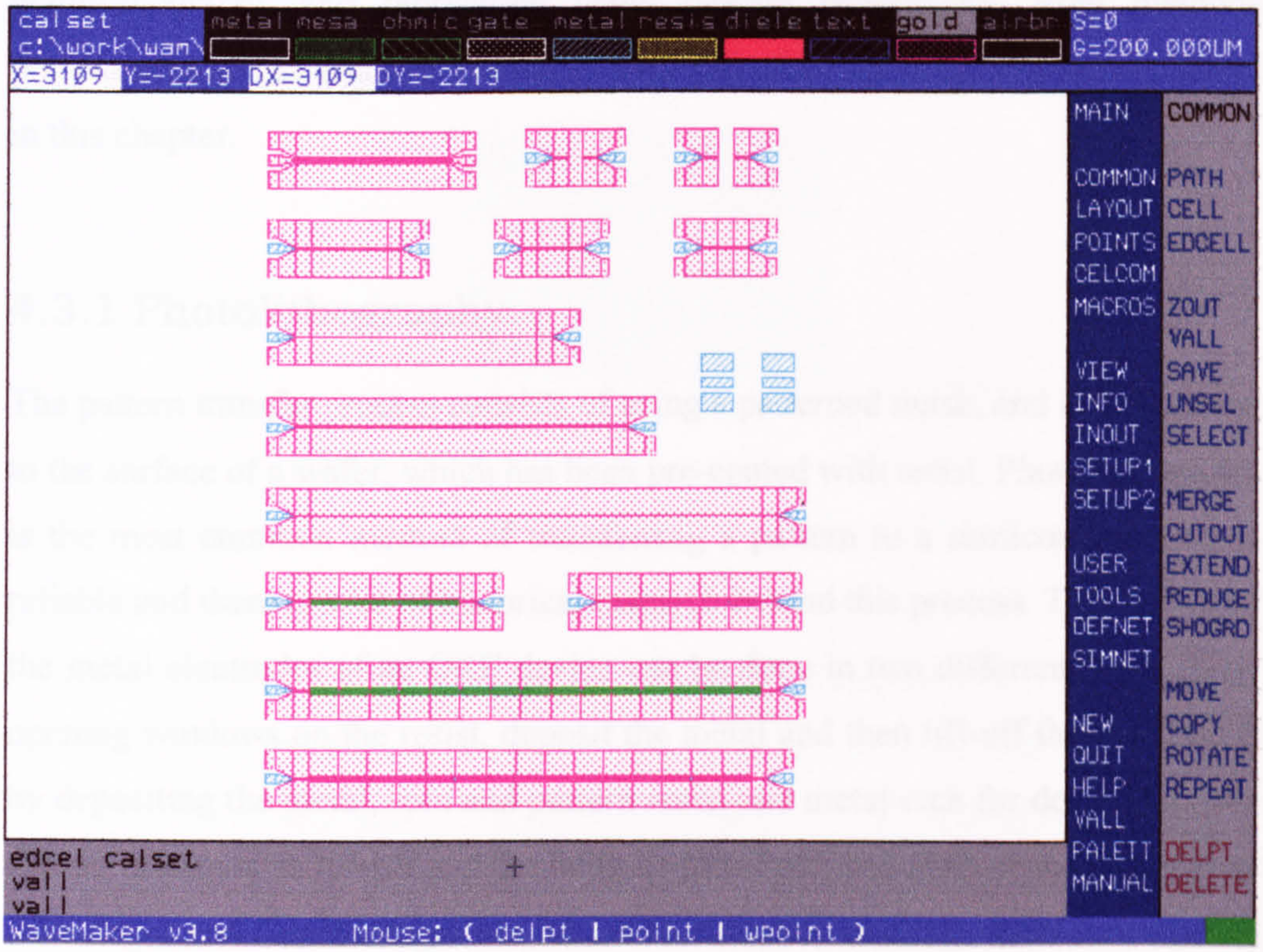

Fig. 4.3. WAM screenshot showing some ORE devices.

There are different layers available on WAM. All the different layers of the fabrication process can be drawn, and specified relative to each other. The pattern contained on the same layer will be written at the same time. The number of layers in a design determines the number of photolithography steps. Once the design is completed, we make use of the computer aided transcription system (CATS) to generate a file understandable by the beam writer. Once in this format, parameters such as job type, spot size, dose and resolution can be set. At

this point, the pattern is ready to be written on a mask plate or directly to the semiconductor sample.

4.3 Fabrication process.

An ORE device can be fabricated with very few steps. If we consider that only two photolithography steps are necessary to create the optical waveguide and the metal electrodes then the fabrication steps can be kept to a minimum. Two different methods of fabrication are included on this section – fabrication using photolithography and fabrication using e-beam lithography. Both methods present advantages and disadvantages over the other and they will be explained in this chapter.

4.3.1 Photolithography.

The pattern transfer process consists of using a patterned mask, and imaging it on to the surface of a wafer, which has been pre-coated with resist. Photolithography is the most common method of transferring a pattern to a semiconductor. It is reliable and there is a lot of historical research behind this process. The pattern of the metal electrodes of an ORE device can be done in two different ways; 1) by opening windows on the resist, deposit the metal and then lift-off the resist or 2) by depositing the metal, spin and pattern resist and metal etch for definition. The former is known as lift-off and the latter as metal etching. Both processes present advantages and disadvantages but for the rectification devices, metal etch worked better. The steps to follow for the fabrication of ORE devices are described below including lift-off and metal etching. The alignment to previous patterns on the sample are made with the help of alignment marks.

Cleaning. The removal of any organic residual and dirt from the semiconductor surface is a vital part of the fabrication process. If a sample is not cleaned properly, problems with the addition and uniformity of any film in contact with the semiconductor will occur. Among other contaminants that can be found on the semiconductor surface are, 1) Dust particles, 2) Grease and wax from

handling and 3) semiconductor particles from cleaving. Rinsing the sample accompanied by the use of an ultrasonic bath is a common way of cleaning GaAs samples. The cleaning process involves the successive use of OptiClear™, acetone and methanol each for 5 min in ultrasonic agitation. The sample is then rinse thoroughly in RO water and blown dry using a N_2 gun. The sample is placed in a hot plate at ~90 ºC for 10 to 15 min to allow any residual moisture to evaporate. OptiClear™ is a non-toxic, biodegradable solvent used to remove wax, pitch and solvent soluble resists from optical and electronic components of glass, ceramic or metal. Acetone and methanol remove remains of resist and molecular contamination. The sample has to be processed immediately after the cleaning process to avoid new contamination.

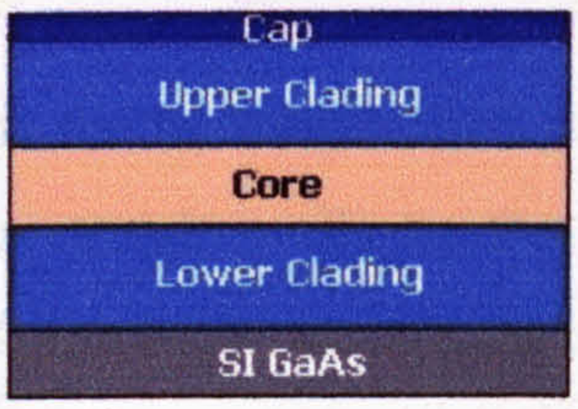

Fig 4.4. Sample at cleaning step. The different layers on the sample are labelled.

Spinning Resist. To transfer the pattern to a semiconductor, the use of a photosensitive polymer is needed. This polymer is commonly known as photoresist or simply resist. The resist is design to have maximum absorption at 330 nm to 430 nm (UV range). The resist that is protected from the light during the exposure step, hardens and cannot be dissolved and washed by the designed developer. Resists of this type are known as positive resists because the image formed in them is the same as the image on the mask. The resist used here is S1818 which is a positive resist sensitive to light at 364 nm. The most important requirements that a resist must satisfy are, 1) capability of resolving minimum feature size, 2) high sensitivity at the specified lamp radiation, 3) good adhesion to the semiconductor and 4) etch resistant. S1818 meets all the above requirements. It gives a uniform thin film, 1.8 μm thick, when spun at 4000 rpm for 30 sec. Good adhesion can be achieved when the relative humidity inside the cleanroom is less than 40 %.

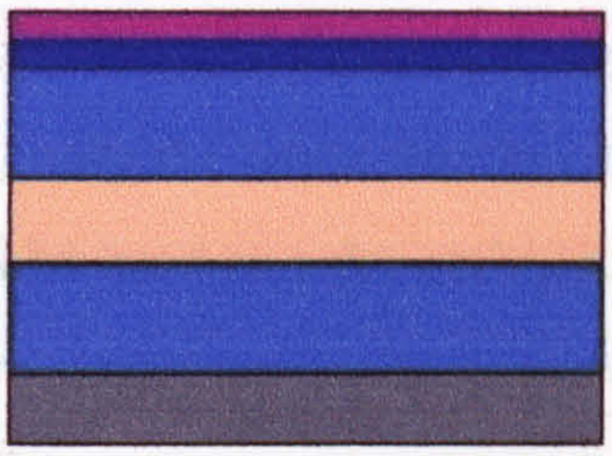

Fig 4.5. Spinning resist.

Softbake. After the resist has been spun, it has to solidify (harden) by extracting all the solvents from the resist. This is achieved with a post-bake at 90 °C for 30 min in a fan assisted convection oven. The sample is now ready for exposure.

Exposure. Contact printing is the technique used to image the pattern into the resist. Contact printing gives straight walls on the resist after developing and allows small features to be defined. The lamp used on the mask aligner is a 200 W Hg short arc lamp delivering an intensity of 5.1 $\mu W/cm^2$. Before exposure of the pattern, the mask has to be cleaned with acetone for 10 min using an ultrasonic bath. This will remove any dust particles as well as any residual photoresist remaining from previous exposures. The mask and sample are positioned in the mask aligner and held to their respective positions by vacuum. The sample is brought in close proximity to the mask and then aligned to it by moving the sample chuck holder. The chuck holder can be move in *x*, *y* and *z* directions and can be rotated. When the sample is finally aligned to the mask, they are brought to physical contact with each other. The sample is then exposed to UV light for 11 sec.

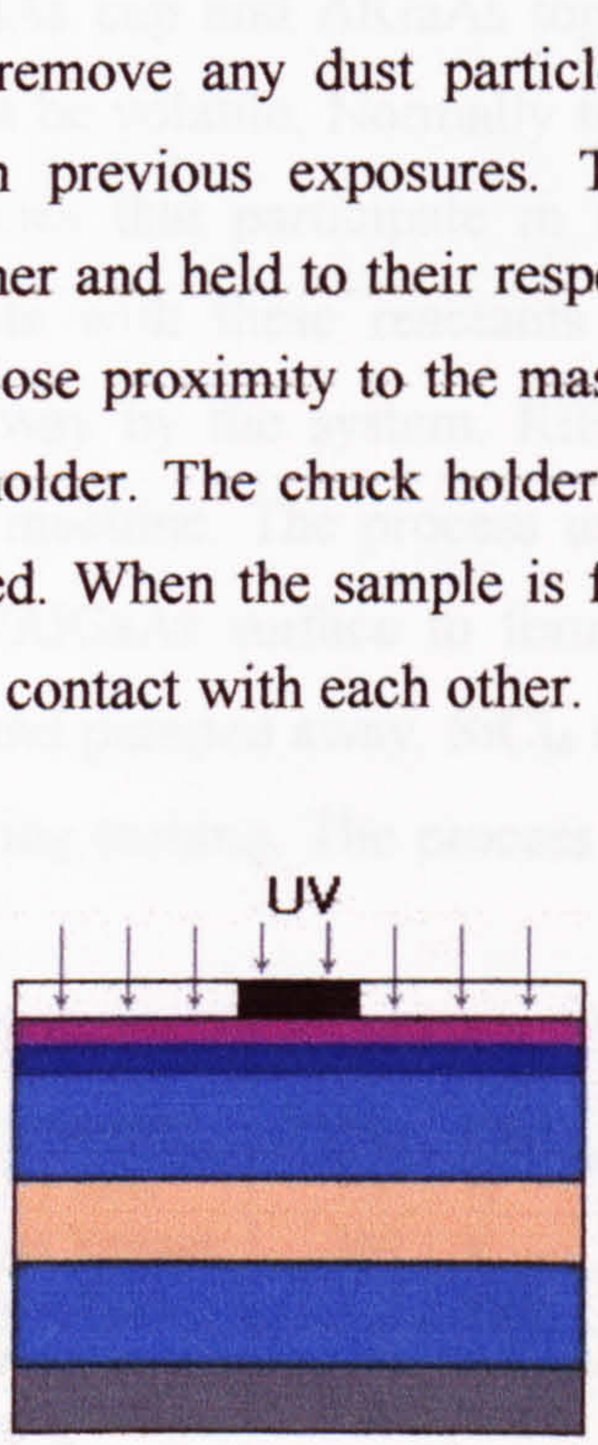

Fig. 4.6. UV exposure. The mask with the black pattern can be seen making contact with the resist layer.

Development. After exposure, the sample is developed using microposit developer. The developer is mixed with RO water in 1:1 ratio. The sample is left in the mixture to develop for 75 sec and then rinse in RO water. S1818 is a positive resist and therefore, only the resist that has not been exposed to the UV light remains. The resist will be used as a dry etching mask.

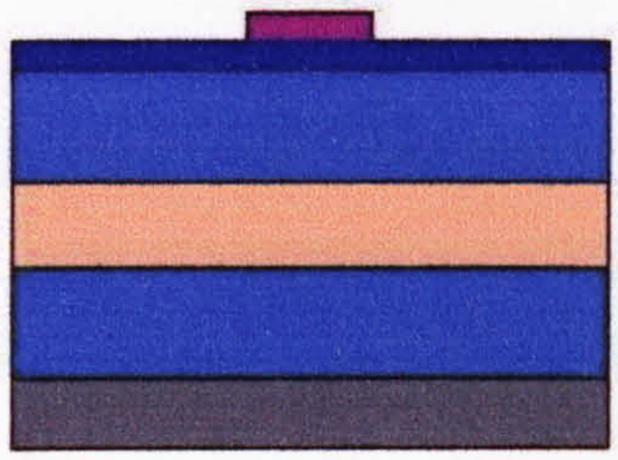

Fig. 4.7. Development. Only the resist that has not been exposed remains.

Postbake. A postbake is given to the sample mainly to toughen the resist so it can better withstand the harsh environment of the reactive ion etching (RIE) process. The postbake is made in a hotplate set at 120 °C for 5 to 10 min.

Etching. Etching of the GaAs cap and AlGaAs top cladding is done by RIE. Chemicals used in RIE must be volatile. Normally free radicals in the chamber are the major reactant species that participate in the chemical process. The semiconductor surface reacts with these reactants and the product of these reactions can be pumped away by the system. RIE is done using an Oxford Plasma Technology RIE-80 machine. The process uses $SiCl_4$ as a reactive gas. $SiCl_4$ reacts with the GaAs/AlGaAs surface to form $AlCl_3$, $GaCl_3$ and $AsCl_3$, which are rapidly desorbed and pumped away. $SiCl_4$ also helps with the removal of native oxides forming during etching. The process recipe can be seen in table 4.1.

Table 4.1. RIE process recipe.

Parameter	**Value**	**Unit**
RF Power	100	W
Bias Voltage	260	V
Flow Rate	9	sccm
Pressure	9	mTorr
Temperature	40	°C

Etched profiles can be highly vertical and smooth when the chamber is clean. Etching rates are typically around 200 nm/min though the AlGaAs etch rate is slightly (5 to 10 %) slower, especially at high Al concentrations. Etch rate depends on sample size. Bigger samples etch slower.

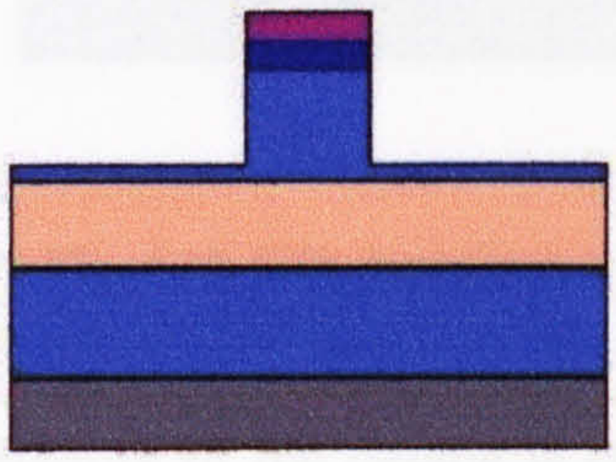

Fig 4.8. Etching.

Strip resist. After etching, the resist has to be removed using acetone. Sometimes, this resist can be difficult to remove and a hot bath at 60 ºC has to be used. The sample is then rinsed in methanol and blown dry.

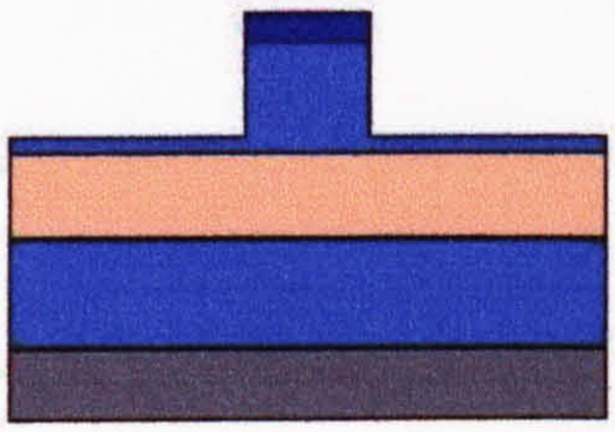

Fig 4.9. Strip resist.

Silica (SiO_2) deposition. Plasma-enhanced chemical vapour deposition (PECVD) silica is deposited on the surface of the semiconductor. This silica layer will act as a buffer layer to reduce optical losses as explained in section 2.5.2. It will also serve as an isolation layer to avoid any current flowing into the semiconductor and this is the reason to use PECVD instead of sputtered SiO_2.

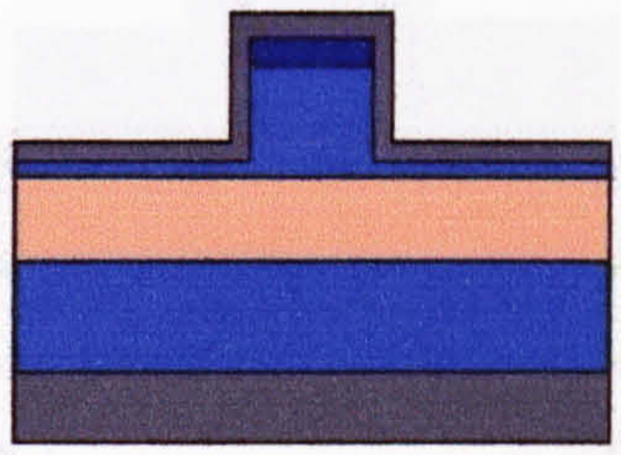

Fig. 4.10. SiO_2 deposition.

At this stage, the optical structure of the device is completed, however, further processing is required to create the electrical structure. As mentioned before, two different ways of defining the metal electrodes on the sample were explored. The two methods use all the common steps mentioned above but they take different flows from this point onwards. Because almost all the steps used are the same as the ones described so far, they will not be explained again unless key differences have to be underlined. The process of the metal structure is explained in the next two subsections.

4.3.1.1 Lift-off.

Taking the sample from the last common step (SiO_2 deposition), the fabrication steps for metal pattern are:

Spinning resist. At this point, the structure is not planar anymore, it is a ridge structure which needs to be patterned again. The photoresist is design to give better results in planar surfaces. Depending in the height of the ridge, the resist layer may not be completely uniform. This is not a big problem because the height of the ridge is only 0.8 μm while the resist is 1.8 μm thick. As is clearly visible, the resist is going to be thinner on top of the ridge than it is in the rest of the structure. This will have an impact when exposing the sample.

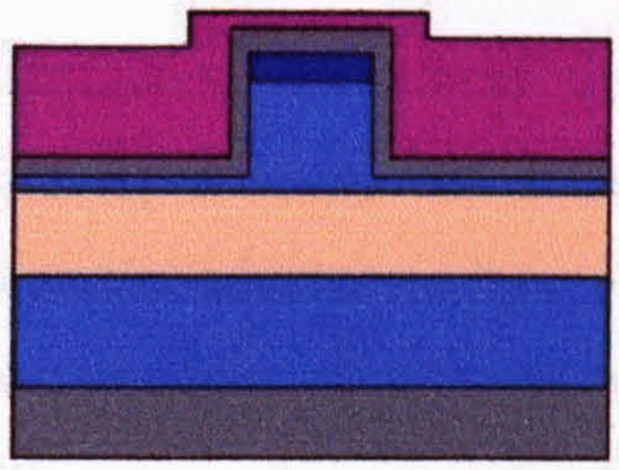

Fig. 4.11. Spinning resist. The thickness of the resist will be different at the top of the ridge compared to the bottom of the trench.

Softbake. ~90 ºC for 30 min.

Exposure. Same process recipe as above. The resist on top of the ridge will experience a different exposure compared to the resist at the bottom of the trench. The developer will therefore work at different rates generating a slight deviation on the dimensions of the original pattern. This problem was shown not to be a significant factor with the devices here, but further investigation has to be done if a new process to compensate for the difference in heights needs to be developed. The sample was exposed for 11 seconds.

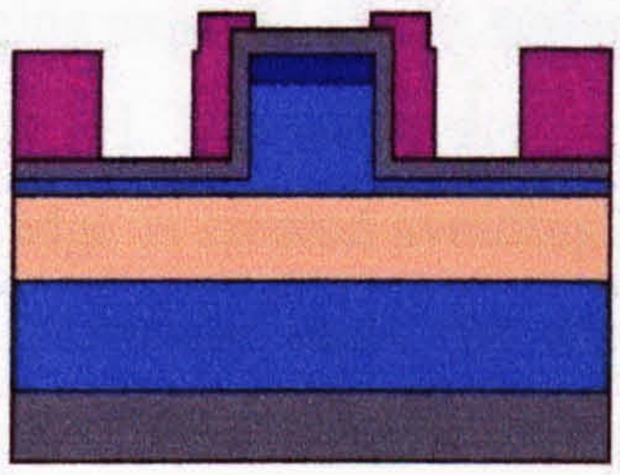

Fig. 4.12. Exposure. The windows for the contacts are now open.

Development. 1:1 mixture, 75 sec.

Metal deposition. The selection of the metal for which the electrodes will be fabricated is gold. The contacts do not need to be ohmic by any means because they are not going to be used to inject current to the device. In principle, any metal will perform well, but thinking on the potential integration of ORE devices

with active components, a standard p-contact was chosen as the metalisation layer. The multi-layer contact is composed of three different metal layers Ti/Pd/Au, 30/13/250 nm. On a p-contact, the Ti layer helps to improve the adhesion of the metal to the semiconductor surface. Pd stops gold diffusing into the semiconductor during the annealing process and Au conforms the metal layer where all the connections to the external word will be made. The thickness of the gold can be change according to the requirements.

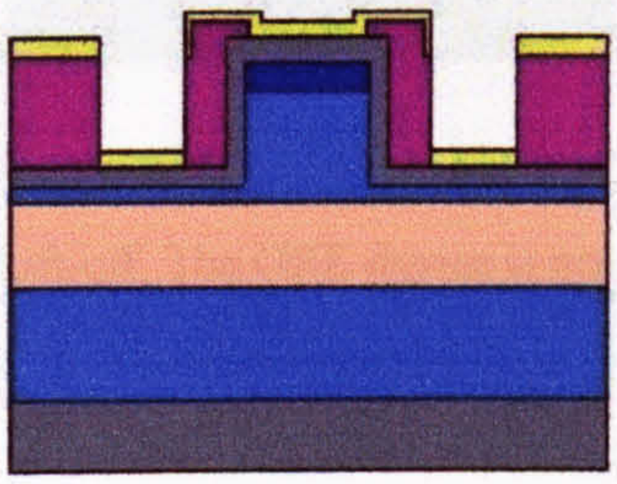

Fig. 4.13. Metal deposition.

Lift-off. Lift-off refers to the process of removing the patterned resist using a solvent leaving a delineated metal pattern behind. In order to be successful, a thick resist has to be used in conjunction with a thin metal layer. To assist the lift-off, the sample before being exposed can be surface-toughened by immersion it in chlorobenzene for 15 min [4]. This will make the surface less affected by the developer and therefore, an edge is created avoiding any metal deposited on the walls of the resist. In this particular case, the success of the lift-off was a function, among other factors, of the gap between electrodes. According to the design of the device, the gap between electrodes is 3 μm which is normally within the resolution of the lift-off but a series of factors combined to make lift-off unsuccessful for an ORE device. These factors are:

- close proximity between electrodes,
- close proximity of the ground electrodes to the ridge and
- no planar surface where lift-off is required.

Lift-off had to be done with the assistance of mechanical rubbing of the sample. Even when the resist was removed from the sample, the problem of scratched

metal surfaces and floppy edges remained. One way around this problem was using a metal etch instead of lift-off. This technique will be explained in section 4.3.1.2.

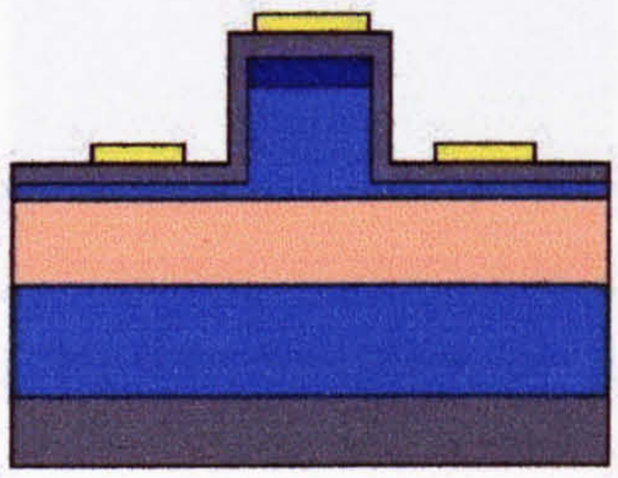

Fig. 4.14. Lift-off. The ORE device is now finished.

4.3.1.2 Metal etching.

A fair amount of research was made on the characterisation of the metal etching mainly due to the high degree of anisotropic etching that can be achieved. Metal etching was done using the ion-milling technique. If we carry-on the process from the last common step described in section 4.3.1 (silica deposition) then the steps involving metal etching as the technique for pattern definition are:

Metal deposition. The p-contact is deposited covering the entire surface.

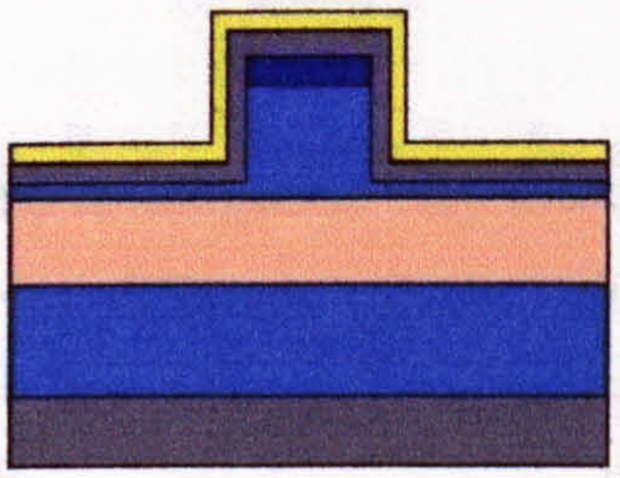

Fig. 4.15. Metal deposition. The metal covers the entire surface.

Spinning resist. As for lift-off. S1818, 4000 rpm, 30 sec.

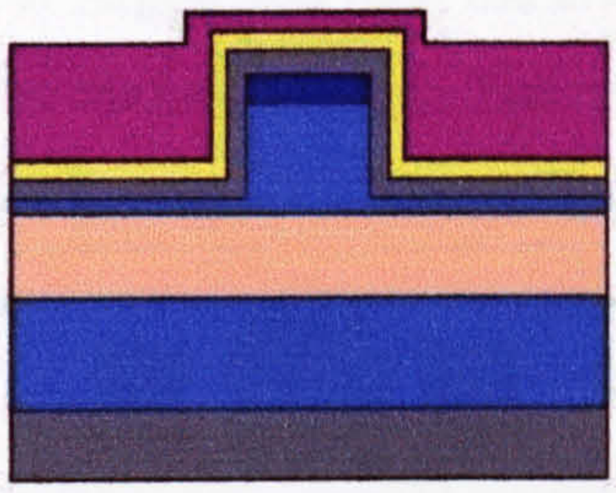

Fig. 4.16. Spinning resist.

Softbake. ~ 90 ℃ for 30 min.

Exposure. The exposure has to be done with the negative mask of the one used for lift-off. 11 sec.

Development. 1:1 mixture, 75 sec.

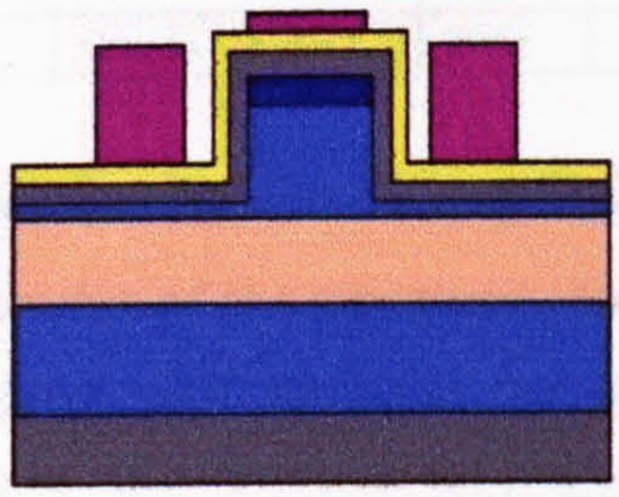

Fig. 4.17. Developing. At this stage the windows for metal etch are open.

Metal Etching. Although this technique is very old and is a completely mature technology, the etch rates for different metals had to be calculated for our specific machine. Ion-milling depends upon momentum transfer for the removal of the material from the substrate. Any material can be milled by this technique, because of the essentially charge-neutral character of the beam. The etch rate depends in the bias of the plasma, the gas used to create the plasma, the distance from the sample to the atom gun and the incident angle. Metal etching was made in several steps as opposite to one continuous run due to the considerable amount of heat in the chamber. The heat is produce by the atom gun and there is no cooling system attached to the mount of the sample. Between steps, the chamber

is cooled with a 10 min run of Argon and then the chamber is left to recover the vacuum. This normally takes about 20 min. The structures to be etched are shown in table 4.2.

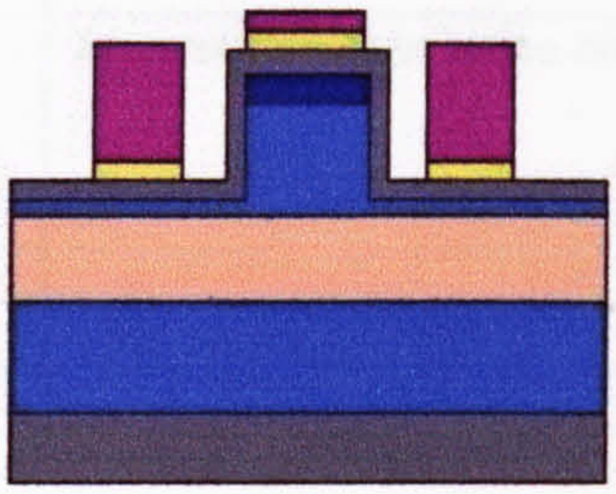

Fig. 4.18. Metal etching.

Table 4.2. p- and n-contact layer structure.

	p-contact		n-contact	
Layer No.	Metal	Thickness (nm)	Metal	Thickness (nm)
1	Ti	13	Au	~10
2	Pd	30	Ge	~10
3	Au	250	Pd	30
4			Au	150

To test the samples and conclude that the etching was successful, the resistance was measured between electrodes of the structure. An ohmic, or schotky contact indicates that there is an electric path between the electrodes and therefore the etch has not been completed. A signal comparable with the noise level indicates that the etching has been completed and the electrodes are isolated. Two optimum runs for p-contact etching are shown in table 4.3 and 4.4 while the optimum run for n-contact etching is shown in table 4.5. Before any run was started, the chamber was pumped down to $1x10^{-6}$ mbar of pressure.

Table 4.3. p-contact dry etching recipe one.

Contact type: p				ORE3-08
Step	Xe (min)	$Xe+SF_6$ (min)	Voltage (kV)	Comments
1	8		2.0	The gas flow was continuously adjusted to reach 2.0 kV. The first 60 sec in every step were used to set this value. For the mixture, the indicator on the Xe valve was set at 127 whilst the SF_6 valve was set at 106 The pressure for the etching using the mixture was $5x10^{-4}$ mbar, and for Xe alone 6-8 $x10^{-4}$ mbar.
2	8			
3	8			
4	8			
5	8			
6	8			
7	8			
8		8		
9		8		
Total	56	16		

Table 4.4. p-contact dry etching recipe two.

Contact type: p				ORE3-11
Step	Xe (min)	$Xe+SF_6$ (min)	Voltage (kV)	Comments
1	10		2.0	Same setting as in recipe one but different step time.
2	10			
3	10			
4	10			
5	10			
6	10			
7		11	1.7	
Total	60	11		

Table 4.5. n-contact dry etching recipe.

Contact type: n				ORE3-test3
Step	Xe (min)	$Xe+SF_6$ (min)	Voltage (kV)	Comments
1	10		2.0	For the mixture, the indicator on the Xe valve was set at 127-128 whilst the SF_6 valve was set at 108. For Xe alone was 129-130. The pressure for the etching using the mixture was $5x10^{-4}$ mbar, and for Xe alone 6-8 $x10^{-4}$ mbar.
2	10			
3	10			
4	10			
5	10			
6		10	1.8	
7	5		2.0	
Total	55	10		

Strip resist. After the metal etching is completed, the resist has to be striped from the sample. This is commonly done by leaving the sample in acetone for 1 hour in a hot bath at a temperature of 55 °C. Sometimes it was necessary to put the sample in ultrasonic bath for 2 to 3 sec to remove the resist completely. After this step, the sample looks the same as Fig. 4.14.

Metal etching showed to be a much better solution over lift-off as the method of contact pattern definition. The main disadvantage of using metal etching is the time it takes to complete one run, However, the alignment proved to be not repeatable for ORE devices, which are longer than 3 mm long. Therefore, a completely different method of pattern transfer had to be explored.

4.3.2 Photolithography photos.

In this section, we show photos of the devices obtained using photolithography. The combination of photolithography and lift-off only worked in very short devices (< 1mm) and never in a repeatable manner. The common problems found using lift-off are illustrated in Fig. 4.19 and Fig. 4.20. These problems can be summarised as: 1) Gold not lifting-off in small gaps, 2) rough edges and 3) breaks. The only advantage of lift-off is simplicity.

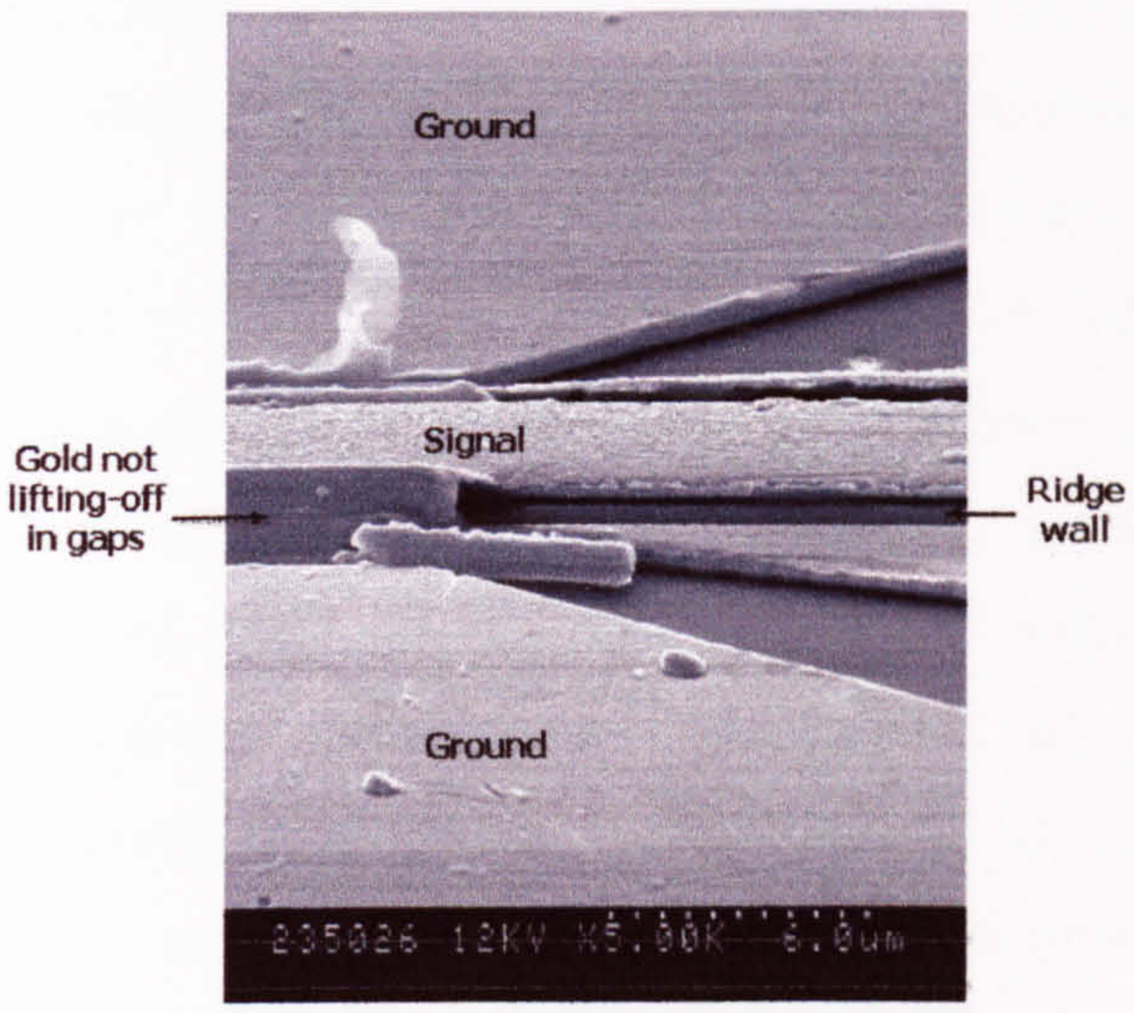

Fig. 4.19. No lift-off in small gaps.

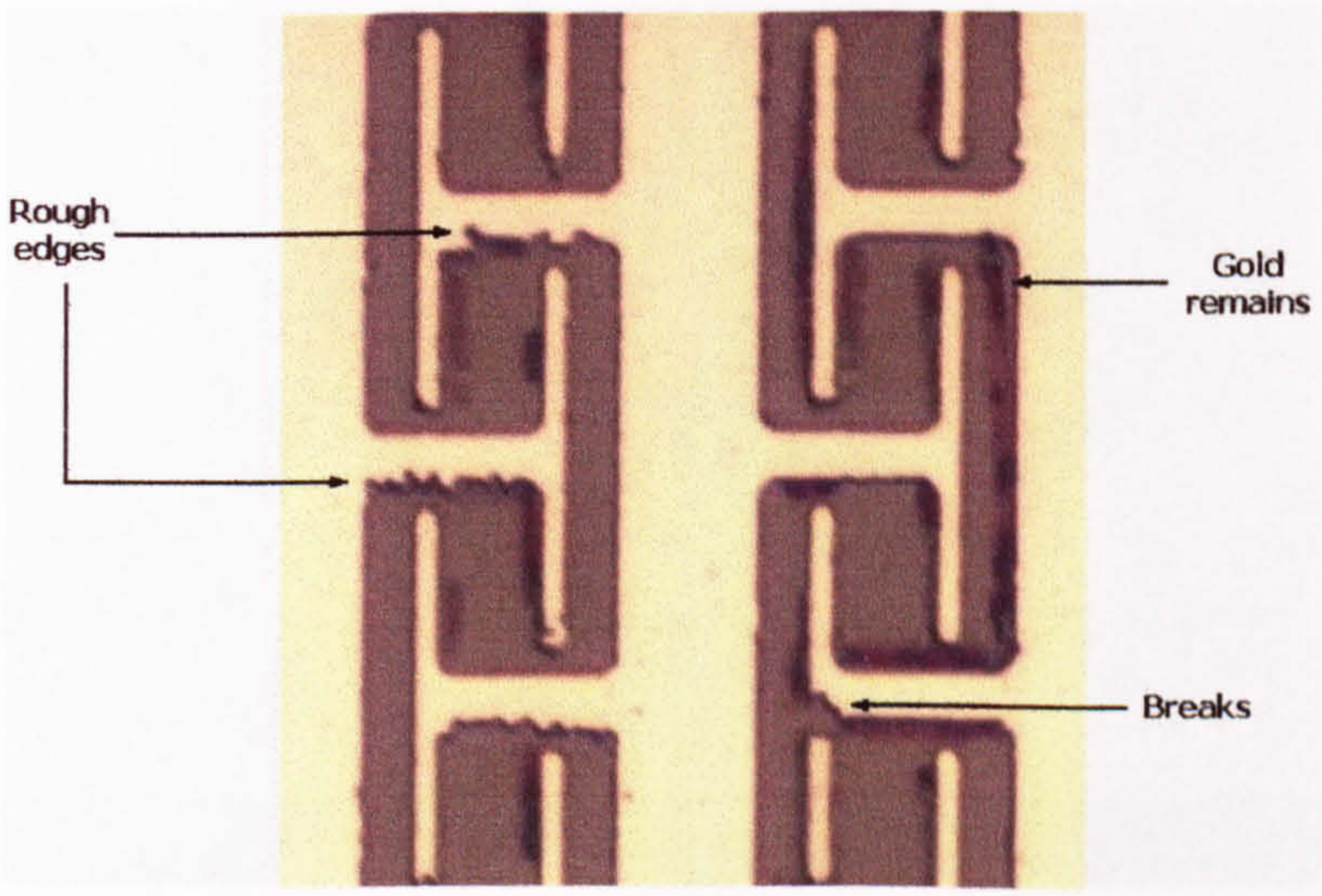

Fig. 4.20. Common problems found using photolithography and lift-off.

The combination of photolithography and metal etching did work well in all the structures fabricated this way. By far our biggest problem was to align the ground electrode on top of the ridge in a repeatable way. This is only limited by the equipment available. The longest device fabricated was a 3 mm long ORE3 device. The main advantages of using metal etch are illustrated in Fig 4.21 and Fig 4.22 and can be summarised as: 1) well defined edges, 2) clean ridge walls and 3) well defined gaps. Again, even when good devices were obtained using this method of pattern transfer, alignment repeatability was a major issue.

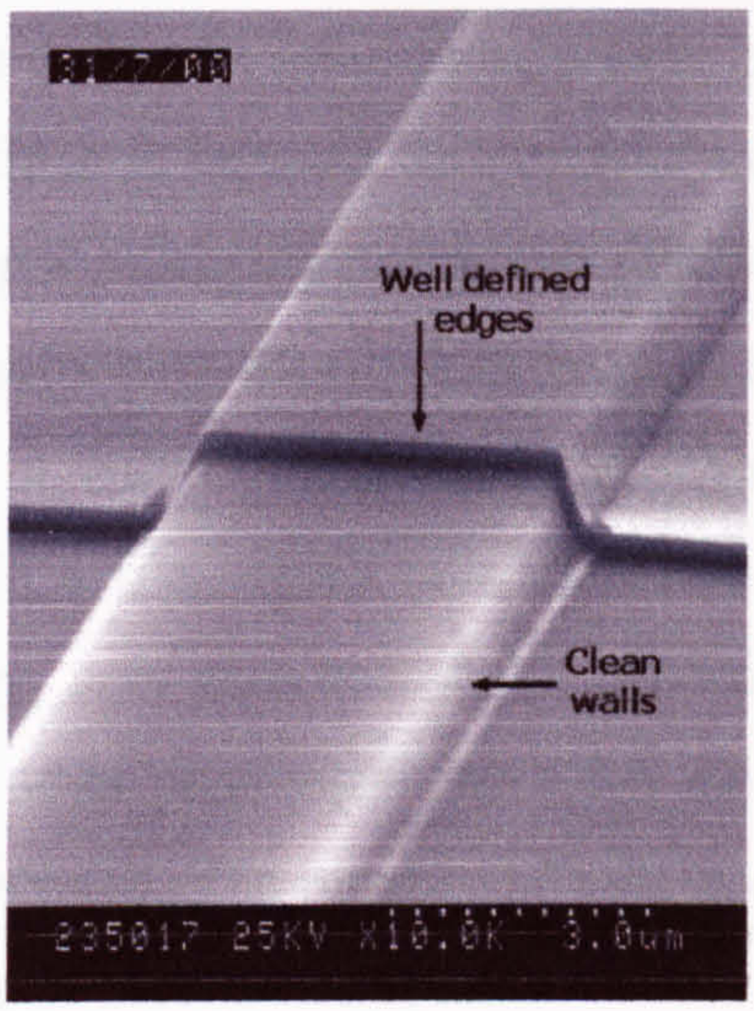

Fig. 4.21. Metal etching results.

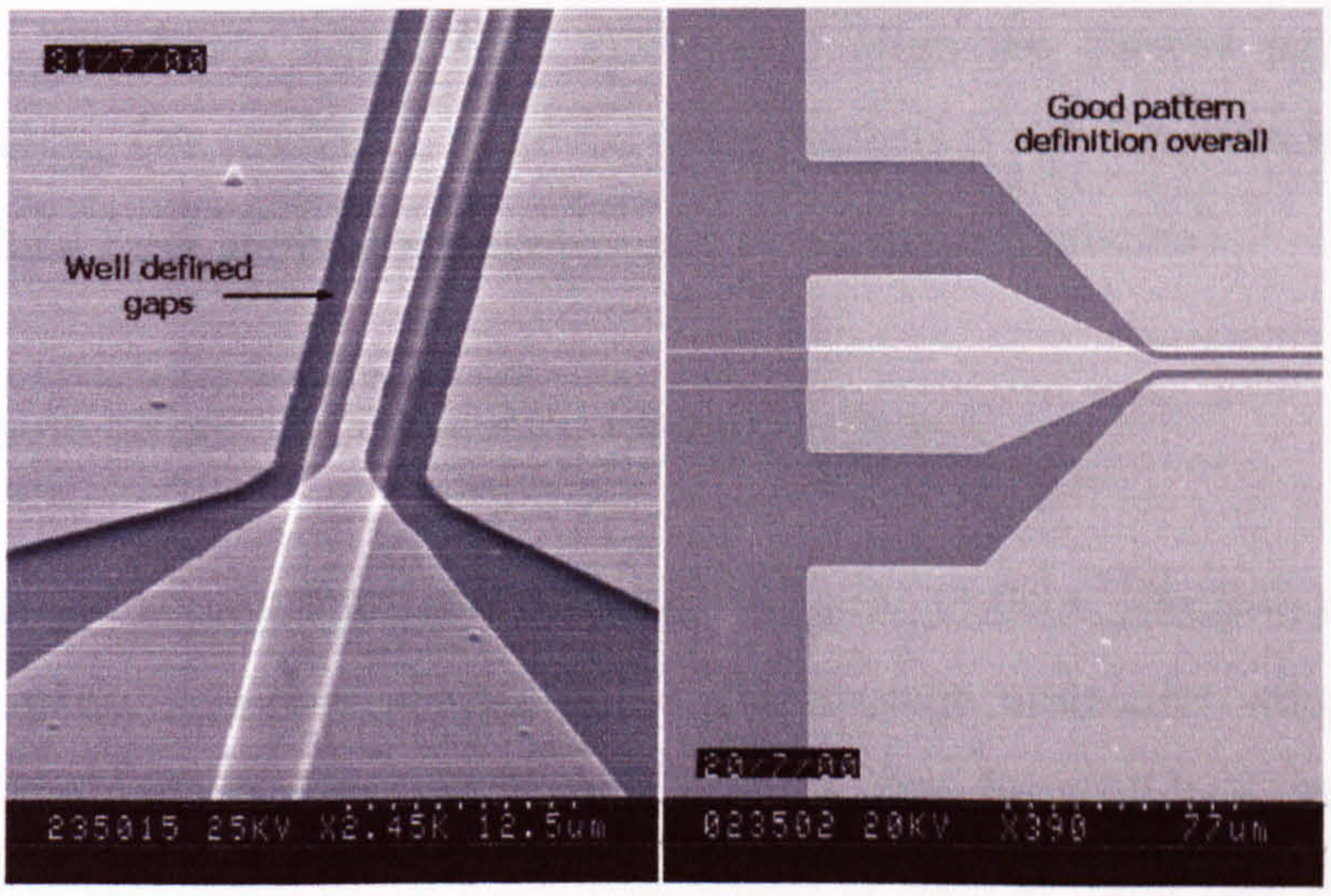

Fig. 4.22 Metal etching gap and pattern definition.

The fact that the final ORE devices are 1 cm long makes photolithography process difficult and unreliable for this type of device. E-Beam lithography was then explored to potentially solve lift-off and alignment repeatability problems. This method is described in next section.

4.3.3 E-Beam lithography and lift-off.

The idea of writing a pattern directly on the chip by e-beam lithography has always been attractive because the level of resolution that can be obtained. E-Beam lithography works under the same principles as photolithography; the use of a sensitive polymer which is exposed with certain dose and energy. The resist utilised for E-beam is polymethylmethacrylate, (PMMA) which is a positive resist. To have better results with lift-off, a bi-layer of resist is used. Every time the beam-writer writes a pattern, it does it through a job definition. This definition is contained in a file, which tells the beam-writer the pattern to be written, the dose, energy, spot size and if the pattern has to be aligned to a previous pattern among other parameters. An ORE device can be fabricated in three jobs but four is preferred. The number of jobs is equivalent to the number of photolithography steps as described above.

In the same way as in section 4.3.1, the fabrication process will be explained gradually. The beam writer uses markers to align the current pattern with previous ones. The resolution achieved using markers is sub-μm, which is a large improvement from photolithography (2 μm in our current process).

Cleaning. As before. Opticlear, Acetone and Methanol.

Spin resist (1st layer). The resist used here is called PMMA. Electron irradiation results in chain scissions, with a fall in the average molecular weight of the polymer. PMMA has a low sensitivity ($3x10^{-5}$ C/cm^2 for a 20-keV beam). This first layer is composed of 15% Elviside which is spun at 5000 rpm for 60 sec. The layer is 1.3 μm thick and is very thick in comparison with the second layer.

Bake. The resist is then bake to remove all the solvents at a temperature of 180 ºC for a period of one hour.

Spin resist (2nd layer). The second layer of resist is now spun. This is a 4% Elviside spun at 5000 rpm for 60 sec. The approximate thickness of this layer is 100 nm.

Bake. The resist is then bake to remove all the solvents at a temperature of 180 ºC for a period of two hours.

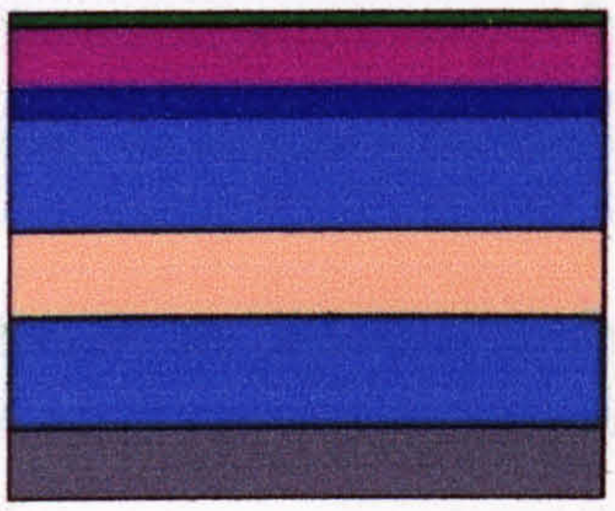

Fig. 4.23. Spinning of a bi-layer resist.

Pattern writing (markers). The sample is loaded into the machine for the first pattern writing. Because alignment of the electrodes and the optical ridge is required, there must be alignment marks to help to locate the features on the sample. There must be a minimum of three markers on the sample to compensate for rotation θ. A set of six square markers of dimensions of 10 μm are written in each corner if the sample. The dose used for this job is 350 C/cm^2 while the spot size is 300 μm diameter.

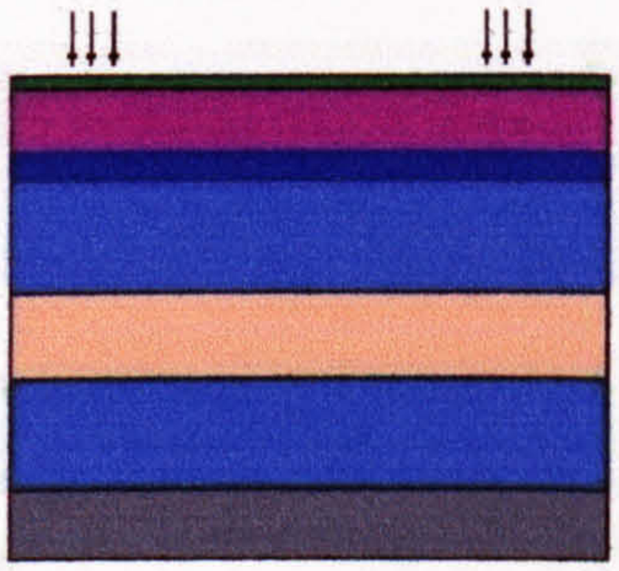

Fig. 4.24. Pattern writing. The markers are located at the four corners of the sample.

Developing. The sample is developed in a 1:1, developer : RO water mixture for 60 sec. The temperature of the developer is maintained at 23 °C during the developing. The bi-layer, react different to the developer and therefore a profile to enhance lift-off is created.

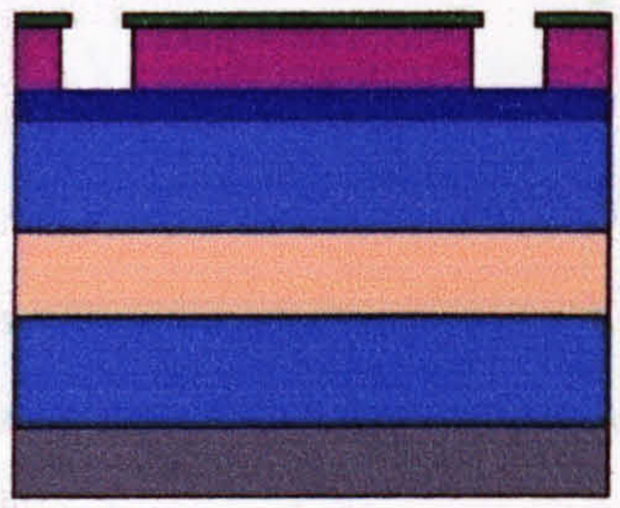

Fig. 4.25. Developing. An undercut in the resist profile is created.

Markers deposition. The markers are deposited to act as alignment marks to the beam writer. Positive markers have to be composed from a metal more reflective than the substrate itself. If this condition is not met, the beam writer will not see them and therefore, will not be able to do the alignment (i.e. Al markers on AlGaAs/GaAs layers are invisible to the machine). In this case, the markers are form by 50 nm of Ti (to improve adhesion) and 100 nm of Au.

Strip resist. The resist is removed using Acetone.

Spin resist (1st layer). 15% ELV, 5000 rpm, 60 sec.

Bake. 180 °C for 1 hr.

Spin resist (2nd layer). 4% ELV, 5000 rpm, 60 sec.

Bake. 180 °C for 2 hrs.

Pattern writing (waveguides). The waveguide pattern is written within the boundaries of the markers.

Developing. 1:1 mixture, 60 sec, 23 °C.

Dry etching. As before. RIE 80, $SiCl_4$ process.

Strip resist. The resist is removed using Acetone.

Spin resist (1st layer). 15% ELV, 5000 rpm, 60 sec.

Bake. 180 °C for 1 hr.

Spin resist (2nd layer). 4% ELV, 5000 rpm, 60 sec.

Bake. 180 °C for 2 hrs.

Pattern writing (signal electrode). Because we are going to use lift-off to pattern the electrodes, they were made in two steps. This decision came from the difficulties found using lift-off with the photolithography process. First, the signal electrode on top of the ridge is written on its own.

Developing. 1:1 mixture, 60 sec, 23 °C.

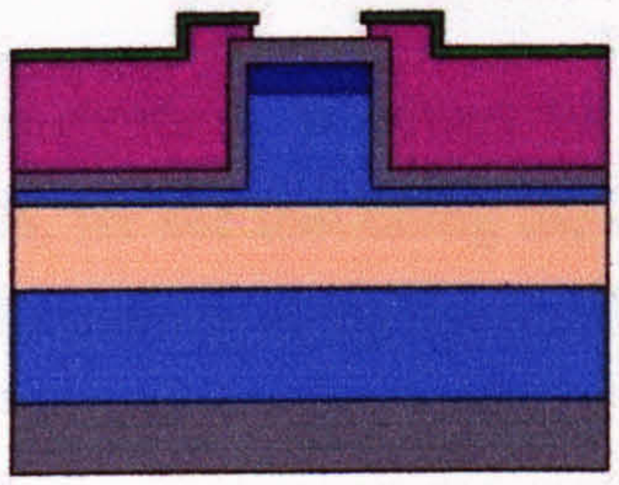

Fig. 4.26. Window opening for the central electrode.

Signal electrode deposition. The signal electrode is deposited. For all the devices made using the beam writer, the p-contact structure was change. This time, 50 nm of NiCr were deposited followed of 400 nm of Au. The thickness of the Au was increased in order to reduce the electrical losses of the device. The reason why only the signal electrode was deposited at this point is to get rid of

lift-off of small gaps next to the ridge walls. This was a major problem during photolithography.

Lift-off. As before. Acetone for 1 hour in a hot bath at a temperature of 55 °C.

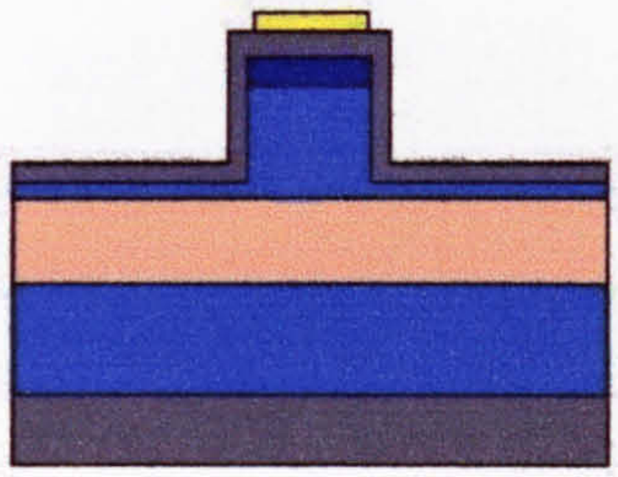

Fig. 4.27. Signal electrode deposition.

Spin resist (1st layer). 15% ELV, 5000 rpm, 60 sec.

Bake. 180 °C for 1 hr.

Spin resist (2nd layer). 4% ELV, 5000 rpm, 60 sec.

Bake. 180 °C for 2 hrs.

Pattern writing (ground electrodes). Windows for the ground electrodes are now open. If we see Fig. 4.28, we see that doing the deposition in two steps, we get rid of the thin resist stripes running along the wall of the ridge.

Developing. 1:1 mixture, 60 sec, 23 °C.

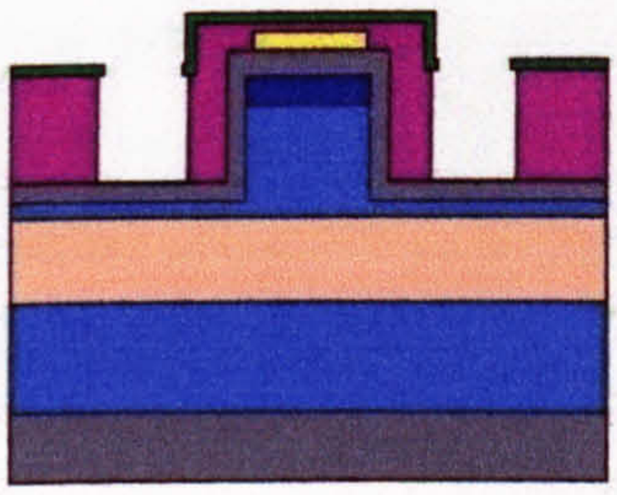

Fig. 4.28. Window opening for ground electrodes.

Ground electrode deposition. As before. NiCr/Au, 50/400 nm.

Lift-off. As before. Acetone for 1 hour in a hot bath at a temperature of 55 ºC.

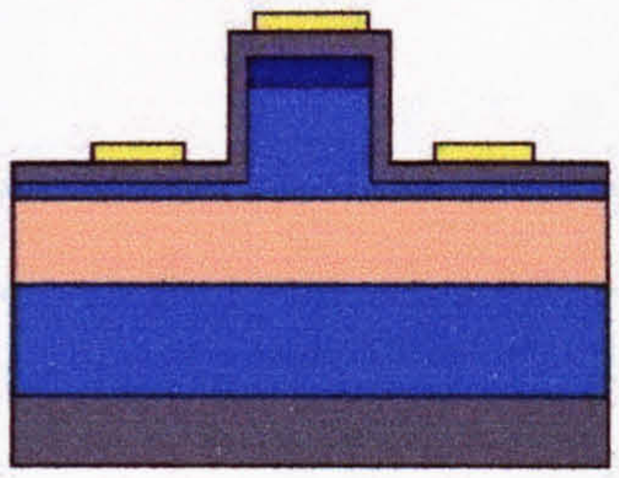

Fig. 4.29. ORE device completed.

After this last step, the ORE device is completed and the structure obtain is the same one as the one shown in Fig. 4.14. ORE3 and ORE4 devices of up to 1 cm in length were fabricated using this method giving excellent results. The only disadvantage of this method is the increased complexity of the process (compared with photolithography) and the cost associated with running an E-beam writer.

4.3.4. E-Beam lithography photos.

In this section, we show photos of the devices obtained using E-Beam lithography and lift-off. ORE3 and ORE4 devices were successfully fabricated. ORE3 devices are shown in Fig. 4.30 and 4.31. Fig. 4.30 shows a whole ORE3 device. The electrodes are 660 μm long including the pads. Most of the ORE devices fabricated are 1 cm long and therefore the majority of the photos only show sections of the devices. By looking at Fig. 4.31, we can observe the accuracy of the alignment between the central conductor and the optical ridge. This kind of precision cannot be achieved using photolithography. The pattern definition is also good at this magnification.

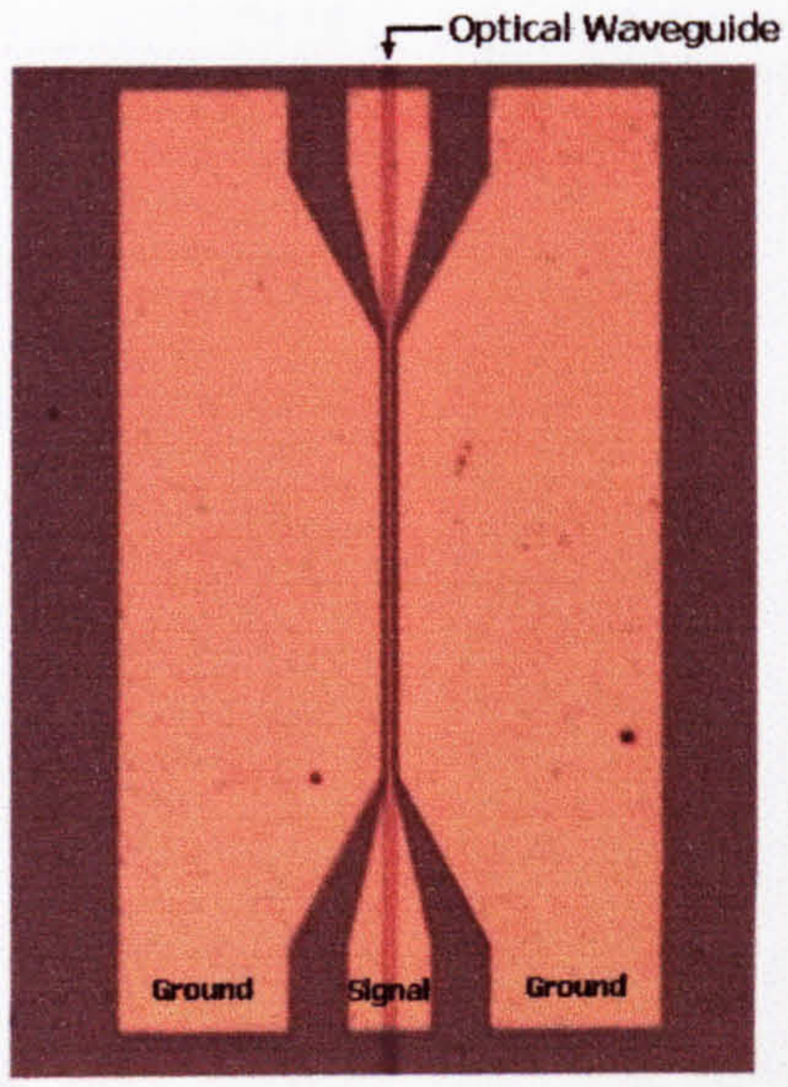

Fig. 4.30. ORE3 device fabricated using e-beam lithography.

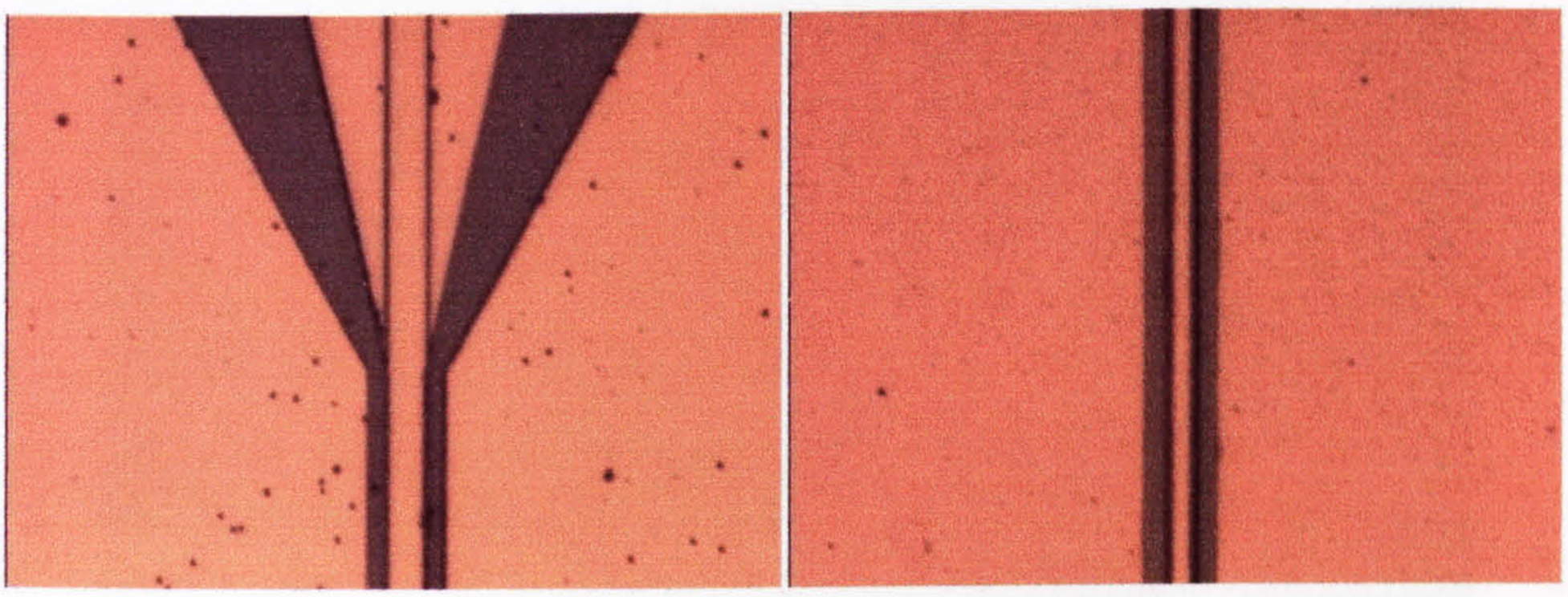

Fig. 4.31. The central electrode is perfectly aligned to the top of the optical ridge.

ORE4 devices were also fabricated and some photos are shown below. Fig. 4.32a shows an ORE4 device with *fin* slow-wave electrodes while Fig. 4.32b shows an ORE4 device with *finpad* slow-wave electrodes. Fig. 4.33 shows a high magnification photo of the central conductor respect to the optical waveguide. The accuracy of the alignment is proven with these photos. The two mayor advantages of e-beam lithography can be named as 1) high accuracy and 2) high repeatability.

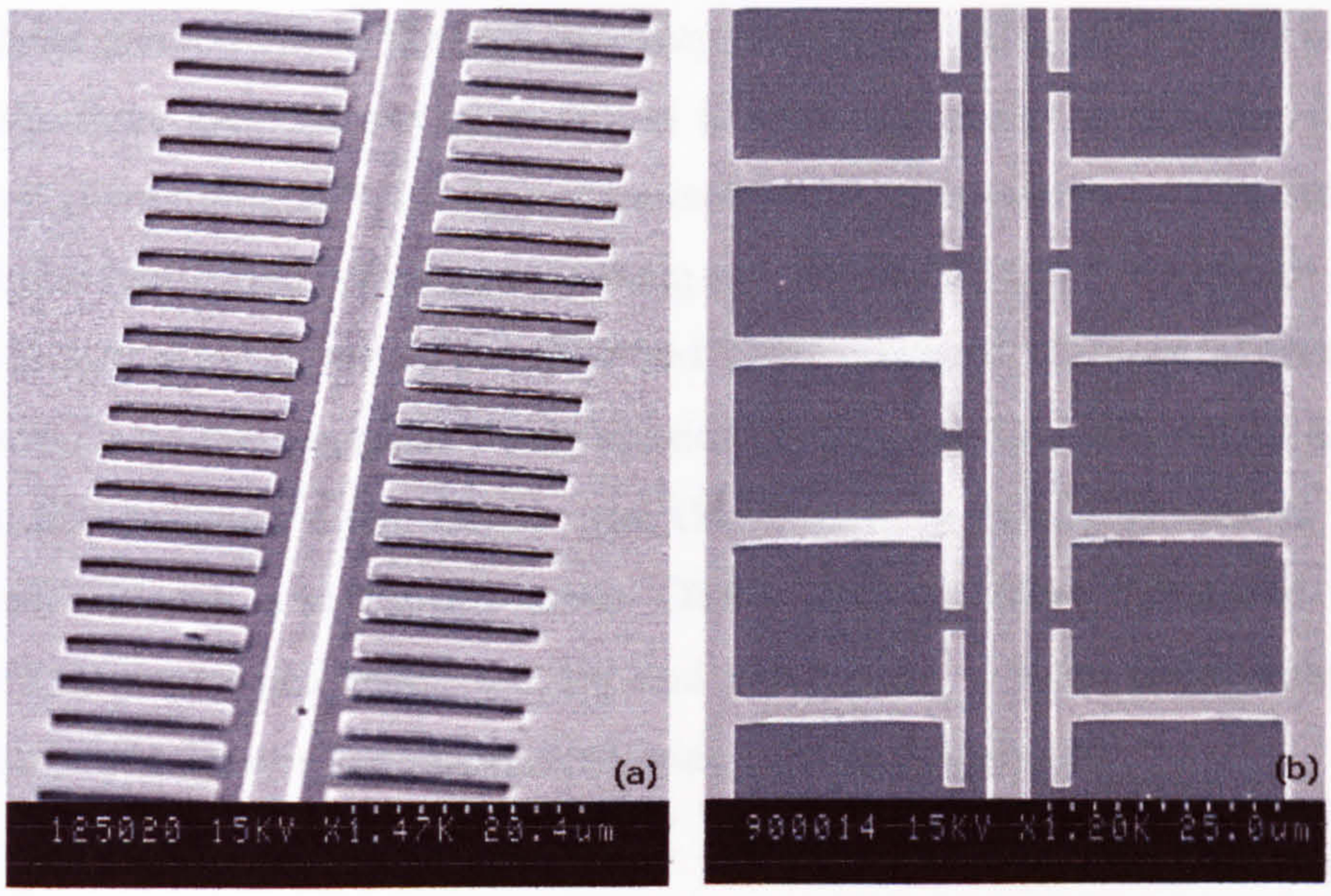

Fig. 4.32. ORE structures.

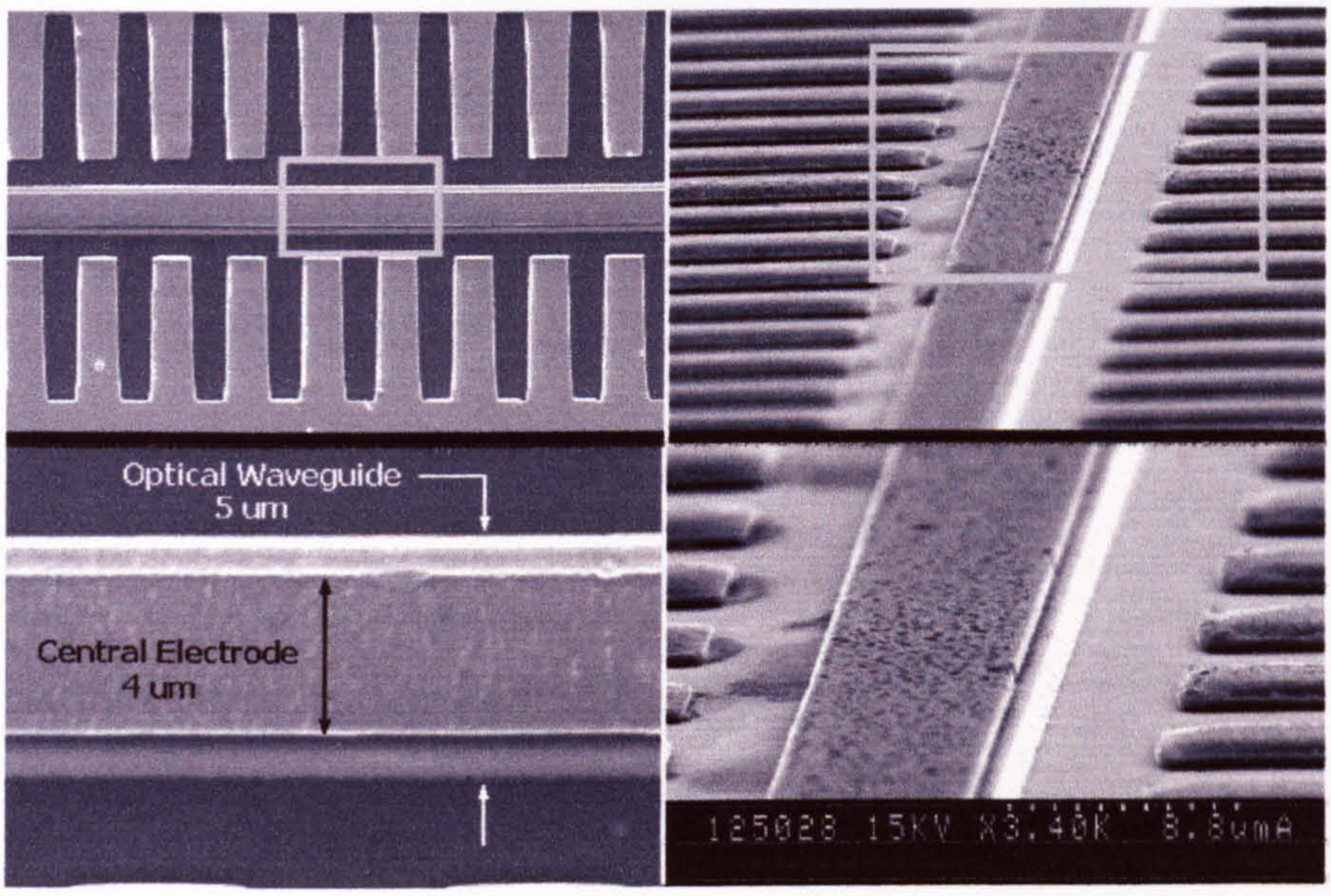

Fig. 4.33. SEM photo showing the alignment of the central electrode on top of the optical ridge in a ORE4 device.

4.4 Conclusions.

Three different methods to fabricate ORE devices have been presented and discussed in this chapter; photolithography and lift-off, photolithography and metal etching and e-beam lithography and lift-off. E-Beam lithography was the

preferred method due to the high accuracy that can be achieved. We still believe that the three methods can be improved if better equipment is available (in the case of photolithography) and an optimised set of experiments is designed. The two main fabrication issues when making an ORE device are: 1) alignment of the central conductor on top of the ridge and 2) achievement of the exact electrode dimensions so the electrical characteristics of the CPW line will not be altered from the designed ones. ORE1 and ORE2 devices where fabricated using photolithography and lift-off, some ORE3 devices where fabricated using photolithography and metal etching and some using e-beam lithography and finally ORE4 devices were fabricated using e-beam lithography.

4.5 References.

1. S. M. Sze, Ed, *VLSI Technology*. 2nd ed., McGraw Hill,1988.

2. R. E. Williams, *Modern GaAs Processing Methods*. Artech House, 1990.

3. S. K. Ghandhi and L. Lane, *VLSI Fabrication Principles*. 2nd ed., John Wiley & Sons Inc. 1994.

4. M. Hatzakis, B. J. Canavello and J. M. Shaw, "Single-Step Optical Lift-Off Process," *IBM J. Res. Develop.*, vol. 24, pp. 452-460, Jul. 1980

5. ORE devices: Experiments.

5.1 Introduction.

The complete design, fabrication and testing of an ORE device at communication wavelengths (1550 nm) has proven to be very challenging. Testing of an ORE device involves a combination of optical and, as we saw on chapter 3, electrical measurements. There will always be different methods of doing a specific measurement, each with their own advantages and disadvantages and optical rectification is not the exception. Finding the optimum test set-up for an ORE device involves a deep understanding of the material used to fabricate the device, the fabrication process itself and the characteristics of the signal produced by optical rectification. The set-up presented in this chapter might well not be, as will by explained at the end of the chapter, the optimum one but it is definitely the best one based in our current research and fabrication resources. The optimum set-up is also discussed through the chapter. There has been, historically, well-known ways of identifying an ORE signal, the most popular being the polarization dependence. The ORE signal is maximum for TE polarization and minimum for TM. This decrement of the signal follows a sin^2 behaviour.

The aim of this chapter is to show the different experimental approaches taken when developing and testing an ORE device, and how these approaches helped to build the optimum rectification device. The ORE devices are grouped in four categories (generations) depending on the device design and/or the wafer composition used. There are four generations of ORE devices and each generation with its respective characterisation is explained here. There is a, so call, optimum experiment that should be done with the ORE devices but alternative options are also reviewed and empirically studied. The fact that the ORE is competing with linear absorption and multi-photon absorption (MPA) makes the device and, in general, the whole experiment a challenge. The ORE device can be designed to work at longer wavelengths [1] but if this device is ever going to find a practical application in modern communication systems, it must work at communication wavelengths where all the effects produced by free carriers are present. It is true that if we fabricate an ORE device on a different electro-optic material such as $LiNbO_3$ or $LiTaO_3$ [2] we can get rid of the signal produced by free carriers, but it would not be possible to integrate such device with current III-V technology. In order to make clear the difference between generations of ORE devices from the beginning of the chapter, a comparison between them is shown in table 5.1. Some fields may not be completely clear at present but they will be as the chapter progresses.

Table 5.1. Comparative table between different generations of ORE devices.

Generation	Wafer composition	Electrode configuration	Velocity-matched
ORE1	B781	one p-contact & one n-contact	No
ORE2	B828	CPW wide central electrode	No
ORE3	A1445	CPW	No
ORE4	A1500	Slow-wave CPW	Yes

A range of wavelengths was used to test all the different generations of ORE devices in this chapter. It was mentioned in chapter 2 that an ORE device is, in principle, an electro-optic modulator working in reverse. The ORE4 devices were first tested as modulators and even when their response was not optimum (V_π was too high), the measurements helped to understand and estimate the nonlinearity of the crystal. The ORE4 devices were also tested as a mode converter with equal success.

It is convenient to mention at this point that every single time we refer to an ORE device, we are referring to the particular devices presented on this thesis and therefore, the concepts must not be generalized to another devices unless indicated on the text.

5.2 ORE signal and accompanying effects.

Optical rectification is present in ORE devices independent of the wavelength of the laser beam. However, for certain wavelengths, it can be accompanied by other effects, some of which are of considerable magnitude. Special care has to be taken when working with semiconductor materials where the light is likely to be absorbed at the wavelength of interest. When only the rectification signal is present on the device, it can be easily identifiable. However, when this signal is accompanied by other effects, the identification of the signal becomes more complicated since these "parasitic" effects can mask the ORE signal. In this section we will discuss how to identify an ORE signal in an ORE device (semiconductor) and which are the other effects competing with it.

5.2.1 Identification of the ORE signal.

The basic conditions that will allow us to identify a signal produced by the ORE can be extracted from the early experiments on optical rectification [3]. These conditions (slightly modified to suit our devices) must be well known before trying to understand any signal generated in an ORE device. Therefore, it is necessary to establish that:

- The signal has the same (or almost the same) time dependence as the laser pulse.
- For a device such as the one shown in Fig. 2.3 in chapter 2, the polarity, but not the magnitude of the signal, changes when the crystal is rotated about the direction of propagation of the laser beam by 180° with respect to the capacitor plates

- The signal has a well-defined dependence on the polarisation of the laser pulse. It is maximum for TE and minimum for TM decreasing in a sin^2 manner.
- The temporal resolution of an ORE signal must be shorter than the temporal resolution of a signal produced by free carriers when the same optical excitation is used. This is true when the optical pulse is shorter than the recombination time of the free carriers on the material (normally ≤ 300 ps for an intrinsic material).

The first three points are true for any rectification device whereas the last one is specific for our devices. If the points described above are fulfil when doing an ORE experiment, it can be concluded that the effect producing the electrical signal is optical rectification. Yet, not everything is so simple!

5.2.2 Accompanying effects.

A signal generated in an ORE device would be, ideally, generated 100% by the optical rectification effect. For this ideal case, all the points described above can be easily used to identify the signal. However, when launching light into an ORE device, a number of parasitic effects such as piezoelectricity, pyroelectricity, and absorption can occur [4]. In addition, if proper care is not taken during the design of the position of the metal electrodes, the laser beam may hit them causing an extra parasitic effect. The generated signal will then be a combination of different effects, and even when optical rectification is one of the components of such combination, the generated signal may not follow the points described in section 5.2.1. Here lies the difficulty and importance of minimizing any parasitic effect. Non-centrosymetric crystals are also piezoelectric crystals and, in the past, this effect had always been associated with optical rectification experiments. Piezoelectricity is a polarization generated by the stress induced by the optical wave on a non-centrosymetric material. As mentioned in [3], the piezoelectric voltage depends strongly on the absorption coefficient of the crystal at the operation wavelength and on its orientation. The piezoelectric voltage is high when the absorption coefficient is also high. However, the ORE devices are

fabricated to minimize absorption and therefore any possible signal due to piezoelectricity is reduced. Moreover, it requires shear stresses to generate a piezoelectric response in GaAs grown in the <100> direction [5], as is the case in our devices. The effect is largest along <111> where d_{14}^{piezo} (the piezoelectric modulus in GaAs relating the strain to the associated electric field) is only –2.7 pm/V. The sign minus only represents the crystal expanding in the <111> axes. When compare d_{14}^{piezo} against the nonlinear coefficient d_{14} for the same material,we can easily see that the piezoelectric constant, and therefore the polarization produced by piezoelectricity is going to be much smaller that the nonlinear polarization. This and the fact that the light is incident along the <110> direction shows that the piezoelectric effect is practically eliminated from the ORE devices.

A polarization induced by heating up a crystal is known as pyroelectricity. For high optical intensities, an ORE device could in principle heat-up, but the use of ultrashort optical pulses (300 fs typically) eliminates this factor. Even in the case where the sample would heat-up, the pyroelectric polarization, like the piezoelectric polarization, would be "slow" compare with the ORE polarization and therefore, they can be discriminated by its temporal resolution. In all the experiments described in this chapter, we could not find any obvious sign of pyroelectricity.

Band-to-band absorption is the biggest of the effects that could accompany optical rectification in a semiconductor. By band-to-band absorption, we understand the excitation of an electron from the valence band E_v, to the conduction band E_c, see Fig. 5.1(a). The energy absorbed from the photon is, $h\nu \geq (E_c - E_v)$ and therefore the absorption depends on the wavelength of the photon. In fact, most of the signal produced by an ORE device when using wavelengths shorter than 800 nm will be due to band-to-band absorption as presented in section 5.4.1. Even when the ORE signal can be mathematically extracted when band-to-band absorption is present [6], it does not offer any practical application. The operating wavelength of the ORE devices, 1550 nm, is far beyond the cut-off wavelength for band-to-band absorption to be of any

significance, and therefore, this signal is automatically eliminated at the operation wavelength. MPA and, in particular, two-photon absorption (TPA) will then become the biggest parasitic effect that can be present. TPA refers to the simultaneous absorption of two photons by one free electron, which gains enough energy to jump the forbidden gap, see Fig. 5.1(b). The total energy absorbed from the two photons is conserved and distributed between the gap's jump and the conduction band. TPA is a nonlinear effect and therefore, is present (within a certain λ range) in any nonlinear material such as GaAs. The geometry of the ORE device plays an important role in determining the amount of the signal that can be detected as is explained in section 5.4.3. Band-to-band absorption and TPA are analysed in more detail throughout the chapter.

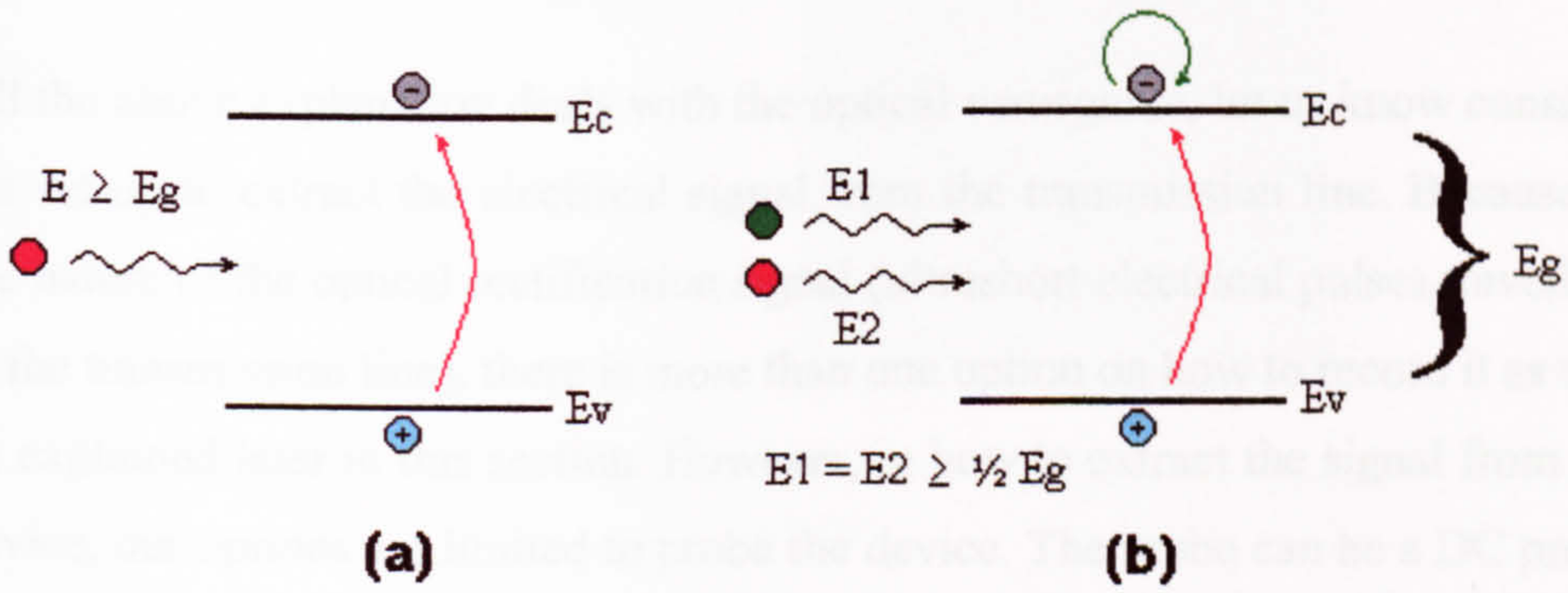

Fig. 5.1. Band-to-band absorption (a) and TPA (b). In both cases, an electron has jumped from the valence band to the conduction band assisted by the incident photons.

5.3 Measurement set-up.

As we have described in chapter 2 and chapter 3, the ORE device consists of two different integrated devices, one optical and one electrical. The first thing to consider is the coupling of light into the optical waveguide. Free space (end-fire) coupling offers flexibility in terms of maximum input power handling and the restriction in the number of optics that can be positioned in the beam path to manipulate the beam is unlimited. It also allows the implementation of a lock-in detection with the aid of an optical chopper, which can be used to detect small electrical signals. The experimental test set-up is sketched in Fig. 5.3. The optical source is a solid-state laser and varies according to the experiment covering

discrete points in wavelength from 800 nm to 2100 nm. The specific laser will be described in the coming sections. The electrical field of the optical beam delivered by the laser oscillates parallel to the optical bench and therefore we can say that is compatible with the TE-like mode of the optical waveguide. A half-wave plate is used to rotate the polarization of the light from TE to TM allowing a scan in polarization. A rotation of 45° on the half waveplate will produce 90° rotation on the linearly polarized light. To verify the polarization rotation, a polarizer is used. The polarizer is optional and can be omitted if the polarization of the light is known perfectly and the waveplate is calibrated. The light is coupled in and out the optical waveguide using x40 microscope objectives. To help with the alignment, a CCD camera is placed at the output of the coupling rig. The microscope objectives are mounted in 3-axis mounting stages whilst the ORE device is mounted in a 4-axis stage (two linear and two angular).

All the above explanation deals with the optical waveguide, let us know consider the set-up to extract the electrical signal from the transmission line. Because of the nature of the optical rectification signal (ultrashort electrical pulses travelling in the transmission line), there is more than one option on how to record it as will be explained later in this section. However, in how to extract the signal from the device, our options are limited to probe the device. The probe can be a DC probe or a microwave probe (MW probe) with broad operation frequency depending on the experiment. To probe the device can be relatively simple but if it is done repetitively, it will cause damage to the electrodes (*see Fig. 5.2*). For high frequency probing, the probe has to become and extension of the transmission line and the accuracy of the measurement depends on how well the device is probed. The bandwidth of the detected signal will be limited by the probe, connectors and cables used. There are alternative methods to probing in order to characterize the electrical signal. They are photoconductivity and electro-optic sampling.

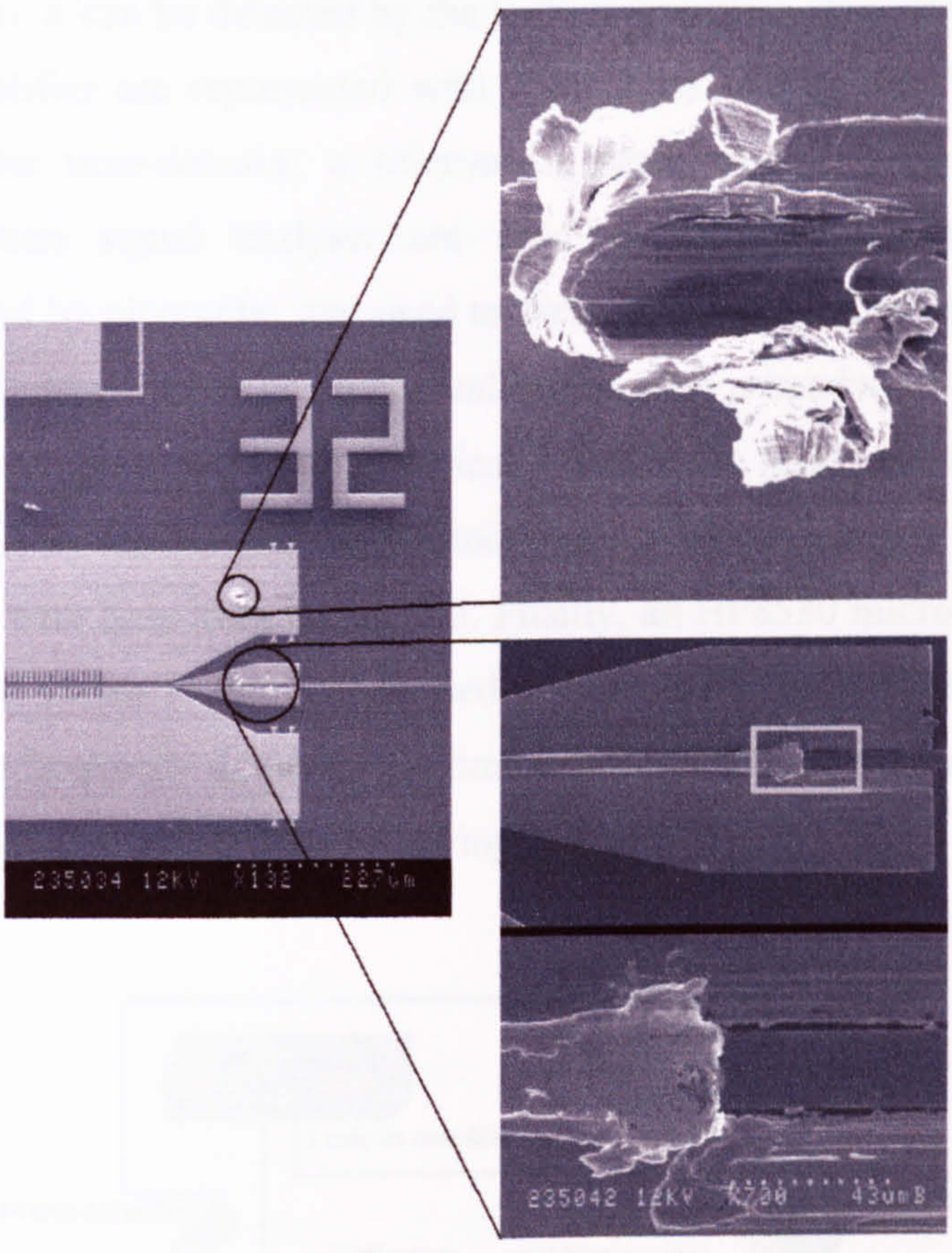

Fig. 5.2. The electrodes of an ORE device wear out after repetitive probing.

Photoconductivity is an elegant option to extract the signal from the ORE device, and can be achieved by integrating a photoconductive switch [7] on a CPW line. To integrate a photoconductive switch presents certain fundamental limitations related to the geometry of the device. A detailed explanation of these limitations and of the switch itself is given in chapter 7. Several other characterisation techniques are described in [8]. Electro-optic sampling is by far the most commonly used. In an ORE device, an electro-optic crystal can be placed in the backside of the sample and if the electrical field can penetrate into the crystal, an optical pulse can then probe the device and measure the reflected signal which will vary with the electrical field of the electrical signal. The most suitable method considering the research capabilities within the department is to direct probe the device to extract the optical rectification signal (Fig. 5.3). To do DC measurements, a DC probe is used in conjunction with an EG&G 5209 lock-in amplifier. The lock-in amplifier is phase-lock to a reference signal given by the

optical chopper. The generated electrical signal will be at this same frequency and therefore it can be detected by the lock-in amplifier. The connections to the lock-in amplifier are represented with black lines in Fig. 5.3. To observe the signal in the time-domain, a microwave probe and a Tektronics CSA830 communication signal analyser are used. A G-S-G 40 GHz MW probe manufactured by picoprobe was used to pick-up the signal from the device. The signal travels to the CSA using coaxial cables with a bandwidth up to 50 GHz. The CSA is triggered with and electrical signal at the same repetition frequency than the laser by means of a fast photodetector. The connections to the CSA are represented with blue lines in Fig. 5.3. Finally, an HP8530 microwave spectrum analyser (not shown in Fig. 5.3) is used together with the MW probe to observe the signal in frequency domain. The limitations of each measurement equipment are described with detail in the following sections.

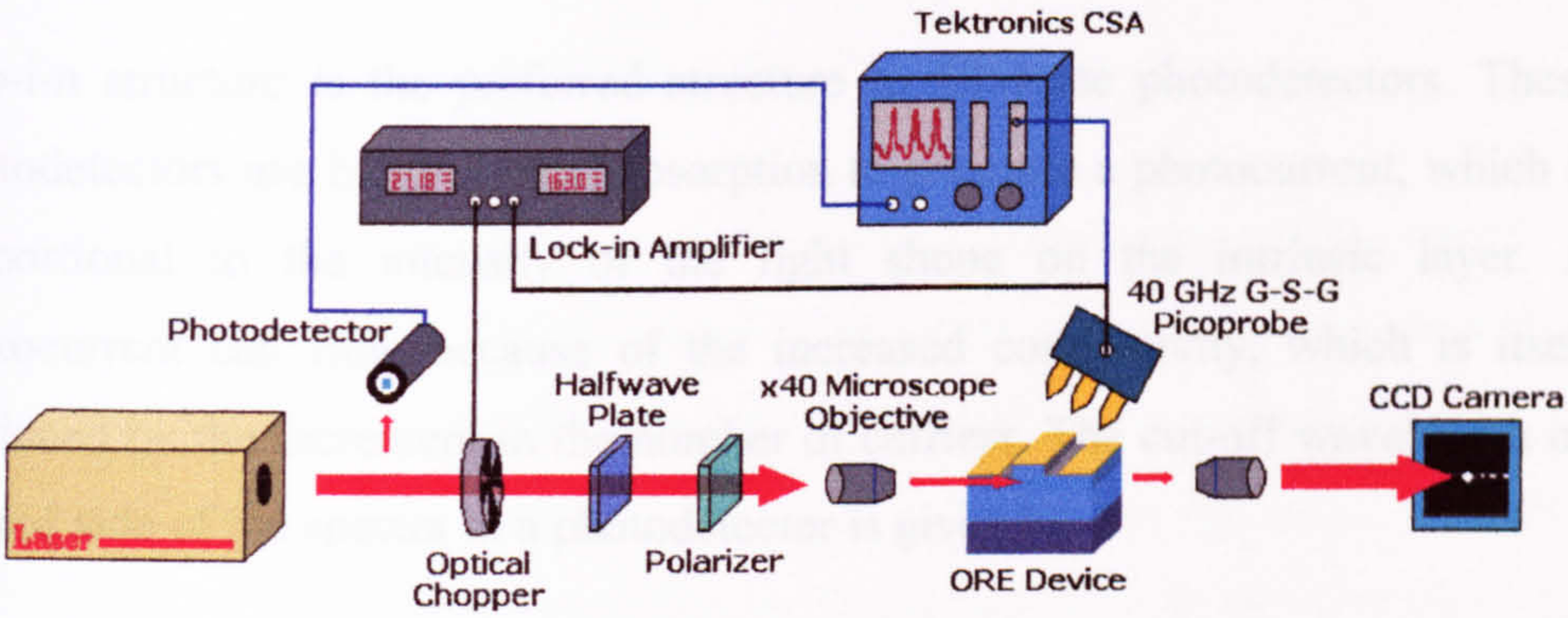

Fig. 5.3. Experimental set-up. The instrument used to record the signal is either a Lock-in Amplifier (black wires) or a fast sampling oscilloscope (blue wires).

5.4 Experimental results.

As was mentioned above, there are four generation of rectification devices. The experimental observation of the first device design, ORE1, was used as feedback for the design of an improved device ORE2. The same applies for devices ORE3 and ORE4. The results obtained by measuring the rectification devices are presented in "chronological" order, from the first fabricated device helping to understand and analyse the effect of free carriers (ORE1) to the final optimum device (ORE4), where an optical rectification signal was recorded. The reasons

why the first generations of devices are not optimum, or viable for rectification may be obvious after having studied previous chapters of these thesis, but keep in mind that the complete design in chapter two and three could not be reached without the understanding of early generation of devices. Early generations of ORE devices have potential for optical rectification but it is the extraction of the signal which presents the biggest challenge and therefore the device had to evolve to enhance the rectification signal and reduce all the other accompanying effects as described in section 5.2.2. The importance of these early generations is such that a comprehensive description of the experiments as well as the explanation of the particular signals detected on every ORE device is given below.

5.4.1 ORE1 devices.

A p-i-n structure is the preferred structure to fabricate photodetectors. These photodetectors use band-to-band absorption to generate a photocurrent, which is proportional to the intensity of the light shone on the intrinsic layer. A photocurrent can flow because of the increased conductivity, which is itself produced by the increment in the number of carriers. The cut-off wavelength on the red side of the spectra in a photodetector is given by:

$$\lambda_C = \frac{hc}{E_g} = \frac{1.24}{E_g(eV)} \quad (\mu m) \tag{5.1}$$

where h is the Planck constant, c is the speed of light in vacuum and λ_c is the wavelength corresponding to the semiconductor bandgap, E_g. When light of a given wavelength $\lambda > \lambda_c$ is illuminating the device, no band-to-band absorption takes place. This opens a window for detection of optical rectification and here rests the interest of the first structure. It was of great interest at this point to try a p-i-n ridge photodetector structure as the ORE1 due to the potential compatibility with a well-established technology. A difference between a p-i-n photodetector and an ORE device that can be pointed out, apart of the operation wavelength, is

that in the last we expect to measure a polarization in form of a voltage while in the former we measure the flow of carriers in the form of a photocurrent.

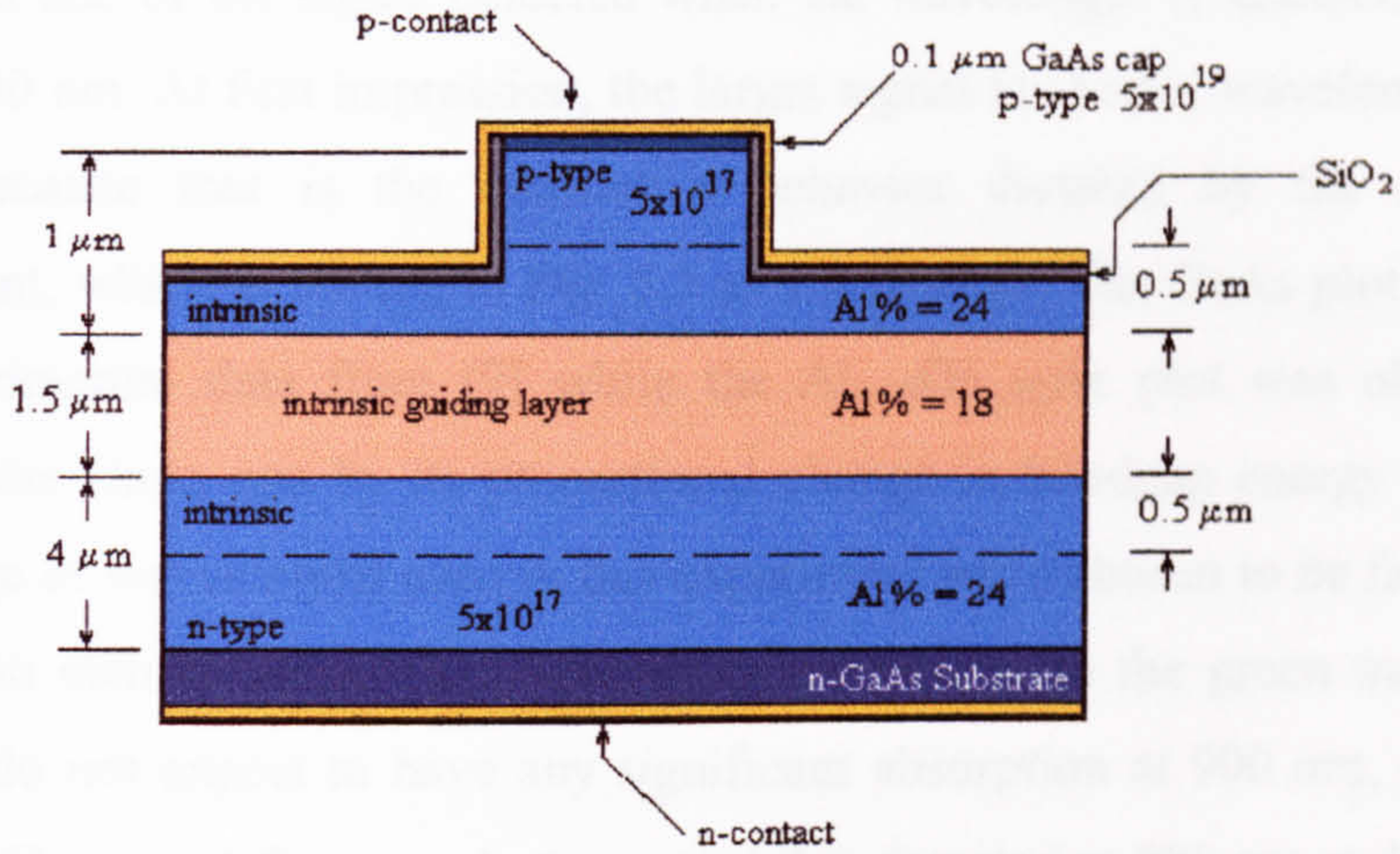

Fig. 5.4. Cross-section of an ORE1 device.

Fig. 5.4 shows a schematic view of the cross section of an ORE1 device. As mentioned above, ORE1 devices are p-i-n structures with epi-layers grown on an n-type doped Gallium Arsenide substrate. The upper cladding consists of a 1 μm layer of $Al_{0.24}Ga_{0.76}As$ of which, 0.5 μm is p-doped and the other 0.5 μm is intrinsic. The top cladding has a heavily doped cap layer to avoid oxidation of the cladding and to improve the p-contact. The guiding layer is intrinsic and consists of a 1.5 μm layer of $Al_{0.18}Ga_{0.82}As$. The lower cladding consists of a 4 μm layer of $Al_{0.24}Ga_{0.76}As$ of which, 3.5 μm is n-doped and the other 0.5 μm is intrinsic as shown in Fig. 5.4. The thickness of the layers follows the design presented in section 2.5.1. There is a 200 nm SiO_2 layer acting as a buffer between the semiconductor and the metallization. This buffer prevents leakage of the optical mode into the metal. The top metallization is a p-contact and on the back of the substrate, there is an n-contact. Both were described on detail in chapter 4. There is no pattern definition on the contacts therefore giving a single top and a single bottom contact.

A tuneable CW Ti:Sapphire laser, working in a wavelength ranging from 800 nm to 900 nm and a power range from 10 to 300 mW, was the optical source in the experiments. The sample was positioned in an end fire rig and the laser beam

was launched into it. An iris and a camera were used to align the system. The device was probed with two dc probes, one identified as *signal*, probing the p-contact and one identified as *ground*, probing the n-contact. The electrical signal was sent to an oscilloscope. The blue curve with black squares in Fig. 5.5 shows the amplitude of the signal detected when the wavelength is scanned from 800 nm to 900 nm. At first impression, the larger signal at shorter wavelength makes sense because that is the qualitative behavior dictated by the absorption coefficient, which is plotted in Fig. 5.5 as a reference. The GaAs plot was build by experimental data from [9] while the $Al_{0.18}Ga_{0.72}As$ plot was obtained by shifting the GaAs one by its proportional change in bandgap energy (120 nm). The range of wavelengths used in this experiment were chosen to be far from the absorption etch of the AlGaAs core layer. According to the green trace in Fig. 5.5, we do not expect to have any significant absorption at 900 nm, or even at 800 nm. This is not the case. A strong signal is detected at 800 nm and decreases for longer wavelengths.

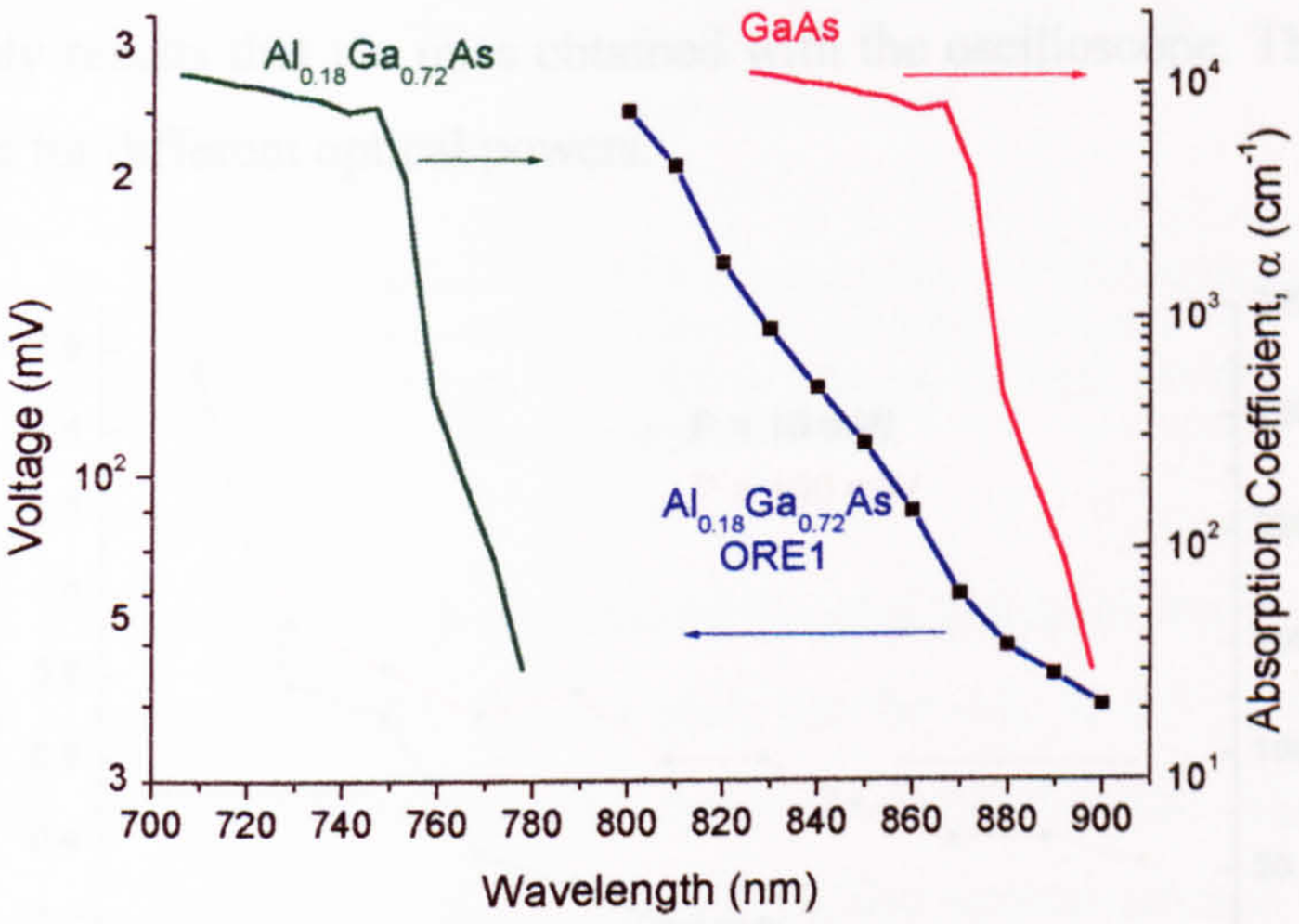

Fig. 5.5. Generated voltage *vs* wavelength for a TE linearly polarized light. Input power before the coupling objective = 85 mW (Blue). GaAs absorption coefficient vs wavelength from ref [9] (Red). $Al_{0.18}Ga_{0.72}As$ absorption coefficient (Green).

To determine exactly what absorption mechanism is generating the signal in Fig. 5.5, the following discussion is presented. The absorption coefficient is a strong function of the wavelength. It is formed by various different absorption

mechanisms depending on the characteristics of the semiconductor and is mainly affected by doping and temperature. When the energy of the photons $h\nu \geq Eg$, band-to-band absorption is the dominant mechanism. However, when $h\nu < Eg$, *linear* absorption mechanisms such as free carrier absorption and intraband absorption as well as *nonlinear* absorption mechanism such as TPA are the possible generators of the signal in the semiconductor. The two linear mechanisms cited above, are not going to be present in a weakly doped material and certainly not on an intrinsic layer [10]. This left us with TPA as the mechanism responsible for the generation of the signal. To check if the signal is produced by TPA, a more precise observation of the dependence of the signal detected against power has to be done. To improve the precision of the detection system, a slight change in the set-up described above was made. Instead of using an oscilloscope to detect the signal, a lock-in detection system was implemented using an optical chopper and a lock-in amplifier as shown in Fig. 5.3. A sweep in wavelength using this detection system is shown in Fig. 5.6 giving the same qualitatively results that the ones obtained with the oscilloscope. The behaviour is the same for different optical powers.

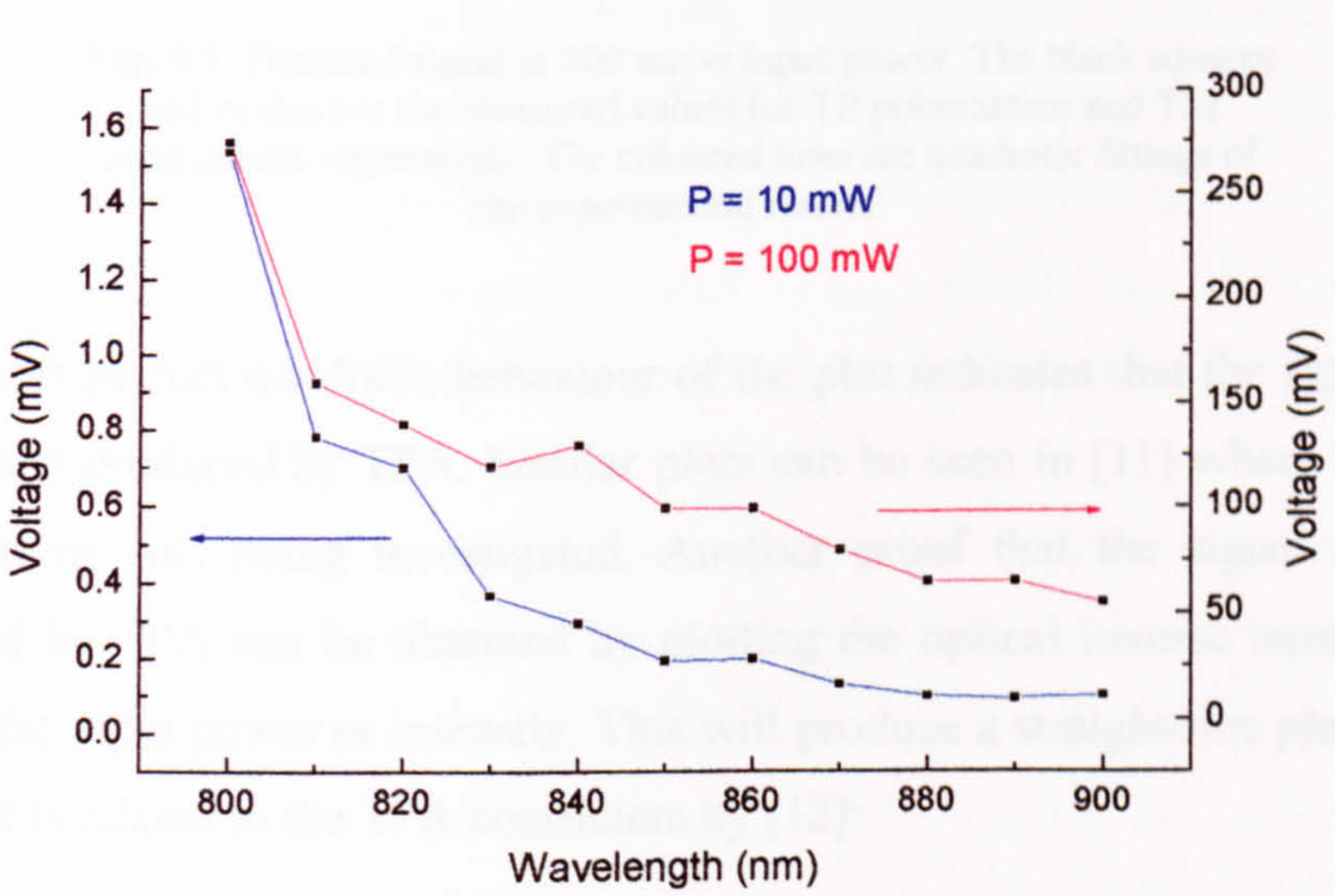

Fig. 5.6. Generated voltage *vs* wavelength for two different optical power. The power shown was measured at the output of the laser.

900 nm was the wavelength chosen to check the dependence of the signal with the optical power because is the point further away from the cut-off frequency. As TPA has a clear dependence in polarization, a half-wave plate and a polarizer

were added to the set-up in order to be able to rotate the polarization going into the device. A sweep in power was then made for TE and TM polarizations. The results are shown on Fig. 5.7. The black squares and circles are the experimental data for TE and TM polarization respectively. The blue and red lines are quadratic fittings of the data helping to observe the trend.

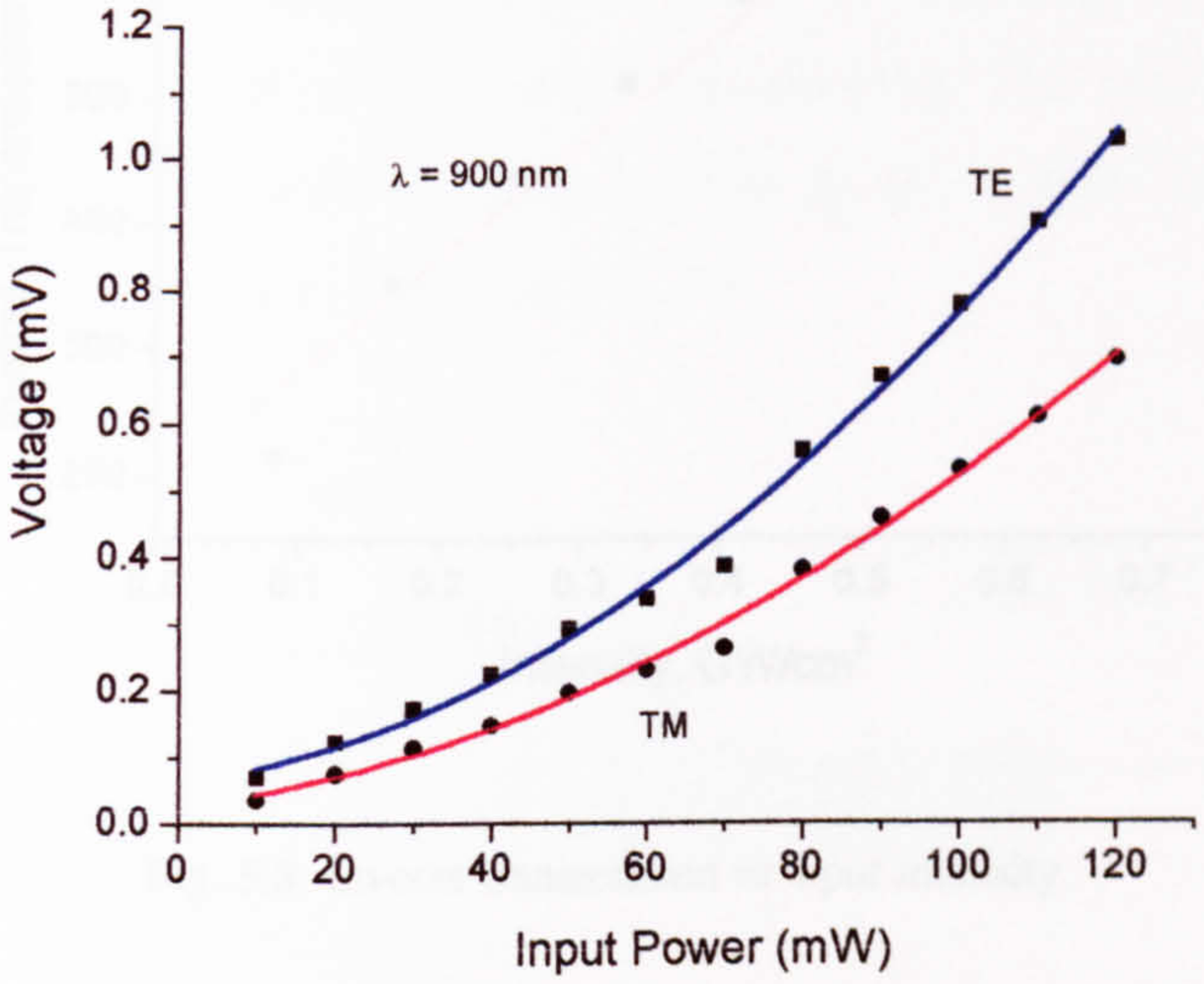

Fig. 5.7. Detected signal at 900 nm *vs* input power. The black squares and circles are the measured values for TE polarization and TM polarization respectively. The coloured lines are quadratic fittings of the experimental results.

The almost perfect quadratic behaviour of the plot indicates that the signal is in effect been produced by TPA. Similar plots can be seen in [11] where the TPA photocurrent was being investigated. Another proof that the signal is being produced by TPA can be obtained by plotting the optical inverse transmission against the input power or intensity. This will produce a straight-line plot, where the slope is related to the TPA coefficient by [12]:

$$\frac{1}{T}=\frac{I_{in}}{I_{out}}=\frac{1}{(1-R)^2\eta e^{(-\alpha_1 L)}}+\alpha_2\frac{\left(1-e^{(-\alpha_1 L)}\right)}{\alpha_1(1-R)e^{(-\alpha_1 L)}}I_{in} \qquad (5.2)$$

where α_1 and α_2 are the linear and two-photon loss coefficients.

The inverse transmission plot is shown in Fig. 5.8. The black squares are the experimental data and the red line is a linear fit to help to see the linear trend of the points.

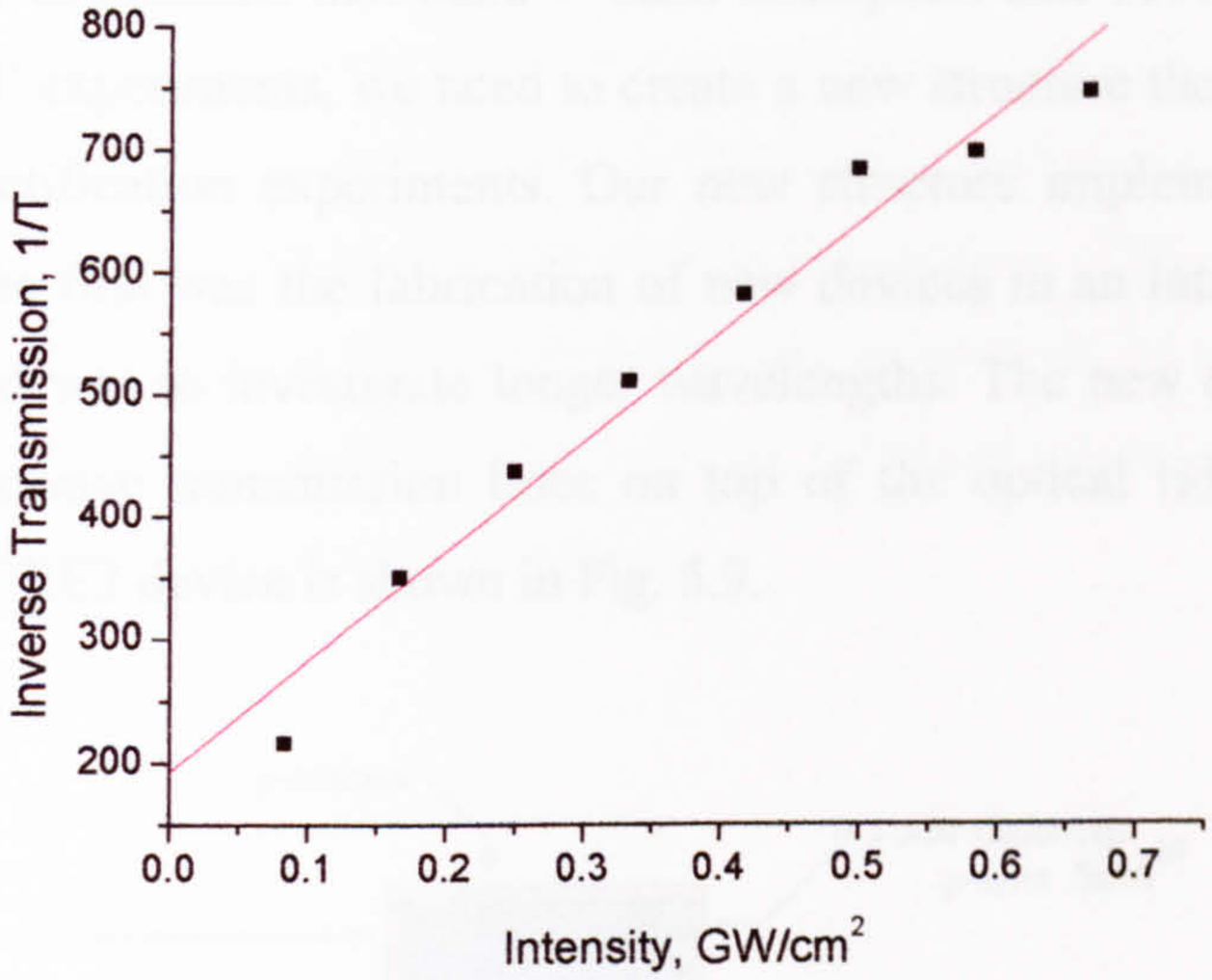

Fig. 5.8. Inverse transmission *vs* input intensity.

The calculated TPA coefficient obtained from the liner fit in Fig. 5.8 and equation 5.2 is $\alpha_2 = 11.58$ cm/GW. Note that the uncertainty of this value may be large because the coupling efficiency was never measured during the experiment. A coupling efficiency of 50% was assumed for the calculations. The value of α_2 found here is consistent with previous experimental results shown in [11]

Being far from the intrinsic absorption edge and the quadratic response or the signal for an incident power, we conclude that TPA is the dominant signal which is masking the ORE signal. Based on the result obtained in the ORE1 devices, the natural progression towards the optimum ORE device is to move to longer wavelengths where TPA is considerably reduced. The temporal resolution of the optical rectification signal will be different to the one produced by TPA. The rectification signal will be shorter than any other signal produced by the movement of free carriers such as TPA. A device capable of handling microwave signals using travelling wave electrodes has, therefore, to be considered in future devices.

5.4.2 ORE2 devices.

5.4.2.1 CW experiments.

Once we have determined that band-to-band absorption and TPA are important factors in ORE experiments, we need to create a new structure that will improve the optical rectification experiments. Our new structure implements two new approaches; the first was the fabrication of new devices in an intrinsic material and the second was to investigate longer wavelengths. The new device, ORE2, contains microwave transmission lines on top of the optical ridge. The cross section of an ORE2 device is shown in Fig. 5.9.

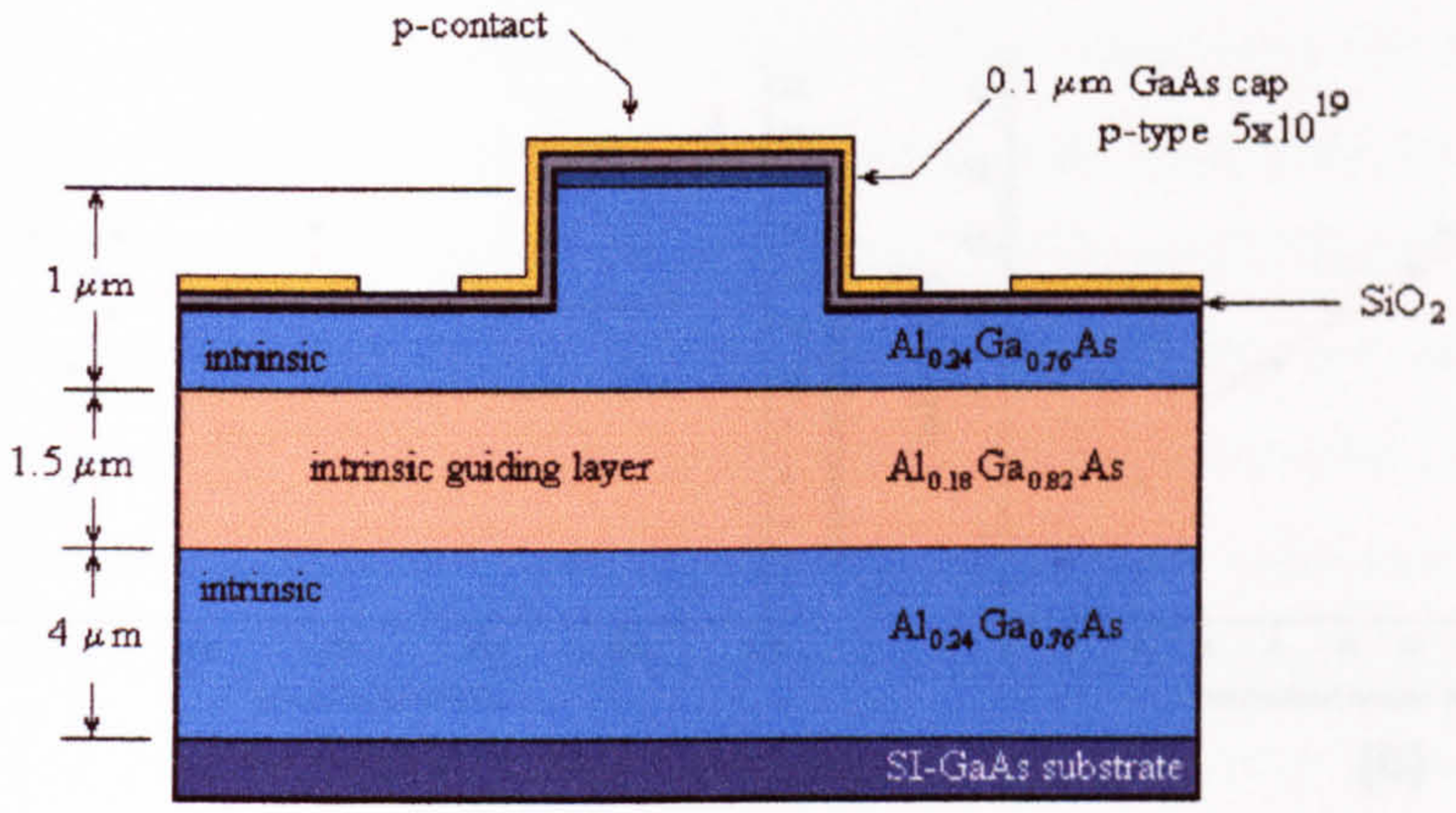

Fig. 5.9. Cross-section of an ORE2 device.

The set-up used in this experiment, was the same one described in last section, but this time, the light source is a CW Nd:YLF laser working at λ = 1047 nm. The average power was 1.8 W, which had to be attenuated using neutral density filters to avoid damage to the facets of the device. Again, the sample was positioned in the end fire rig, and probed with two individual dc probes. The electrical signal was detected with a lock-in system. When plotting the detected voltage versus input power (Fig. 5.10a), a different behaviour than the one exhibited by the p-i-n structures can be observed. No appreciable difference was observed between TE and TM polarisation. Monitoring the output power, we realised that it followed the same behaviour as the detected voltage (Fig. 5.10a). This can be seen more clearly in Fig. 5.10b. The saturation shown in Fig. 5.10a,

could be due to the saturation of states in the semiconductor bands. At powers above at around 65 mW, no more free carriers are available to keep increasing the signal. This is also a consequence of using intrinsic layers in ORE2 devices. To try to find out the phenomenon that is producing the voltage in the sample, the inverse transmission versus input power was plotted (Fig. 5.10c). Although the plot in Fig. 5.10c does not look as linear as the plot in Fig. 5.8, it is still adequate to say that we are measuring TPA in the sample. This does not mean that the ORE signal is not in the sample but is still being mask by other effects. A possible solution to this problem is to perform temporal experiments at higher wavelength and/or use short electrical pulses.

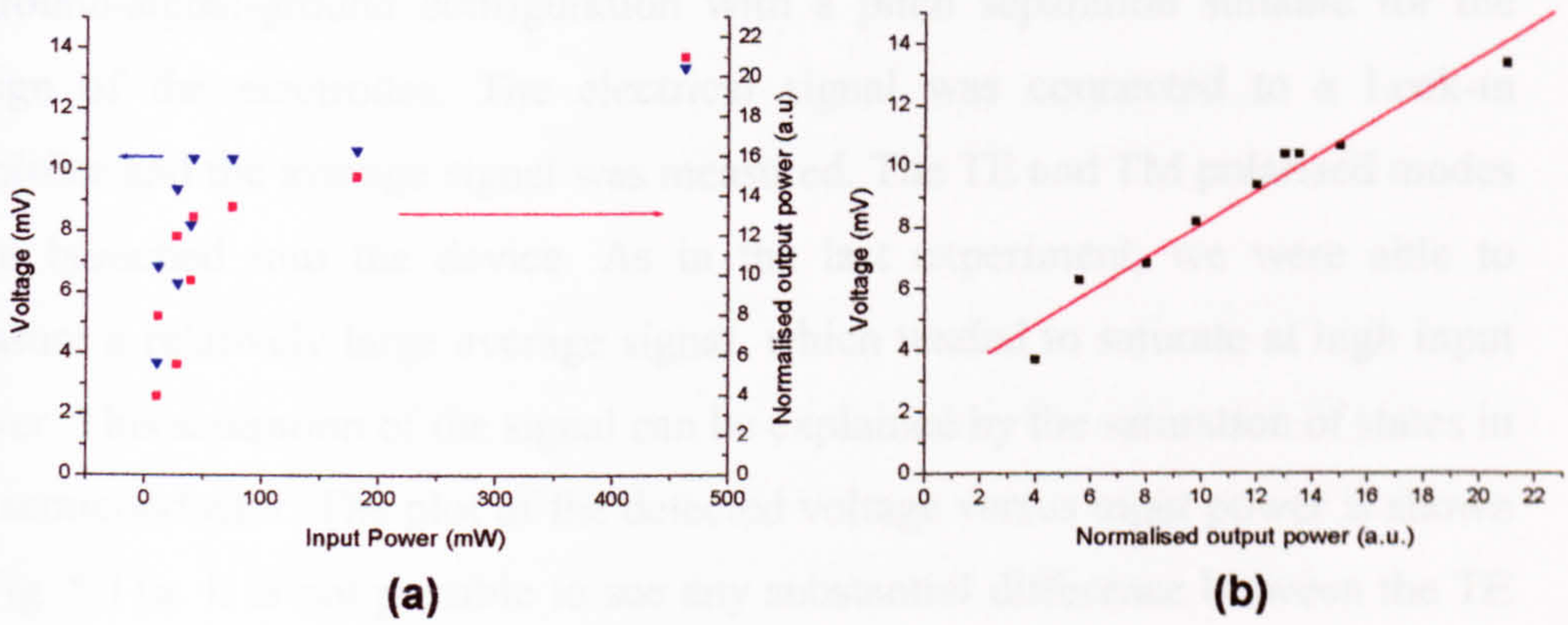

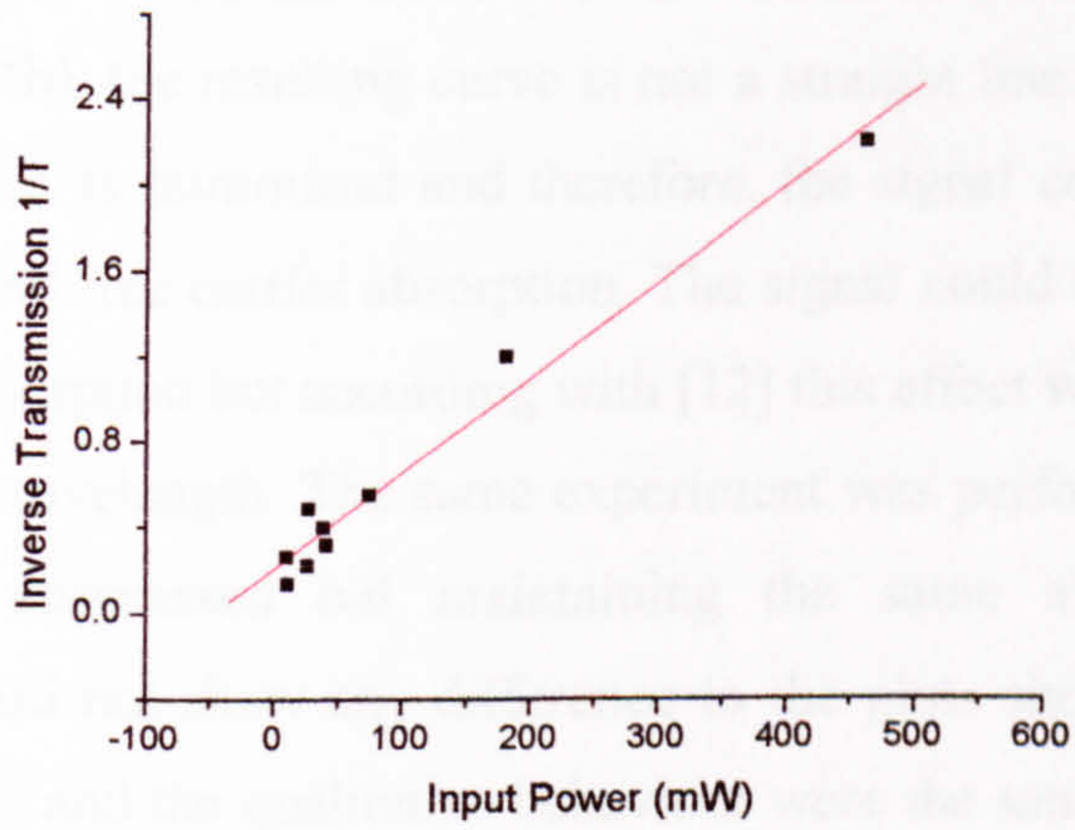

Fig. 5.10. (a) Detected voltage and output power against input power. This time the quadratic dependence is not very clear and saturation can be observed. (b) Output voltage and output power have the same dependence with the input power. (c) Inverse Transmission plot.

5.4.2.2 Pulsed experiments.

If we perform an experiment where the energy of the photons is below the half band gap of the material, we expect to eliminate, or at least reduce considerably, the TPA signal (main component in previous experiments). The reduction on the TPA signal increases our chances to detect the ORE signal. If a pulsed laser is used in the experiment, the temporal response of the signal can be analysed based in the justification given at the end of section 5.4.1. The pulsed experiments were performed using a mode-locked NaCl:OH⁻ F-centre laser, operating at the wavelength of 1616 nm, producing pulses of duration 25 ps at a repetition rate of 82 MHz. Again, the output of the laser was end-fire coupled to the optical rectification device. The device was probed with a 40 GHz probe. The probe has a ground-signal-ground configuration with a pitch separation suitable for the design of the electrodes. The electrical signal was connected to a Lock-in amplifier and the average signal was measured. The TE and TM polarised modes were launched into the device. As in the last experiment, we were able to measure a relatively large average signal, which tended to saturate at high input power. This saturation of the signal can be explained by the saturation of states in the semiconductor. The plot of the detected voltage versus input power is shown in Fig. 5.11a. It is not possible to see any substantial difference between the TE and TM polarised modes, which means that the ORE signal is still being masked by another effect. When the inverse transmission is plotted versus the input power (Fig. 5.11b), the resulting curve is not a straight line. At this wavelength, the signal of TPA is minimized and therefore, the signal could be produced by residual TPA, and free carrier absorption. The signal could also be generated by three-photon absorption but according with [12] this effect will also be minimum at the working wavelength. The same experiment was performed again with the mode locking suppressed but maintaining the same average power. The measurements did not show any difference to the plots show in Fig. 5.11. The numerical values and the qualitative behaviour were the same. This experiments validates the use of a CW measurement system in a pulsed experiment in the sense that a difference on the plot for the transmission inverse is clearly seen.

The next step of the experiment consisted in connecting the electrical signal to a sampling oscilloscope to observe the temporal resolution of the electrical signal.

Unfortunately, problems to trigger the signal were found and no observation could be obtained at this point.

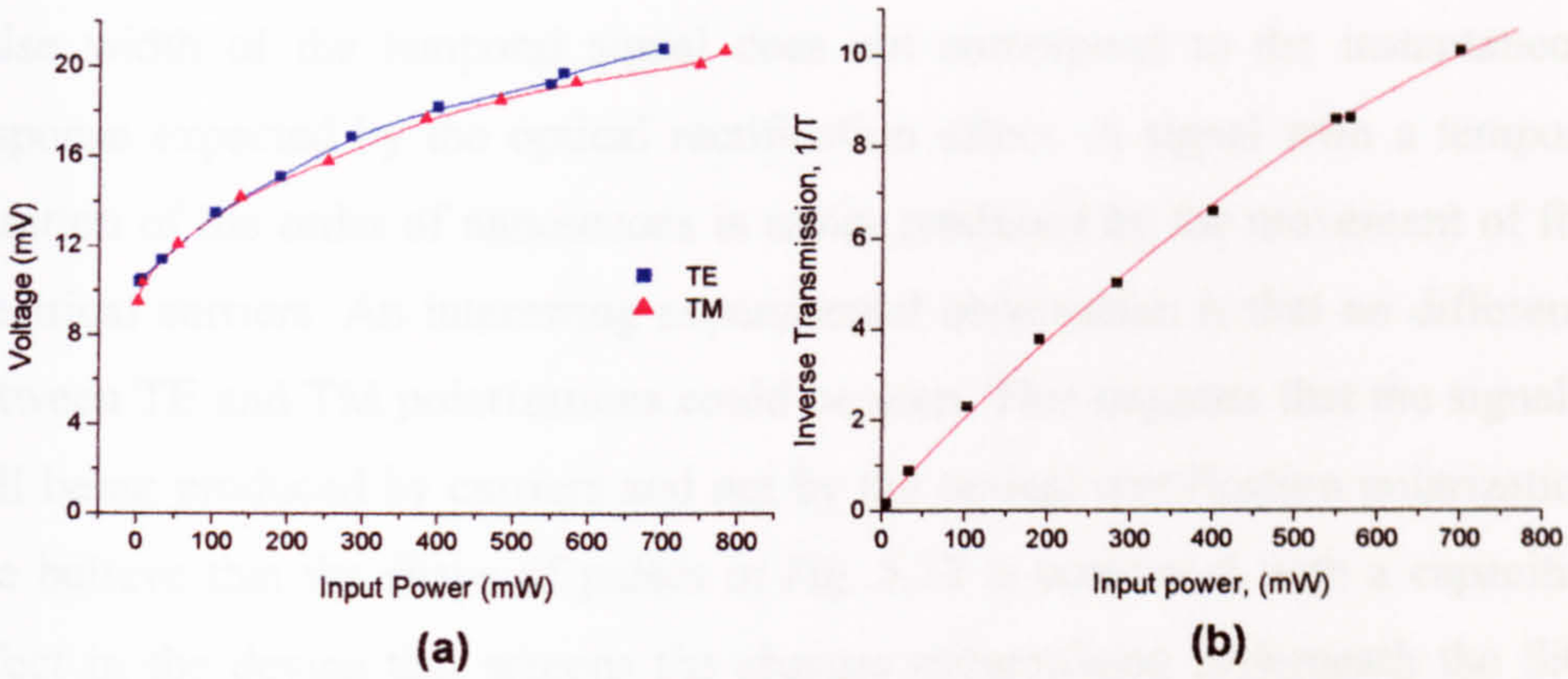

Fig. 5.11. Detected voltage (a) and transmission inverse (b) for an ORE2 device at 1620 nm.

Up to now, there is not real proof of optical rectification. One reason is that the lock-in amplifier is not able to resolve any difference because it detects V_{rms} values. Another reason is that the electric field is too far away from the optical field because the electrodes cover both, the ridge and the etched region.

At this point of the research, the importance of having a temporal experiment was evident. So far, there has been no proof that a train of pulses is been generated on the device. Further experiments were carried out on the same ORE2 devices using an optical parametric oscillator (OPO) working at λ=1500 nm with a pulse width of around 400 fs. This time, electrical pulses were detected, observed and measured. Based on previous experience and on the difficulty to trigger the sampling head, a microwave spectrum analyser with a free running trigger was used just to see if there was a periodic signal travelling on the electrodes of the ORE device. The spectrum analyser proved that a periodic signal was present on the device. The repetition rate of the electrical signal being detected was 84 MHz, which is in agreement with the repetition rate of the OPO.

A 500 MHz oscilloscope was used to analyse the electrical pulses. The pulse train obtained can be seen in Fig. 5.12. The pulse width at FWHM is 2.77 ns. The 11.9 ns correspond to the repetition rate of the laser. Theses pulses detected on the ORE2 device (an intrinsic structure) are very encouraging. However, the pulse width of the temporal signal does not correspond to the instantaneous response expected by the optical rectification effect. A signal with a temporal duration of the order of nanosecons is easily produced by the movement of free electrical carriers. An interesting experimental observation is that no difference between TE and TM polarizations could be seen. This suggests that the signal is still being produced by carriers and not by the optical rectification polarization. We believe that the shape of pulses in Fig. 5.12 is consistent with a capacitive effect in the device that screens the charges accumulated underneath the SiO_2 buffer under the electrode area. TPA is still believed to be the cause of these electrical pulses and further investigation was done to clarify this.

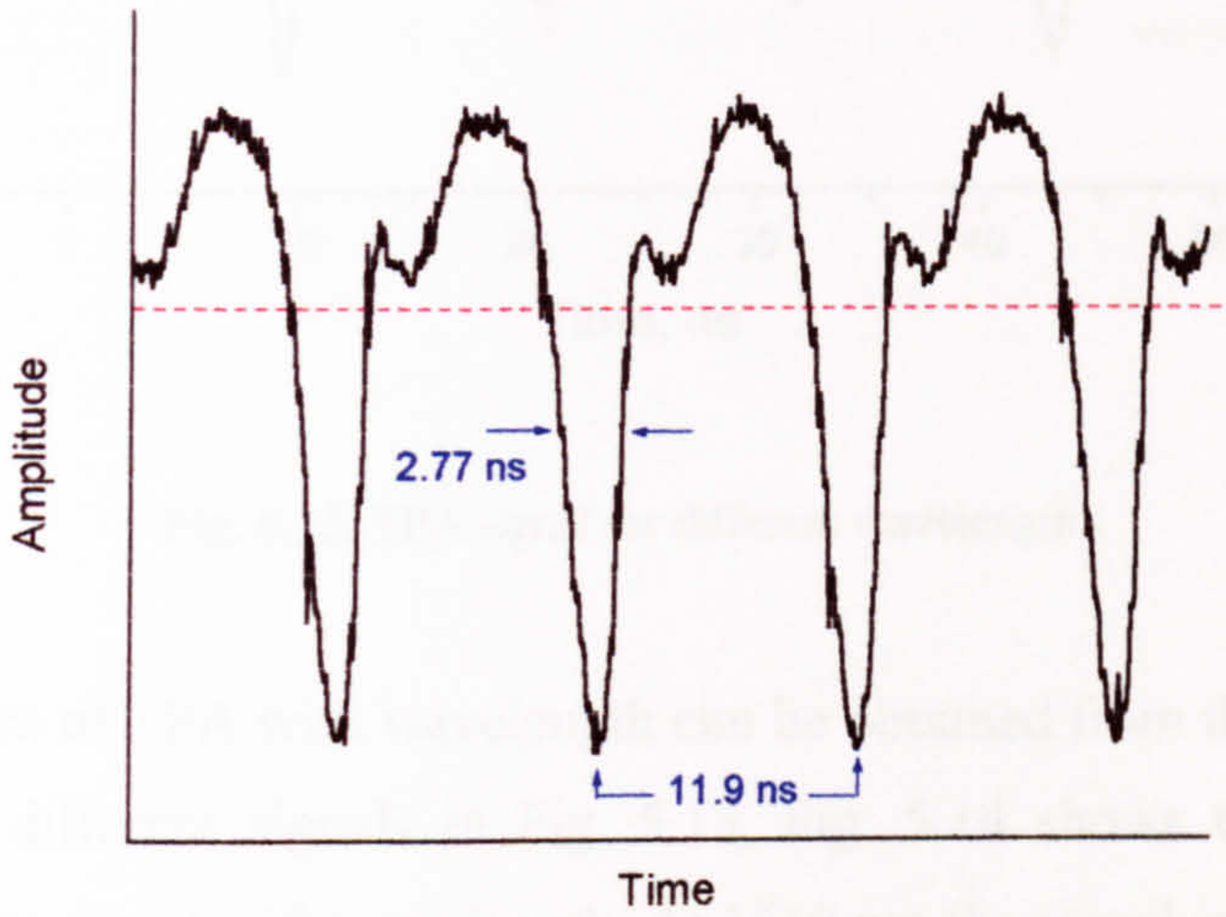

Fig. 5.12. Pulses detected with a 500 MHz oscilloscope.

An experiment using a tuneable laser was then designed to determine the wavelength dependence of the pulsed signal. The optical excitation was in the form of an OPO delivering 30 mW of average power. The pulse width was ~ 260 fs FWHM and the tuning range from 1420nm to 1510 nm. The results are shown in Fig 5.13. The electrical pulse width is 3.313 ns FWHM for all the wavelength range. The 11.66 ns correspond to the repetition rate of 85.76 MHz. No signal could be detected at wavelength of 1510 nm and above. The different traces do

not have a common baseline because the equipment used was a sampling head, which only detects AC signals. The extra shoulder in the pulse is caused for the impedance mismatch between the device and the measurement system.

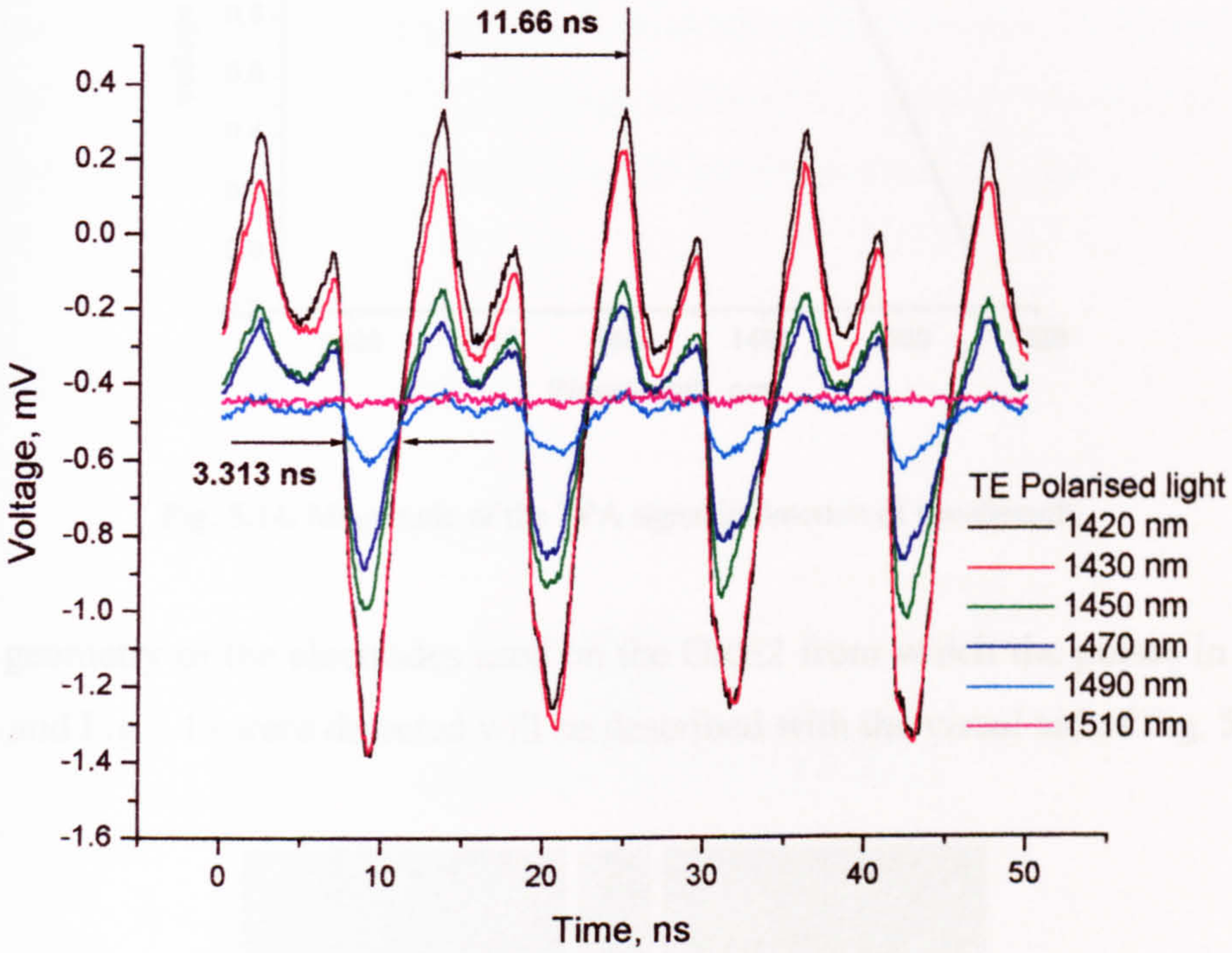

Fig. 5.13. TPA signal for different wavelengths.

The dependence of TPA with wavelength can be obtained from the peak-to-peak values of the different signals in Fig. 5.13, Fig. 5.14 shows the drop of the amplitude of the signal with wavelength. At 1510 nm the signal is too small to be detected by our equipment. This result should be interpreted carefully. In one hand, the 1510 nm compares to the edge of the TPA signal estimated in equation 2.6 (1500 nm). In the other hand, it is well known that the TPA tail goes well into longer wavelengths, particularly for the TE polarisation. The conclusion drawn from this experiment is that the most significant part of the TPA signal can in fact be eliminated by working at wavelengths longer that 1510 nm.

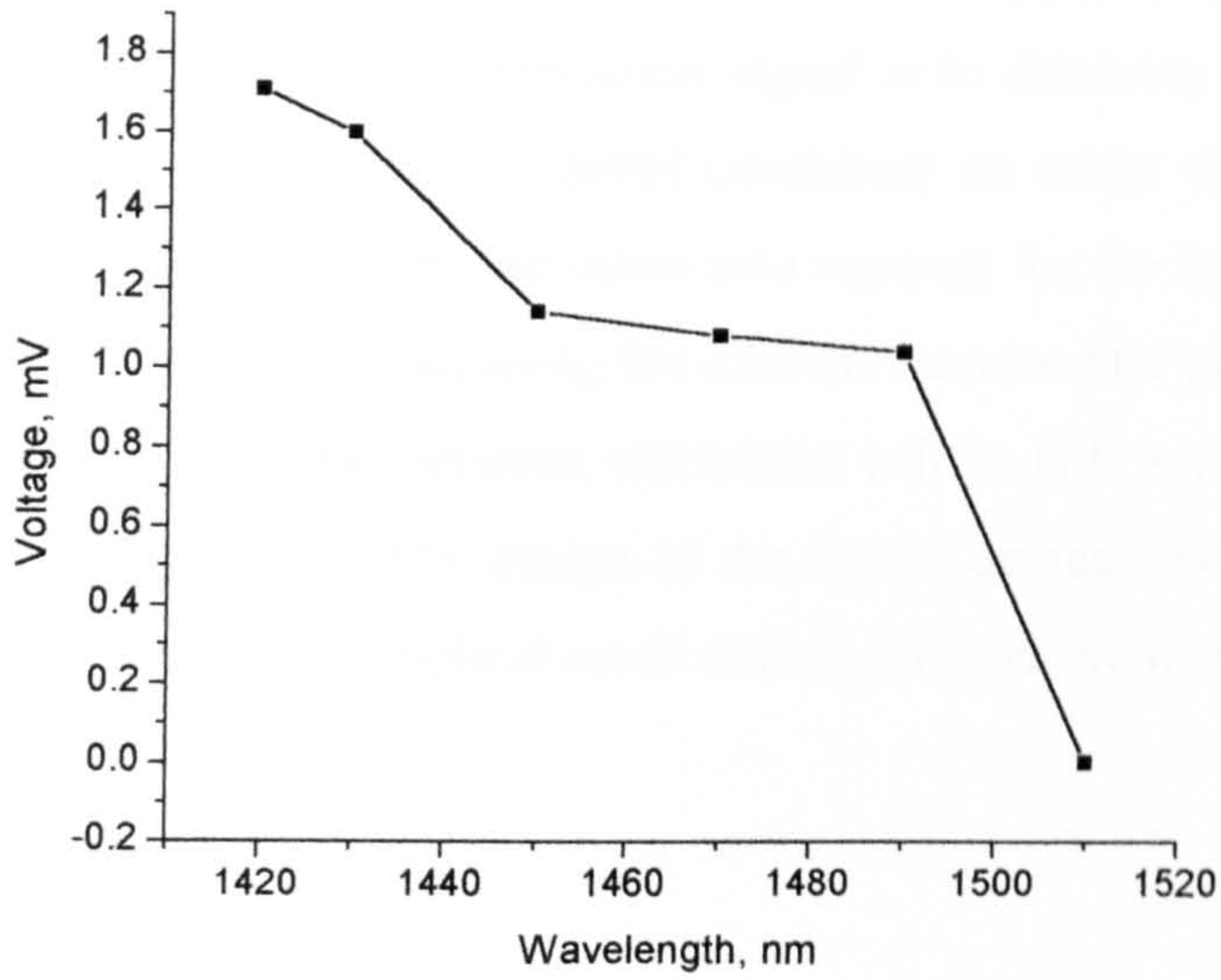

Fig. 5.14. Magnitude of the TPA signal in function of wavelength.

The geometry of the electrodes used on the ORE2 from which the pulses in Fig. 5.12 and Fig 5.13 were detected will be described with the visual aid of Fig. 5.15.

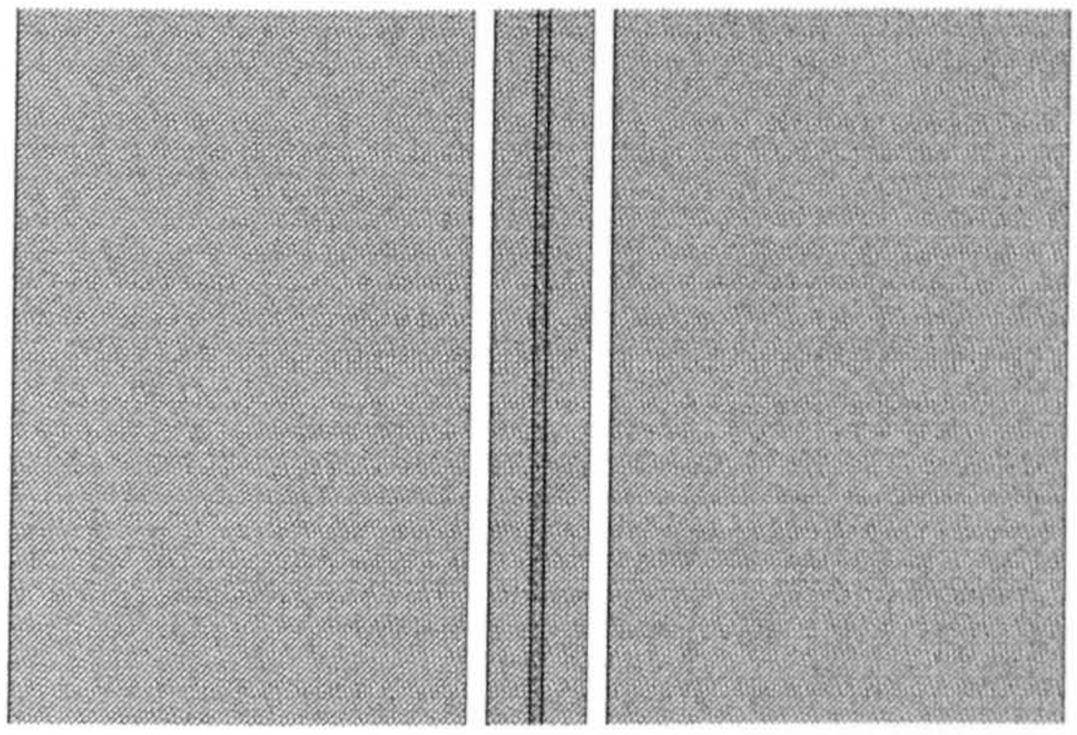

Fig. 5.15. Top view of the ORE2 device use to record the signals shown in Fig. 5.13.

Fig. 5.15 shows the schematic of the top view of an ORE2 device. It contains ground-signal-ground electrodes with the following dimensions: gap between electrodes, 9 μm; major electrode width, 200 μm; minor electrode width, 44 μm; waveguide width, 5 μm; electrode length, 1 cm; sample length, 1.2 cm. As usual, there is a silica buffer layer between the semiconductor and the electrodes. All the layers are intrinsic with exception of the GaAs cap layer, which is heavily doped.

Still, the ORE2 device is not optimised for detection of optical rectification. One key point to detect the optical rectification signal is to fabricate the electrodes very close together and to have a central conductor no wider that the optical waveguide ridge. This approach was taken into account for the third generation of devices, which were fabricated using the electron beam writer due to the small dimensions involved (the gap between electrodes will be below the limit of our optical lithography process). The design of the ORE3 devices will improve the overlap between the electrical optical mode and the microwave mode.

5.4.3. ORE3 devices.

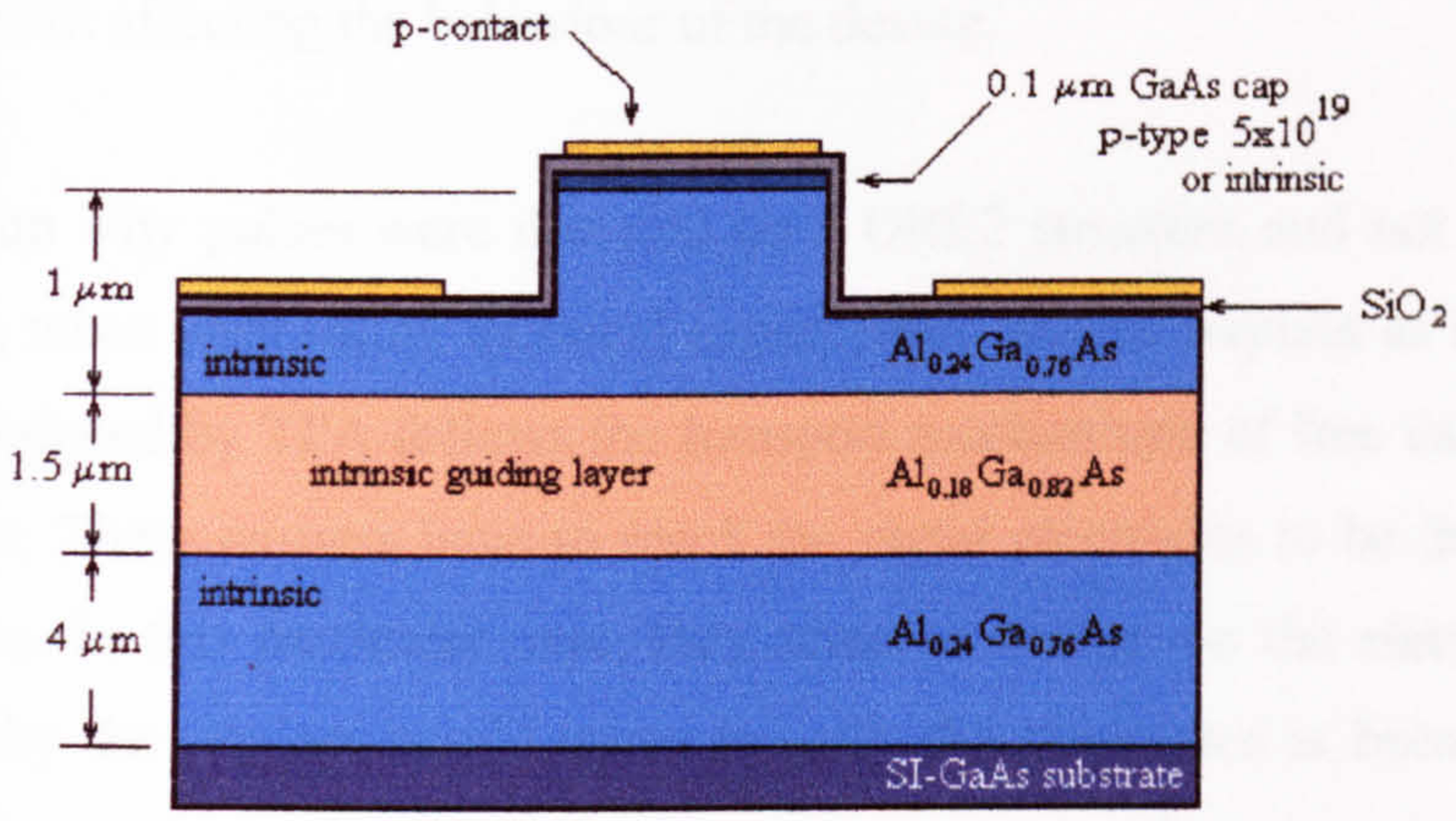

Fig. 5.16. ORE3 device.

The knowledge in ORE devices obtained up to know allows us to have a better electrode design for generation three. There were not many experiments on these devices because at this point we knew that the design was not complete until the creation of velocity matched structures. These devices were more an exercise to master the fabrication process described in chapter 4. The third generation of optical rectification devices have the central electrode exactly on top of the ridge. They are non-velocity match structures. The cross section of an ORE3 device is shown in Fig. 5.16 where the central electrode sits exclusively on top of the ridge. The distance between electrodes is 2.5 μm. The ORE3 devices were fabricated on two different wafer structures where the only difference between

them was the cap layer; in one of the structures, there was a heavily doped p-type cap while on the other an intrinsic cap layer tops the structure. This was made with the idea of seeing the influence of a doped layer in the structure, which might interfere with the rectification signal.

The same set experiments described in section 5.4.2.2 with the tunable OPO were carried-on on the ORE3 devices, but no signal could be detected on the sampling oscilloscope. However, the signal obtained from the lock-in amplifier was very similar to the one shown in Fig. 5.11. This indicates that there is a small signal coming out of the device but, again, the system is not sensitive enough to detect it. The presence of a heavily doped cap layer did not show any difference respect to the intrinsic layer. This is because the optical field is too far from this layer and therefore not affecting the behaviour of the device.

The reason why pulses were detected on a ORE2 structure and not in a ORE3 structure, when performing identical experiments, can be explain as follows: the signal produced by TPA follows the transport mechanisms of free carries on the core layer. These carriers have to reach the metal electrodes to be drained from the device. In this particular case, they screen a charge on the electrodes. The reason why the carriers would move towards the electrodes is because we are probing the device and there is an electrical potential difference associated with the probe. The probe in general, will be more negative on the ground electrodes than it is on the signal electrode. Free carriers can only move a finite distance before they are recombined. This distance is know as the Debye Length, L_D and is given by [13]:

$$L_D = \sqrt{\frac{\varepsilon_s kT}{q^2 n_0}} \tag{5.3}$$

where ε_s is the dielectric constant of the semiconductor, k is the Boltzmann constant, T is the temperature, q is the elementary charge and n_0 is the carrier's equilibrium concentration. ε_s for $Al_xGa_{1-x}As$ can be calculated with the following expression [14]:

$$\varepsilon_S = 13.18 - 3.12x \tag{5.4}$$

The ORE2 and ORE3 devices have an n_0 value of 10^{14} cm^{-3} to 10^{15} cm^{-3} in the core layer. From equation 5.4, ε_s for an 18% Aluminium concentration is 12.61. L_D can be calculated for both values of n_0. $L_{D(10^{14})} = 424.41$ nm and $L_{D(10^{15})} = 134.21$ nm, which means that the free carriers will move a distance between 134 nm and 424 nm before they recombine. In addition, all the carriers generated in the core will move much less than the above estimation because they need to get over the heterostructure. Fig. 5.17 shows a representation of what happen with the free carriers when they are generated by TPA in (a) an ORE2 device and (b) and ORE3 device.

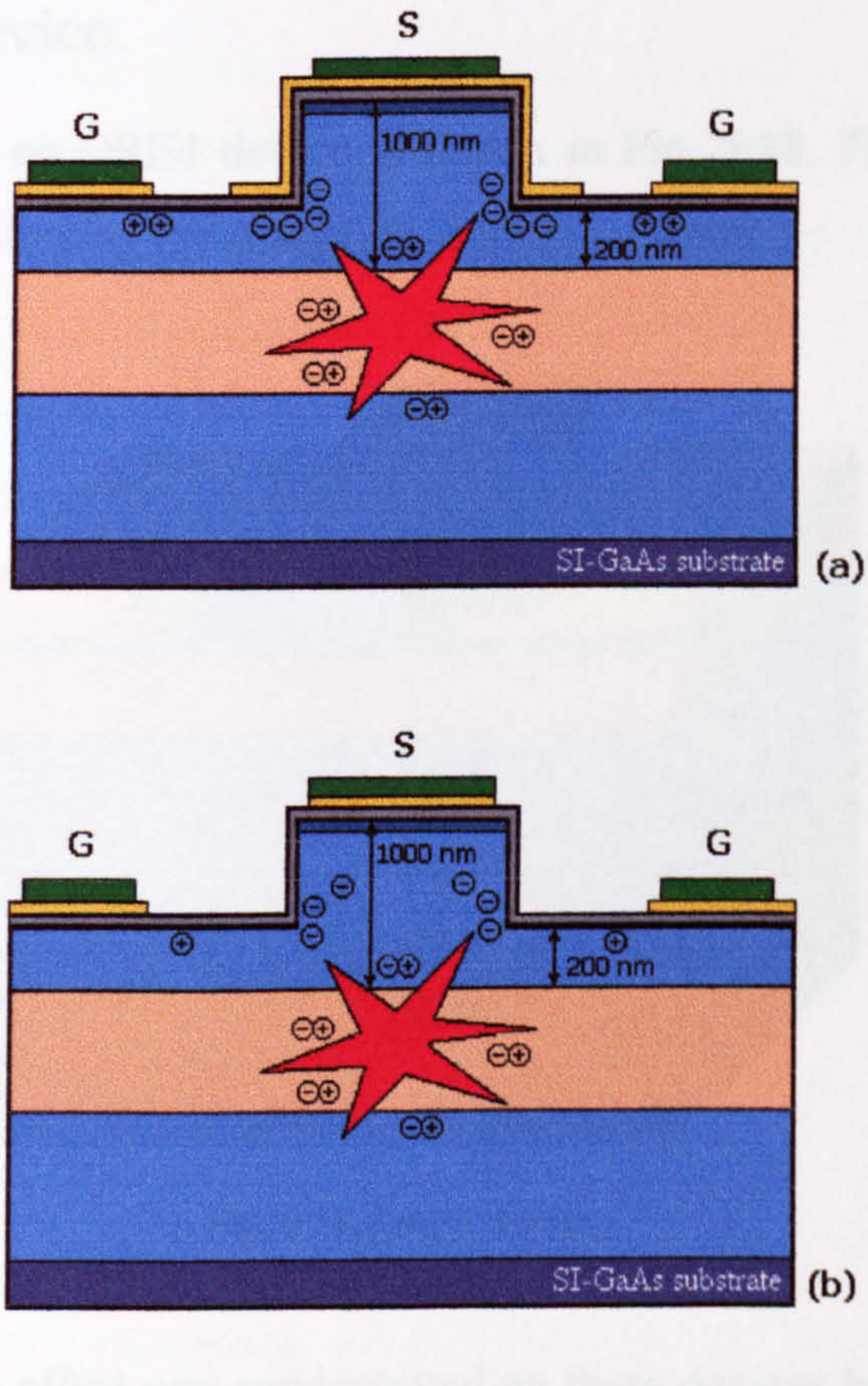

Fig. 5.17. TPA generated carriers in (a) an ORE2 device and (b) and ORE3 device.

In an ORE 2 device (Fig. 5.17a), the electrodes are very close to the active region and therefore the carriers have to travel a distance of around 200 nm to start to accumulate underneath the signal electrode. This accumulation generates the

signal that we are measuring. However, to accumulate carriers underneath the signal electrode in a ORE3 device (Fig. 5.17b), they would have to travel about 1000 nm which is more that two times L_D. That does not happen and therefore no signal is generated in this case.

Again, ORE3 devices are not optimum to extract a rectification signal from the device but in terms of understanding the devices is invaluable. Once the fabrication process was proofed in ORE3 devices, the fabrication of velocity-matched devices or ORE4 devices was initiated. The results are shown in the next section.

5.4.4 ORE4 device.

A 3D schematic of an ORE4 device is shown in Fig. 5.18. These devices are velocity matched following the design presented in chapter 3.

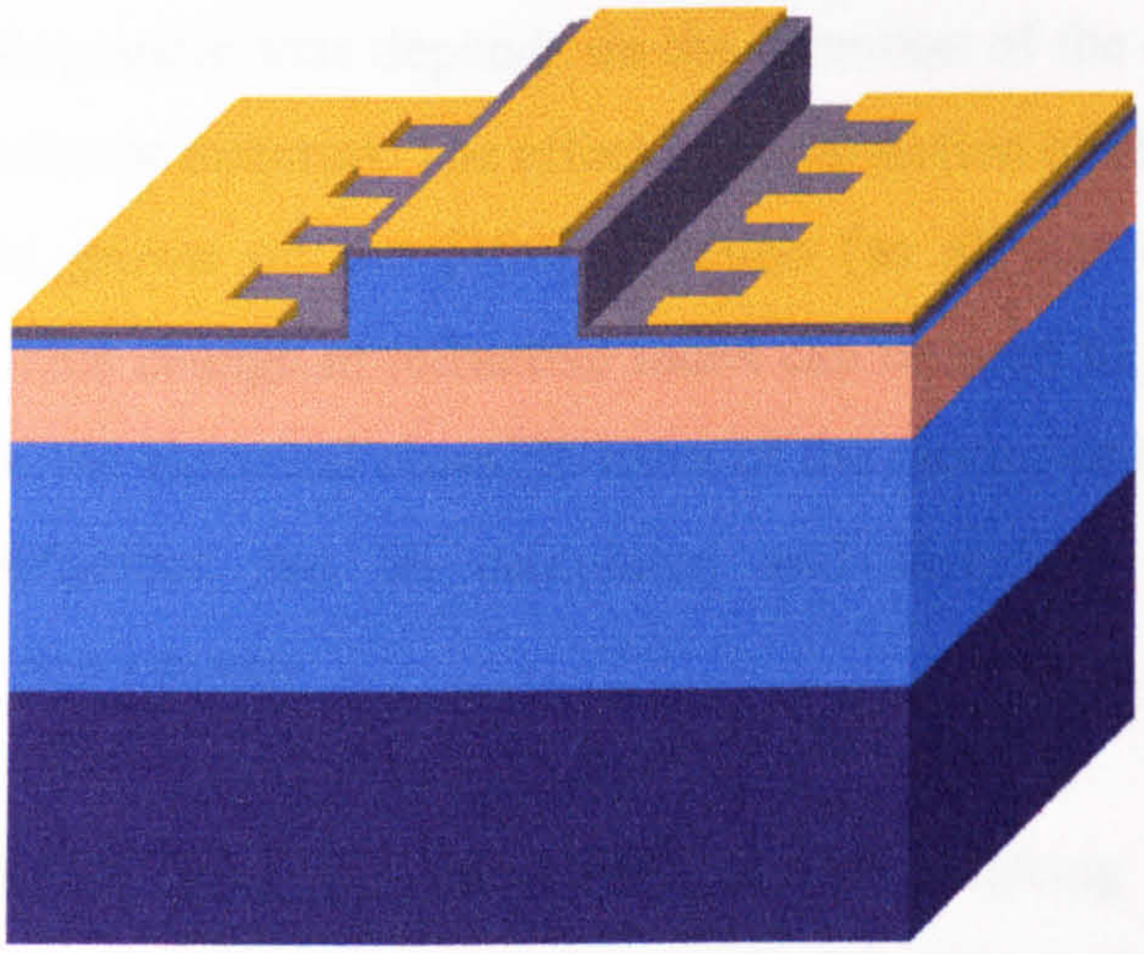

Fig. 5.18. ORE4 device.

Most of the research effort was concentrated on these devices because, as it was explained in chapter 2, these are the ideal devices in terms of extraction of the rectification signal. From previous experiments, we know that the signal generated by the device may be smaller that the higher resolution of a sampling head hence a microwave spectrum analyser was used. A microwave spectrum analyser has higher sensitivity and dynamic range than any existing sampling

oscilloscope and therefore if we use it as a detection system, we should be able to detect smaller signals. Obviously, the signals will be captured in the frequency domain. These signals can then be converted to the time domain for analysis.

Before performing the rectification experiments in the ORE4 device, we decided to try them first as electro-optic modulator, and mode converter, since the structure is very similar for these three devices. The sort of information we can gain by performing this experiments is to confirm the right crystallographic orientation and estimate the nonlinear coefficient of the material.

5.4.4.1 As electro-optic modulator.

GaAs being a crystalline material can manifest the electro-optic, or Pockels effect. This effect can be considered as the opposite effect to optical rectification (chapter 2, equation 2.6). The electro-optic effect provides a change in refractive index proportional to an applied electric field [15]. The effect of the electric field along the crystallographic axis depends on the direction of the electric field and the type semiconductor material. The effect of the direction of the electric field in a GaAs structure grown on the [100] direction (as all our ORE devices) is detailed in [16]. This change in refractive index can be used to produce intensity modulators. From the electrical characteristics of the electro-optic modulator, the electro-optic coefficient can be calculated and therefore the rectification nonlinear coefficient known.

Fig. 5.19 shows the bias for the ORE4 device working as electro-optic modulator. A voltage was symmetrically applied between the signal and the ground electrodes. 45° degrees linearly polarized light was launched into the device. A polarizer with cross-polarization with respect to the input was place at the output. The signal was detected with a photodetector. The transmission factor for the cross-polarized electro-optic modulator as a function of the applied voltage is shown in Fig. 5.20. From this results we can calculated a V_π voltage of 21 V. The experimental data were passed on to Bubke for further processing. An effective nonlinear coefficient $\chi_{eff} = 9\text{x}10^{-14}$ s/m$\sqrt{W}$ accounting for the overlap

integral was obtained. This value compares very close to Bubke's theoretical calculations [17] for GaAs with growing direction [100]. The value reported in the paper is $\chi_{eff} = 8.3\text{x}10^{-14}$ s/m$\sqrt{W}$, but for an impedance of 60Ω, which is closer to our structure, a value of $\chi_{eff} = 10\text{x}10^{-14}$ s/m$\sqrt{W}$ is expected. As we can see from the values above, our crystallographic orientation and electrode configuration is the correct one for a rectification device.

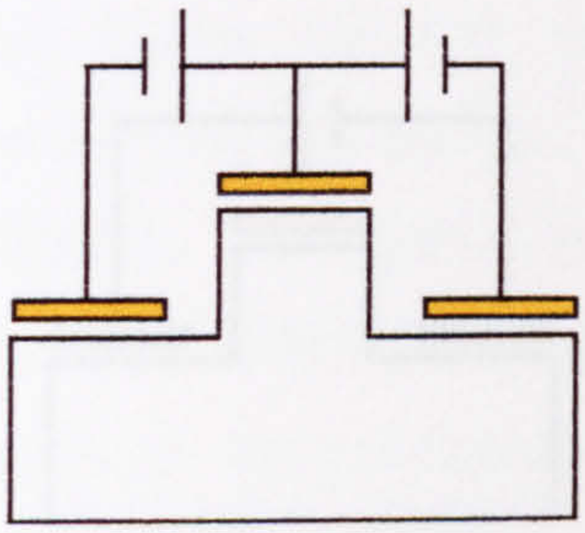

Fig. 5.19. ORE4 as electro-optic modulator.

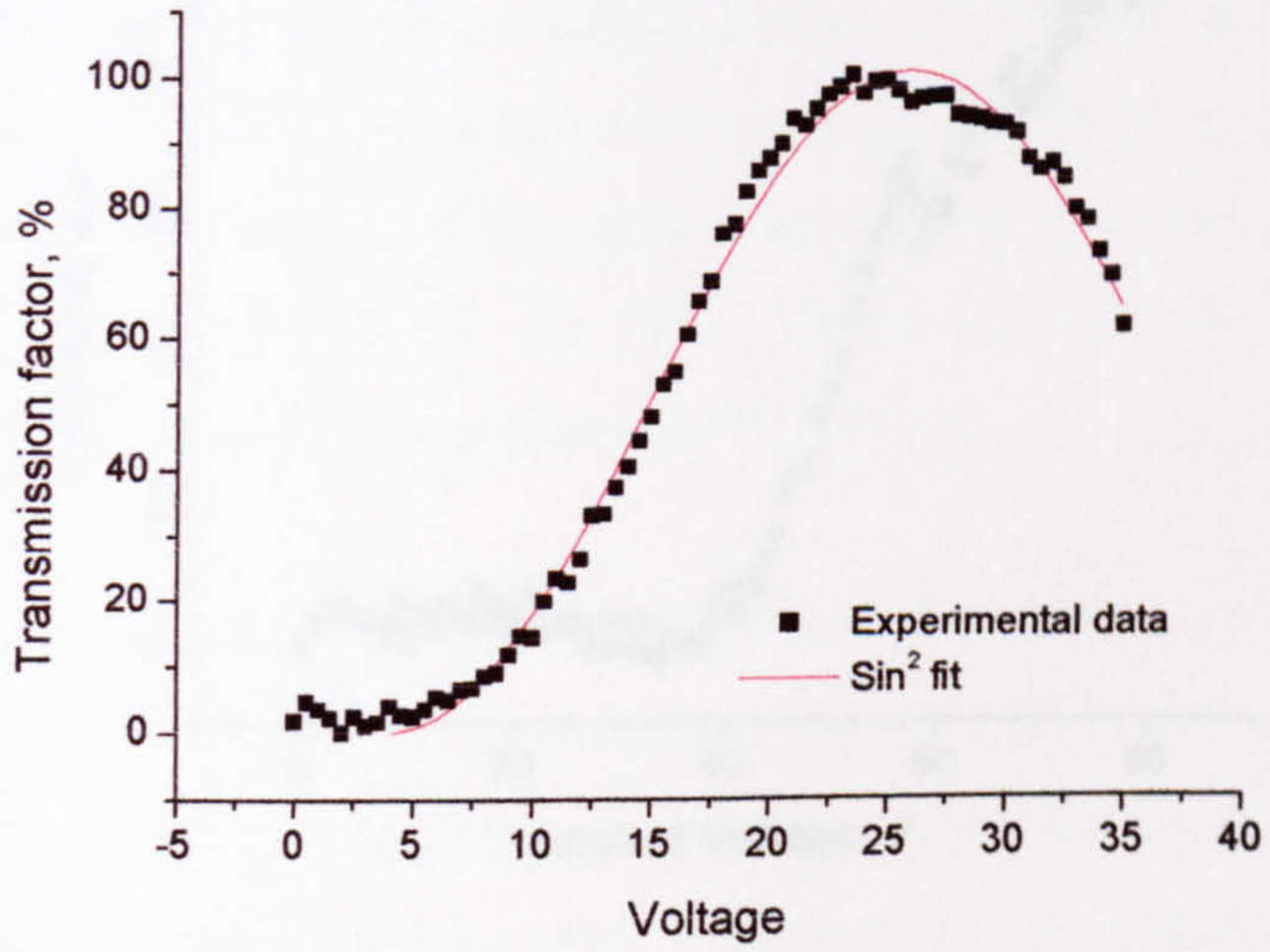

Fig. 5.20. Transmission factor for the cross-polarized electro-optic modulator as a function of the applied voltage.

5.4.4.2 As polarization converter.

Another way to operate the ORE4 device is as polarization converter. Here, a high voltage is applied to achieve mode conversion [18].

Fig. 5.21 shows the bias of the ORE4 device working as mode converter. The voltage was applied between the two ground electrodes. TE linearly polarized light was launched in to the device and a polarizer set to pass TM was place at the output. The results of this experiment are shown in Fig. 5.22. At a voltage of around 45 V we start to see the mode conversion. The percentage of conversion at 80 V is around 20 %. Again, the experimental data was passed on to Bubke who confirmed again that the measurements fit well the theoretical analysis [19].

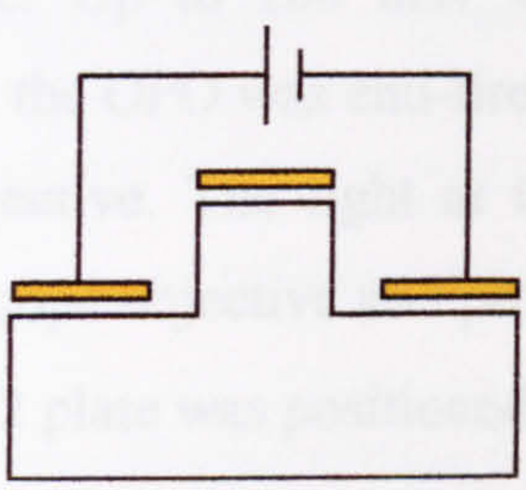

Fig. 5.21. ORE4 as polarization converter.

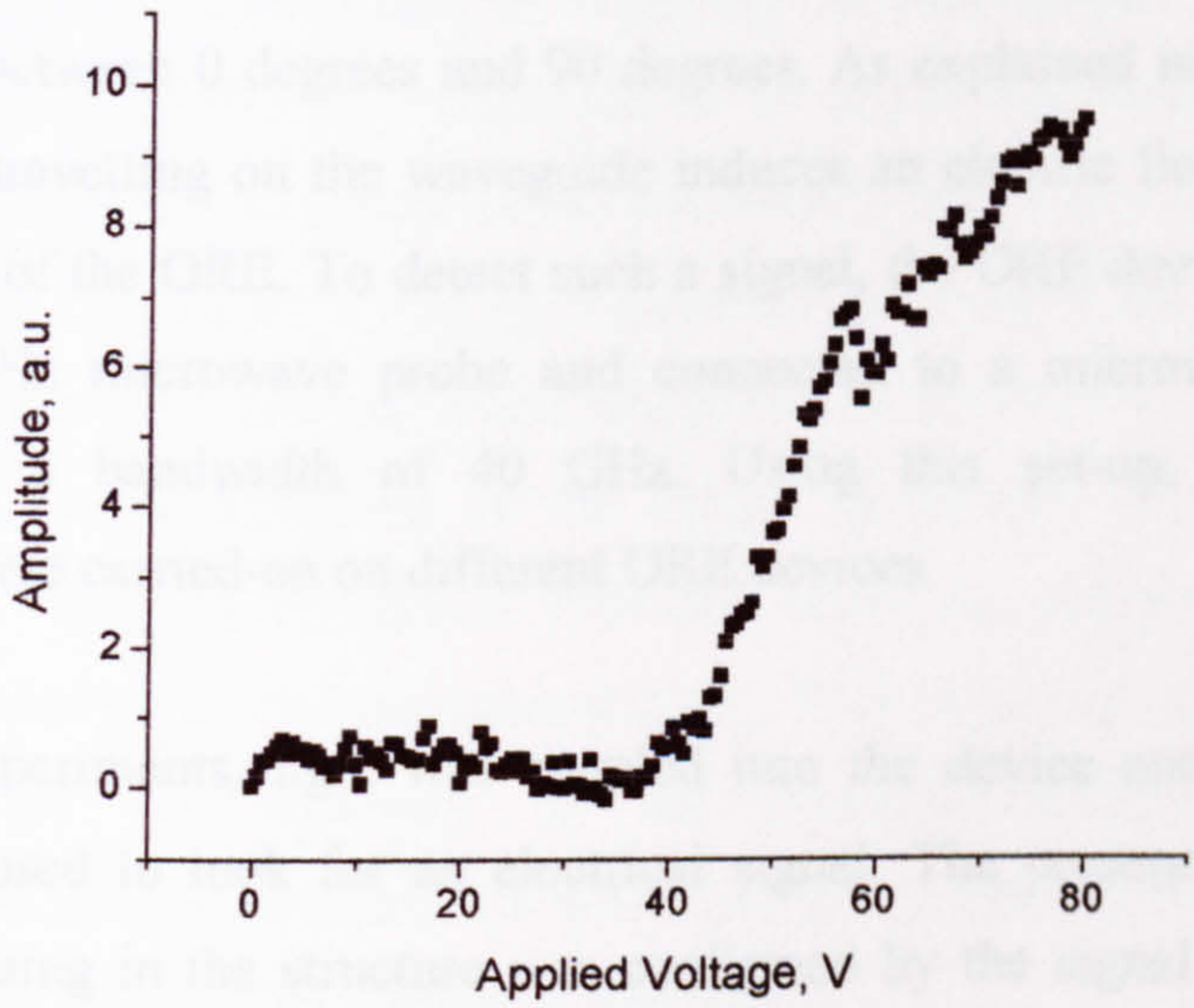

Fig. 5.22. Transmission characteristic for the polarization converter.

5.4.4.3 The rectification device.

After demonstrating that the material and the ORE4 device are consistent with well-known applications, the ORE4 devices were tested for optical rectification. The experimental results presented here are from *Dev00*, *Dev32*, *Dev68* and *Dev80*. *Dev00* uses *plain* electrodes while the other three have slow-wave electrodes. The difference among the latter is the design of the slow wave

electrode, which is detailed in table 3.1. Reference is also made to *Dev44* and *Dev56*. The dimensions of these two devices are summarised in table 3.2.

The experimental set-up used can be described as follows: the optical source was an optical parametric oscillator (OPO) with a repetition rate of 86.7 MHz and a pulse width of 250 fs FWHM. The OPO could be tuned from 1480 nm to 1580 nm at its signal output. An average power of 30 mW could be maintained over the whole wavelength range. Up to 100 mW was obtained for the shorter wavelengths. The beam from the OPO was end-fire coupled into the ORE device using a x40 microscope objective. The light at the output of the device was collected using a x20 microscope objective and projected onto a CCD camera to help with the alignment. A $\lambda/2$ plate was positioned on the optical path before the input lens to manipulate the polarization state going into the device. The polarization direction could be altered continuously from TE to TM by rotating the $\lambda/2$ plate between 0 degrees and 90 degrees. As explained in chapter 2, the optical mode travelling on the waveguide induces an electric field in the CPW line by means of the ORE. To detect such a signal, the ORE device was probed using a 40 GHz microwave probe and connected to a microwave spectrum analyser with a bandwidth of 40 GHz. Using this set-up, a number of experiments were carried-on on different ORE devices.

In the first experiments, light was coupled into the device and the spectrum analyser was used to look for an electrical signal. The presence of electrical pulses propagating in the structure was confirmed by the signal detected (Fig. 5.23). The fundamental frequency peak was centred at the repetition rate of the laser. The signal shown in Fig. 5.23 has an amplitude of –65 dBm. We believe that velocity-match imperfections within the ORE device and the high loss associated with the transmission line attenuate and disperse the signal. This explains the weak signal obtained. The fact that the signal is weak does not allow us to connect a sampling oscilloscope and observe the electrical pulse directly. Alternative ways of seeing the temporal resolution of the pulse have to be used. One of these alternatives is described below.

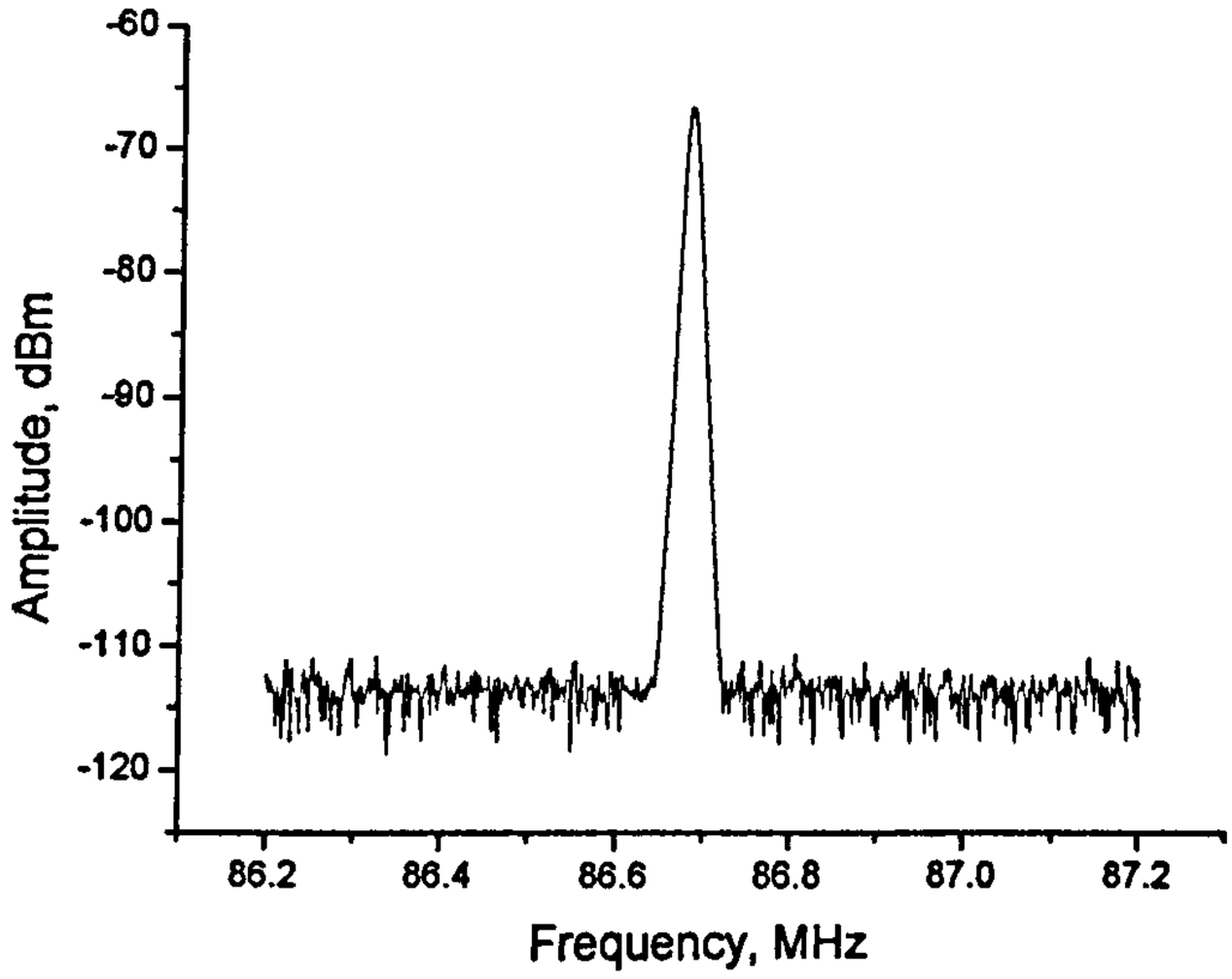

Fig. 5.23. Typical electrical signal obtained from an ORE4 device.

The second experiment consisted on sweeping the wavelength over the whole working range of the OPO. The amplitude of the signal was considerably higher for shorter wavelengths, evidence of the two-photon absorption (TPA) tail. At λ = 1580 nm, the TPA signal is almost completely suppressed, however there is a small contribution from band tail states which acts as an offset to the ORE signal. The optimum results according to the design philosophy of the device are obtained at an input wavelength of 1580 nm where the detrimental effects of multi-photon absorption are minimized [12]. This does not mean that other wavelengths are not explored. In the contrary, different wavelength measurements help to understand the behaviour of the ORE devices. These will be explained on detail on the following paragraphs.

The full set of experiments will be described for *Dev80*. *Dev 80* illustrates most of the required characteristics of a rectification device. It is then compared with the other devices, which may present better or worst performance. Fig. 5.24 shows the electrical signal obtained for a λ = 1570 nm for TE and TM polarizations. The ideal plot would have the amplitude of the TM signal very close to the noise level but this is not the case. There is therefore a background signal superimposed to the relative difference between TE and TM. The input power P_{in} was 35 mW. P_{in} on this chapter is defined as the power at the output of

the laser. A good approximation is to consider that 60% of this power is coupled into the device.

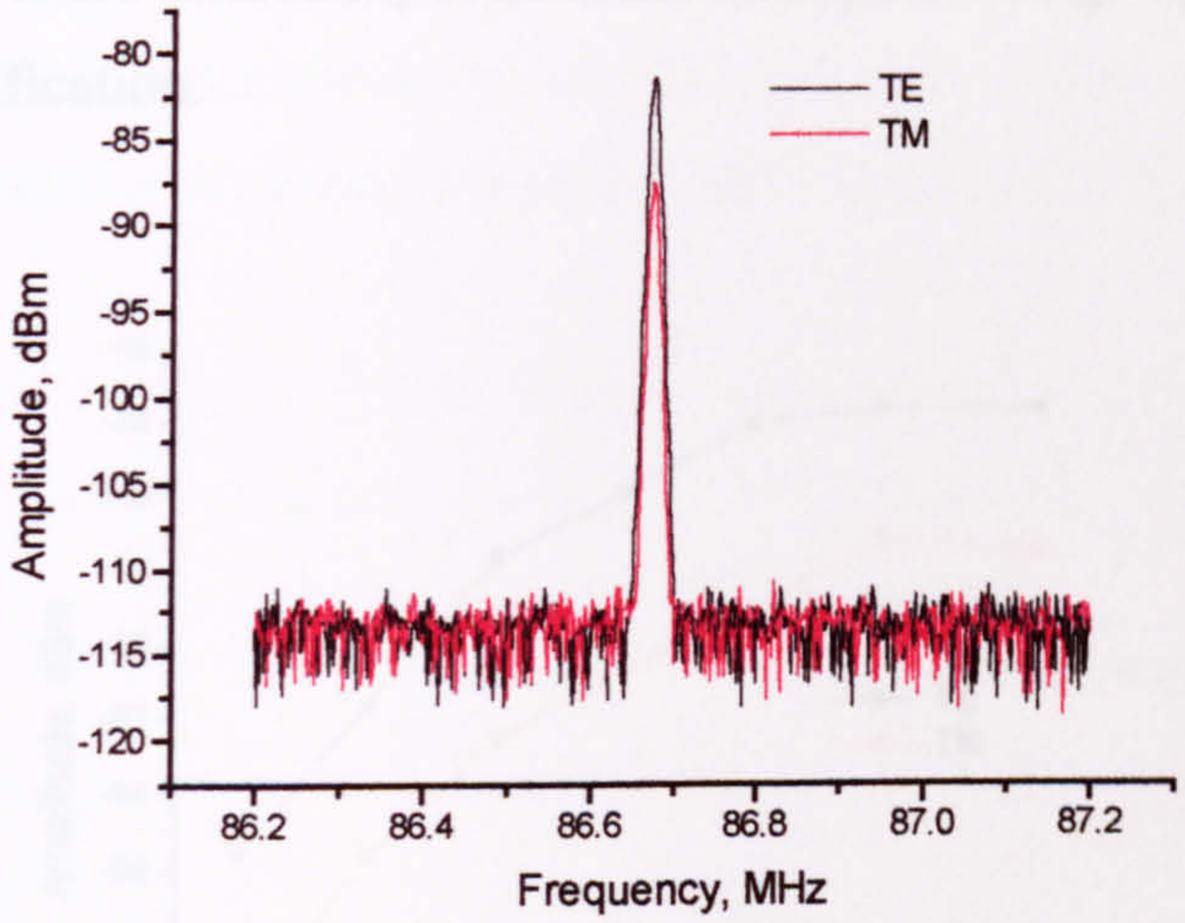

Fig. 5.24. Electrical signal produced by *Dev80*. λ=1570 nm, P_{in} = 35 mW.

The wavelength was swept keeping the power constant and a clear decrease of the signal's amplitude was observed (see Fig. 5.25). This is in agreement with the explanation given above about the TPA tail being reduced at wavelengths around 1580 nm. The trace in Fig. 5.25 is for λ = 1570 nm and P_{in} = 35 mW

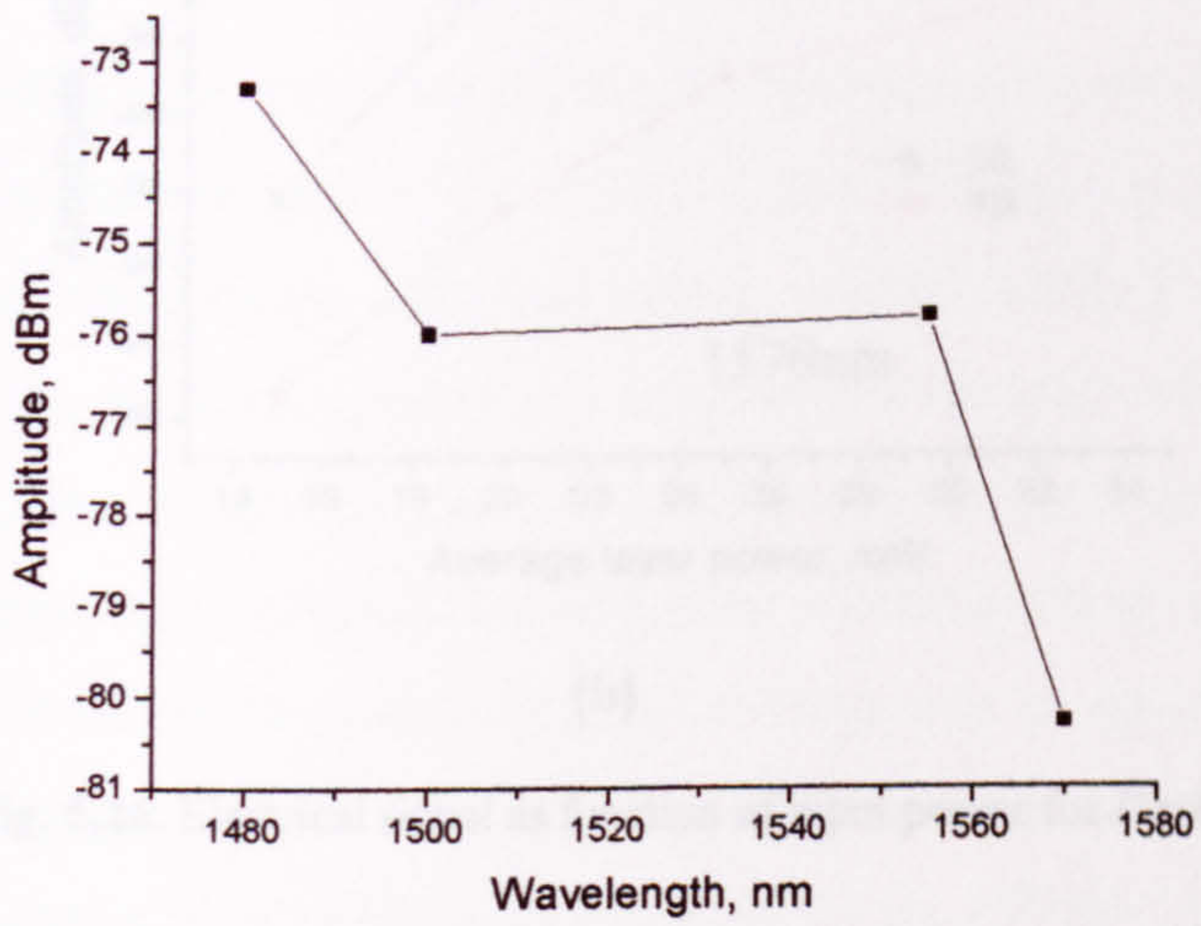

Fig. 5.25. Wavelength dependence of the electrical signal in *Dev 80*.

We also looked at the variation of the electrical signal as a function of input power for two different wavelengths. Fig. 5.26a shows the results for λ = 1555

nm while Fig. 5.26b shows the results for $\lambda = 1570$ nm. The general trend shows that the signal increases with power as well as the ratio between TE and TM. The signal seems to reach saturation, even when we expect it to go up all the way for the case of rectification.

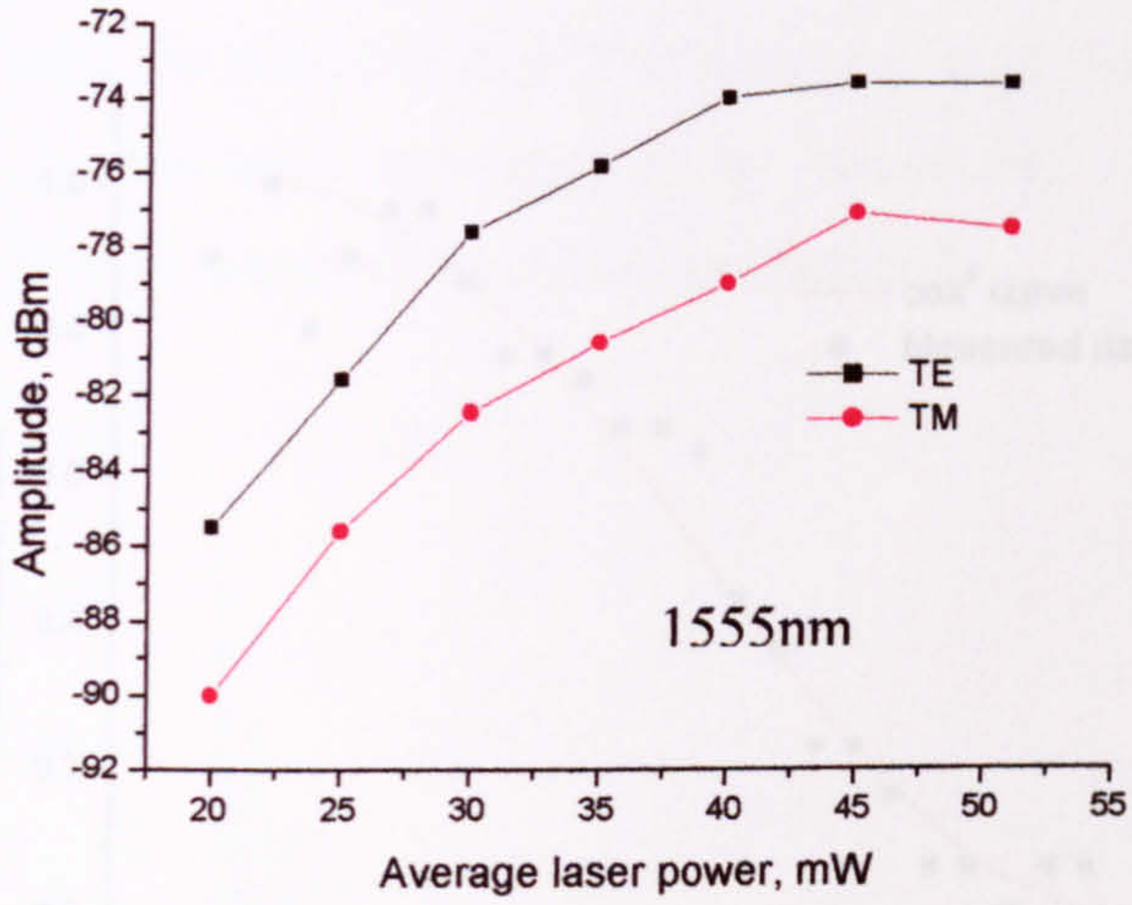

(a)

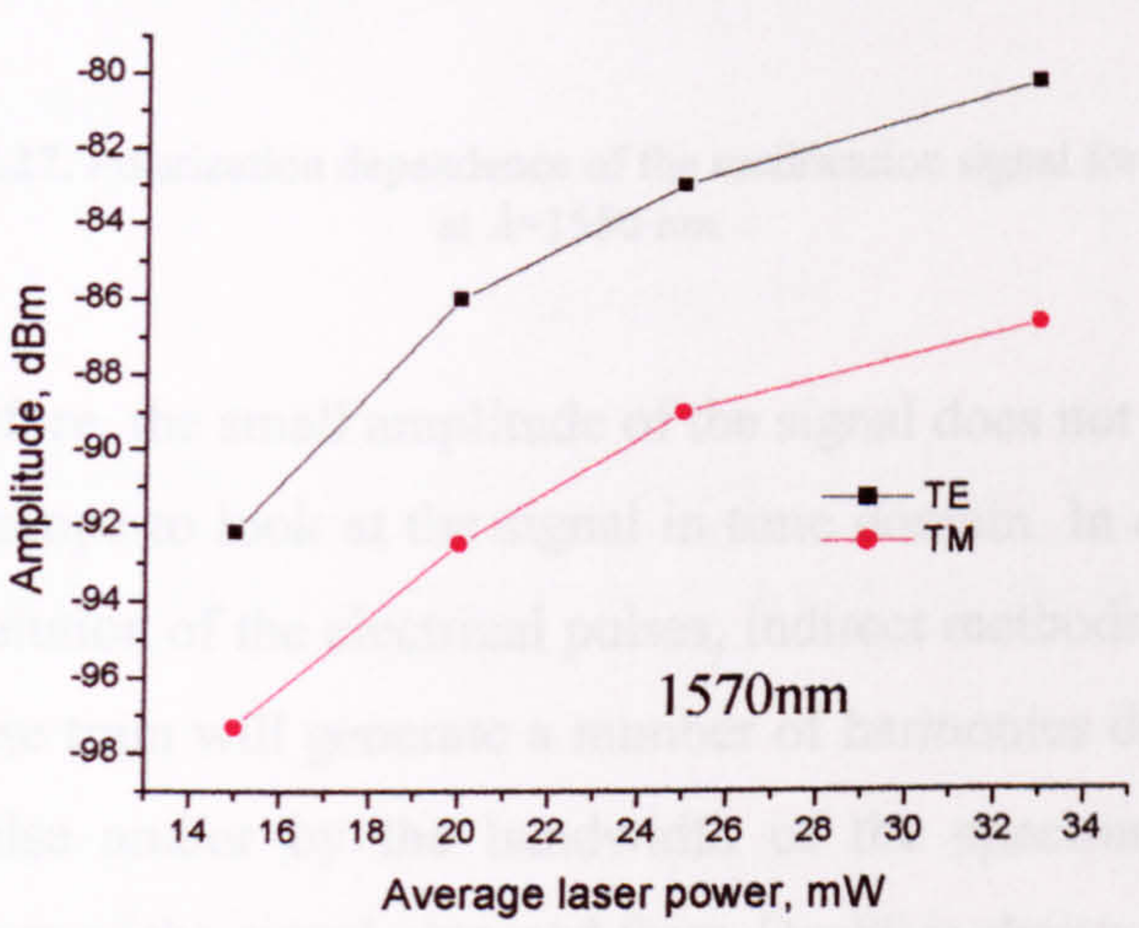

(b)

Fig. 5.26. Electrical signal as function of input power for *Dev80*.

The saturation seen in Fig. 5.26a can be explained by using our assumption of the existence of an offset signal present on the device. The rectification signal, which can be represented by the difference between TE and TM does not saturate it does get bigger with power. What saturates is only the background signal giving the saturation shape to the curve.

The polarization dependence of the ORE signal is shown in Fig. 5.27. The solid squares are the experimental points taken for different input polarization states while the solid red line is a $\cos^2$ curve only plotted to help visualize the trend. The electrical signal has a maximum for TE input polarization and minimum for TM input polarization as expected from an ORE signal. $\lambda = 1550$ nm.

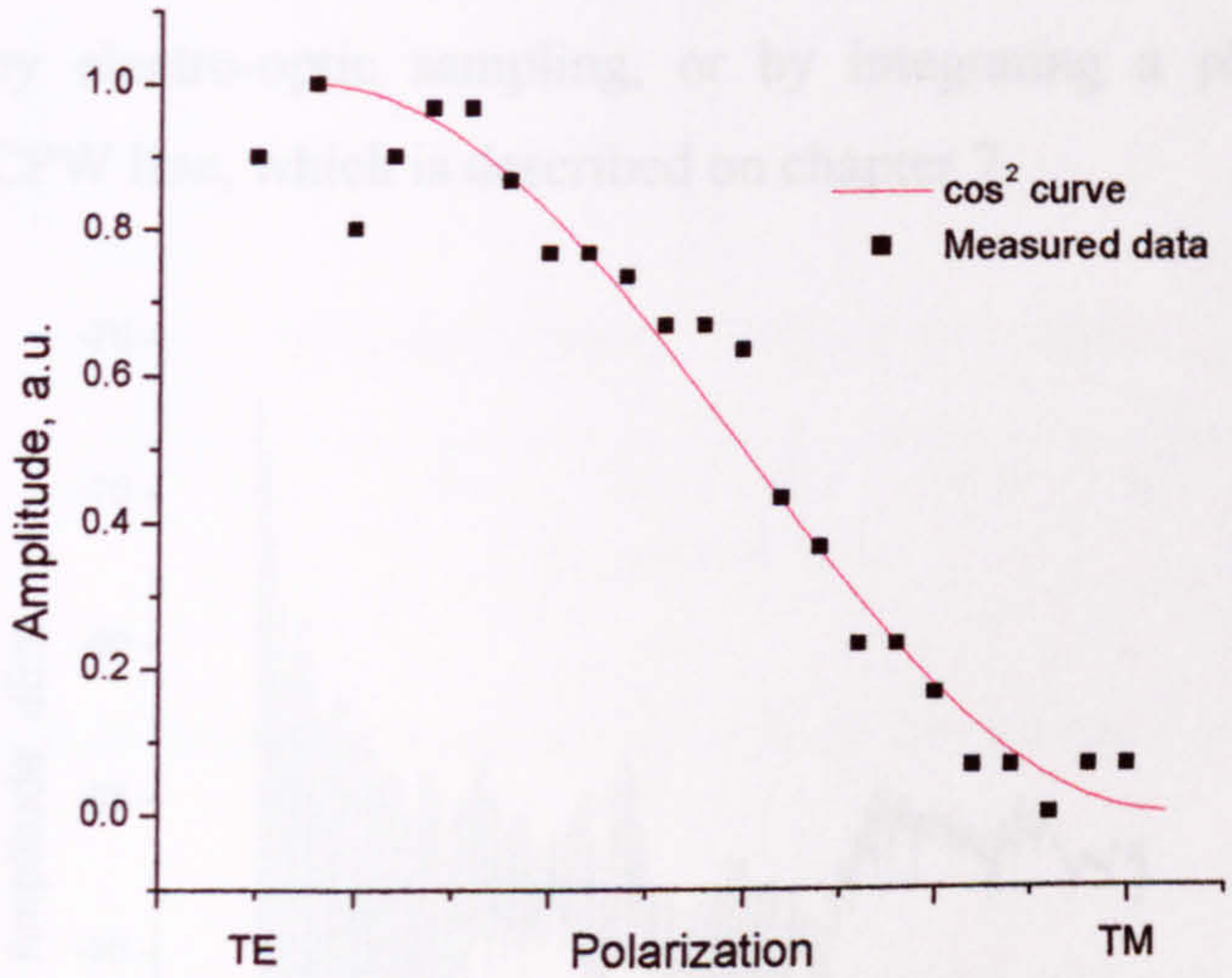

Fig. 5.27. Polarization dependence of the rectification signal for *Dev80* at λ=1550 nm.

As mentioned before, the small amplitude of the signal does not allow us to use a sampling oscilloscope to look at the signal in time domain. In order to estimate the temporal resolution of the electrical pulses, indirect methods have to be used. An electrical pulse train will generate a number of harmonics determined by the width of the pulse and/or by the bandwidth of the spectrum analyser. The frequency spectrum of the signal obtained from *Dev80* is shown in Fig. 5.28. Our first attempt to analyse the pulse in time domain was to apply a fast Fourier transform (FFT) algorithm to the frequency spectrum shown in Fig. 5.28. The spectrum corresponds to a pulse with width of 47 ps, FWHM. Because there is no phase information in the signal obtained from the spectrum analyser, this approximation would be only valid in the case where the measurement system is perfect and all the harmonics are affected equally. In addition, we may be integrating most of the signal's noise, as we do not have a method to eliminate it,

causing a significant error in the transformation. Another method to analyse the pulse in time domain, is using the envelope of the spectra and calculate the 3 dB bandwidth. By doing this, a pulse width of 3.7 ns FWHM is obtained. This is comparable to the signal obtained by TPA. This result is not a contradiction with the proof of optical rectification as we recognised there is a TPA offset in the detected signal. The pulse therefore must have a more complex shape that cannot be reconstructed with the available data. The temporal resolution of the pulse can be obtained by electro-optic sampling, or by integrating a photoconductive switch on the CPW line, which is described on chapter 7.

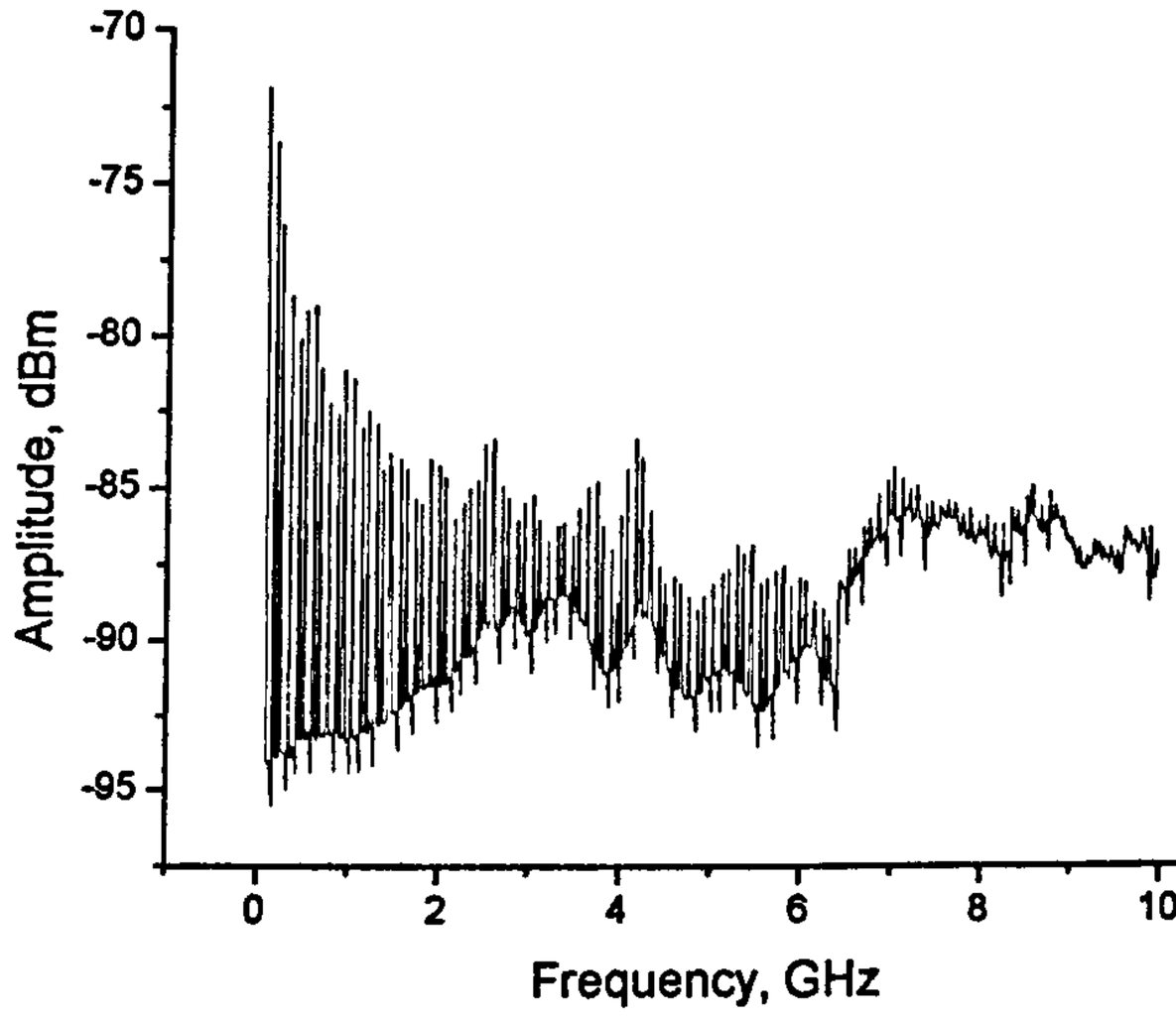

Fig. 5.28. Frequency spectrum of the electrical signal from *Dev80*. The harmonics are spaced 86.7 MHz which corresponds to the repetition rate of the laser. *Inset:* Frequency spectrum converted into the time domain by using FFT.

The set of measurements performed on the ORE4 device points to optical rectification as being the main mechanism producing the signal. A signal detected even at wavelengths where TPA is greatly reduced and the clear polarization dependence of the signal is consistent with the expectations of the optical rectification effect.

Another device characterised under the previous set of experiments was *Dev68*. This device presented strong rectification characteristics even at $\lambda = 1480$ nm. The electrical signal detected by the spectrum analyser at this wavelength with

P_{in} = 45 mW is shown in Fig. 5.29. There is a clear difference between the two polarization states. This difference is larger than the one shown in Fig. 5.24.

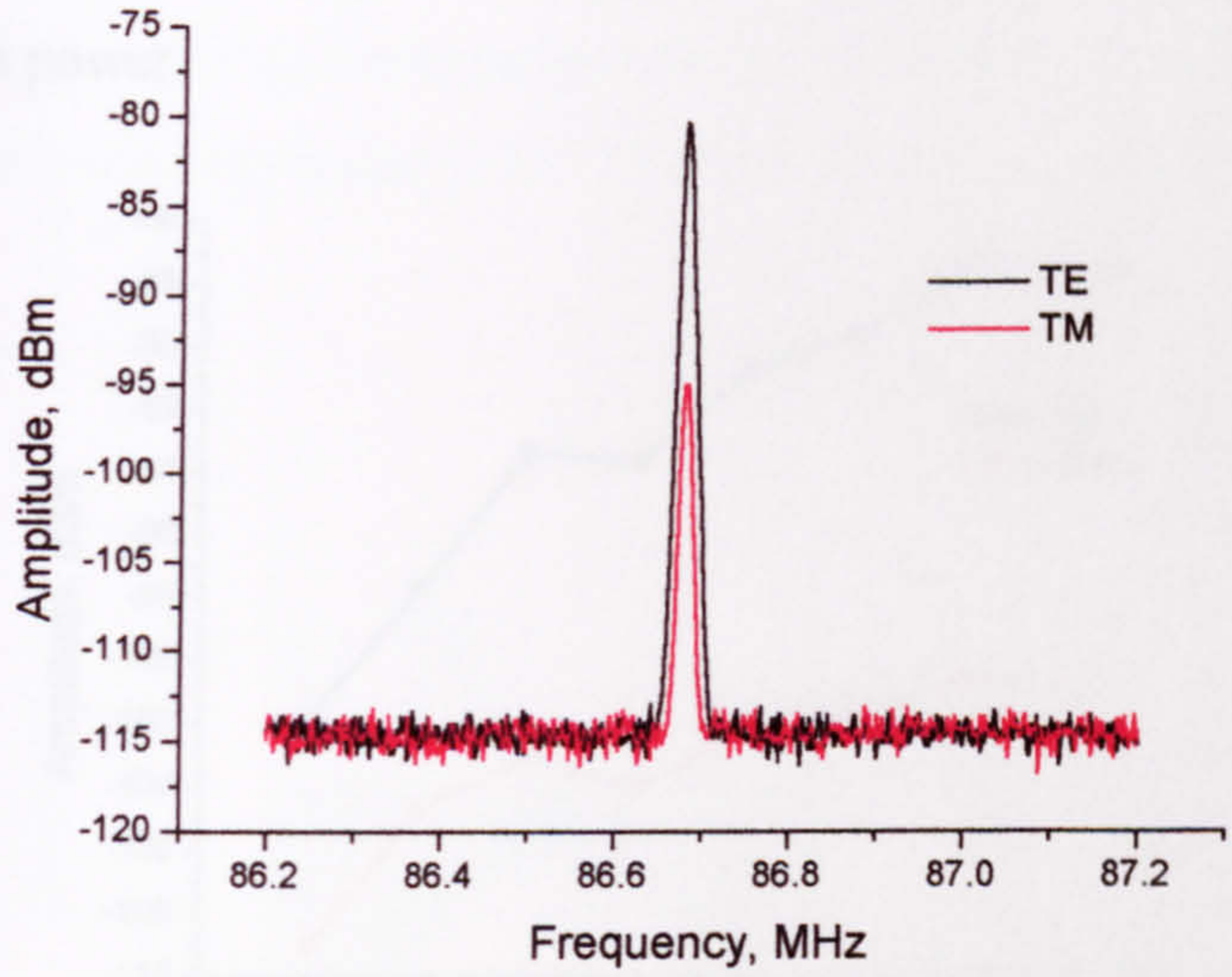

Fig. 5.29. Electrical signal produced by *Dev68*. λ=1480 nm, P_{in} = 45 mW.

A sweep on wavelength was done next. The dependence of the signal for TE and TM polarized light is shown in Fig. 5.30. The TM signal remains almost constant over the whole range, as we would expect while the TE signal decreases with wavelength.

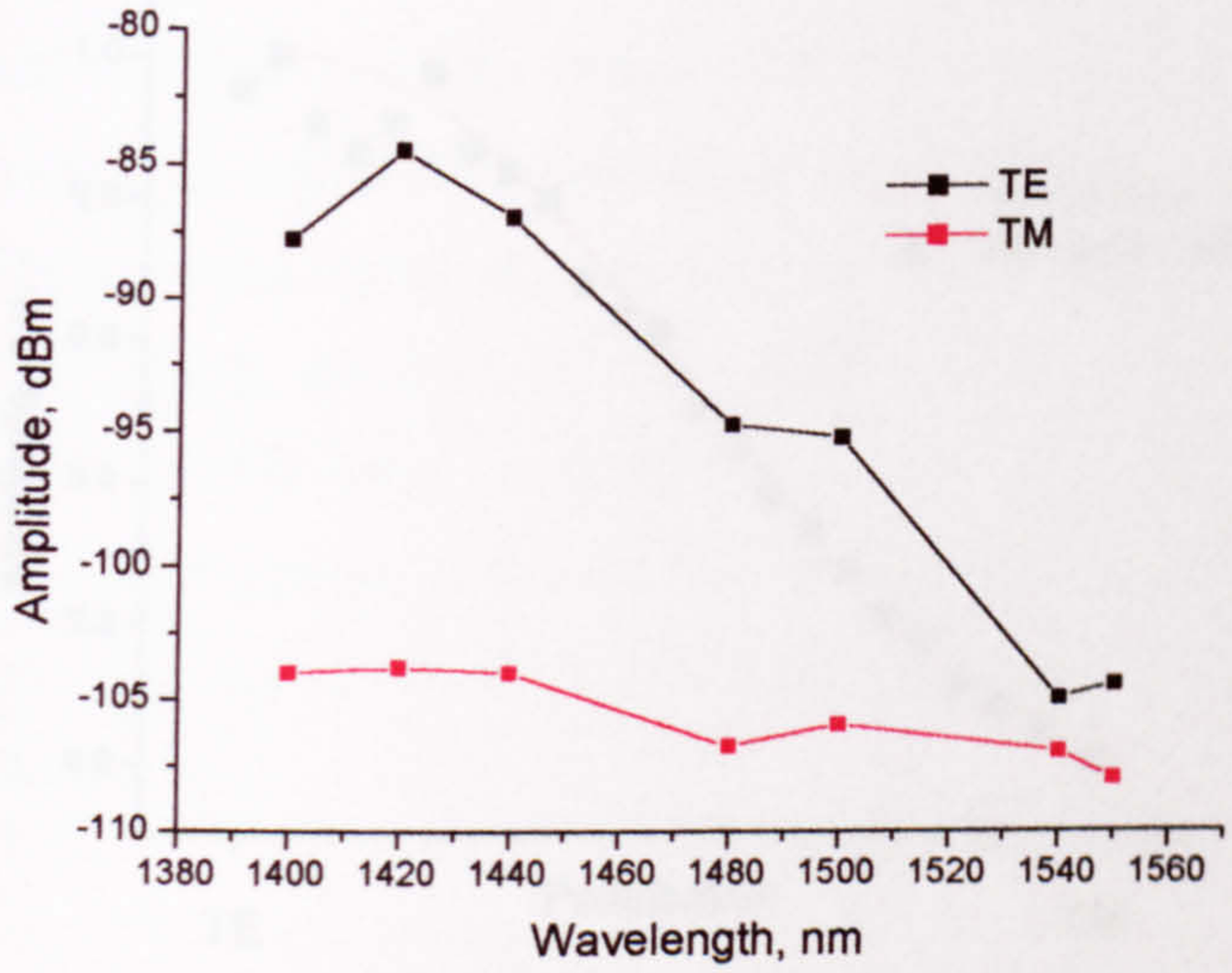

Fig. 5.30. Electrical signal as function of wavelength for *Dev68*.

The behaviour of the signal with power is shown in Fig. 5.31. Again, saturation can be observed but probably not in the same magnitude as for *Dev80*. The important point to notice is that the relative difference between TE and TM increases with power.

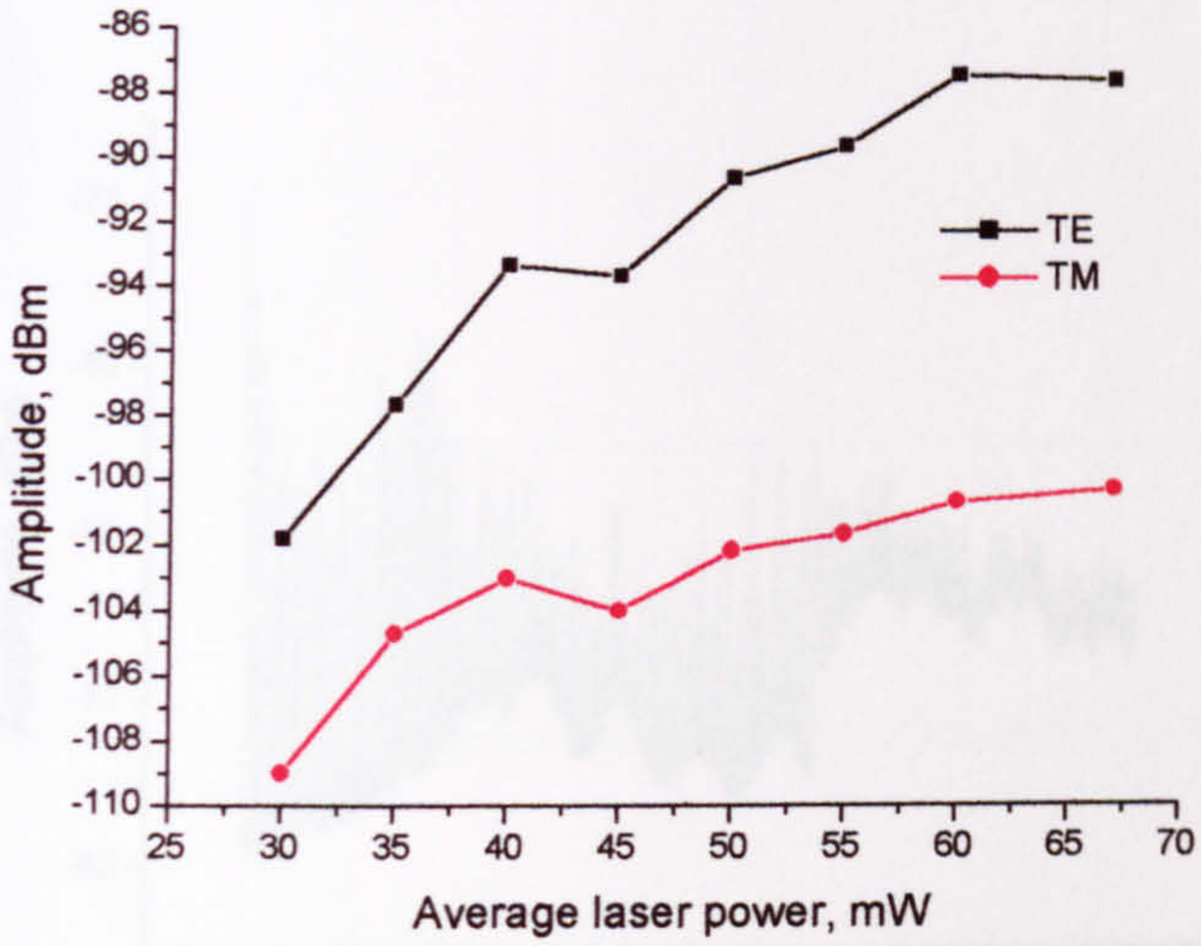

Fig. 5.31. Electrical signal as function of input power for *Dev68*.

Probably the most important measurement is the polarization dependence. This dependence was measured and the results are plotted in Fig. 5.32. Again, the measured data (black squares) followed a clear cos^2 dependence.

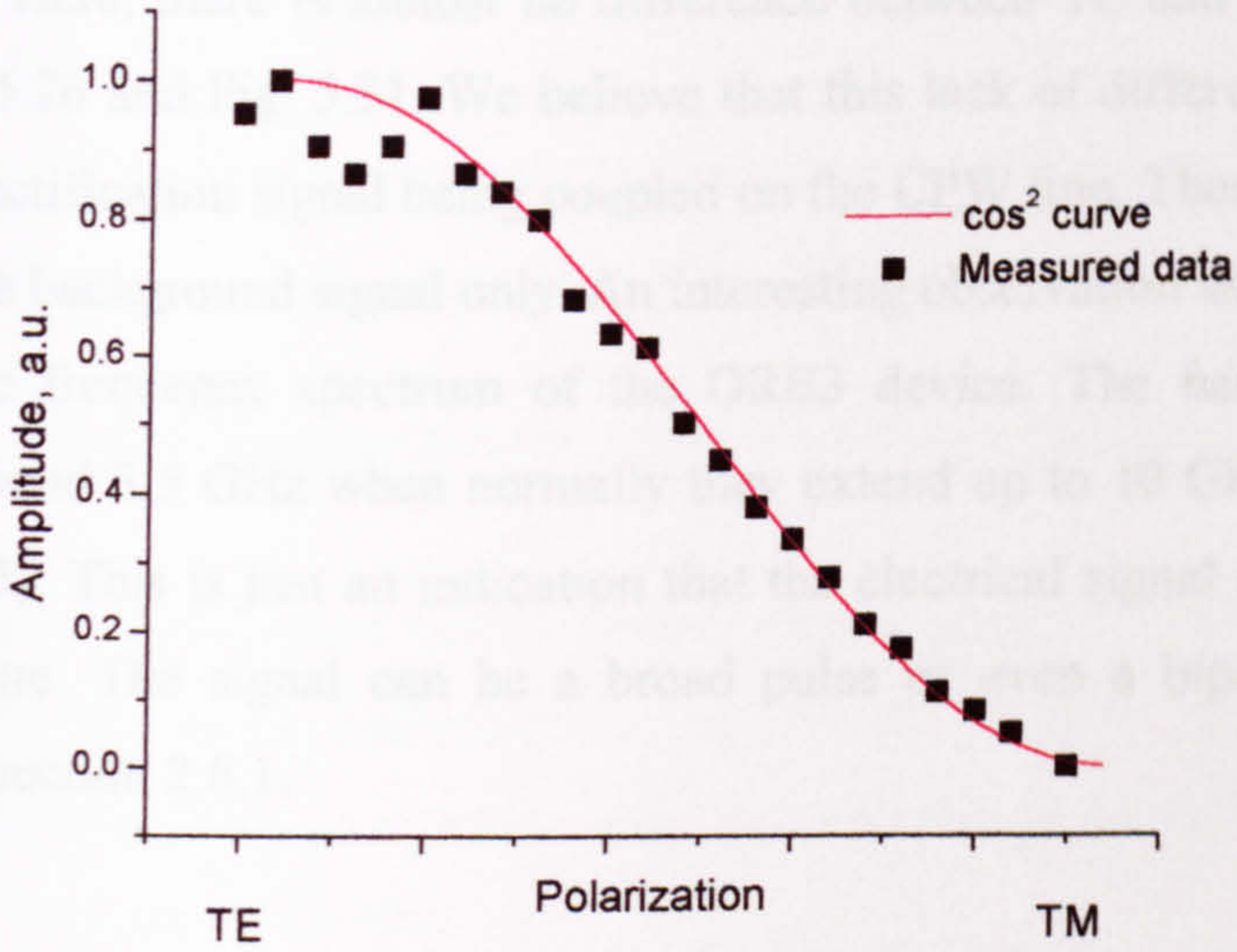

Fig. 5.32. Polarization dependence of the rectification signal for *Dev68* at λ=1480 nm.

The polarization dependence measurement gives confidence of the origin of the electrical signal: optical rectification. Finally, the frequency spectrum was taken for *Dev68* and plotted in Fig. 5.33. It is clear from Fig. 5.33 is that our frequency spectrum is very broad and consistent with an ultrashort electrical pulse being detected. Dev68 was also tested at $\lambda = 1570$ nm with the same qualitative results.

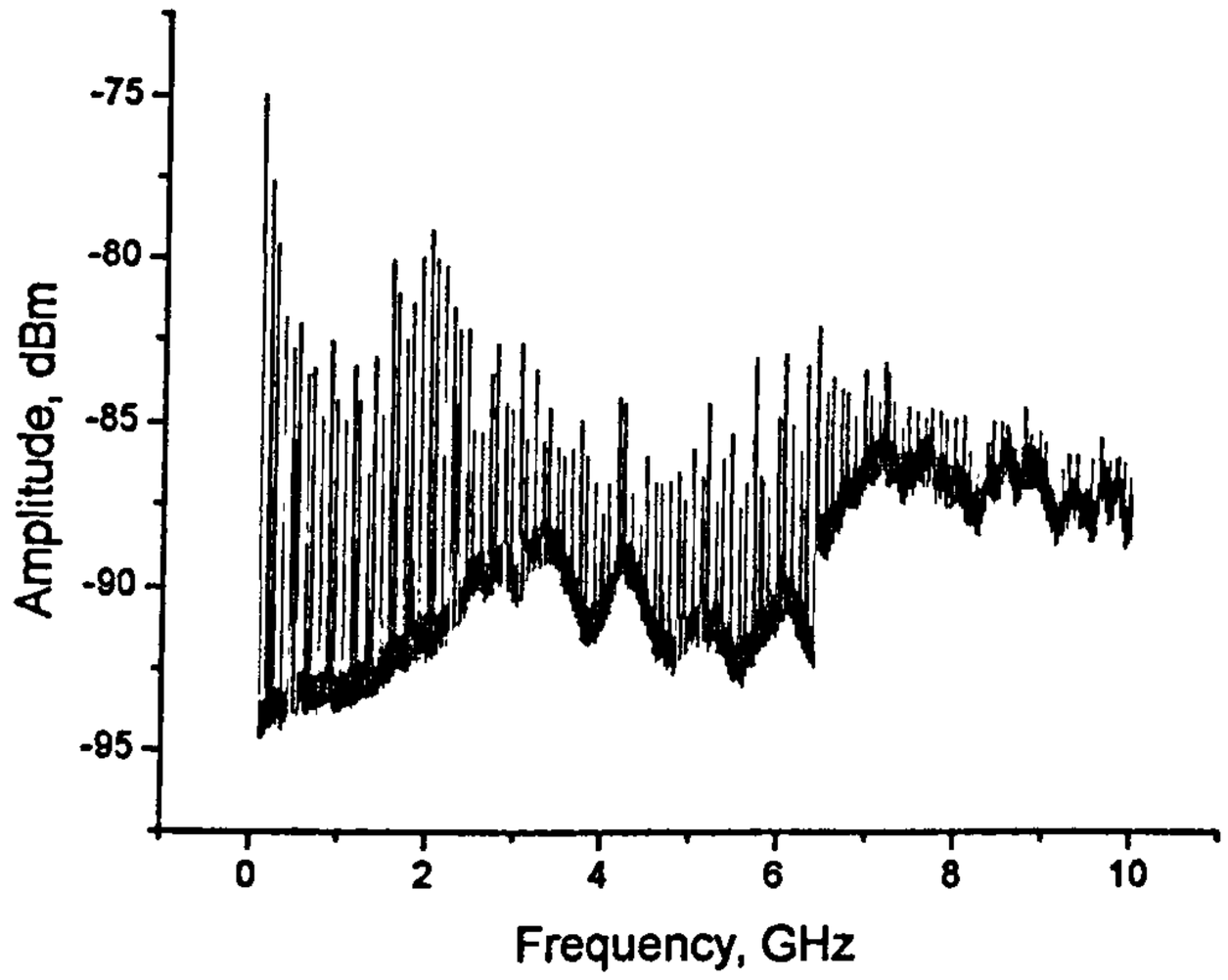

Fig. 5.33. Frequency spectrum of the electrical signal from *Dev68*.

Just as a comparison, an ORE3 device was measured at this point. The behaviour of the electrical signal as a function of the input power at $\lambda = 1570$ nm is shown in Fig. 5.34. Here, there is almost no difference between TE and TM as is the case in Fig. 5.26 and Fig. 5.31. We believe that this lack of difference is due to the lack of rectification signal being coupled on the CPW line. Therefore, we are looking at the background signal only. An interesting observation was done when recording the frequency spectrum of the ORE3 device. The harmonics only extend to around 3.5 GHz when normally they extend up to 10 GHz and above (see Fig. 5.35). This is just an indication that the electrical signal is not a short pulse this time. The signal can be a broad pulse or even a bipolar pulse as explained in section 2.6.1.

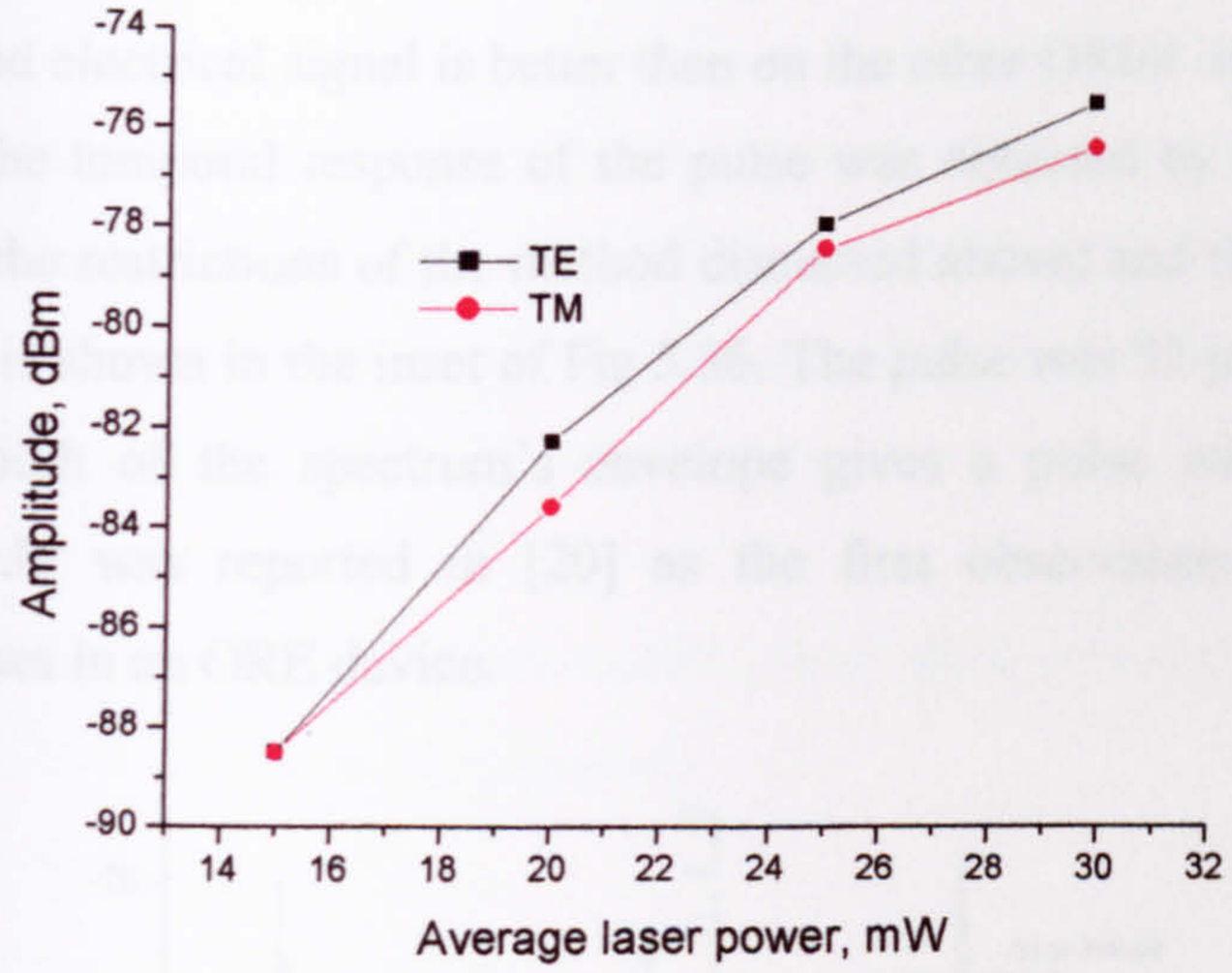

Fig. 5.34. Electrical signal as function of input power for *Dev00*.

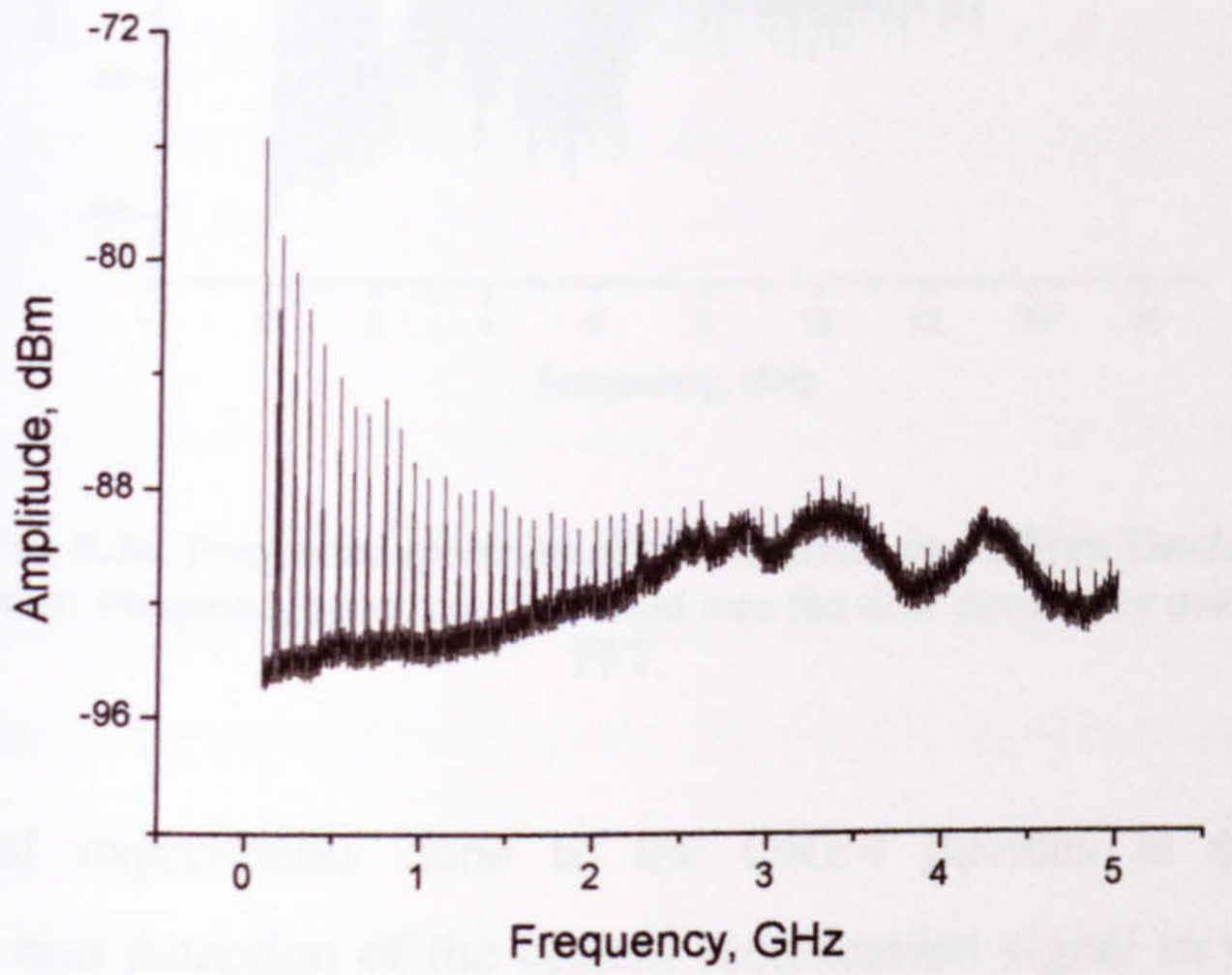

Fig. 5.35. Frequency spectrum of the electrical signal from *Dev00*.

Following these results, more ORE4 devices were measured. *Dev44* and *Dev56* present almost the same characteristics as *Dev80*. There is not an obvious difference between them. In any case this devices have to be looked at greater detail as was the case for *Dev80*.

Dev32 however, did present an interesting frequency spectrum. It was the only device to generate clear harmonic signals up to 16 GHz. This spectrum is shown

in Fig. 5.36. A reason of why this is occurring is that the velocity-match between the optical and electrical signal is better than on the other ORE4 devices. Just for illustration, the temporal response of the pulse was obtained by the use of the FFT (see all the restrictions of the method discussed above) and the pulse in the time domain is shown in the inset of Fig 5.36. The pulse was 32 ps FWHM. The 3 dB bandwidth of the spectrum's envelope gives a pulse width of 4.9 ns FWHM. *Dev32* was reported in [20] as the first observation of ultrashort electrical pulses in an ORE device.

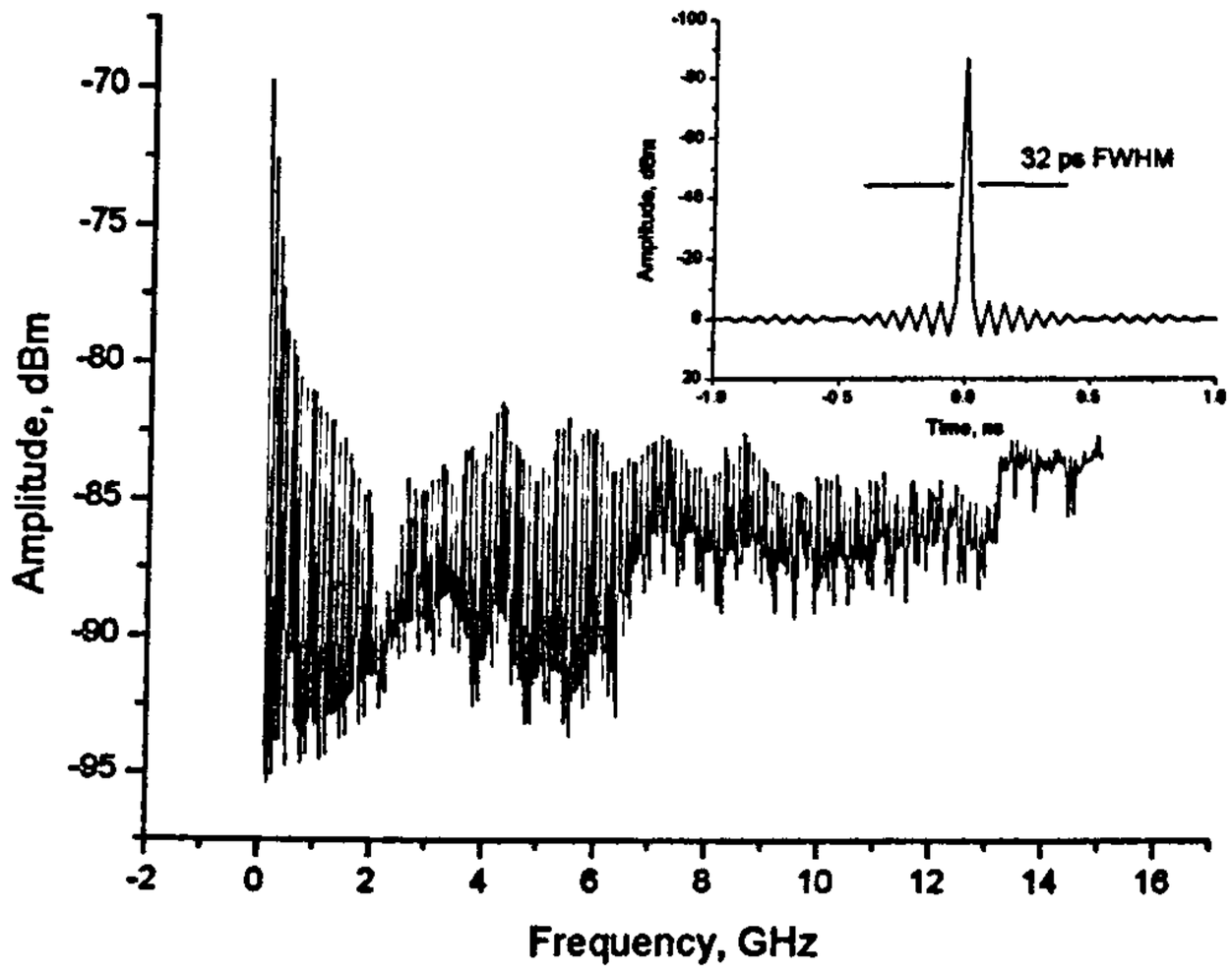

Fig. 5.36. Frequency spectrum of the electrical signal from *Dev32*.
Inset: Frequency spectrum converted into the time domain by using FFT.

From the final experiments done to the ORE4 devices is clear that the discrimination and detection of the optical rectification signal in waveguides is not a trivial matter. We have identified *Dev32* as the device with most potential for rectification given the fact that is the one that generates a larger number of harmonics. We believe that the velocity-match between the optical and electrical structure in the ORE4 devices is still not ideal and therefore a much efficient device can still be created. The very short dimensions of the electrodes and the gaps between them add complexity to the modelling of the transmission line which is not include in commercial software. The thickness of the electrodes has to be increased to reduce losses. Just by addressing these two points, the efficiency of the ORE devices can be considerably increased.

5.5 Conclusions.

This chapter described the experimental approach taken to develop an ORE device. The design made use of four different generations each contributing with information and knowledge towards the optimum ORE device. Such information can be summarised in the following bullet points:

- ORE1. Effect of doped layers, band-to-band absorption and TPA.
- ORE2. TPA and pulsed experiments.
- ORE3. Reduction of TPA.
- ORE4. Optical rectification.

Although ORE4 devices gave an electrical signal that is in agreement with optical rectification, there is still more work that can be done in the future to improve the detection capability of the device. The proposed future work is summarised in chapter 7.

The ORE4 devices proved the following three points: 1) we have electrical pulses coming out of the device, 2) we have very clear polarization dependence of the signal and, 3) the width of the electrical pulses cannot be confirmed until photoconductive sampling or electro-optic sampling is used on the ORE device.

We identified *Dev32* as the best device of the batch followed in second place by *Dev68* and finally *Dev80* in third place. The efficiency of the ORE devices can be improved by a doing a more accurate design of the device.

The power of the input optical signal could be increased to increase the amplitude of the electrical signal, but we believe that this will not do any qualitative difference in the results but will generate more lateral effects that will mask again the rectification signal i.e. MPA.

5.6 References

1. S. Graf, H Sigg and W. Bächtold, "High-frequency electrical pulse generation using optical rectification in bulk GaAs," *Appl. Phys. Lett.* vol. 76, pp. 2647-2649, 2000.

2. A. Nahata and T. F. Heinz, "Generation of subpicosecond electrical pulses by optical rectification," *Optics Letters*, vol. 23, pp. 867-869, 1998.

3. B. N. Morozov and Y. M. Aivazyan, "Optical rectification effect and its applications (review)," *Sov. J. Quantum Electron.* vol. 10, pp. 1-16, Jan 1980.

4 B. N. Morozov, "Salient Features of Recording the Optical Rectification Signal from Nonlinear Optical Crystals," *Measurement Techniques.* vol. 40, No. 5, pp. 413-421, 1997.

5. D. J. Robins, "Piezoelectric properties of GaAs, " *in Properties of Gallium Arsenide, Third Ed.* pp. 223-224, 1996.

6. M.Cada, "Optical Harmonic Mixers," *IEEE J. Quantum Electron.* vol. 31, pp. 269-277, 1995.

7. D. H. Auston, "Picosecond optoelectronic switching and gating in Silicon," *Appl. Phys. Lett.* vol 26, pp. 101-103, 1975.

8. T. Pfeifer, H. -M. Heiliger, T. Löffler, C. Ohlhoff, C. Meyer, G. Lüpke, H. G. Roskos and H. Kurz, "Optoelectronic On-Chip Characterization of Ultrafast Electric Devices: Measurement Techniques and Applications," *IEEE J. Sel. Topics in Quantum Electron.* vol. 2, pp. 586-603, 1996.

9. D. D. Nolte, "Table of GaAs optical fuctions at 300 K, "*in Properties of Gallium Arsenide, Third Ed.* pp. 207-213, 1996.

10. J. S. Blakemore, "Semiconducting and other major properties of gallium arsenide," *J. Appl. Phys.* vol.53, pp. R123-R181, 1982.

11. M. M. Karkhanehchi, J. H. Marsh and D. C. Hutchings, "Polarization dependence of two-photon absorption in an AlGaAs waveguide autocorrelator," *Applied Optics*, vol. 36, pp. 7799-7801, 1997.

12. J. S. Aitchison, D. C. Hutchings, J. U. Kang, G. I. Stegeman and A. Villeneuve, "The Nonlinear Optical Properties of AlGaAs at the Half Band Gap," *IEEE J. Quantum Electron.* vol. 33, pp. 341-348, 1997.

13. S. M. Sze, *Physics of Semiconductor Devices, 2nd ed.* John Wiley & Sons, 1981, p. 639.

14. S. Adachi, "GaAs,AlAs,and $Al_xGa_{1-x}As$: Material parameters for use in research and device applications," *J. Appl. Phys.* vol 58, pp. R1-R29, 1985.

15. R. C. Alferness, "Waveguide Electrooptic Modulators," *IEEE Trans. on Microwave Theory and Techniques*, vol. MTT-30, pp. 1121-1137, 1982.

16. S. Y. Wang, S. H. Lin and Y. M. Houng, "GaAs travelling-wave polarization electro-optic waveguide modulator with bandwidth in excess of 20 GHz at 1.3 μm," *Appl. Phys. Lett.*, vol. 51, pp. 83-85, 1987.

17. U. Peschel, K. Bubke, D. C. Hutchings, J. S. Aitchison, and J. M. Arnold, "Optical rectification in a travelling-wave geometry," *Phys Rev A*, vol. 60, pp. 4918-4926, 1999.

18. F. Rahmatian, N. A. F. Jaeger, R. James and E. Berolo, "An Ultrahigh-Speed AlGaAs-GaAs Polarization Converter Using Slow-Wave Coplanar Electrodes," *Photonics Technology Letters*, vol. 10, pp. 675-677, 1998.

19. K. Bubke, personal communication.

20. V. Loyo-Maldonado, H. K. Lee, C. R. Stanley, S. Venugopal-Rao, K. Moutzouris, M. Ebrahimzadeh and J. S. Aitchison, " Generation of Ultrashort Electrical Pulses in Semiconductor Waveguides," *IEEE Photonics Technology Letters*, vol. 15, pp. 428-430, 2003.

6. AlGaInAs Semiconductor Q-switched Lasers.

6.1 Introduction.

Ultrafast devices such as the ORE devices described in this thesis, can find application in telecommunication systems. However, unless they can be operated with a semiconductor laser, they cannot be considered as a real option. The exploration of a potential semiconductor source to be used in combination with an ORE device was therefore, an important part of this thesis. Optical rectification being a nonlinear effect requires of a certain level of power to operate. The three most common techniques utilised to generate pulses in semiconductor lasers are: mode-locking, q-switching and gain switching. The high repetition rate associated with mode-locking reduces the pulse power of the laser. The pulses produced by gain switching are a consequence of the gain being turned on and off and therefore the pumping energy is present only a fraction of the repetition rate. Q-switching uses the aid of saturable absorption to compress the energy in a giant pulse that last a fraction of the repetition rate. The pulse power in a Q-switched laser is considerable higher than the one produced by gain switching under similar average power.

The current most common material systems used in the fabrication of long wavelength semiconductor lasers are InGaAsP (P-quaternary) and AlGaInAs (Al-quaternary). Recently, the search for improved performance and thermal stability of long wavelength semiconductor lasers (operating around 1.5 μm) has led to the increasing interest in the InGaAs/AlGaInAs quantum well material system as an alternative to InGaAsP. Al-quaternary systems and P-quaternary systems have many similar properties such as the range of bandgaps (i.e. emitting wavelengths), carrier mobility and refractive index. However, an important difference exists between them: Al-quaternary material has a larger conduction band offset ($\Delta E_c/\Delta E_g$) [1]. Due to the larger conduction band offsets in the InGaAs/AlGaInAs system ($\Delta E_c/\Delta E_g$ = 0.7) compared to InGaAsP ($\Delta E_c/\Delta E_g$ = 0.4), electron confinement in the quantum well can remain strong with increasing temperature, allowing lasers to be operated without cooling (see Fig. 6.1). This higher confinement can also help to reduce leakage current densities. As a direct consequence of the larger offset in the conduction band, the valence band offset gets shorter. This will reflect in faster hole escape times and a speed-up in the absorption recovery. Some recent publications, [2], [3] and [4], have shown that in applications where high temperature operation is especially important, Al-quaternary lasers are expected to perform better than those fabricated in P-quaternary systems. Al-quaternary is therefore the system of choice for our Q-switched lasers.

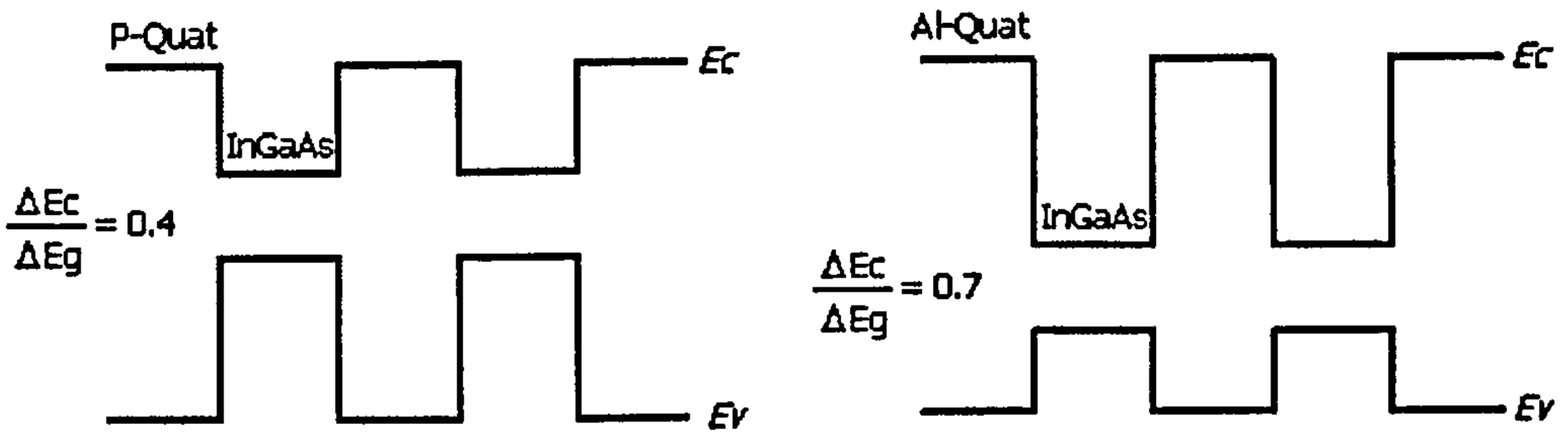

Fig. 6.1. conduction band offsets for (a) P-quaternary material and (b) Al-quaternary material.

Q-switched lasers find their applications in communication and sensing systems where a short pulse source with a controllable repetition rate is required. The

width of the pulse from a Q-switched laser is typically in the order of 10 ps to 100 ps, depending on the length of the cavity. Q-switched semiconductor lasers are always multi-section diodes and they must have at least one absorber section (introducing saturable loss into the cavity) and one gain section. In multiple quantum well (MQW) material, a reverse bias section can be used as a saturable absorber which can then either passively Q-switch, or mode-lock the laser depending on the relative length of the gain and absorber section. In this chapter, we report the first demonstration to our knowledge; of passive Q-switching in a MQW two-section InGaAs/AlGaInAs laser diode emitting at 1.582 μm [5].

6.2 Q-switching.

It is not the aim of this thesis to give a detail review on the physics behind the Q-switching of semiconductor lasers. However, an introductory explanation is given in this section. For further reference, please refer to [6] and [7].

Q-switching of diode lasers by rapidly switching the intracavity loss is a simple technique for producing optical pulses with high repetition rates and high peak powers. It involves deliberately introducing a time-dependent loss into the cavity. With high loss present, the gain due to the population inversion can reach large levels without laser action occurring. The high loss prevents laser action while energy is being pumped into the exited state of the medium. If, when a large population inversion is achieved, the cavity loss is suddenly reduced, laser oscillations can then begin. However, the threshold gain is now much less than the actual gain ensuring a very rapid build-up of laser oscillation. All the available energy in fact is emitted in a single, large pulse. This quickly depopulates the upper lasing level to such and extent that the gain is reduced below threshold and lasing action stops.

The variations in the optical loss that is necessary for Q-switching can be produced through passive means using a saturable absorber, or through active means when the loss is directly modulated by an external optical or electrical element. An advantage of diode lasers is that the gain section and the saturable

absorber are fabricated monolithically and have exactly the same material composition.

The typical configuration used for Q-switching semiconductor lasers consists of two-sections, where the long section is forward biased to produce gain in the device and the short section is reverse biased to suppress lasing in the structure. The long section forms the gain section whilst the short section forms the saturable absorber. An schematic of the laser if shown in Fig. 6.2.

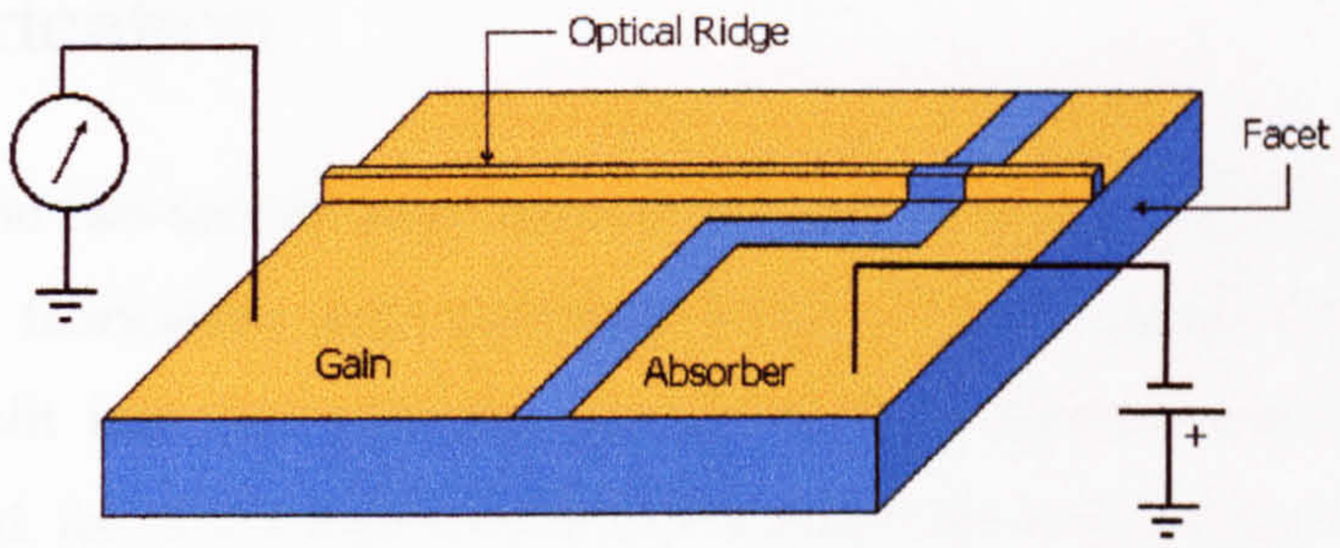

Fig. 6.2. Schematic of a two-section laser. The p-contact is splitted into 2 sections, the gain which is forward bias and the absorber which is reverse bias. The gain is also the longer section.

6.3 Material System.

The material used to fabricate the devices consists of six pairs of 7 nm InGaAs wells sandwiched by 8 nm $Al_{0.2}Ga_{0.27}In_{0.53}As$ barriers. The p-doped upper cladding consists of a 1.5 μm layer of AlInAs with a p^+ contact layer of 200 nm InGaAs on top. The n-doped lower cladding consists of a 500 nm layer of AlInAs grown on top of a 600 nm layer of InP (buffer). The whole structure has been grown lattice matched ($x+y = 0.47$) to an InP substrate. Table 6.1 summarises the layer structure.

The electron confinement energy in the well for this structure is expected to be around 225 meV, derived from the models presented in [2] and [8].

Table 6.1. Layer structure of the wafer used to fabricate the lasers.

Repeats	Thickness (Å)	Material	Dopant	Type	Conc (cm^{-3})
1	2000	InGaAs	Zn	P	$5.0x10^{18}$
1	15000	AlInAs	Zn	P	$5.0x10^{17}$
1	1220	$Al_{0.2}Ga_{0.27}In_{0.53}As$		I	
6	80	$Al_{0.2}Ga_{0.27}In_{0.53}As$		I	
6	70	InGaAs		I	
1	1300	$Al_{0.2}Ga_{0.27}In_{0.53}As$		I	
1	5000	AlInAs	Si	N	$5.0x10^{17}$
1	6000	InP buffer	Si	N	$2.0x10^{18}$
	31420	= total thickness		18 layers	

6.4 Fabrication

A photo of the two-section laser fabricated is shown in Fig. 6.3 and will help to illustrate the fabrication steps described below. In a two-section laser, the p-contact is split into two sections, one of which is forward biased, the other reverse biased, forming a gain section and saturable absorber both monolithically integrated in a single laser chip. The device dimensions were 450 μm long gain section with a 50μm long absorber. There is also a 10 μm separation between the two sections. The isolation resistance between the absorber and the gain section was typically > 1 kΩ. Two SEM pictures of the lasers are shown in Fig 6.3.

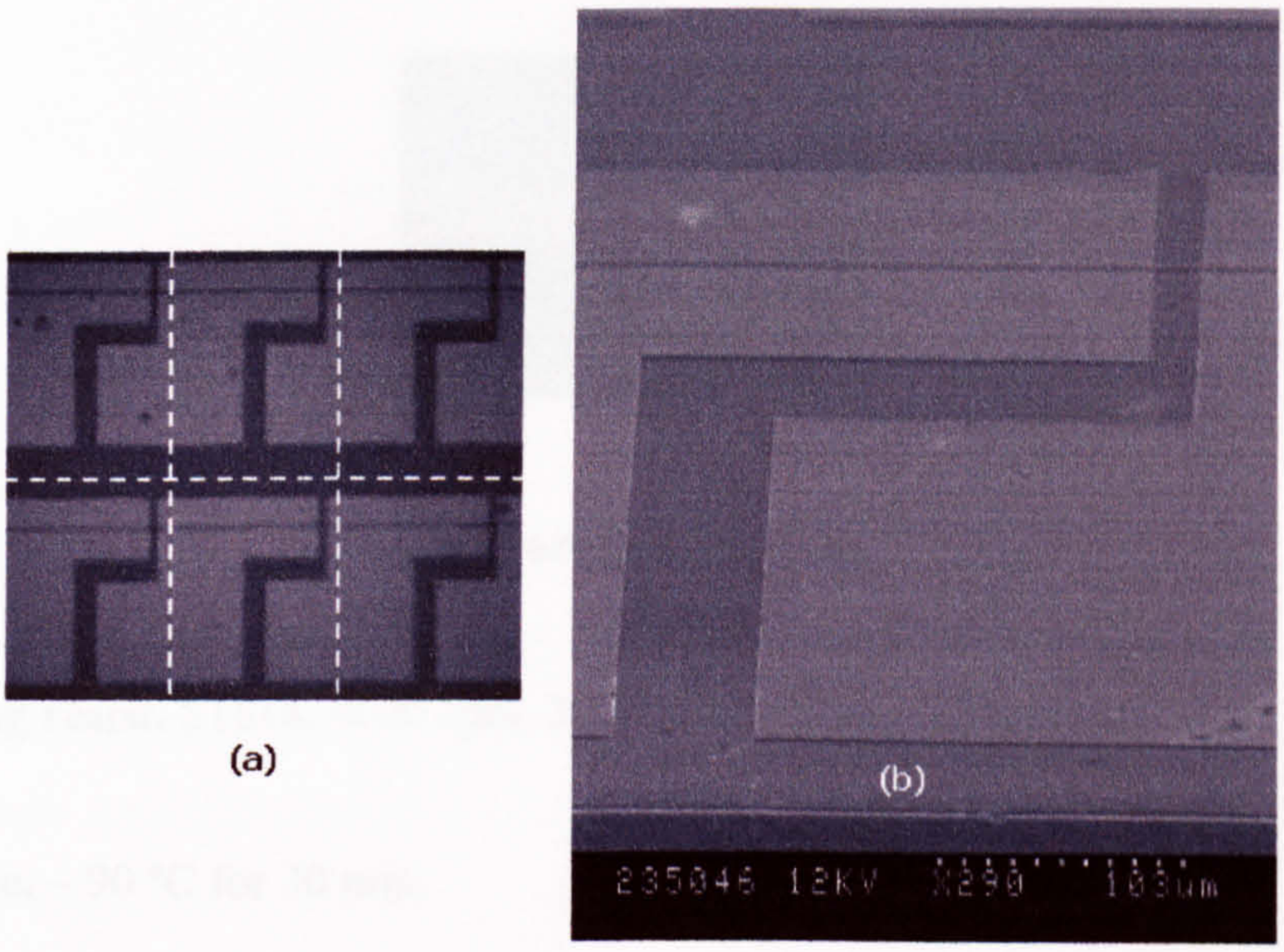

Fig 6.3. SEM photos of the lasers. (a) lasers before cleaving. The white dotted lines shows where the sample will be cleaved. (b) close-up of the laser. The gap between electrodes at the ridge level is 10μm.

A cross section of the material used for fabrication showing the relevant epi-layers is shown in Fig. 6.4.

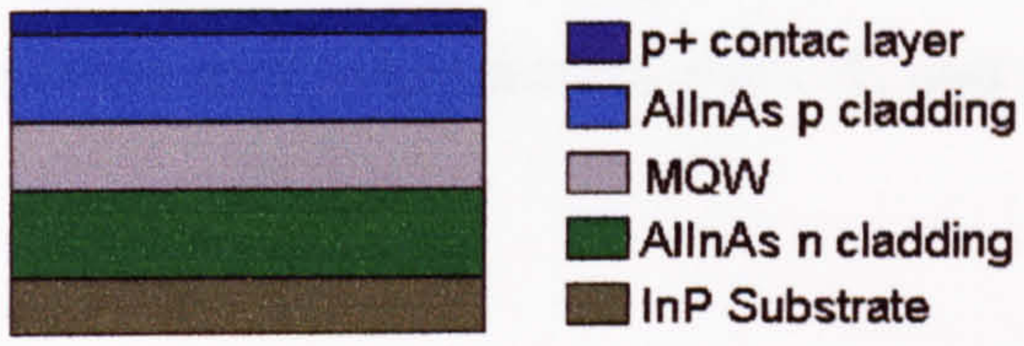

Fig. 6.4. Schematic cross section of the epi-layers of the Al-quaternary material.

As we did in chapter 4, the fabrication steps will be described on detail at every stage of the process. All the process which are common with those described in chapter 4 will not be described again. Please refer to that chapter for details.

Cleaning. Opticlear, acetone and methanol.

Silica (SiO_2) deposition. 200 nm PECVD SiO_2. SiO_2 will be used as etching mask for the ridge. For the ORE devices (see chapter 4), we use the resist as the etching mask because the etch depth was only 0.8 μm. For the lasers, the etch depth will be 1.6 μm and the resist will not stand the etch process.

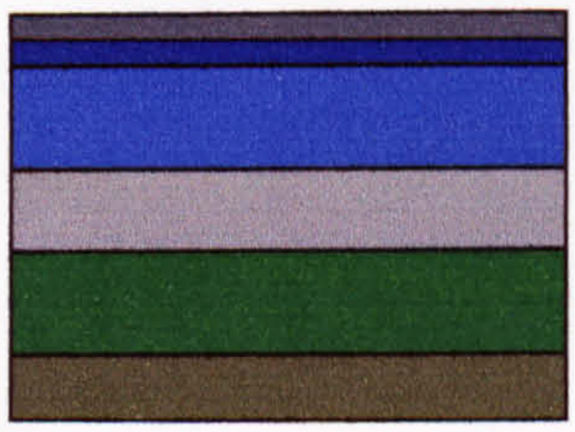

Fig. 6.5. SiO_2 deposition.

Spinning resist. S1818, 4000 rpm, 30 sec.

Softbake. ~ 90 ºC for 30 min.

Exposure. Ridge mask, 11 sec.

Development. 1:1 mixture, 75 sec.

Dry etching of SiO_2 ridges. The dry etching of the SiO_2 was done on a BP80 machine. The gas mixture used in the process was C_2F_6 and the etch time was 5 min.

Strip resist. Acetone.

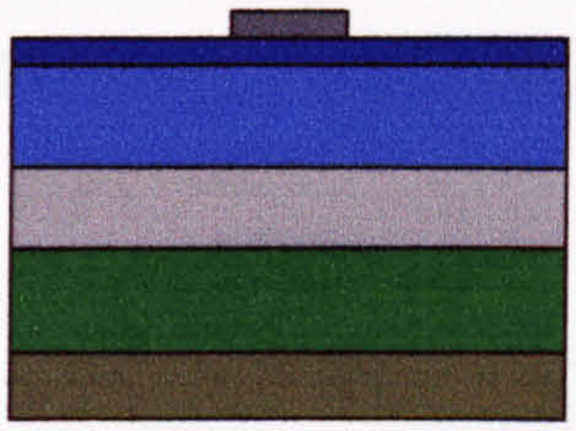

Fig. 6.6. Sample after SiO_2 etching and strip resist.

Etching. The dry etching was done on a ET340 machine which again is a chemical assisted etching. The Q-switched laser devices were based on a ridge waveguide structure, which was etched using a CH_4/H_2 process to a depth of 1.6 μm. Before each run, the chamber was purge of O_2 for 10 min. The process parameters used on the ET340 machine are summarised in table 6.2.

Table 6.2. ET340 process recipe.

Parameter	Gas mixture	Amount	Units
Gas flow	CH_4/H_2	50/100	%
Gas flow	CH_4/H_2	10/100	sccm
Etch pressure	--	50	mtorr
Forward RF power	--	50	W

Strip SiO_2 mask. 4:1 buffered HF was used to remove the SiO_2 mask. The sample was immerse in HF for ~12 sec and then rinse thoroughly with RO water. The sample was then blow-dry using a N_2 gun.

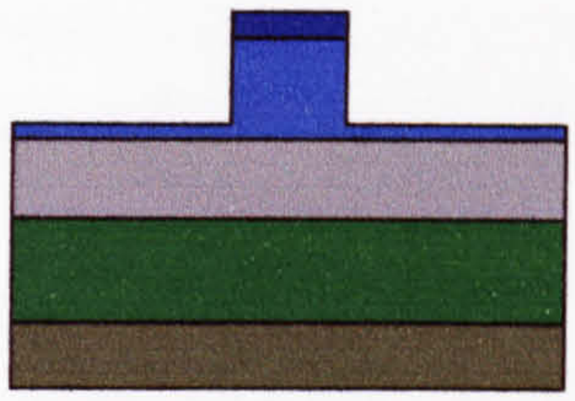

Fig. 6.7. Sample after dry etching and strip resist.

Silica (SiO_2) deposition. 200 nm PECVD SiO_2 for isolation.

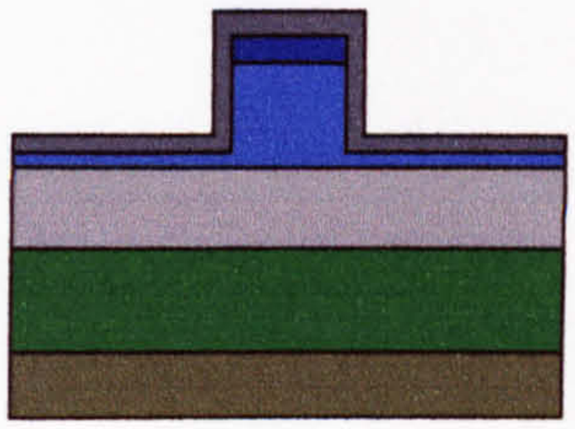

Fig. 6.8. SiO_2 deposition.

Spinning Resist. The next photolithography step, which starts here, will define a window on top of the ridge. This alignment is critical and therefore more accuracy is needed. The resist used in this step is S1805. This resist has exactly the same properties as S1818 described in chapter 4. The difference is that for the same spinning conditions, S1805 will be 0.5 μm thick as oppose to 1.8 μm. This thinner resist allows for a contact alignment, which is physically closer to the semiconductor. This, in consequence, makes the alignment more accurate. S1805 was spun at 4000 rpm for 30 sec.

Softbake. 90 °C for 30 min.

Exposure. Window opening mask. The exposure time is now 3.5 sec for S1805.

Development. The development of the contact window is done in a number of repetitive steps. The same 1:1 mixture used for S1818 is used for S1805. The sample has to be developed for 15 sec then rinse in RO water and blow-dry. The

sample is inspected under the microscope using a yellow filter. If the window is not open yet, develop for 5 more seconds. Rinse, blow-dry and inspect under the microscope. Repeat this steps until the contact window is clearly defined.

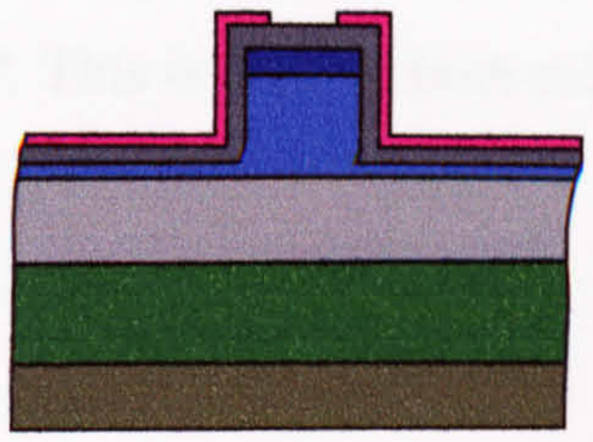

Fig. 6.9. Contact window definition.

Hard Bake. The resist is baked at 120° C for 30 min. This will harden the resist allowing it to stand the HF etch next.

Wet Etching. The SiO_2 exposed by the window opened in the resist was wet etched using 4:1 buffered HF. This etching will eventually create a direct contact to the semiconductor surface where current can be injected.

Strip resist. Acetone. Hot bath at 60 ° C for 10 min if necessary.

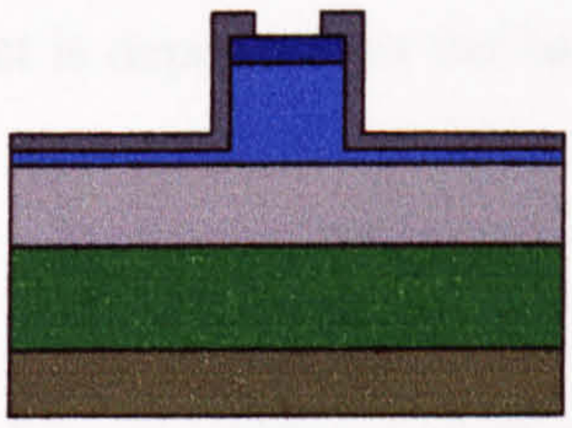

Fig. 6.10. Sample after contact window opening.

Spinning resist. S1818, 4000 rpm, 30 sec.

Softbake. ~ 90 °C for 30 min.

Exposure. Contact mask, 11 sec.

Development. 1:1 mixture, 75 sec.

Metal deposition. Evaporated p-contact. To make sure the ridge's walls are covered after the "standard" evaporation, a further 150 nm of gold are deposited with the sample rocked 45°. This is done in both sides of the ridge.

Lift-off. Acetone.

Thinning. One of the most important features in a laser are the facets. The facets act as mirrors defining the laser cavity. The performance of the laser depends, among other things, on the quality of the facets. To achieve high quality facets, the sample has to be cleaved without introducing stress to the material. The samples will cleave without any stress if it is thin.

The sample is mounted on a cover slip epi-side down using S1818 resist and baked for at least 20 min. The sample is then lapped using 9 μm Al_2O_3 powder until a thickness around 200 μm is achieved. Using 3 μm Al_2O_3 powder, the sample is lapped further until a thickness of ~160 μm is achieved. The sample can now be remove from the mount and take to the next step.

Metal deposition. N-contact is deposited on the backside on the sample (the one that has just been lapped).

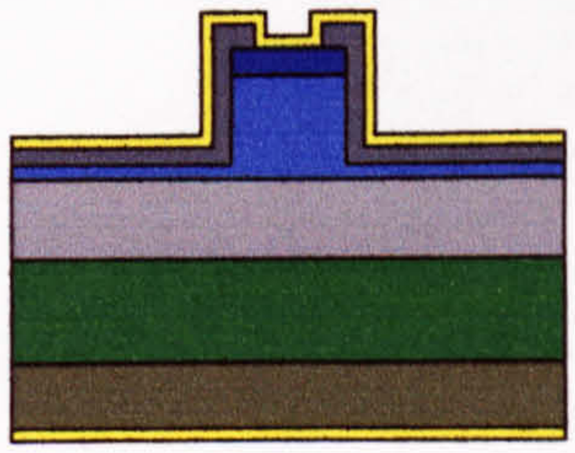

Fig. 6.11. Final laser structure.

Annealing. In a laser structure current will be injected to the semiconductor and therefore ohmic contacts are required to reduce the resistance to the current flow. Normally, after depositing metal to a semiconductor surface, a Schottky contact

is generated. By annealing the sample, this Schottky contact can be turned into an ohmic one. Annealing is a thermal process that promotes the diffusion of the metal into the semiconductor. This diffusion will create a smooth metal-semiconductor interface in terms of the conduction band energy levels and therefore an ohmic contact is obtained. The annealing temperature is set by the eutectic temperature of the metal-semiconductor system [9] and the annealing method used. In this case, rapid thermal annealing (RTA) is used. The sample is annealed at 360 °C for 60 sec.

6.5 Experimental results.

Experiments were carried out using a pulsed laser current supply to forward bias the gain section. A DC voltage supply was used to reverse bias the absorber. The light from the laser was coupled into a single mode fibre, which was connected either to a 45 GHz InGaAs photodetector and sampling oscilloscope or to an optical spectrum analyser. The experimental set-up is shown in Fig. 6.12.

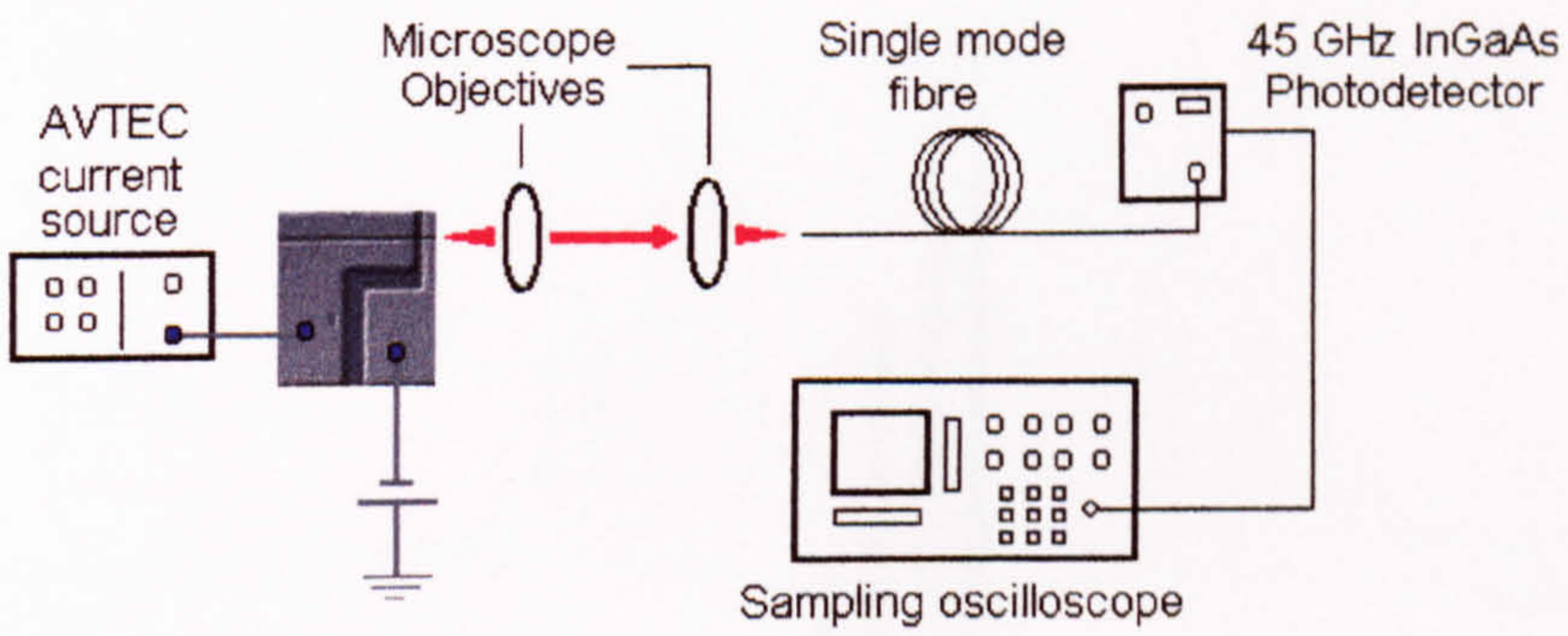

Fig 6.12. Experimental set-up.

The devices were initially tested without any bias applied to the absorber, in a non Q-switched regime. Fig. 6.13 shows the light-current characteristics of a typical device where the threshold current was 76 mA. The light-current curve shows the well-known "snap-on" behaviour commonly observed in lasers with a saturable absorber in the cavity. The presence of the saturable absorber is also indicated by the slightly increase in the threshold current from that of an all-

active laser of 500 nm, which was measured at around 50 - 60 mA. Fig. 6.14 shows the operating spectrum for the device, with zero reverse bias applied to the absorber section, centred at 1.582 μm.

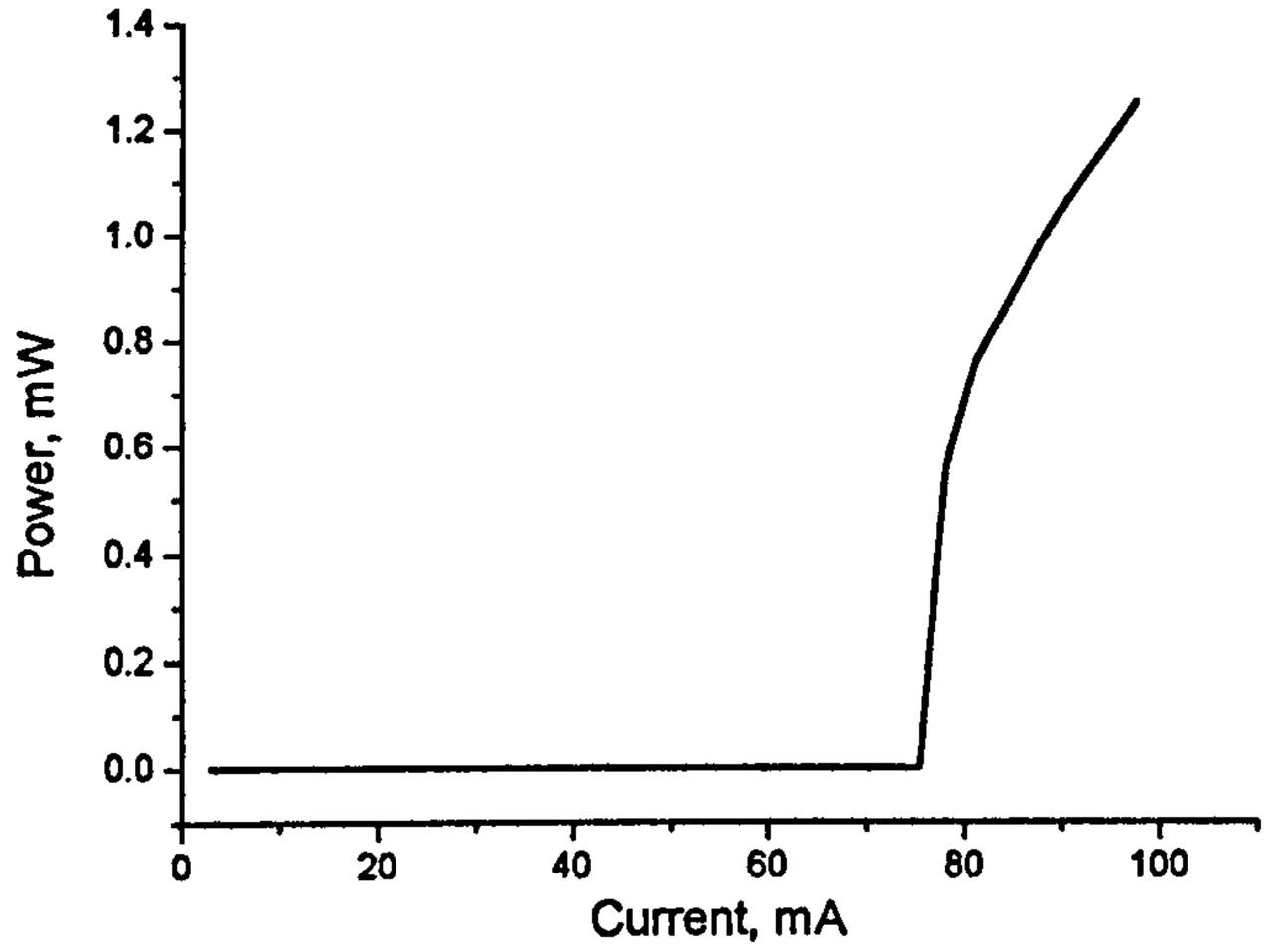

Fig. 6.13. Light-current curve of the two-section InGaAs/AlGaInAs laser. The two different slopes follow the "snap-on" behaviour due to the presence of the saturable absorber in the cavity.

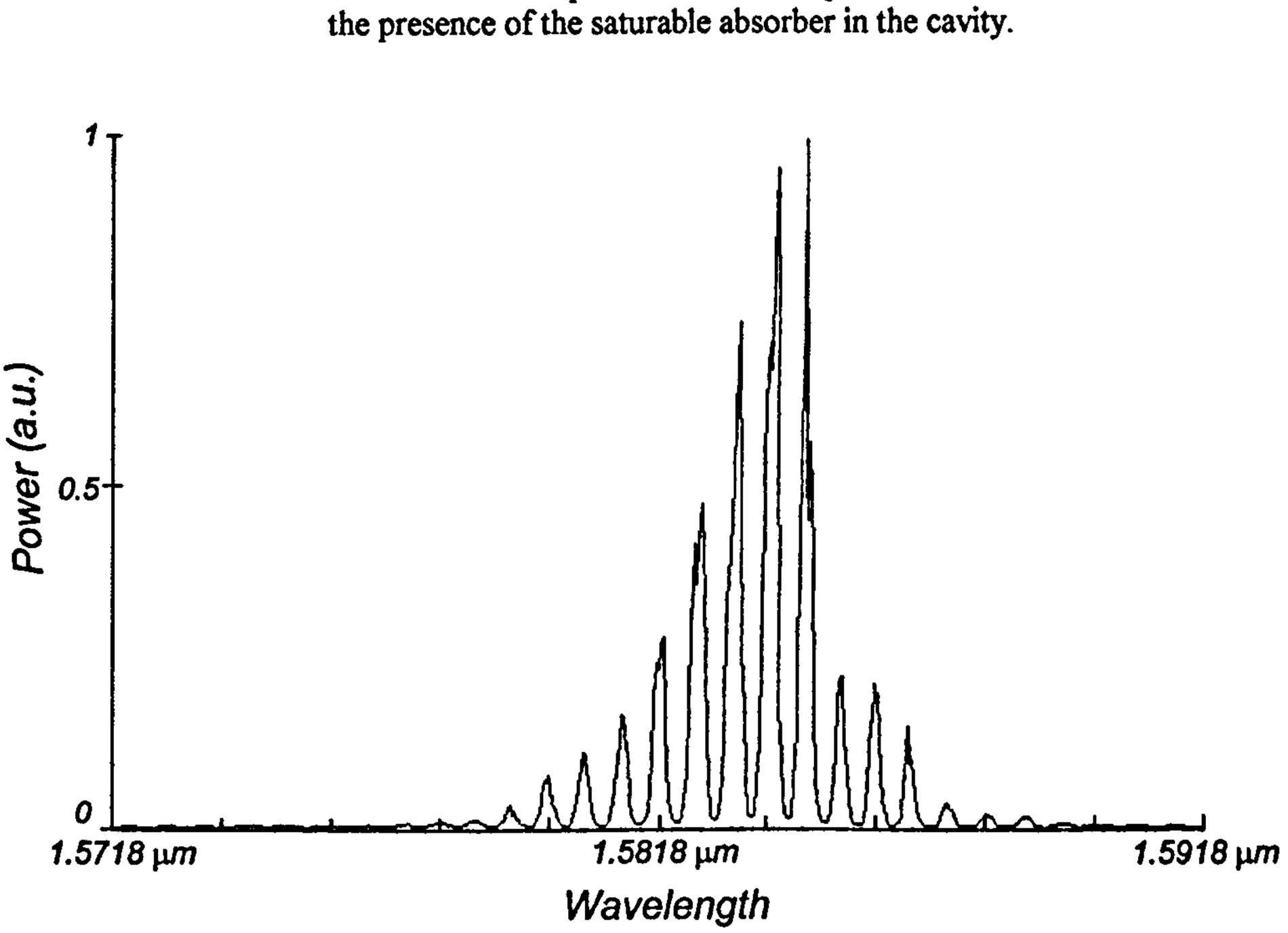

Fig. 6.14. Optical spectrum at zero bias.

To Q-switch the laser, the absorber was reverse biased between 1 V and 5 V. The change in the spectrum was then monitored. For specific bias conditions, an

increase in the number of longitudinal modes, suggesting short pulse formation in the cavity, was observed. Fig. 6.15 shows the operating spectrum for the laser with 1.2 V reverse bias on the absorber and pumped just above threshold, which resulted to be the most stable conditions for Q-switching. A shift of 7.5 nm to longer wavelengths can be seen in the spectrum of Fig. 3 compared with the spectrum in Fig. 2. This is also explain by the presence of the saturable absorber. Maintaining the bias conditions mentioned above, the optical signal was connected to the photodetector and Q-switched operation observed at a repetition rate of about 1 GHz. The pulse train is shown in Fig. 6.16 where the pulse width FWHM is < 500 ps limited only by the speed of the sampling oscilloscope. Finally, the pumping conditions were varied and as you increase the current in the bias section, the repetition rate could be controlled between 1 GHz and 2.5 GHz.

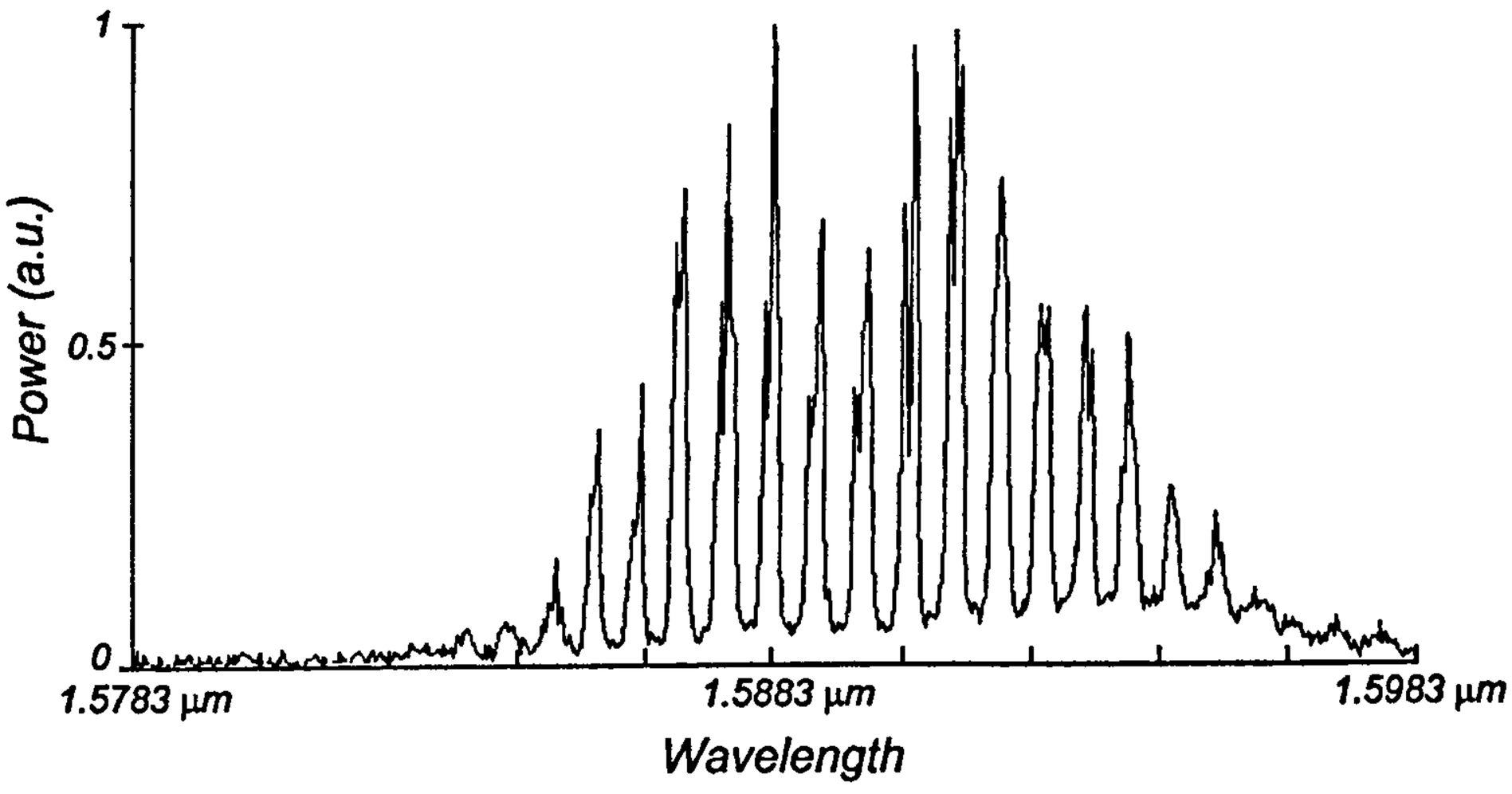

Fig. 6.15. Optical spectrum at 1.2 V reverse bias and pumped current just above threshold.

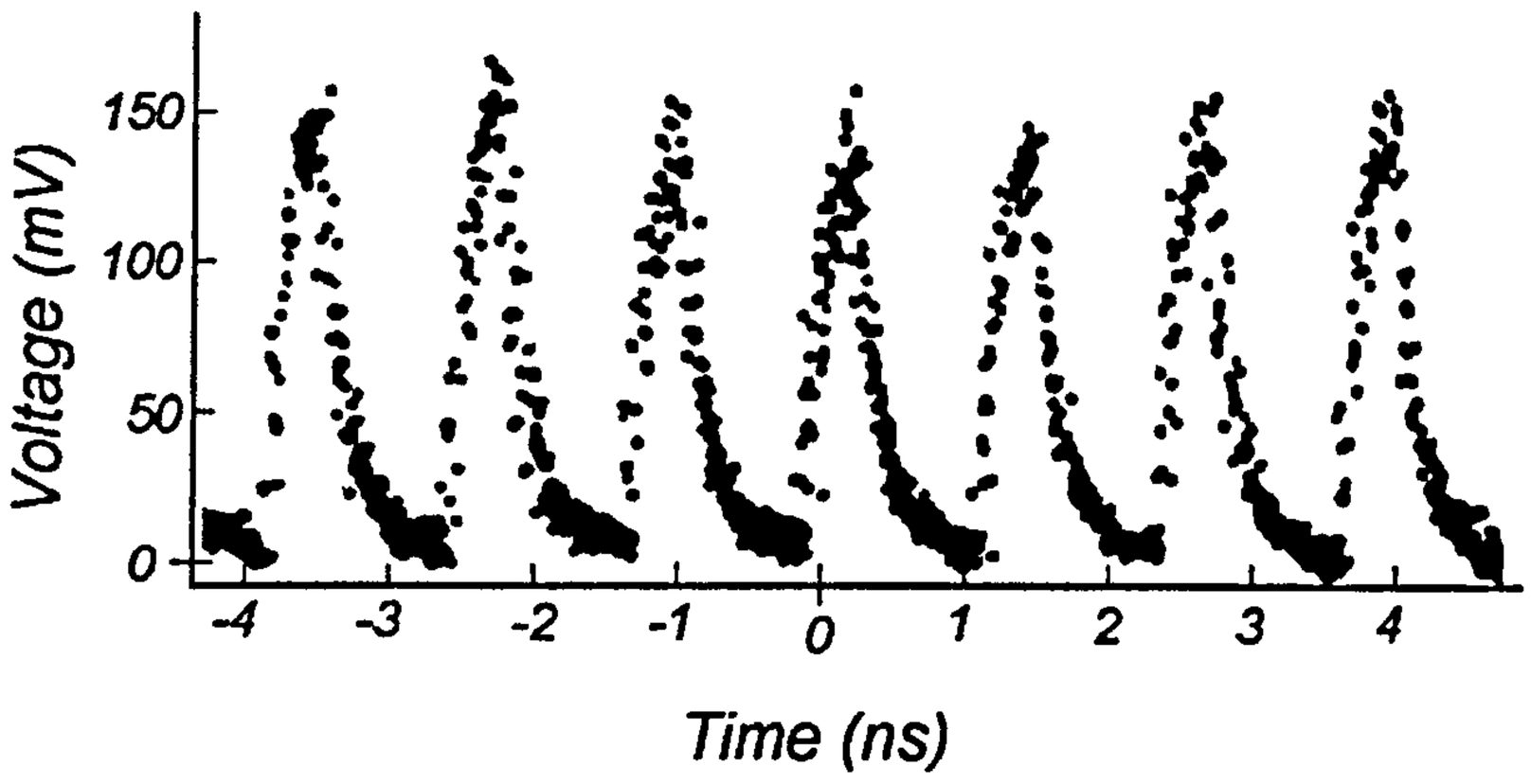

Fig. 6.16. Pulse train extracted from the sampling oscilloscope at approximately 1GHz.

6.6 Conclusions.

In this chapter, we have provided the basis of q-switching as well as the fabrication process. More important, we have also demonstrated passive q-switched operation of InGaAs/AlGaInAs MQW lasers with repetition rates of 1 to 2.5GHz. The devices a real alternative to conventional InGaAsP devices at communications wavelengths. The fact that this lasers can be used in conjunction with an ORE device has still to be demonstrated.

6.7 References.

1. M. Allovon and M. Quillec,"Interest in AlGaInAs on InP for optoelectronic applications," *IEE PROCEEDINGS-J*, vol. 139, pp. 148-152, 1992.

2. J. Minch, S. H. Park, T. Keating and S. L. Chuang, "Theory and Experiment of $In_{1-x}Ga_xAs_yP_{1-y}$ and $In_{1-x-y}Ga_xAl_yAs$ Long-Wavelength Strained Quantum-Well Lasers," *IEEE Journal of Quantum Electronics*, vol. 35, pp. 771-782, 1999.

3. T. Higashi, S. J. Sweeney, A. F. Phillips, A. R. Adams, E. P. O'reilly, T. Uchida, T. Fujii, "Observation of Reduced Nonradiative Current in 1.3-μm AlGaInAs-InP Strained MQW Lasers," *IEEE Photonics Tech Letters*, vol. 11, pp. 409-411, 1999.

4. J. W. Pan and J. I. Chyi, "Theoretical Study of the Temperature Dependence of 1.3-μm AlGaInAs-InP Multiple-Quantum-Well Laser," *IEEE Journal of Quantum Electronics*, vol. 32, pp. 2133-2138, 1996.

5. V. Loyo-Maldonado, S. D. McDougall, J. H. Marsh, J. S. Aitchison and C. C. Button, "Demonstration of passive Q-switching in multiquantum well InGaAs/AlGaInAs diode laser," *Electron. Lett.* vol.36, pp. 952-953, 2000.

6. D. Z. Tsang and J. N. Walpole, "Q-Switched Semiconductor Diode Lasers," *IEEE Journal of Quantum Electronics*, vol. QE-19, pp. 145-156, 1983.

7. P. Vasilev, *Ultrafast Diode Lasers: Fundamentals and Applications*, Chapter 3, Artech House, 1995

8. J. Böhrer, A. Krost and D. B. Bimberg, "Composition dependence of band gap and type of lineup in $In_{1-x-y}Ga_xAl_yAs$/InP heterostructures," *Applied Physics Letters*, vol. 63, pp. 1918-1920, 1993.

9. S. K. Ghandhi and L. Lane, *VLSI Fabrication Principles.* 2nd ed., John Wiley & Sons Inc. 1994.

7. Future Work.

7.1 Introduction.

A number of future experiments and ideas have been identified towards the optimisation of the ORE devices described on this thesis. The aim of this chapter is to state these ideas for future development. Perhaps the most important of the ideas is the integration of a photoconductive switch in the ORE devices to allow on-chip characterization of the electrical pulses. The photoconductive switch is explained in some detail.

7.2 Higher peak power.

Previous optical rectification experiments on bulk GaAs use peak powers of at least three orders of magnitude more than the peak power used on this thesis (see table 2.1). The use of higher peak power in our structures may increase the amplitude of the optical rectification signal but may also generate a higher background signal produced by MPA. In any case, the experiment will help to the further understanding of the devices. The maximum peak power that can be sustained by the ORE devices before facet damage is not known. From previous

experience if the optical pulse width is kept at ~300 fs at tens of MHz repetition rate, powers of at least 5 kW can be achieved.

7.3 Use of 1ps pulses.

The use of femtosecond pulses in ORE experiments allows the use of high peak power. However, by launching femtosecond optical pulses in an ORE device, femtosecond electrical pulses will be generated. The loss experimented by electrical femtosecond pulses travelling in a transmission line will be considerably greater that the one experimented by picosecond pulses. The use of picosecond pulses will inherently generate a bigger rectification signal without necessarily increasing the optical peak power. The use of 1 ps optical pulses is believed to be a very interesting experiment to clarify the importance of a velocity-matched device.

7.4 Detailed analysis of the optical signal.

Due to the lack of availability of equipment while doing the ORE4 experiments, the input and output optical signal were never studied in detail. The output optical signal can provide information on whether absorption is happening in the device or not. It can also determine the corresponding absorption mechanism.

7.5 Photoconductive switch.

Ultrafast electronics and optolectronics are common topics nowadays. Over the last twenty years, ultrafast instrumentation has been developed in order to characterise new materials and devices. The interaction of ultrashort laser pulses with a variety of crystals for generation of electrical pulses has left behind the typical detection systems (sampling oscilloscopes) and new techniques for characterisation of electrical pulses have been developed. The most common and well-documented techniques for high time resolution of electrical signals are photoconductive sampling [1] and electro-optic sampling [2]. Photoconductive

sampling is preferred in our case because its potential for integration with the ORE devices. A comparison between these two techniques is given in [3]. There have been many materials utilised as a photoconductive substrate, but radiation damaged silicon-on-sapphire (SOS) and radiation damaged GaAs have been the most reported in the literature. These materials show very small carrier lifetimes, which is desirable for ultrafast switching.

7.5.1 The photoconductive effect.

The resistivity of semiconductor materials such as GaAs, or silicon can be altered by illuminating the surface of the material with an optical source whose photon energy is greater then the semiconductor bandgap energy. The absorbed photons generate electron-hole pairs with an efficiency near unity. This effect, termed photoconductivity, has been used for numerous applications, principally in high-speed photo-detectors [4] and high-speed sampling gates [1] with sub-millimetre dimensions, and high-power switches [5]. The rate at which the photoconductive effect produces electron and hole current carriers in bulk semiconductor material is dependent only on the power of the optical source.

Since the resistivity change in a photoconductive device is completely dependent upon the illuminating optical source and very short, high-power optical pulses can be easily generated with lasers, the magnitude of the resistance change can be made very large in a very short period. Thus, the resistance of a photoconductive device can be varied over many orders of magnitude, from a relatively large impedance to a relatively low impedance in a very short period of time, and serve as a very fast-closing, very precisely controlled, high-power or low-power switch.

7.5.2 The switch.

Photoconductive switches use carriers in excess to create a short circuit or an open circuit between two metal contacts separated by a semiconductor medium. Radiation-damaged Silicon-on-Sapphire (RD-SOS) [6], radiation damaged Gallium Arsenide (RD-GaAs) [7] and, in recent years, low temperature grown

GaAs (LT-GaAs) [8] have commonly been used as the photoconductive material between the metal contacts. The typical photoconductive switch configuration is a microwave waveguide with a gap, which exposes the photoconductive material used as a substrate. An schematic of a photoconductive switch is shown in Fig. 7.1.

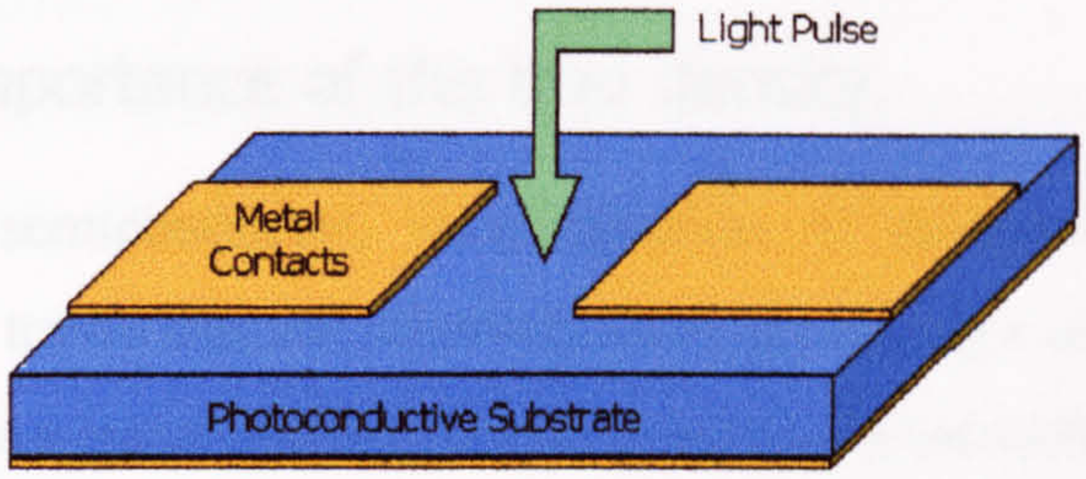

Fig. 7.1. Schematic diagram of a photoconductive switch.

The operation of the photoconductive switch can be described as follows. Typically, one end of the waveguide is biased at a few volts. When the gap in the waveguide is not optically illuminated little current flows across the gap. Illumination of the photoconductive material within the gap by photons whose energy exceeds the energy difference between the conduction and valence bands of the semiconductor results in the photogeneration of electron-hole pairs. These photogenerated free carriers change the conductivity within the gap and allow current to flow. The temporal duration of the electrical pulse generated is primarily determined by the lifetime of the photogenerated carriers as well as by the geometry of the switch. The photoconductive response in some reported switches, is as little as 700fs FWHM [9]. The initial pulse at zero propagation distance has a fast rise time determined by the laser pulse width and the time constant of the circuit. The fall time, which is usually longer, depends mostly on the decay of the photogenerated carriers.

Ultrafast photoconductive switches can also be use to sample transient electrical waveforms. If the switch is illuminated with an ultrashort optical pulse during the passage of a transient electrical waveform, current will flow across the gap for

the duration of the sampling period determined by the impulse-response of the switch and the temporal duration of the optical pulse.

The metal contacts forming the switch are normally chosen to be ohmic contacts, in this way the current will flow easily from the substrate to the metal.

7.5.2.1 The importance of the trap density.

In an intrinsic semiconductor, recombination is determined by radiative transitions. These transitions are relatively slow, producing a long-lasting current waveform which is a major problem for picosecond photoconductor applications. Direct-gap semiconductors have radiative lifetimes of a few nanoseconds. Indirect-gap materials can have lifetimes that are considerably longer, extending into the millisecond range in some cases. Clearly, alternative materials and techniques must be used to produce the fast current decays that are necessary for picosecond applications.

An effective method of reducing the free carrier lifetime is to introduce a moderate density of defects into the semiconductor which act as a traps and recombination centres. This has been achieved by radiation damage, diffusion of impurities, or the use of materials with large densities of naturally occurring defects such as polycrystalline and amorphous semiconductors. The low temperature growth of GaAs has also been used to introduce traps.

The capture time, τ_c can be estimated from the equation 7.1:

$$\tau_c = \frac{1}{N_t \sigma_c V_{th}} \tag{7.1}$$

where N_t is the trap density, σ_c the capture cross section, and V_{th} is the thermal carrier velocity.

The dependence of the relaxation time as a function of the dose when radiation damage is the method to induce traps can be found in Ref. [6].

A potential method to increase the number of traps in the semiconductor is the introduction of vacancies. This method has not been reported before for the fabrication of photoconductive switches. Free vacancy disordering in semiconductor material is among the facilities available in the department would be worth exploring it mainly because this technique is highly area selective. Using this technique, small and localised switches can be fabricated.

7.5.3 Photoconductive sampling system.

Here we propose photoconductive sampling as being the most efficient way to detect the electrical pulses generated by an optical rectification device. Typical set-ups can be found in [10] and [11]. An optical pulse will generate the electrical pulse that will travel along the microwave waveguide through the ORE device while a second optical pulse will switch on and off the photoconductive switch. A schematic diagram of the sampling system is shown in Fig. 7.2. The input optical beam, the generation beam, passes through an optical chopper and is focused onto the optical rectification device. The second optical beam, the sampling beam, travels a path with a variable length and is focused onto the photoconductive switch. The path length of the sampling beam can be varied in such a way that it arrives at the sampling switch before, during, or after the arrival of the optical pulse at the optical rectification device. The output from the sampling switch is fed into the input of a lock-in amplifier. In this case, the wavelength of the sampling beam is different to the wavelength of the generation beam, which produces the ORE. An OPO can be used as generation beam while a Ti:Sapphire or even a Nd:YAG laser can be used as sampling beam. If the switch can be activated by TPA, then the OPO beam can be used as generation and sampling beam. This option may also been considered.

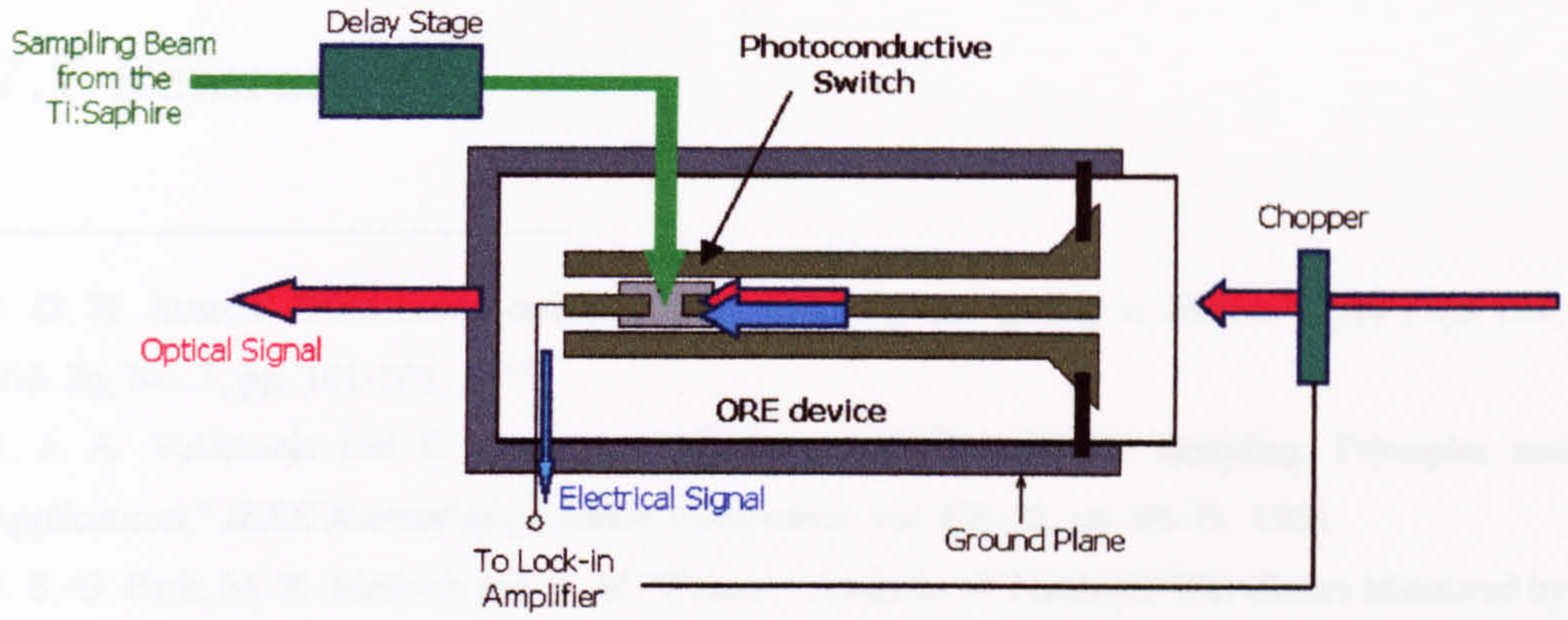

Fig. 7.2. Optical rectification device with an integrated photoconductive switch.

In the optical rectification device, the surface material is AlGaAs, which gives the possibility to integrate a photoconductive switch on the same substrate. A small area of the surface can be selected to introduce some traps and reduce the capture time. If the gap between the electrodes is located in this area, the switch is then completed.

7.6 Conclusions.

A few future experiments have been proposed in this chapter. Undoubtedly, the integration of a photoconductive switch in the ORE devices will complete the electrical characterisation of the devices. The integration of the switch present fabrication challenges such as the introduction of traps in a localised area and the location of the switch on top of the optical ridge.

7.7 References.

1. D. H. Auston, "Picosecond optoelectronic switching and gating in Silicon," *Appl Phys Lett*, Vol. 26, No. 3, pp. 101-103, 1975.

2. J. A. Valdmanis and G. Mourou, "Subpicosecond Electrooptic Sampling: Principles and Applications," *IEEE Journal of Quantum Electronics*, vol. QE-22, pp. 69-78. 1986.

3. S.-G. Park, M. R. Melloch and A. M. Weiner, "Analysis of Terahertz Waveforms Measured by Photoconductive and Electrooptic Sampling," *IEEE Journal of Quantum Electronics*, vol. 35, pp. 810-819. 1999.

4. R. B. Hammond, "In:P:Fe Photoconductors as Photodetectors," *IEEE Trans Electron Devices*, vol. ED-30, pp. 412-415, 1983.

5. G. Mourou et al., "High Power Switching with Picosecond Precision," *Appl Phys Lett*, Vol. 35, pp. 492-495, 1979.

6. P. R Smith, D. H. Auston, A.M. Johnson and W. M. Augustyniak, "Picosecond photoconductivity in radiation-damaged silicon on sapphire," *Appl Phys Lett*, Vol. 38, No. 1, pp. 47-50, 1981.

7. D. H. Auston and P. R. Smith, "Picosecond optical electronic sampling: Characterization of high-speed photodetectors," *Appl Phys Lett*, Vol. 41, No. 7, pp. 599-601, 1982.

8. Y. Cai et al., "Design and performance of singular electric field terahertz photoconducting antennas," *Appl Phys Lett*, Vol. 71, No. 15, pp. 2076-2078, 1997.

9. H.-H. Wang, P. Grenier, J. F. Whitaker, H. Fujioka, J. Jasinski and Z. Liliental-Weber "Ultrafast Response of As-Implanted GaAs Photoconductors," *IEEE Journal of Selected Topics in Quantum Electronics*, vol. 2, pp. 630-635, 1996.

10. S. C. Moss, J. F. Knudsen and D. D. Smith, "Linearity of response of ultrafast photoconductive switches: critical dependence upon ion-implantation and fabrication conditions," *Journal of Modern Optics*, vol. 35, pp. 2007-2030, 1988.

11. M. Matloubian, H. Fetterman, M. Kim, A. Oki, J. Camou, S. Moss and D. Smith, "Picosecond Optoelectronic Measurement of S Parameters and Optical Response of an AlGaAs/GaAs HBT," *IEEE Trans on Microwave Theory and Techniques*, vol. 38, pp. 683-686, 1990.

Conclusions.

Throughout the content of this thesis, the design, fabrication and characterization of an optical rectification device have been studied. In the end, single-mode optical waveguides in conjunction with slow-wave electrodes were used to create a device where optical rectification was detected. With only 1.8 dB/cm optical propagation losses, the ORE devices are low loss at communication wavelengths. The CPW lines used in ORE devices present very high loss and velocity-matched devices are paramount for signal detection. Due to the high precision and repeatability while fabricating ORE devices, e-beam lithography and lift-off techniques were the preferred method for fabrication. Four generation of devices were necessary to achieve a device from which we could extract an optical rectification signal without being masked by another signal produce by free carrier absorption mainly in the form of two photon absorption. In our final experiment, we managed to obtain a signal with the following characteristics: 1) Pulsed signal at the repetition rate of the laser beam. 2) A signal with broad frequency spectrum suggesting very short pulses and, 3) A signal with a $\sin^2$ polarization dependence. These are all requisites and characteristics of an optical rectification signal. The signal was obtained using an OPO operation at wavelengths ranging from 1440 nm to 1580 nm. The pulse width was 300 fs FWHM and the repetition rate ~88 MHz. The estimated peak power going into the ORE device is around 0.5 kW. To be able to detect rectification signal with

such a low power is an achievement on its own which is never been reported before. The rectification signals were small in magnitude, around –70 dBm, and therefore they had to be detected using a microwave spectrum analyser with a noise floor level of –120 dBm. The obtained results clearly show the potential of the devices for optical to microwave conversion.

Good results were also obtained on the semiconductor lasers but we believe that further optimisation of the ORE devices needs to be done before these lasers can be used to generate rectification signals. Nevertheless, these lasers were the first demonstration of passive q-switching in Al-quaternary material system.

Finally, a big emphasis is made on the integration of a photoconductive switch with the ORE devices. Due to the amount of time and effort required to eliminate all the parasitic effects masking the rectification signal, this option could not be explored in this thesis but the conception of the idea is developed in chapter 7.

Optical rectification in semiconductor waveguides shows great potential for optical to microwave conversion. This thesis is the first attempt to create a device of such a kind and should be use as the basis for future research. The topics covered in this work are from the most variety ranging from optical waveguide design and fabrication, CPW design and fabrication, semiconductor lasers design and fabrication, microwave characterisation of transmission lines, high-speed characterisation of optoelectronic devices, non-linear optics and multi-photon absorption phenomena. Therefore is obvious that a more in deep research has to be done in most of these topics in order to create the ultimate ORE device.